# STEM-EELS investigation of ferroelectric proximity effects in transition metal oxide thin films (SrRuO , NdNiO )

Chia-Ping Su

université PARIS-SACLAY

# STEM-EELS investigation of ferroelectric proximity effects in transition metal oxide thin films ($SrRuO_3$, $NdNiO_3$)

*Étude STEM-EELS des effets de proximité ferroélectriques dans les films minces d'oxyde de métal de transition ($SrRuO_3$, $NdNiO_3$)*

**Thèse de doctorat de l'université Paris-Saclay**

École doctorale n° 564: Physique en Ile-de-France (EDPIF)
Spécialité de doctorat: Physique
Graduate School: Physique, Référent: Faculté des sciences d'Orsay

Thèse préparée dans le **Laboratoire de Physique des Solides** (Université Paris-Saclay, CNRS), sous la direction d'**Alexandre GLOTER**, directeur de recherche

**Thèse soutenue à Paris-Saclay, le 10 février 2023, par**

**Chia-Ping SU**

## Composition du jury

Membres du jury avec voix délibérative

| | |
|---|---|
| **Pierre-Eymeric JANOLIN**<br>Professeur des Universités, Laboratoire Structures, Propriétés et Modélisation des Solides (UMR 8580), CentraleSupélec, Université Paris-Saclay, France | Président |
| **Bénédicte WAROT**<br>Directrice de recherche, Centre d'Élaboration de Matériaux et d'Etudes Structurales, France | Rapportrice & Examinatrice |
| **Jérôme PACAUD**<br>Maître de conférences (HDR), Institut Pprime (UPR 3346), Université de Poitiers, France | Rapporteur & Examinateur |
| **Matthieu BUGNET**<br>Chargé de recherche, Laboratoire Matériaux: Ingénierie et Science (UMR 5510), Université de Lyon, France et Visiting associate professor, University of Leeds, United Kingdom | Examinateur |

THESE DE DOCTORAT
NNT : 2023UPASP018

université PARIS-SACLAY

ÉCOLE DOCTORALE
Physique en Île-de-France (PIF)

**Titre:** Étude STEM-EELS des effets de proximité ferroélectriques dans les films minces d'oxyde de métal de transition ($SrRuO_3$, $NdNiO_3$)

**Mots clés:** microscopie électronique à transmission à balayage, spectroscopie de perte d'énergie des électrons, oxyde de métal de transition, ferroélectricité, effet interfacial, nanostructure

**Résumé:**
Développer les propriétés physiques uniques des couches minces d'oxyde de métal de transition (TMO) est un objectif de longue date en physique du solide. Dans le cas où un couche mince de TMO est en contact avec un matériau ferroélectrique (FE), la ferroélectricité impacte profondément les propriétés structurelles et électroniques du TMO, variant éventuellement avec la configuration de la polarisation FE. Cependant, la complexité des effets d'interface nécessite encore une compréhension globale notamment en raison de la richesse des degrés de liberté impliqués.
Cette thèse explore principalement les effets d'interface entre le matériau FE et les couches minces de TMO à l'échelle nanométrique. La microscopie électronique à transmission à balayage (STEM) en conjonction avec la spectroscopie de perte d'énergie électronique (EELS) fournit une étude microscopique des couches minces, de leur hétérostructures et nanostructures avec une résolution spatiale et spectrale élevée. Dans un premier temps, les signatures spectroscopiques EELS des excitations plasmoniques du massif et des surfaces sur des couches minces et des nano-structures de $SrVO_3$ sont abordées. L'objectif est de mettre en relation ces excitations avec la structure électronique et la nanostructuration sur un métal corrélé référentiel afin d'établir la sensibilité à une description nanométrique d'une transition métal-isolant de ces signatures. La présence de fortes résonances plasmoniques de surface localisées avec un facteur de qualité élevé est également démontrée sur diverses nanostructures à la fois par des simulations et des expériences, indiquant que $SrVO_3$ a le potentiel en tant que matériau plasmonique alternatif. Deuxièmement, l'évolution des configurations des domaines FE pour les films minces à hétérostructure FE $PbTiO_3$ pris en sandwich par les électrodes à base de TMO ($SrRuO_3$) est observée en fonction de l'épaisseur du film. En augmentant l'épaisseur, les domaines FE évoluent d'un type de complexe de fermeture de flux vers des domaines de type $a/c$. En outre, l'analyse microscopique révèle que la configuration du domaine FE imprime sur la structure des électrodes $SrRuO_3$, par exemple en contrôlant leur mosaïcité cristallographique. Enfin, des hétérostructures FE $Pb(Zr,Ti)O_3$ avec différentes couches de TMO ($LaMnO_3$ et $NdNiO_3$) et avec des épaisseurs de film FE variables sont etudiés. Nous rapportons que la configuration FE peut être contrôlée par le choix de la couche tampon TMO en raison de different mecanismes de relaxation des contraintes dans ces hétérostructures. Une évolution similaire des contrainte peut être obtenue en modulant l'épaisseur du film FE, contrôlant ainsi les propriétés structurelles et électroniques du $NdNiO_3$ voisin.
Ces descriptions nanométriques STEM-EELS rapportent plusieurs couplages et contrôles structurels différents aux interfaces entre le matériau FE et la couche mince de TMO permettant un développement ultérieur dans le TMO nanostructuré accompagné de matériau FE.

université PARIS-SACLAY

ÉCOLE DOCTORALE
Physique en Île-de-France (PIF)

**Title:** STEM-EELS investigation of ferroelectric proximity effects in transition metal oxide thin films ($SrRuO_3$, $NdNiO_3$)

**Keywords:** scanning transmission electron microscopy, electron energy-loss spectroscopy, transition metal oxide, ferroelectricity, interfacial effect, nanostructure

**Abstract:**
Developing the unique physical properties of transition metal oxide (TMO) thin films has been a long-standing goal in solid-state physics. In case a TMO thin film is in contact with a ferroelectric (FE) material, the ferroelectricity profoundly impacts the structural and electronic properties of the TMO, possibly varying with the configuration of the FE polarization. However, the complexity of the interfacial effects still needs a comprehensive understanding due to the rich degrees of freedom involved.
This thesis mainly explores the interfacial effects between FE material and TMO thin film at the nanoscale. Scanning transmission electron microscopy (STEM) in conjunction with electron energy-loss spectroscopy (EELS) provides microscopic investigations of thin film heterostructures and nanostructures with high spatial and spectral resolution. At first, the EELS spectroscopic signatures of bulk and surface plasmonic excitations on $SrVO_3$ thin films and nanostructures are addressed. The goal is to relate these excitations to the electronic structure and the nanostructure on a referential correlated metal, in order to establish how sensitive these signatures are to a nanometric description of a metal-insulator transition. The presence of intense localized surface plasmon resonances with a high-quality factor is also demonstrated on the various nanostructures through both simulations and experiments, indicating $SrVO_3$ has the potential as an alternative plasmonic material. Secondly, the evolution of FE domain configurations for FE $PbTiO_3$ thin film heterostructures sandwiched by TMO-based electrodes ($SrRuO_3$) is observed as a function of FE film thickness. By increasing the FE film thickness, the FE domain configuration evolves from a complex flux-closure type to a $a/c$ type domain. Further, microscopic analyses reveal that the FE domain configuration imprints on the crystal orientations of the $SrRuO_3$ electrodes, controlling their crystallographic mosaicity. Lastly, FE $Pb(Zr,Ti)O_3$ thin film heterostructures with different TMO buffer layers ($LaMnO_3$ and $NdNiO_3$) and with varying FE film thicknesses are investigated. We report that the FE domain configuration can be controlled by the choice of buffer layer due to different strain relaxation mechanisms within the whole heterostructure. Moreover, modulating the FE film thickness can affect the structural and electronic characteristics of the neighboring $NdNiO_3$ layer.
These STEM-EELS nanometric descriptions report varying couplings and structural control at the interfaces between FE material and TMO thin film, allowing further research into ferroelectric proximity effects in nanostructured TMO.

# Résumé

L'oxyde de métal de transition (TMO) et ses hétérostructures font partie des sujets fascinants de la physique de l'état solide. Les métaux de transition, comme le vanadium ($3d^1$) et le nickel ($3d^7$), ont des orbitales $d$ partiellement remplies, et présentent de fortes interactions électron-électron. Dans le cas de la pérovskite TMO (c'est-à-dire la structure $ABO_3$), qui est constituée de 6 atomes d'oxygène liés à un métal de transition central, l'hybridation entre le métal de transition-3$d$ et l'oxygène-2$p$ donne lieu à une levée de dégénérescence de l'énergie des orbitales $d$ et participe au couplage entre degrés de liberté de charge, de réseau, d'orbite et de spin de la TMO. De nombreuses propriétés uniques résultent de ces degrés de liberté et de leurs couplages, comme la transition métal-isolant (MIT), la supraconductivité à haute température et une magnétorésistance colossale, qui font défaut aux semi-conducteurs classiques ou à d'autres composés métalliques.

Il est possible de renforcer artificiellement le couplage entre les degrés de liberté de la charge et du réseau, par exemple à l'interface entre un matériau ferroélectrique et un film mince de TMO. Il est alors possible de moduler les propriétés structurelles et électroniques de TMO par différentes polarisations ferroélectriques et configurations de domaines du matériau ferroélectrique adjacent.

Ces recherches ont été menées en collaboration avec plusieurs groupes de recherche de l'Université de Genève et de l'Université de Strasbourg, fournissant des techniques d'analyse planaire ou massique, telles que la microscopie à force atomique (AFM), la diffraction des rayons X (XRD), la microscopie à force piézoélectrique (PFM), et des mesures de transport. Cependant, il est nécessaire d'étudier les propriétés physiques près de l'interface à l'échelle nanométrique, en particulier à l'échelle atomique, ce qui peut être réalisé par la microscopie électronique à transmission à balayage (STEM) en conjonction avec la spectroscopie de perte d'énergie des électrons (EELS).

Tout au long de la thèse, nous présentons trois exemples de TMO. La première partie de cette thèse analyse les propriétés plasmoniques du $SrVO_3$ (SVO). Le SVO est considéré comme un prototype pour l'étude des interactions fortes électroniques, et sa signature spectroscopique dans les gammes de l'infrarouge et du visible n'a pas encore été rapportée à l'échelle nanométrique. De plus, cette étude peut être utilisée pour démontrer l'efficacité de notre EELS monochromatique dans la mesure des excitations à basse énergie de TMO. La présence de résonances de plasmons de surface localisés (LSP) avec des facteurs de haute qualité est démontrée sur les différentes nanostructures à la fois par des simulations et des expériences. L'objectif de cet exemple est de relier les structures électroniques de TMO et les effets de surface et d'interface. Ensuite, pour en revenir aux matériaux ferroélectriques, nous étudions une série d'hétérostructures ferroélectriques en couches minces de $PbTiO_3$ (PTO) prises en sandwich par des électrodes de $SrRuO_3$ (SRO) à base de TMO, dans lesquelles les couches de PTO sont d'épaisseurs variables. Les configurations de domaines ferroélectriques sont examinées en contrôlant l'épaisseur de la couche de PTO. De plus, nos résultats indiquent également que le ferroélectrique peut affecter les électrodes de SRO voisines, ainsi qu'induire des domaines cristallins de SRO. Enfin, dans la continuité d'une hétérostructure similaire, des hétérostructures ferroélectriques en film mince de $Pb(Zr,Ti)O_3$ (PZT) avec deux types de couches tampons TMO ($LaMnO_3$ (LMO) et $NdNiO_3$ (NNO)) et avec des épaisseurs variables de PZT sont étudiées. En raison des différentes couches tampons, la direction de polarisation ferroélectrique du PZT peut être inversée, et la polarisation ferroélectrique est capable de moduler les propriétés structurelles et électroniques des couches NNO.

# Propriétés plasmoniques du $SrVO_3$, du massif aux nanostructures

Compte tenu de ses riches propriétés physiques, le $SrVO_3$ sert de prototype pour l'étude du couplage des corrélations électroniques et des effets interfaciaux dans le TMO. Tout d'abord, les calculs *ab-initio* basé sur théorie de la fonction de densité dépendant du temps (TDDFT) dans l'approximation de la densité locale adiabatique (ALDA) ont révélé une excitation électronique du SVO à 1,35 eV dans la région infrarouge, correspondant à l'excitation plasmonique globale du SVO, et ont fourni l'énergie plasmonique et la dispersion de l'énergie dans des conditions dipolaires et non dipolaires, qui étaient en bon accord avec les mesures expérimentales EELS à résolution de momentum. En outre, dans des conditions non dipolaires (transfert de moment $q > 0$), le plasmon de surface disparaît, et le spectre retrouve les caractéristiques proches du plasmon du massif. La dispersion d'énergie sur 0,5 $Å^{-1}$ est d'environ 170 meV, ce qui est beaucoup plus petit que dans la plupart des matériaux plasmoniques.

De plus, nous avons observé des propriétés plasmoniques dans des nanostructures SVO, telles que des « slab » quasi-infinies, des demi-batons et des fentes, qui sont fabriquées par faisceau d'ions focalisé (FIB). Ces nanostructures présentent des modes LSP de type Fabry-Perot qui sont comparables aux simulations dans le domaine temporel à différences finies (FDTD) effectuées par le logiciel Lumerical. Les nanostructures SVO présentent plusieurs modes LSP, dont le pic d'énergie plasmonique et la distribution spatiale sont fortement influencés par les caractéristiques géométriques des nanostructures, telles que la forme et le rapport d'aspect. Plusieurs modes LSP présentent une largeur totale à mi-hauteur (FWHM) inférieure à 100 meV, et le SVO a des facteurs de qualité d'environ 2 à 5 dans une plage de 0,2 à 0,9 eV. La comparaison du facteur de qualité du plasmon de surface du SVO avec d'autres matériaux plasmoniques connus suggère que le SVO peut être appliqué au domaine plasmonique.

Enfin, le nanorod de SVO a démontré un plasmon de type massif dans des conditions non dipolaires, confirmant que la mesure EELS non dipolaire peut sonder l'excitation électronique de type massif, même dans la nanostructure. La différence de structures électroniques entre les zones du cœur et de l'enveloppe du nano-battons est probablement liée à une transition métal-isolant. Comme la nanostructure propose l'apparition du MIT associé aux effets interfaciaux, les deux chapitres suivants sont consacrés à la description du couplage entre les hétérostructures de couches minces ferroélectriques et le TMO.

# Ingénierie des domaines d'hétérostructures ferroélectriques en couches minces de $PbTiO_3$

Le matériau ferroélectrique implique le couplage des degrés de liberté de la charge et du réseau, présentant une polarisation électrique spontanée et commutable, souvent accompagnée de plusieurs domaines ferroélectriques avec des directions de polarisation uniformes. Les configurations de domaines ferroélectriques, en particulier dans les hétérostructures de films minces, sont fortement influencées par les conditions limites mécaniques et électrostatiques, ce qui entraîne le développement de diverses configurations de domaines aux propriétés distinctes. Ce chapitre examine une série d'hétérostructures de film mince de $PbTiO_3$ prises en sandwich par des électrodes de $SrRuO_3$ de 55 cellules unitaires (uc), en croissance sur un substrat de $DyScO_3$ (DSO) orienté $(110)_o$, et dont l'épaisseur du film mince de PTO varie de 23 à 133 uc. Cette série d'échantillons a été étudiée par une combinaison d'images AFM, XRD, microscopie à balayage de nanodiffraction de rayons X (SXDM) et STEM, révélant leurs périodicités et les configurations des domaines ferroélectriques. Cette étude a été réalisée en collaboration avec le groupe de l'Université de Genève, qui a fourni cette série d'échantillons de PTO et les mesures d'AFM, XRD, et SXDM.

En augmentant l'épaisseur du film mince de PTO, la configuration du domaine évolue d'un état complexe de type fermeture de flux vers le domaine ferroélectrique $a/c$ typique. Néanmoins, tous les échantillons ont des configurations de domaine périodiques et peuvent être divisés en deux régions présentant des comportements structurels distincts selon l'épaisseur. L'influence de l'épaisseur du film sur les configurations de domaines ferroélectriques est révélée. En outre, il existe une corrélation entre les déformations anisotropes et les distorsions structurelles des domaines ferroélectriques dans les couches de PTO, ce qui entraîne une réorientation de la structure cristalline de la couche supérieure de SRO. Ces travaux suggèrent que les effets ferroélectriques peuvent influencer les propriétés des couches adjacentes.

# Contrôle des propriétés des hétérostructures en couches minces de $NdNiO_3$ par la ferroélectricité

Le couplage entre les degrés de liberté du réseau et de la charge, qui sont associés à la ferroélectricité, est abordé dans le chapitre précédent. Après avoir exploré les matériaux ferroélectriques, ce chapitre se penche sur la façon dont les matériaux ferroélectriques influencent les propriétés électroniques et structurelles des TMOs. Ce chapitre se concentre sur l'étude du nickelate de $NdNiO_3$ associé à un film mince ferroélectrique de $Pb(Zr,Ti)O_3$. La première section présente les hétérostructures de couches minces ferroélectriques PZT en utilisant différentes couches tampons à base de TMOs et une couche de surface NNO, sur un substrat $SrTiO_3$. L'utilisation de couches tampons à base de NNO et de $LaMnO_3$ permet d'obtenir des couches PZT avec des directions de polarisation ferroélectrique opposées. L'orientation cristalline de la couche tampon et la distribution de la déformation dans l'hétérostructure sont des paramètres clés pour inverser la direction de polarisation ferroélectrique. En outre, les couches de surface NNO présentent une distribution inhomogène de la composition chimique, ce qui indique que le contrôle des propriétés de la couche NNO de recouvrement à l'aide de la méthode de la couche tampon reste à réaliser.

La deuxième section se concentre sur les hétérostructures PZT avec une couche tampon NNO et des épaisseurs de PZT variables. Les différentes épaisseurs conduisent à différentes configurations de polarisation ferroélectrique et démontrent des caractéristiques structurelles et électroniques distinctes de l'ensemble des hétérostructures à couche mince. Avec la réduction de l'épaisseur du PZT, de multiples orientations cristallines sont observées dans la couche tampon NNO, et le mécanisme de relaxation des contraintes dans la couche PZT devient plus complexe. L'épaisseur de la couche ferroélectrique et de la couche tampon variable peut être utilisée pour accorder les propriétés de la couche ferroélectrique puis de la couche de nickelate voisine, en modulant leur structure et, par conséquent, leurs propriétés électroniques.

Pour conclure, cette thèse porte sur l'étude des couplages interfaciaux entre les matériaux ferroélectriques et le film mince de TMO par l'utilisation des techniques STEM-EELS. Cette recherche vise à démontrer les propriétés MIT contrôlables du film mince de TMO en appliquant un champ ferroélectrique. Nous fournissons plusieurs exemples de la façon dont les matériaux ferroélectriques et le TMO interagissent à l'interface, entraînant des changements remarquables dans les propriétés structurelles et électroniques des films minces de TMO. Cette thèse détaille le rôle fondamental des interfaces entre matériau ferroélectrique et TMO et fournit une base pour les recherches futures, notamment en lien avec les applications.

# Acknowledgements

I would like to begin by saying that I am deeply grateful to everyone who assisted me in completing my doctoral thesis. I am especially grateful to my supervisor, Alexandre Gloter, who always guided and supported me throughout my Ph.D. period. Alexandre Gloter was especially instrumental in helping me comprehend complex concepts and experiments. He was always willing to make time to answer my questions, review my drafts, and provide constructive feedback. His guidance and encouragement were invaluable to me. I couldn't have successfully completed my thesis without his support and assistance.

I would also like to express my gratitude to my collaborators. First, Dr. Matteo Gatti from Ecole Polytechnique, Dr. Kari Ruotsalainen, and Dr. Alessandro Nicolaou from Synchrotron SOLEIL, all helped us with samples and calculations related to $SrVO_3$. Second, the group at the University of Geneva, Dr. Céline Lichtensteiger, Dr. Marios Hadjimichael, and Ludovica Tovaglieri, provided a series of $PbTiO_3$ samples and outstanding measurements. Last, the group at the University of Strasbourg, Dr. Daniele Preziosi, Dr. Guillaume Krieger, and Dr. Nathalie Viart, supplied a series of $NdNiO_3$ samples and conducted in-depth measurements. All my collaborators provided us with valuable samples and supported our investigations, and their expertise was essential in helping us to interpret the data and draw meaningful conclusions.

It is my pleasure to extend my gratitude to all of the jury members, Bénédicte Warot, Pierre-Eymeric Janolin, Jérôme Pacaud, and Matthieu Bugnet, for their valuable comments and suggestions. Their detailed and insightful feedback was instrumental in helping me refine and improve my work.

Thanks must be extended to the Ministry of Education of Taiwan and the Université Paris-Saclay for their financial support over the past three years. I appreciate the opportunities they gave me to learn and grow. In particular, Lihtien Hsu at the Bureau de Representation de Taipei en France has been instrumental in the scholarship process.

I would like to thank all my friends and colleagues at LPS. They inspired and motivated me, and were always there to support me. Finally, I want to thank my parents for their support throughout my academic journey. Without their encouragement, I wouldn't have had the opportunity to come to France and finish my Ph.D. degree.

In conclusion, I would like to express my sincere appreciation to all those who have supported me in various ways during my thesis. Thank you all for being a part of this journey and helping me reach this far.

蘇家平 *Chia-Ping*
*Paris, February 2023*

# Contents

# Chapter 1

# Introduction

**Contents**



## 1.1 Transition metal oxide (TMO) and its degrees of freedom

Transition metal oxide (TMO) and its heterostructures are probably one of the most interesting topics in solid-state physics [1, 2, 3, 4]. Since the TMO has partially filled $d$ orbitals (e.g., $3d^1$ of vanadium and $3d^7$ of nickel) and narrow $3d$ bands, it is necessary to take into account the strong electron-electron interactions. Consequently, these strong electronic correlations give rise to charge, lattice, orbital, and spin degrees of freedom [4, 5]. These degrees of freedom and their couplings lead to unique physical properties, such as metal-insulator transition (MIT) [6], high-temperature superconductivity [7], and colossal magnetoresistance [8], which are less presented or do not coexist in conventional semiconductors or other metal compounds.

The couplings between these degrees of freedom can be artificially enhanced, for instance, in nanostructures or at interfaces between two different materials. It is the case when a ferroelectric (FE) material is in contact with a TMO. At this interface, there are significant interactions between the charge and lattice orderings due to the FE effects, and emergent physical properties are expected [9, 10, 11, 12]. At first approximation, the FE ordering (primary lattice-governed instability) couples with the TMO's transport properties (primary charge-governed properties). Indeed, FE polarization can inject charges into the TMO to screen the FE potential, thereby modulating its resistivity [13]. In principle, large resistive switching, up to the control of the MIT, might be obtained by polling up or down FE polarization. The interaction between charge and lattice orderings makes the situation more complex than simple charge modulation due to FE gating. For instance, the properties of TMO might also be affected by its lattice modulation imprinted from the FE distortions of the neighboring FE material [9]. Oxygen networks in perovskites are strongly correlated with orbital ordering, and this ordering is likely to be influenced by the neighboring FE material, when the FE polarization direction of the nearby FE material is reversed, and could impact the transport properties as well [10, 11].

From the present example, a clear goal can be identified: controlling the structural and electronic properties of TMO by a FE thin film. However, the complexity of interfacial phenomena often prevents their realization, or a clear understanding of the primary parameters is still lacking. In this thesis entitled "*STEM-EELS investigation of ferroelectric proximity effects in transition metal oxide thin films* ($SrRuO_3$, $NdNiO_3$)", I will try to bring elements to address the complexity of such interfacial couplings among TMO thin films by scanning transmission electron microscopy and electron energy-loss spectroscopy (STEM-EELS). In order to achieve such a goal, I notably use the new capability given by monochromated and/or Cs-corrected microscopes.

## 1.2 The contribution of quantitative microscopic descriptions in TMO

While all the orders interact and might play a role in each other, the lattice and charge instabilities seem crucial, and the STEM-EELS technique enables us to obtain their microscopic descriptions. STEM imaging is able to investigate FE properties at atomic resolution, notably in thin film heterostructures and their interfaces. Further, local charges can be revealed by EELS spectra, such as by measuring the valence states of transition metals. In chapter 2, I briefly describe our STEM-EELS equipment and its abilities in these aspects. Further, elements to address the complexity of interfacial couplings among TMOs will be addressed through the following three chapters:

As a prelude to discussing ferroelectricity, in chapter 3, I first discuss the infrared properties of $SrVO_3$ (SVO) by STEM-EELS. SVO is a prototype of correlated metal [14], which can be used to investigate strongly electronic interactions. In addition, its spectroscopic signature has not yet been reported at the nanoscale. The goal is to link the electronic structure of TMO and interfacial effects. Several questions are addressed by combining monochromated EELS measurements with numerical simulations. Additionally, monochromated EELS is capable of measuring low-energy plasmonic excitations with high-energy resolution. We examine the presence of strong plasmon excitations (a possible indication of metallicity) in conjunction with the calculated EELS loss function derived from time-dependent density-functional theory (TDDFT) done by our collaborators. As expected, the plasmon excitation of correlated metal has a small energy dispersion among plasmonic materials. Following the observation of the bulk plasmon, we then investigate the localized surface plasmon (LSP) resonances on SVO nanostructures and compare them with numerical simulations by the finite-difference time-domain (FDTD) method. Furthermore, the quality factors of the LSP resonances on the SVO nanostructures are quantified, and the possibility of SVO as a potential alternative plasmonic material is discussed. Finally, I present how EELS can efficiently measure the bulk-type plasmon on the SVO nanostructure with nanometric resolution. It is reported that MIT exists at the surface of a SVO nanorod, which is indeed a prerequisite for quantitatively investigating MIT in nanos-

tructures as a result. Momentum-resolved EELS under dipole or non-dipole conditions, accompanied by FDTD simulations, enable us to be deep into the electronic properties of SVO. This work is done in collaboration with Dr. Matteo Gatti from the École Polytechnique, Dr. Kari Ruotsalainen, and Dr. Alessandro Nicolaou from the Synchrotron SOLEIL, who performed the TDDFT calculation and offered valuable advice. These results have been published in *Advanced Optical Materials* [15].

Turning to ferroelectricity, in chapter 4, I focus on a series of FE $PbTiO_3$ (PTO) thin film heterostructures. The complexity of the FE domains in thin film heterostructures has motivated a dozen works [16, 17, 18, 19, 20]. However, FE materials in contact with electrodes have received fewer studies than those in contact with insulators (e.g., $SrTiO_3$). One reason might be the difficulty of performing piezoresponse force microscopy (PFM) when a thick top electrode is deposited. Therefore, I report microscopic investigations of the FE domain evolution with respect to a series of PTO thin films sandwiched by TMO-based electrodes ($SrRuO_3$, SRO), whose PTO layers have varying thicknesses. Furthermore, different FE domain configurations imprint on the structures of the SRO electrodes and control their crystallographic mosaicity. This work was done in collaboration with Dr. Céline Lichtensteiger from the Université de Genève in Switzerland, who synthesized this series of samples. Different types of STEM images, strain analysis by geometric phase analysis (GPA), atomic-resolved images, and fast Fourier transform (FFT) analysis enable us to comprehend the FE domain configurations and the impact on the neighboring SRO electrodes. STEM microscopic measurements are compared with the results obtained through atomic force microscopy (AFM), X-ray diffraction (XRD), and scanning X-ray nanodiffraction microscopy (SXDM) at the synchrotron by our collaborators from the group of Prof. Jean-Marc Triscone, department of quantum matter physics (DQMP), Université de Genève, especially Dr. Céline Lichtensteiger, Dr. Marios Hadjimichael, and Ludovica Tovaglieri. Combining all these techniques provides systematic investigations of these samples, allowing us to understand how the FE domain configuration evolves across a series of layers and how they affect neighboring layers. A manuscript is being prepared for the publication of these results.

As a continuation of the similar thin film heterostructures, in chapter 5, I present the STEM-EELS investigation of a series of $NdNiO_3$ (NNO) thin films, which are in contact with FE $Pb(Zr_{0.2},Ti_{0.8})O_3$ (PZT) layers. It is known that FE polarization switching enables modulating the orbital occupancy, magnetic moment, and charge density of TMO, associated with interfacial polar distortion [10, 11]. However, a study has not yet been reported to determine how the evolution of FE polarization switching as a function of film thickness relates to structural and electronic properties, such as strain relaxation and MIT temperature modulation. With the aim of controlling the properties of NNO thin films by the FE domain of the PZT layer, in the first part, I report that different buffer layers ($LaMnO_3$ and $NdNiO_3$) have the ability to inverse the FE polarization direction of the PZT. Additionally, their NNO capping layers exhibit structural and chemical compositional inhomogeneity.

In the second part, a series of NNO-buffered PZT thin film heterostructures with varying PZT film thicknesses exhibit controllable structural and electronic properties of the NNO buffer layers. These thin film heterostructures were synthesized by Dr. Daniele Preziosi from Université de Strasbourg. This work was done in collaboration with Dr. Daniele Preziosi, Guillaume Krieger, and Dr. Nathalie Viart, who provided a series of samples and measurements of PFM, XRD, and X-ray absorption spectroscopy (XAS). Combining all of these approaches provides systematic insight into the properties of NNO controlled by FE effects.

Finally, in chapter 6, the results of our investigations are summarized.

# Chapter 2

# Electron microscopy and spectroscopy

**Contents**



## 2.1 Scanning transmission electron microscopy (STEM)

Scanning transmission electron microscopy (STEM) is considered to be one of the most effective techniques for investigating the material's structural and electronic properties at the atomic scale. The electron beam is focused to a sub-nm probe and scanned over a sample, resulting in scattered electrons due to electron-matter interactions. The image detectors collect these scattered electrons at various scattering angles and form STEM images, which reveal the material's structural information, such as crystal structure, strain distribution, and domain configuration. Furthermore, electron energy-loss spectroscopy (EELS) is used to collect inelastically scattered electrons, which are linked to the material's electronic properties. This thesis aims to investigate the coupling between the charge and lattice degrees of freedom in the TMO. Therefore, a combination of STEM and EELS enables us to obtain a nanoscale analysis of TMO, such as ferroelectric domain configurations, atomic displacements, strain distribution, plasmonic excitations, and chemical composition. As a result of the STEM-EELS technique, we are able to combine the information contained in real space with spectral information, notably with the nanometric resolution.

However, before discussing how the microscope operates, we would like to point out the spatial resolution limitation of STEM [21].

$$d = 0.61\lambda/sin\alpha \tag{2.1.1}$$

where $d$ is the minimum attainable size of the probe restricted by the diffraction limit, $\lambda$ is the electron wavelength, and $\alpha$ is the convergence semi-angle. In practice, in a spherical aberration-corrected STEM with fifth-order aberration correctors, the minimum attainable size of the probe is typically determined by chromatic aberration, and the convergence semi-angle can be rewritten as $\alpha_{chrom} = 1.2\sqrt{\lambda/(C_c\Delta E/E_0)}$ [22], where $C_c$ is the chromatic aberration coefficients, $\Delta E$ is the energy spread, and $E_0$ is the operating voltage. The minimum attainable size of the probe $d_{chrom}$ is then given by:

$$d_{chrom} \approx 0.5\sqrt{C_c \cdot \frac{\Delta E}{E_0} \cdot \lambda} \tag{2.1.2}$$

Observing equation 2.1.2, the resolution can be improved in some ways. The first possible parameter is $\lambda$; the electron wavelength decreases by increasing the operating voltage. However, it could damage the sample with a knock-on effect. Because of that, we operate the electron microscope at 100 keV (electron wavelength of 3.7 pm) rather than the typical 200 keV (electron wavelength of 2.5 pm), thus reducing damage and maintaining high performance. The second possible parameter is $\Delta E$; a monochromator, an energy filter, can reduce the energy spread. Our monochromator achieves a few meV-width zero-loss peak in EELS (operated at lower voltage) [23]. The last possible parameters are $C_s$ and $C_c$; the aberration corrector can correct the geometric aberrations (i.e., spherical aberration, coma, astigmatism) until the $5^{\text{th}}$-order component [24]. However, the chromatic aberration is relatively challenging to fix; nevertheless, the $C_c$ is not a huge value ($\sim 1$ mm), and the small energy broadening $\Delta E$ of a cold-field emission gun, can reduce its influence. With the advancements in aberration corrector and monochromator, spatial and spectral resolutions have increased dramatically, making it possible to perform a wide range of studies in TMOs.

## 2.2 Operating principles of STEM

A cross-section of the Nion-UltraSTEM column is shown in figure 2.1. The elements of STEM and their operating principles will be discussed in more detail in this section.

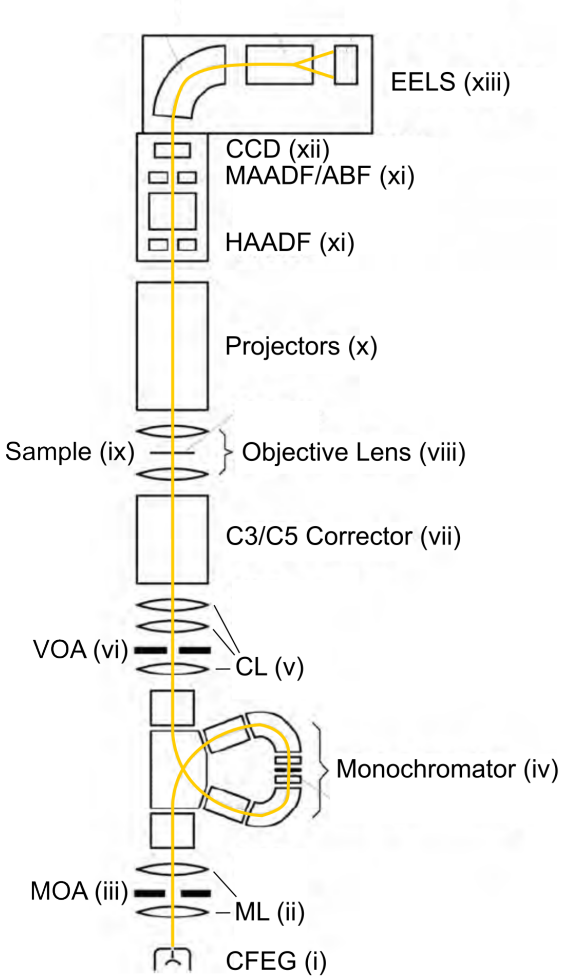


**Figure 2.1:** Schematic cross-section of Nion UltraSTEM™ with a monochromator. The electron beam travels from bottom to top, marked in yellow. Reproduced from ref. [23].

In the beginning, a cold-field emission gun (CFEG, part i) generates a high-density electron beam extracted from a sharpened tip (cathode) by a strong electric field. CFEG can achieve extremely high brightness (typically $10^9 A \cdot cm^{-2} \cdot sr^{-1}$), a source size of a few nanometers, and a small energy spread (0.2-0.3 eV). It has the best behaviors than other types of guns, such as the Schottky field emission gun (SFEG) and thermionic gun, which are 3 to 4 orders of magnitude weaker in brightness, larger source size ($\sim$ 25 nm for the SFEG; $\sim$ 5 µm for the thermionic gun), and higher energy spread (0.6-0.8 eV for the SFEG; $\sim$ 1 eV for the thermionic gun).

Next, the electron beam will pass through the monochromator (part iv), which is an energy filter for reducing the energy spread. Before entering the monochromator, two round lenses (ML, part ii) and a monochromator aperture (MOA, part iii) restrict the electron beam to have a suitable angular range. The structure of our monochromator, which consists of several multipole lenses and magnetic prisms, is shown in more detail in figure 2.2(a). The electron beam is bent by 75° through the main prism (prism I) and entered into an alpha-type energy filter. Then, the electron beam is dispersed by energy through one of the auxiliary prisms (prism II), which bends the electron beam by 105°. The energy-selective slit allows only the electron beam with limited energy spread to pass through it. The other auxiliary prism (prism III) concentrates the dispersed electron beam. Finally, the main prism (prism I) bends the filtered electron beam back to the same axis as the incoming electron beam. Figure 2.2(b) shows the performance of monochromated zero-loss peak (ZLP) with full width at a half maximum (FWHM) of 9 meV [25]. The monochromator dramatically improves spectral resolution and opens the opportunity to explore the EELS fine structure (Figure 2.2(c)), which is crucial for studying the EELS spectrum at low energy range, such as the sub-eV plasmon excitations.

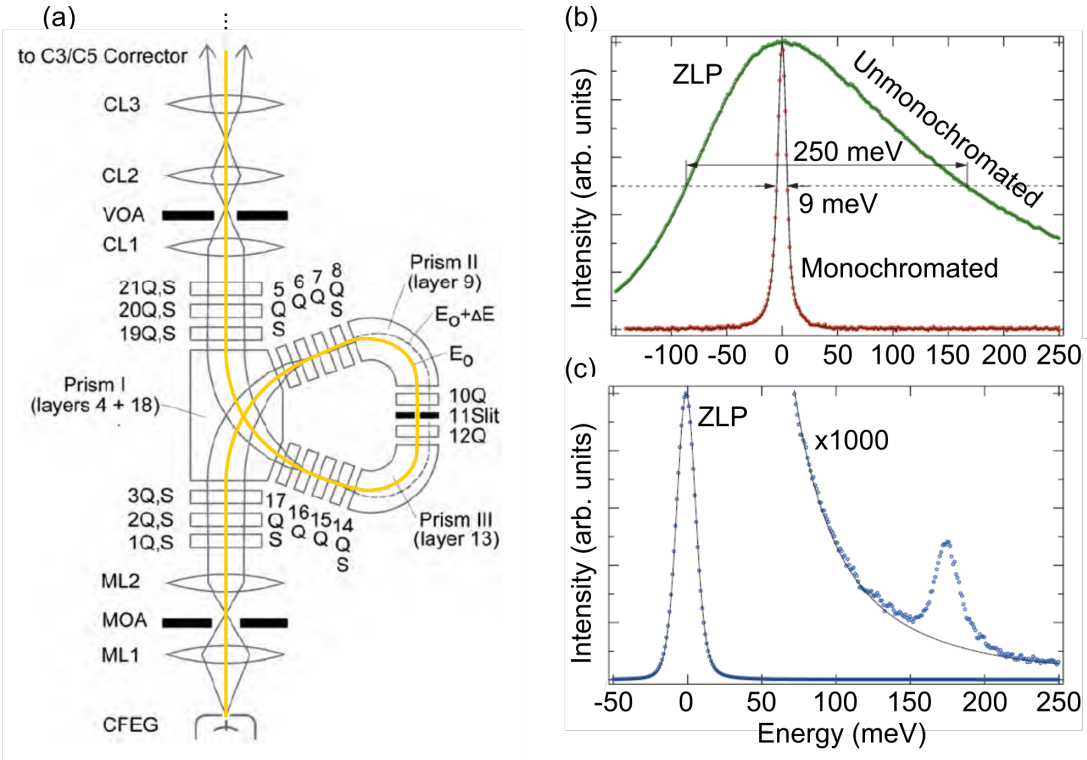


**Figure 2.2:** (**a**) Schematic cross-section of the monochromator, which is the part iv in figure 2.1. (**b**) The comparison between monochromated (9 meV) and unmonochromated (250 meV) zero-loss peak (ZLP) with 60 keV operating voltage and 1 meV per channel of the energy dispersion. (**c**) By using a monochromator, an optical phonon peak in h-BN at 173 meV can be revealed. Reproduced from ref. [23, 25].

Turning back to figure 2.1, the condenser lens (CL, part v) and a virtual objective aperture (VOA, part vi) control the electron beam's spot size and current density, influencing the spatial resolution. Then the electron beam enters a C3/C5 aberration corrector (part vii), which corrects the geometrical aberrations. The objective lenses (part viii), which comprise two magnetic pole pieces, focus the electron beam at the sample plane (part ix) with a typical convergence angle of 30 mrad. Then the magnetic coils are used to shift the electron beam on the $x$-$y$ plane for scanning the sample.

A projector lens (part x) is used to adjust the magnification of the image or the diffraction and project it on the detectors to record the signals. There are three image detectors (part xi): the high-angle annular dark-field (HAADF) detector, the mid-angle annular dark-field or annular bright-field (MAADF/ABF) detector, and the bright-field (BF) detector that collect the scattered electrons at different angular ranges and form STEM images (discussed in section 2.3.1). The CCD detector (part xii) reveals the Ronchigram and diffraction pattern, which can be used to align the electron beam trajectory and aberration or to find the sample crystallographic orientation.

Finally, the scattered electron beam enters the EELS spectrometer (part xiii), where the electron beam is bent 90° by a magnetic prism, then dispersed according to its kinetic energy. An electron spectrometer records the number of electrons present at each energy range and obtains an electron energy loss spectrum. Electrons that do not lose energy are found at the zero energy-loss position (i.e., ZLP), while the spectrum is divided into the low-loss and core-loss regions, depending on the energy of the electron (discussed in section 2.4.1).

## 2.3 STEM imagings

### 2.3.1 HAADF, MAADF, and ABF images

There are three imaging detectors equipped in our microscope (part xi in figure 2.1) that can simultaneously obtain three types of images with different information [22], the schematic diagram is shown in figure 2.3.

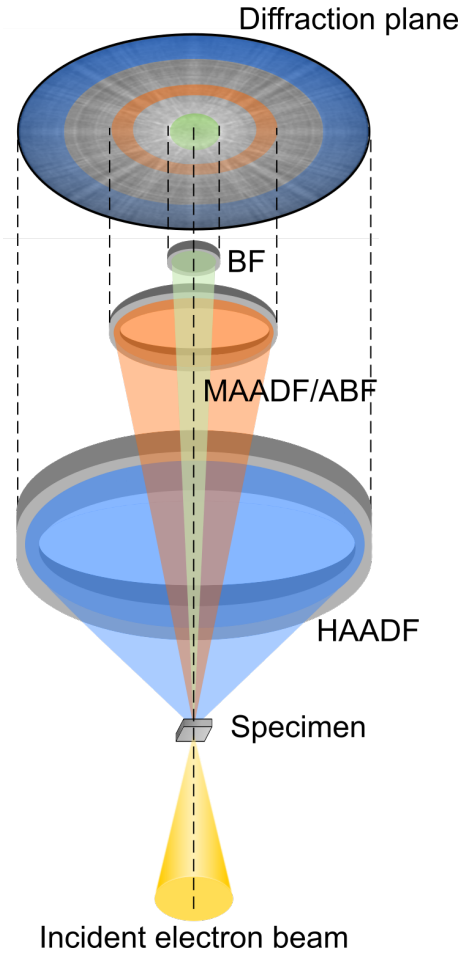


**Figure 2.3:** Schematic diagram of the STEM imaging modes. The three principal detectors collect scattered electrons from different angular ranges, and form high-angle annular dark-field (HAADF), mid-angle annular dark-field (MAADF) or annular bright-field (ABF), and bright-field (BF) images. The BF detector is circular, while the others are ring-shaped. In addition, the MAADF and ABF images can be switched by changing the camera length, and the collection angular range changes accordingly. The typical collection angular range of the HAADF image is from 80 to 200 mrad, the MAADF image from 30 to 60 mrad, the ABF image from 15 to 30 mrad, and the BF image from 0 to 10 mrad.

#### High-angle annular dark-field imaging (HAADF)

The HAADF image detector is an annular detector that collects the high-scattering angle electrons (typical $> 80$ mrad). At the high scattering angle, thermal diffuse scattering (TDS) is dominant, which is inelastic phonon excitation caused by thermal lattice vibration. As a result, the intensity of the HAADF image increases dramatically with the atomic number $z$, the intensity $\propto z^{\zeta}$ ($\zeta = 1.5$-2, typically 1.7); thus, the HAADF image is also called the $z$-contrast image. The HAADF image is most commonly used in STEM imaging due to its accuracy and stability in locating the atomic position, revealing the atomic structures of materials. For instance, atomic positions are used to calculate atomic displacements for each atom, which indicate the ferroelectric polarization (it will be discussed in figure 2.5) and strain field map (it will be discussed in section 2.3.4).

#### Middle-angle annular dark-field imaging (MAADF)

The MAADF detector collects diffracted or inelastically scattered electrons within the scattering angles, typically between 30-80 mrad. Compared to the HAADF image, the MAADF image has a higher signal-to-noise ratio for crystal disorder and strain. This is an effective technique for observing ferroelectric domains, notably at or near the domain wall, where strains are present.

Figure 2.4(a) compares the HAADF and MAADF images for ferroelectric *a*- and *c*-domains of $PbTiO_3$ thin film heterostructure, which will be described in chapter 4. The thin film exhibits the coexistence of *a*- and *c*-domains that correspond to areas where the ferroelectric polarization lies within or perpendicular to the thin film plane, demonstrated in figure 2.4(b). Through the HAADF image, it is difficult to determine the location or period of the ferroelectric domains; in contrast, the MAADF image displays a more apparent ferroelectric domain contrast. Additionally, some local regions with stronger or weaker intensities (such as the acute corner of the ferroelectric domain near the bottom interface) indicate defects or strains. Furthermore, the "diffraction pattern" can be obtained through the FFT transformation shown in figure 2.4(c), which provides information on the crystal structure in the reciprocal space. "Diffraction pattern" is quoted in-between brackets since the image displaying the FFT is often the logarithm of the modulus of the FFT, resembling a diffraction pattern, but the phase is still encoded, and information on the real space still there. Based on this FFT image, we can then filter the diffraction spot of interest and reveal information about this spot in real space (e.g., spatial distribution) through inverse FFT transformation, shown in figure 2.4(d). The FFT analysis will be used in chapters 4 and 5 to discuss domain-related issues.

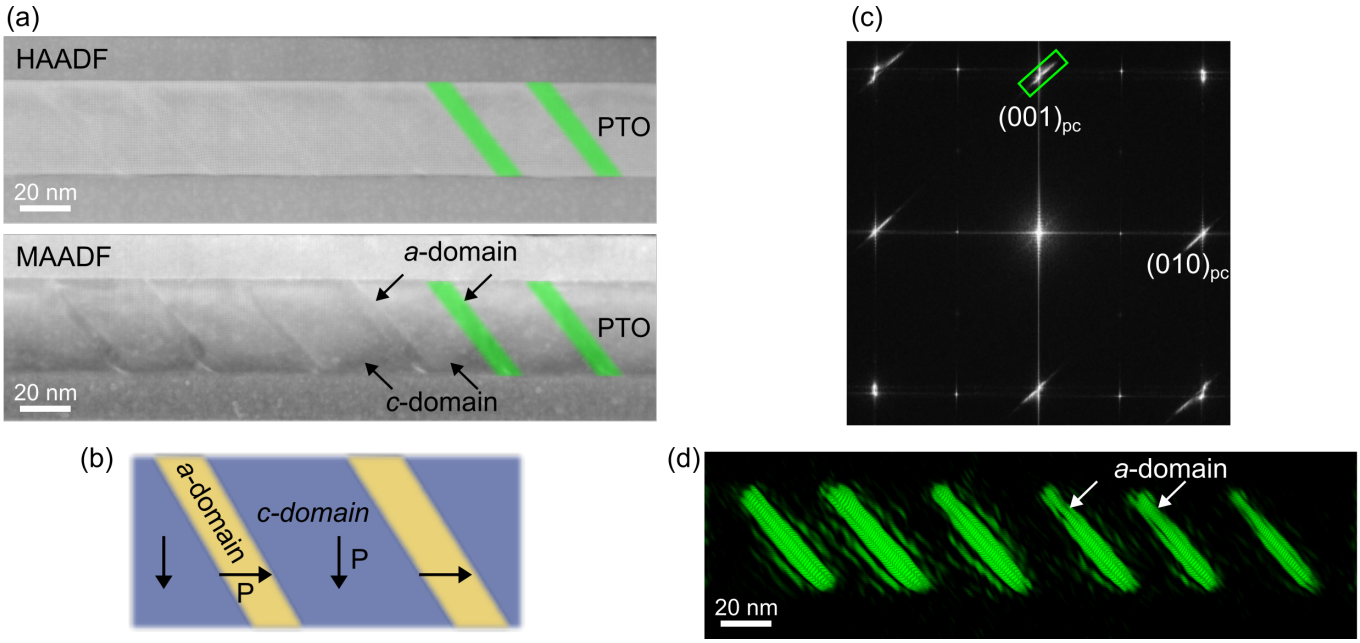


**Figure 2.4:** (**a**) Typical ferroelectric *a*- and *c*-domains of the $PbTiO_3$ thin film heterostructure are observed by the HAADF and MAADF images, the latter enhancing the contrast of the domains. (**b**) Schematic diagram of the ferroelectric *a*/*c* domain. (**c**) A fast Fourier transform (FFT) image of the HAADF image in (a). The superstructure features (marked in the green rectangle) correspond to ferroelectric domains. (**d**) FFT-filtered pattern by selecting a part of the superstructure from the FFT image reveals the spatial distribution of ferroelectric *a*-domains.

### Annular bright-field imaging (ABF)

As the detector is capable of collecting electrons in different angular ranges by adjusting the camera length, we can adapt the collecting angles to 15-30 mrad and use the same detector as MAADF, allowing us to obtain an ABF image. ABF image is a phase-contrast image that enables us to visualize both heavy and light elements, such as oxygen of light element. The HAADF image cannot reveal the signal of oxygen due to the relatively small atomic number compared with other elements. Additionally, the contrast of the bright-field image is inverse to the dark-field image, with the heavy element appearing as dark spots.

The atomic-resolved HAADF and ABF images provide the possibility of observing the ferroelectric polarization direction on each unit cell directly. For instance, in figure 2.5, in the case of the ferroelectric $Pb(Zr_{0.2},Ti_{0.8})O_3$ thin film with an upward ferroelectric polarization, the *B*-site atom (Zr/Ti in this case) and the oxygen exhibit off-centering atomic displacements. Due to the tetragonal structure of $Pb(Zr_{0.2},Ti_{0.8})O_3$ both the *B*-site atom and oxygen shift in the same direction, but the oxygen is displaced further than the *B*-site atom, resulting in the upward electric dipole (it will be discussed in chapter 5).

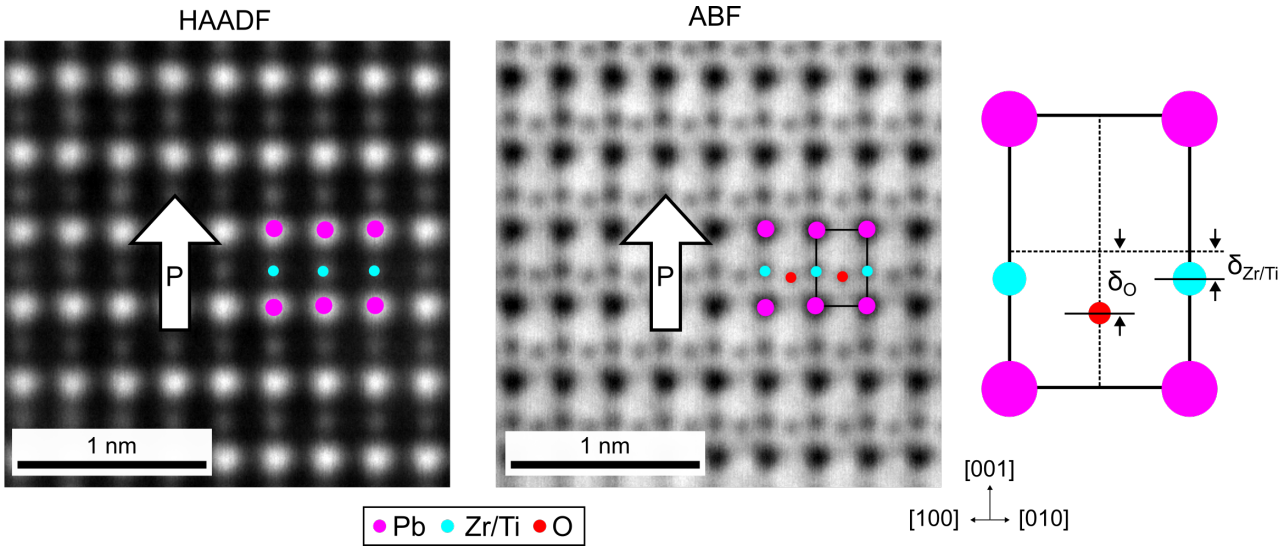


**Figure 2.5:** Atomic-resolved HAADF and ABF images of the $Pb(Zr_{0.2},Ti_{0.8})O_3$ ferroelectric thin film reveal the atomic displacements which correspond to the ferroelectric polarization. The *B* cations (Zr/Ti atoms, cyan) have atomic displacements toward the bottom with respect to the *A* cations (Pb atoms, magenta). It is only the ABF image that reveals the position of oxygen atoms (red), which have atomic displacements toward the bottom in excess of the *B* cations. Therefore, the non-ambiguous formation of a ferroelectric dipole points toward the upper part of the figure. In many cases, only HAADF images are measured, and the ferroelectric polarization direction is then assessed in the case described in the right part of the figure, assuming that the oxygen atoms are more displaced than the *B* cations, in the same direction. It is noted that the sample was observed along the [110] axis.

Once we have the ABF images, more structural information can be revealed, such as the oxygen octahedral distortion (it will also be discussed in chapter 5). However, the high-quality ABF image is always challenging. Due to the ABF image mixing the coherent and incoherent electrons, all the parameters need to be well-aligned, such as the zone axis orientation, the collection angles of the detector, the residual aberration, and sample thickness.

### 2.3.2 Optimization of atomic-resolved STEM image

When acquiring the atomic-resolved STEM images, several environmental parameters (such as vibration or noise, having different contributions to mostly low-frequency noise) or instrument instability (such as sample drift and backlash, temperature instability from the water chiller, high voltage ripple with frequencies in the several 10 kHz regimes) could affect the quality of the images. To increase the credibility of the atomic displacement and lattice distortion measured from the STEM images, we took a series of fast-scan (low exposure time) images, which have a low signal-to-noise ratio but minimize the environmental noise. A script based on the Gatan DigitalMicrograph software can align the series of images and then merge them into an image with a higher effective exposure time. In our case, this technique typically used 20 images with 1 µs exposure time per pixel (figure 2.6(a)); that is to say, the final image has an effective exposure time of 20 µs per pixel (figure 2.6(b)). According to the FFT image of the optimized image, the radius of the yellow circle in figure 2.6 is 10 $nm^{-1}$ in reciprocal space, which indicates that the spatial resolution is below 1 Å. The value is close to the limitation of our microscope; more precisely, a theoretical resolution limit of $\sim$ 0.75 Å is estimated by equation 2.1.1 (at 100 keV and a 30 mrad convergence semi-angle). It obviously improves the image's quality, making follow-up analysis more reliable.

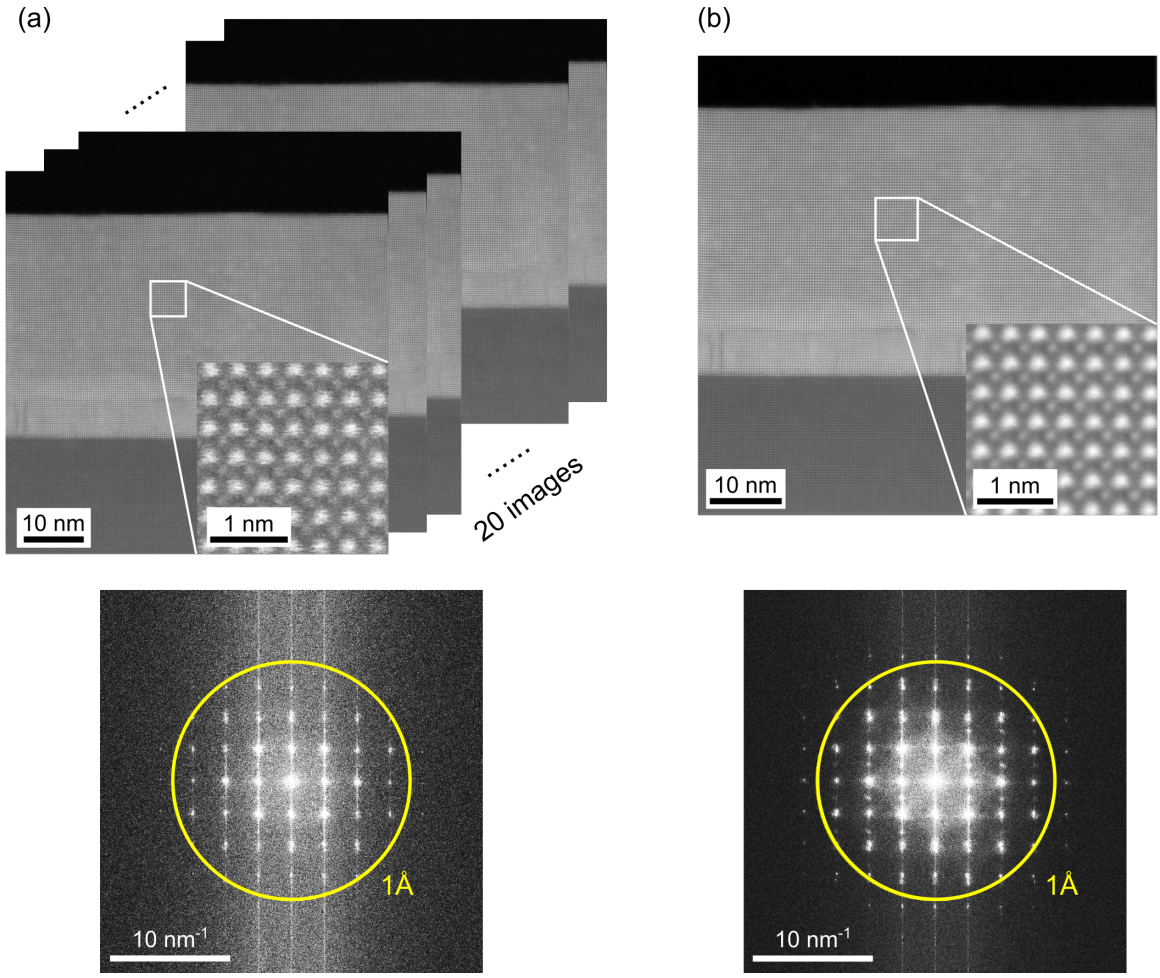


**Figure 2.6:** (**a**) A series of fast-scan (1µs exposure time per pixel) HAADF images and an FFT image from a single HAADF image. (**b**) An aligned HAADF image (effective 20 µs exposure time per pixel) is obtained by combining 20 fast-scan HAADF images in (a), and its FFT image indicates a spatial resolution $< 1$ Å.

### 2.3.3 Polarization analysis: Atomic displacement arrow map

Since we improve the atomic-resolved STEM images' quality in section 2.3.2, accurate measurements of atomic displacements can be achieved, associated with ferroelectric polarization. With the aid of the image filters and atomic arrow map script, the atomic displacements and corresponding ferroelectric polarization can be calculated by the script from D. R. G. Mitchell in Gatan DigitalMicrograph software.

Using the $PbTiO_3$ thin film with upward ferroelectric polarization as an example. First, the image quality can be further improved by the Richardson-Lucy deconvolution and ABSF (average background subtracted filter) image filters; the raw image and the filtered image are displayed in figures 2.7(a) and (b), respectively. The software identifies the large atoms (*A*-site atoms) and fits the center of each atom by the center of gravity method, shown in magenta spots in figure 2.7(c). The software then finds the positions of the small atoms (*B*-site atoms) and again uses the same fitting method to calculate their centers with respect to the large atoms, shown in blue spots in figure 2.7(c). As a result, we have the measured and computed centers of the small atoms, respectively. The difference between the measured and computed centers of the small atoms indicates atomic displacement. The inverse of the atomic displacement direction represents the direction of the electric dipole (according to figure 2.5), and polarization direction is demonstrated by the yellow arrows in figure 2.7(d). This software will be used to quantitatively determine the polarization direction of ferroelectric domains.

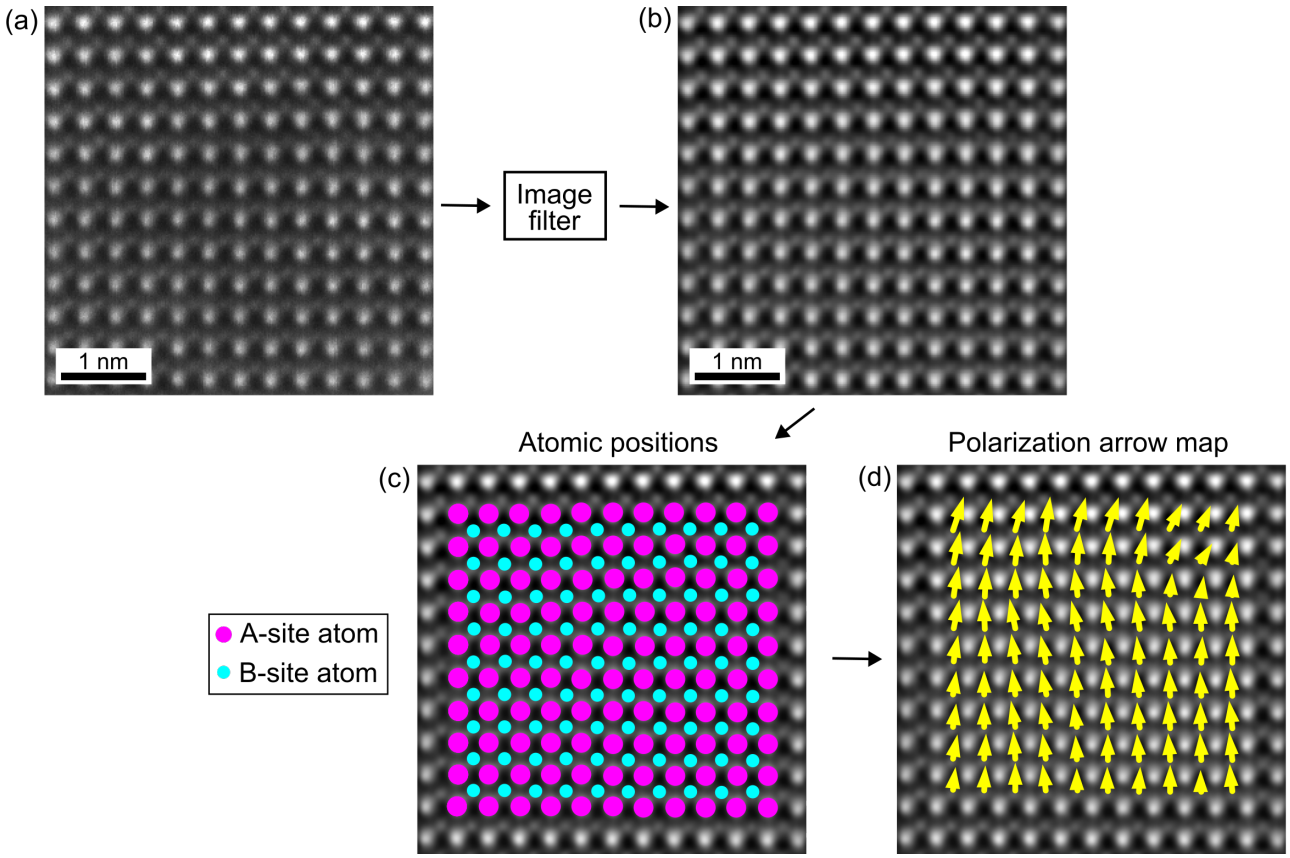


**Figure 2.7:** A flow diagram for calculating an atomic displacement arrow map. An atomic-resolved image of the ferroelectric PTO layer will be optimized first by image filters, and the raw image and filtered image are shown in (**a**) and (**b**), respectively. (**c**) The software identifies the large (*A*-site atoms, magenta) and small atoms (*B*-site atoms, cyan), and then computes the positions of the small atoms with respect to the large atoms by the center of gravity method. (**d**) The difference between the measured and computed positions of the small atoms represents the atomic displacements, and the opposite direction of the atomic displacement of *B*-site atoms indicates the ferroelectric polarization direction (yellow arrows), according to the discussion in figure 2.5.

### 2.3.4 Strain analysis: Geometric phase analysis (GPA)

Further STEM image analysis has been done using geometric phase analysis (GPA), a method to quantify the strain field from an atomic-resolved STEM image [26]. The GPA is based on a power spectrum of the image and calculates the displacement field by using the Bragg spots in the diffraction pattern; then, strain distributions can be evaluated. The equation 2.3.3 shows the relation between the phase $P_{\mathbf{g}}(\mathbf{r})$ the displacement field $u(\mathbf{r})$:

$$P_{\mathbf{g}}(\mathbf{r}) = -2\pi \mathbf{g} \cdot u(\mathbf{r}) \tag{2.3.3}$$

where $\mathbf{g}$ is reciprocal lattice vector and $\mathbf{r}$ is position. By choosing two noncollinear vectors $\mathbf{g} = (\mathrm{g}_1, \mathrm{g}_2)$ in the diffraction pattern (see figure 2.9(b)), equation 2.3.3 can be written as a matrix in the orthogonal $xy$-coordinate system:

$$\begin{bmatrix} P_{\mathrm{g}_1} \\ P_{\mathrm{g}_2} \end{bmatrix} = -2\pi \begin{bmatrix} \mathrm{g}_{1x} & \mathrm{g}_{1y} \\ \mathrm{g}_{2x} & \mathrm{g}_{2y} \end{bmatrix} \begin{bmatrix} u_x \\ u_y \end{bmatrix} \tag{2.3.4}$$

Therefore, we have the displacement field $u(\mathbf{r}) = u(x, y)$ in the form of a matrix as:

$$\begin{bmatrix} u_x \\ u_y \end{bmatrix} = -\frac{1}{2\pi} \begin{bmatrix} \mathrm{g}_{1x} & \mathrm{g}_{1y} \\ \mathrm{g}_{2x} & \mathrm{g}_{2y} \end{bmatrix}^{-1} \begin{bmatrix} P_{\mathrm{g}_1} \\ P_{\mathrm{g}_2} \end{bmatrix} \tag{2.3.5}$$

Then, the lattice distortion tensor $e$ can be computed from the gradient of the displacement field $u(x, y)$:

$$e = \begin{bmatrix} e_{xx} & e_{xy} \\ e_{yx} & e_{yy} \end{bmatrix} = \begin{bmatrix} \frac{\partial u_x}{\partial x} & \frac{\partial u_x}{\partial y} \\ \frac{\partial u_y}{\partial x} & \frac{\partial u_y}{\partial y} \end{bmatrix} \tag{2.3.6}$$

This tensor $e$ can be furthur decomposed into a symmetric term $\varepsilon$ and an antisymmetric term $\omega$:

$$\varepsilon = \frac{1}{2}(e + e^T) \tag{2.3.7a}$$

$$\omega = \frac{1}{2}(e - e^T) \tag{2.3.7b}$$

By substituting equation 2.3.6 into equations 2.3.7, we find that:

$$\varepsilon = \begin{bmatrix} \varepsilon_{xx} & \varepsilon_{xy} \\ \varepsilon_{yx} & \varepsilon_{yy} \end{bmatrix} = \begin{bmatrix} \frac{\partial u_x}{\partial x} & \frac{1}{2}(\frac{\partial u_x}{\partial y} + \frac{\partial u_y}{\partial x}) \\ \frac{1}{2}(\frac{\partial u_y}{\partial x} + \frac{\partial u_x}{\partial y}) & \frac{\partial u_y}{\partial y} \end{bmatrix} \tag{2.3.8a}$$

$$\omega = \begin{bmatrix} \omega_{xx} & \omega_{xy} \\ \omega_{yx} & \omega_{yy} \end{bmatrix} = \begin{bmatrix} 0 & \frac{1}{2}(\frac{\partial u_x}{\partial y} - \frac{\partial u_y}{\partial x}) \\ \frac{1}{2}(\frac{\partial u_y}{\partial x} - \frac{\partial u_x}{\partial y}) & 0 \end{bmatrix} \tag{2.3.8b}$$

where $\varepsilon$ and $\omega$ represent strain and rotation tensors, respectively. The $\varepsilon_{xx}$ and $\varepsilon_{yy}$ are the strain distributions in the $x$- and $y$-axis, $\varepsilon_{xy}$ is the shear strain, and $\omega_{xy}$ is rotation.

Finally, the strains and rotation can then be presented in the following equations, and a corresponding schematic is shown in figure 2.8.

$$\varepsilon_{xx} = \frac{\partial u_x}{\partial x} \tag{2.3.9a}$$

$$\varepsilon_{yy} = \frac{\partial u_y}{\partial y} \tag{2.3.9b}$$

$$\varepsilon_{xy} = \frac{1}{2}\left(\frac{\partial u_x}{\partial y} + \frac{\partial u_y}{\partial x}\right) \tag{2.3.9c}$$

$$\omega_{xy} = \frac{1}{2}\left(\frac{\partial u_x}{\partial y} - \frac{\partial u_y}{\partial x}\right) \tag{2.3.9d}$$

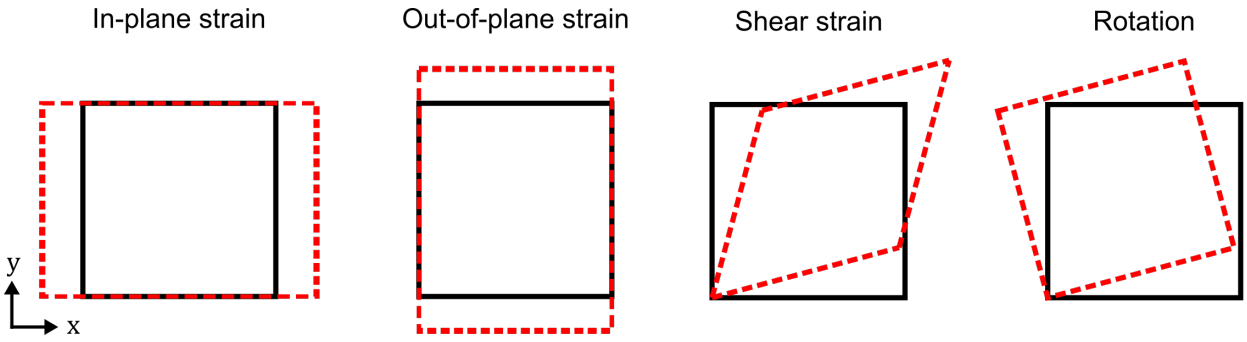


**Figure 2.8:** Schematic diagrams of different deformations measured by geometric phase analysis (GPA), from left to right representing in-plane strain ($\varepsilon_{xx}$), out-of-plane strain ($\varepsilon_{yy}$), shear strain ($\varepsilon_{xy}$), and rotation ($\omega_{xy}$), respectively.

The GPA can efficiently investigate the strain distribution in the thin film heterostructure. For instance, figure 2.9(a) shows the ferroelectric thin film with the *a*- and *c*-ferroelectric domains (the same sample was presented in figure 2.4). The GPA enables us to observe these domains within another aspect. First, the masks (yellow circle) are used to select two reciprocal vectors **g** from the power spectrum of the image in figure 2.9(b). The phase maps in the real space (figure 2.9(c)) are extracted from the phase parts of these two masks, and the strain fields can be obtained by equations 2.3.3 and 2.3.9. The strains in thin film heterostructure can be revealed (figure 2.9(d)), possibly associated with strain relaxation, flexoelectricity, and ferroelectric polarization. In the present case, we show what the GPA refers to the "out-of-plane strain" in figure 2.9(d), which, more precisely, corresponds to the lattice expansion along the growth direction when compared to the reference substrate. In the ferroelectric layer, the red part indicates the regions where a strong out-of-plane lattice expansion, while the green part corresponds to the reduced out-of-plane lattice as compared to the substrate. Since the ferroelectric polarization implies a strong lattice distortion along the ferroelectric vectors, the red and green colors correspond to the regions where the ferroelectric vectors lie out or within the thin film plane.

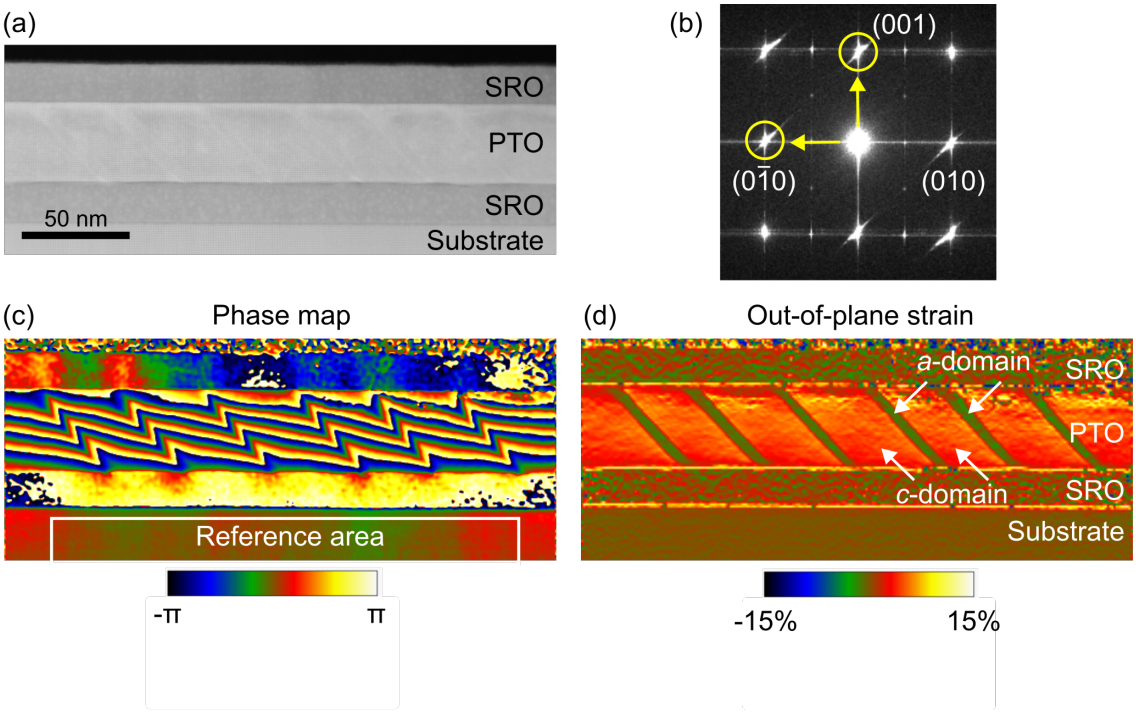


**Figure 2.9:** (**a**) A HAADF image of a thin film heterostructure consisting of a $PbTiO_3$ ferroelectric layer, two $SrRuO_3$ electrodes, and a substrate. (**b**) The power spectrum of (a). Two diffraction spots (yellow circles) are selected and extracted their phase parts to form a phase map in (**c**). In addition, a part of the substrate is chosen as a reference area. (**d**) Based on the phase map presented in (c), for instance, the out-of-plane strain can be calculated by equations 2.3.3 and 2.3.9b.

## 2.4 Electron energy-loss spectroscopy (EELS)

### 2.4.1 EELS spectrum

When an electron beam interacts with a specimen, the electrons may undergo inelastic scattering and lose their kinetic energies, and the EELS spectrometer (part xiii in figure 2.1) then collects these transmitted electrons. The magnetic prism disperses the electron beam based on the energy, and a spectrum is obtained as a function of loss energy.

Electrons within a material are excited by the incident electron beam, causing them to scatter to available electronic states (in a one-electron approximation). Thus the EELS can map the empty electronic states above the Fermi level and reflect some useful elements of the density of electronic states, such as chemical composition and bonding situation. EELS is also an analysis technique that provides significant information about collective electronic structures associated with the inter- and intra-band transitions, including those encountered in plasmon excitations [27]. The typical EELS spectrum is shown in figure 2.10, which can be considered two principal regions based on the range of energy: the low-loss region ($< 50$ eV), and the core-loss region ($> 50$ eV).

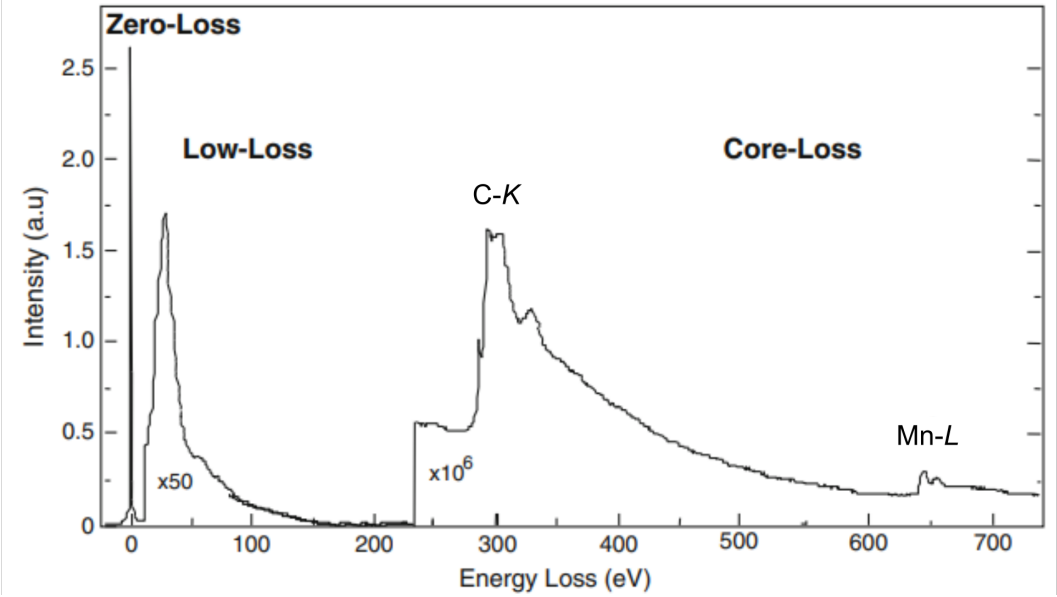


**Figure 2.10:** A typical EELS spectrum, consisting of the zero-loss peak ZLP, low-loss region ($< 50$ eV), and core-loss region ($> 50$ eV). Reproduced from ref. [22].

#### Low-loss region

The low energy-loss region ($< 50$ eV) indicates the information of phonons, excitons, inter- and intra-band transitions (valence and conduction bands), and collective oscillation (such as plasmon excitations). An extremely high-intensity peak at zero energy-loss position corresponds to non-scattered and elastically scattered electrons, known as the zero-loss peak (ZLP). The full width at half maximum (FWHM) of ZLP can be examined as the spectral resolution. In addition, the ratio of the ZLP intensity and the total inelastic

signal is commonly used to estimate the relative thickness of the specimen. The thickness measurement is essential when discussing the surface and bulk properties. With the monochromator, such low-energy excitations can now be investigated (discussed in figure 2.2(c)). In chapter 3, we will focus on plasmon excitations located below a few eV.

**Core-loss region**

The core-loss region represents the electronic transitions from the inner shells (such as O-*K*, Ti-*L*, Ni-*L*, and Nd-*M* edges) to the empty states of the conduction band and thus carries characteristic information about materials. Intensity fluctuations at the EELS edges indicate fine structures containing rich chemical information. For instance, the energy shift of titanium-*L* or nickel-*L* edges primarily corresponds to their valence states, revealing the charge issue.

### 2.4.2 Data acquisition: Spectrum imaging

Since the HAADF image and EELS spectra provide different information, it is possible to combine both signals, known as spectrum imaging. Figure 2.11 shows a spectrum imaging three-dimensional data cube, which consists of two spatial axes ($x$- and $y$-axis) and one axis of electron energy-loss. When an electron beam scans the sample, the HAADF detector and EELS detector will acquire the signals simultaneously; that is to say, each pixel of the HAADF image corresponds to one EELS spectrum. We can extract an EELS spectrum at a specified position in the HAADF image (cyan column in the spectrum imaging data cube in figure 2.11).

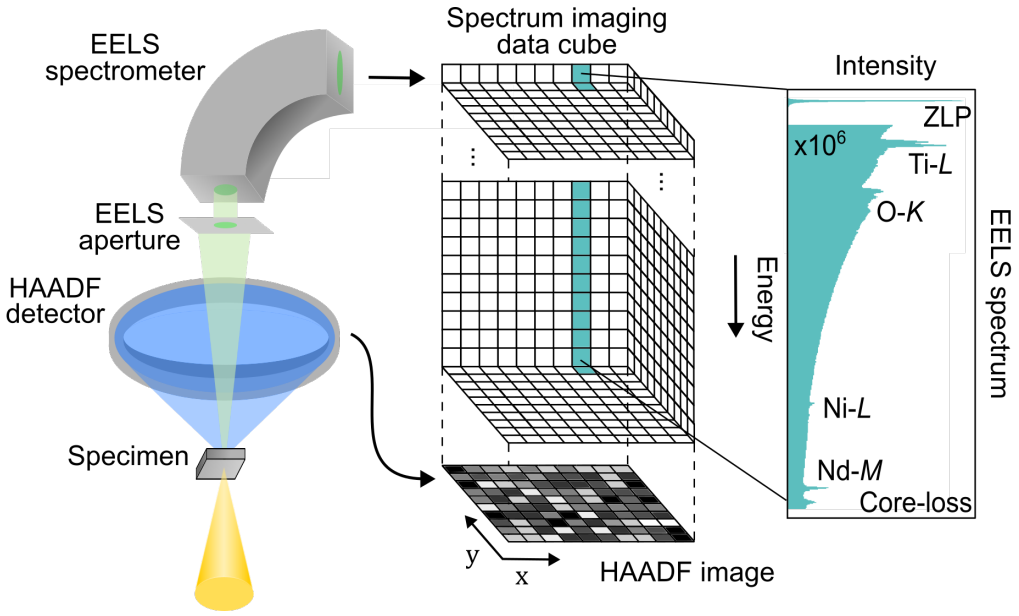


**Figure 2.11:** The spectrum imaging technique. It collects a three-dimensional data cube with a HAADF image (spatial $x$- and $y$-axis) and corresponding EELS spectra (an energy-axis) at each pixel in the HAADF image.

### 2.4.3 Energy-filtered STEM-EELS map

By using the spectrum imaging technique, we are able to obtain the spatial image and associated spectrum, which greatly enhances our ability to interpret data. For instance, in figure 2.12, we can extract a sub-plane (yellow planes in the spectrum imaging data cube) and obtain energy-filtered STEM-EELS maps. With the energy-filtered STEM-EELS maps, we can observe the localized surface plasmon (LSP) resonances of the nanostructures (they will be discussed in chapter 3), and the chemical composition maps of thin film heterostructures (they will be discussed in chapter 5).

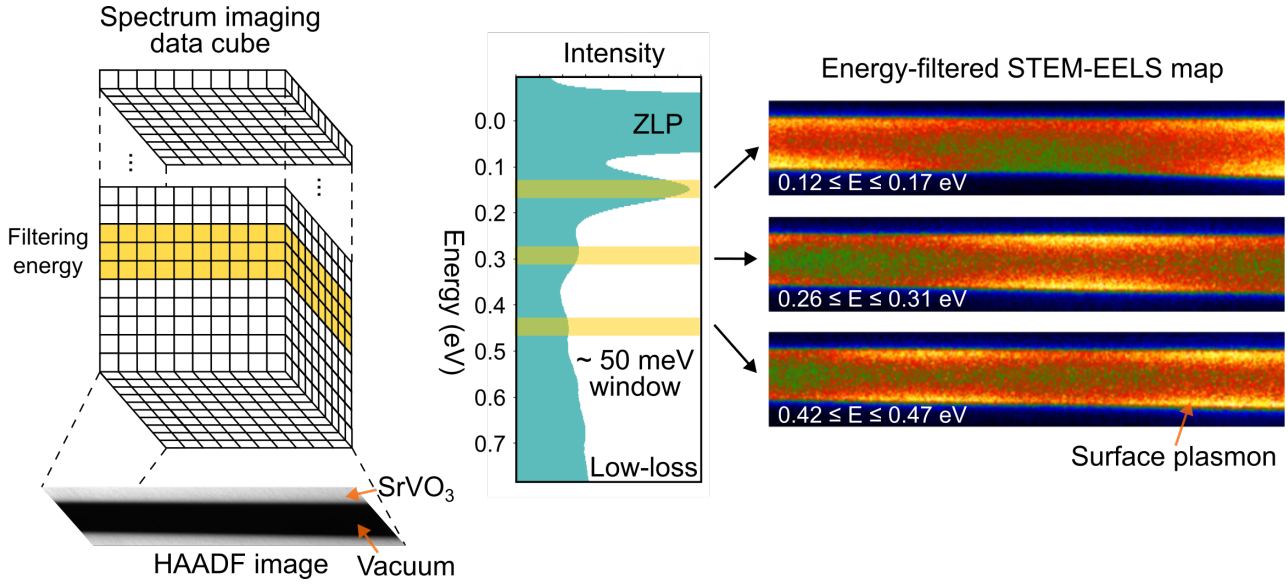


**Figure 2.12:** By selecting an energy range of interest (yellow windows presented in the EELS spectrum) from an EELS spectrum imaging data cube, an energy-filtered STEM-EELS map is generated, revealing the spatial distribution of the chosen spectroscopic signature.

### 2.4.4 Momentum-resolved EELS

As we discussed earlier, the EELS collects inelastically scattered electrons, and the differential cross-section of inelastic scattering can be described by the Born approximation, which can be written as [28]:

$$\frac{\partial^2\sigma}{\partial E\partial\Omega} \approx q^{-4}\sum_f |\langle\psi_f\,|exp(i\mathbf{q}\cdot\mathbf{r})|\,\psi_0\rangle|^2 \times \delta(E_f - E_0 - E) \tag{2.4.10}$$

where $q$ is momentum-transfer (also known as scattering vectors), $\mathbf{r}$ is the effective radius of the excitation, $\psi_0$ and $\psi_f$ are initial- and final-state wavefunctions, and their corresponding energies $E_0$ and $E_f$, respectively. Then, the exponential term can be expanded as follows:

$$exp(i\mathbf{q}\cdot\mathbf{r}) \cong 1 + (i\mathbf{q}\cdot\mathbf{r}) + (i\mathbf{q}\cdot\mathbf{r})^2/2! + \cdots \tag{2.4.11}$$

Consequently, for small $q$, the dipole transition (second term in equation 2.4.11) dominates; for large $q$, the high-order terms enhance the intensity of monopole and quadrupole transitions.

It is noted that the EELS cross-section is similar to the one for non-resonant inelastic X-ray scattering (NIXS). Several NIXS works [29] have reported dipole-forbidden *d-d* excitations at larger scattering vectors; however, those methods lack the spatial resolution. Resonant inelastic X-ray scattering (RIXS) [30] makes the investigation of these electronic excitations go further with more options for the selection rules, and similar possibilities are not present in EELS. Nevertheless, momentum-resolved EELS (also called angle-resolved EELS) can describe low-energy electronic excitations, such as *d-d* excitation in TMO, with higher spatial and spectral resolution [31].

The setup of the momentum-resolved EELS is shown in figure 2.13. By displacing the EELS aperture, we can select different scattering vectors. As a result, this technique can be useful for understanding the symmetry of electronic excitations in anisotropic materials [32], the phonon dispersion in the local regions, like vibrational spectroscopy [33, 34], the optical response of plasmonic [35] and as mentioned, non-dipolar contribution. Additionally, the energy dispersion of plasmon excitation at small $q$ was reported as $E = E_p + \alpha(\hbar^2/m)q^2$, where $E = E_p$ is plasmon energy at $q = 0$ and $\alpha$ is a coefficient [36]. The behavior of plasmon excitations on nanostructures will be discussed in chapter 3 under dipole and non-dipole conditions, notably with nanometric resolution.

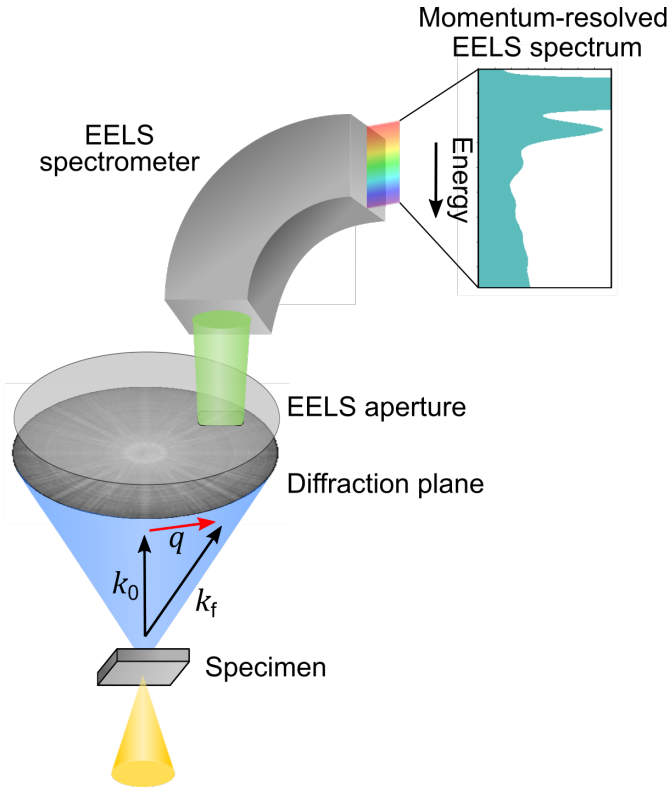


**Figure 2.13:** Schematic diagram of the momentum-resolved EELS experimental setup. The incident electrons with $k_0$ direction are scattered into $k_f$ direction, and the difference between $k_0$ and $k_f$ represents the momentum-transfer $q$. The momentum-transfer selection was achieved by inserting a rectangular EELS aperture in the diffraction plane, allowing the scattered electron with a particular momentum-transfer to enter into the EELS spectrometer.

## 2.5 Summary

This chapter presents the working principles of STEM-EELS and its analysis techniques. STEM imaging provides rich spatial information at atomic resolution, which is especially useful for revealing the behaviors of ferroelectric domains and strain distributions of thin film heterostructures. Additionally, the EELS spectrum discloses electronic fine features under dipole and non-dipole conditions, as well as illustrates the spectroscopic signatures in real space through the spectrum imaging technique. It is evident that the combination of STEM-EELS is a powerful tool for analyzing the coupling between ferroelectric ordering and the properties of TMOs, allowing a more local understanding of materials at the nanometric scale.

# Chapter 3

# Plasmon properties of $SrVO_3$ bulk and nanostructures

**Contents**



## 3.1 Introduction: $SrVO_3$ correlated metal oxide

In this chapter, we examine the electronic properties of strontium vanadium oxide $SrVO_3$ (SVO), which has $3d^1$ electron configuration of the transition metal V. It has been reported to have a high conductivity of $\sim 10^4$ S·cm$^{-1}$, high charge carrier density of $\sim 10^{22}$ cm$^{-3}$ [37]. SVO exhibits remarkable optical transparency in the visible range as a transparent conductor material [14]. The transparent property is caused by the transition from the O-2$p$ to

unoccupied V-3*d* bands (*p*-*d* excitation, also known as charge transfer excitation), whose energy exceeds $\sim$ 4 eV (above the visible range). Additionally, the plasmon excitation energy, which is associated with electron transfer within the V-3*d* bands (known as *d*-*d* excitation), is located in the infrared spectrum; therefore, it exhibits a bulk plasmon of 1.3 eV [38]. This SVO bulk plasmon can be described as a Drude-type plasmon with a charge density of 1.7x$10^{22}$ $cm^{-3}$ corresponding to the V-3$d^1$ band and a mass enhancement due to strong electronic correlations.

Based on the strong electron correlation, the SVO is considered a novel transparent conductor in comparison to the traditional transparent conductor of tin-doped indium oxide (ITO) [39]. The doped oxide semiconductors usually have lower charge carrier density ($\sim 10^{21}$ $cm^{-3}$) than correlated materials that drive their plasmon energies ($\sim 0.7$ eV) below the visible range without a need for a strong enhanced effective mass [14]. Furthermore, the transparent property and electronic correlations of SVO, which are associated with the bandwidth, can be tuned by several parameters, such as crystallinity [37] and lattice mismatch [40, 41]. Electron correlations within the vanadium Wadsley conductors (metallic $VO_2$(B) and $V_6O_{13}$) can induce redshift plasmon energy and lead to enhanced transparency in the visible and infrared ranges [42]. Additionally, it has been reported that $SrNbO_3$ has higher transparency due to lower plasmon energy in the ultraviolet regime resulting from its Nd-4$d^1$ electron configuration [43]. As a result, it has been described that electron correlations in 3*d* and 4*d* TMOs are responsible for the plasmon energy. The SVO bulk plasmon excitation and its energy dispersion will be discussed through EELS measurements and TDDFT calculations in the following section.

Surface plasmons are known to exist on the surface of metallic nanostructures, and several oxide nanostructures have been reported on localized surface plasmons (LSP), such as ITO [44], $BaSnO_3$ [45], and $MoO_2$ [46]; however, the presence of LSP on SVO nanostructures has not been reported or discussed. As the LSP can be observed several tens of nanometers away from the surface of nanostructures, we will use EELS in the aloof beam mode to measure the LSP with nanometric spatial resolution. The LSP can be estimated by its quality factor [47], which can be compared with other plasmonic materials.

In addition to surface plasmons, bulk plasmon excitation may be related to another electronic phenomenon. For instance, SVO was reported that metal-insulator transition (MIT) occurs at reduced dimensionality, such as thin film, and exhibits thickness-dependent MIT with a critical thickness of 2-3 unit cells [48], and occurs at nanodomain or interface [49]. Bulk plasmons are generally expected to be more localized, particularly when probed through the non-dipole transition [50]. We have been able to measure the bulk and surface plasmon excitations under dipole and non-dipole conditions by momentum-resolved EELS, and the properties of SVO plasmons at the nanoscale can then be investigated.

Considering the SVO's rich physical properties, it represents a prototype to study the role of electron correlations in the transition metal *d* bands, associated with interfacial effects.

Through plasmon excitations of SVO, this chapter aims to answer the following questions:

- How does the electronic structure of SVO correlate with the behaviors of the plasmon excitations and energy dispersion?
- What are the behaviors of LSP in different SVO nanostructures, and is numerical simulation capable of reproducing them?
- How can EELS efficiently measure the bulk-type plasmon excitation on nanostructure with nanometric resolution?

## 3.2 Plasmon properties of $SrVO_3$

### 3.2.1 Bulk plasmon

The purpose of this section is to analyze SVO plasmon excitations by EELS in order to gain an overview understanding of the plasmonic behavior of this material. Figure 3.1(a) shows the EELS spectrum of micrometrical SVO particles at a distance greater than 300 nm from any lateral surface and a local thickness above 300 nm; under these conditions, a bulk plasmon is expected to dominate. The spectrum displays well-defined features, notably an intense and sharp peak at 1.35 eV, and is in agreement with the calculation of time-dependent density-functional theory (TDDFT) using the adiabatic local-density approximation (ALDA) in figure 3.1(b) (calculation done by M. Gatti).

The plasmonic excitation within the V-3*d* band (*d*-*d* transition) can be identified at the peak of 1.35 eV (experiment) and 1.7 eV (theory); and the transition from the O-2*p* band to V-3*d* band (*p*-*d* transition) is located at 3-4 eV for both experiment and theory. In addition, the dip ($\sim$ 2.5 eV) in between the *d*-*d* and *p*-*d* transition represents transparency in the visible range, as discussed in ref. [14].

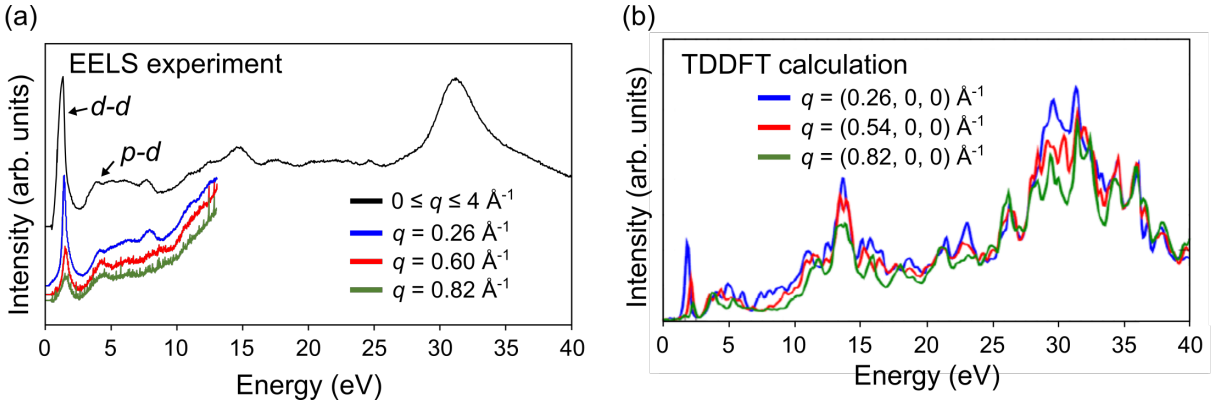


**Figure 3.1:** The electron loss function of micrometrical SVO particles as a function of momentum-transfer $q$, obtained from (**a**) EELS experiment and (**b**) time-dependent density-functional theory (TDDFT) calculation using the adiabatic local-density approximation (ALDA). It is noted throughout this chapter that the reciprocal lattice vector is expressed as $2\pi/a$ ($Å^{-1}$), where $a = 3.841$ Å is the lattice parameter of SVO, and then the momentum-transfer $q$ is defined accordingly. The TDDFT calculation was performed by our collaborators.

### 3.2.2 Behaviors of the bulk and surface plasmons

The bulk plasmon of SVO is found on a very thick sample, which is assumed to be quasi-bulk. We then turn our attention to the case of bulk and surface plasmons that might happen in the case of thinner slab geometries. We measured the plasmon excitations on the SVO slabs with various thicknesses $t$ of 240 nm, 120 nm, and 50 nm. First, under the dipole condition ($q = 0$), the thickest slab ($t = 240$ nm, figure 3.2(a)) shows a bulk plasmon peak ($\omega_b$) at 1.35 eV, as we observed on the micrometric SVO particles in figure 3.1. The medium thickness slab ($t = 120$ nm, figure 3.2(b)) exhibits the bulk plasmon peak and an additional peak at $\sim 1.1$ eV, which corresponds to surface plasmon excitation ($\omega_s$), due to the relation between the bulk and surface plasmon written as $\omega_s = \omega_b/\sqrt{2}$. The thinnest slab ($t = 50$ nm, figure 3.2(c)) exhibits only the surface plasmon peak at about 0.9 eV. As a result of the thinner thickness samples (SVO slabs with 120 nm and 50 nm thickness), the presence of surface plasmon is caused by the increased interfacial contribution of the slab's entry and exit planes (top and bottom interfaces of the slab).

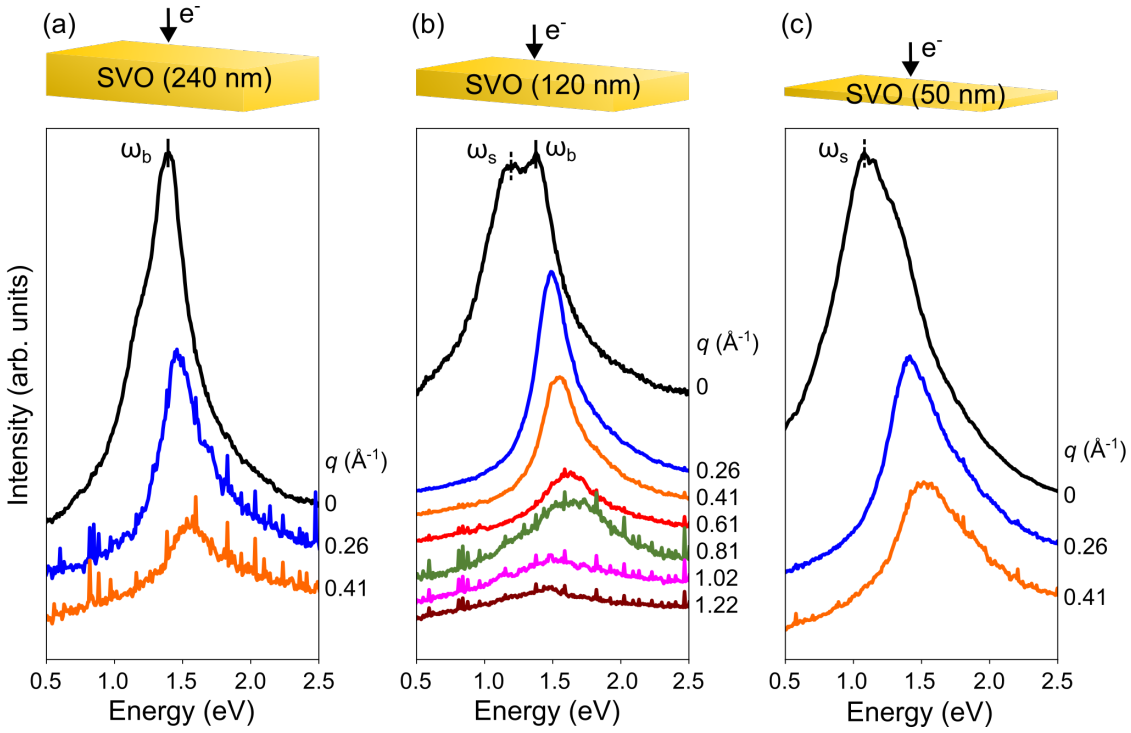


**Figure 3.2:** A series of momentum-resolved EELS spectra of the SVO slabs with the thickness of (**a**) 240 nm, (**b**) 120 nm, and (**c**) 50 nm. Where $\omega_b$ and $\omega_s$ represent the bulk plasmon (at 1.35 eV) and surface plasmon (at 0.7-1.1 eV), respectively.

Under the non-dipole conditions ($q > 0$), the surface plasmon vanishes for the slabs of all thicknesses, and the spectra retrieve the bulk-type plasmon features. The surface plasmon disappears because its intensity at $q > 0$ rapidly decreases with $q^{-3}$. With increasing $q$, the transformation from the bulk plasmon to surface plasmon has also been observed from other plasmonic materials [51, 52]. Nevertheless, the effect of thickness on energy dispersion is stronger than in most plasmonic materials. For instance, when the silver thin

film exceeds 20 nm, its energy dispersion of surface plasmon becomes negligible [52].

Figure 3.3 compares the energy dispersion of the plasmon peaks between the EELS experiment (gray) and the TDDFT calculation (red and blue). At $q = 0$, the surface plasmon peak locates in a range between 0.7 and 1.1 eV; in contrast, the bulk plasmon peak always shows at 1.35 eV. For $q > 0$, the plasmon peaks are independent of the thickness; the energy difference at the same $q$ for all the slabs is less than 40 meV. Further, the energy dispersion across 0.5 $Å^{-1}$ is about 170 meV, which is much smaller than in most plasmonic materials. For example, the plasmon energy dispersion of Ag is $\sim$ 0.4 eV over 0.4 $Å^{-1}$ [53]. This weak plasmon energy dispersion is certainly limited by the V-3*d* band. It is here to note that this dispersion seems larger than what is measured for TMOs that correspond to crystal-field excitation within 3*d* bands [54]. The energy dispersion of the SVO excitation is indeed way larger than that of *d*-*d* crystal-field excitations; for instance, the CoO and NiO cases have been reported with energy dispersions below 100 meV over 5 $Å^{-1}$ [29]. As a result of these differences, the SVO 1.35 eV loss is more likely to exhibit plasmonic character than pure crystal-field excitation.

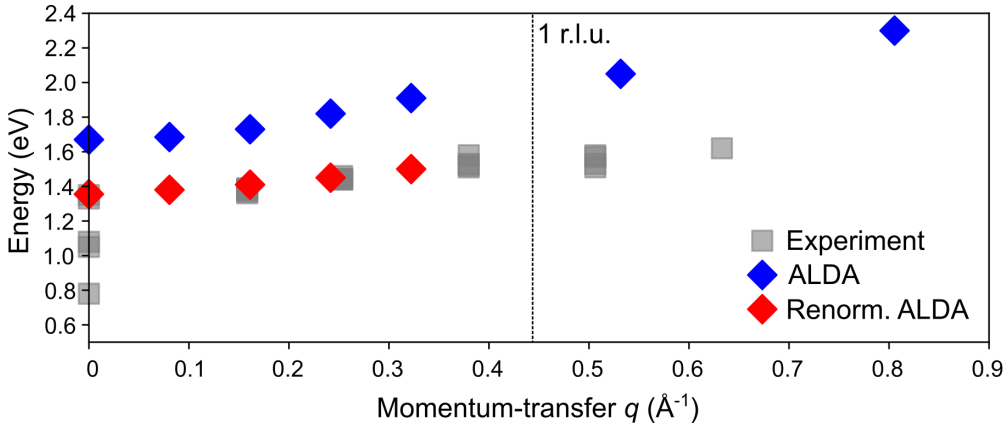


**Figure 3.3:** A comparison of the $q$-dependence of plasmon energy between the EELS experiment (gray square), ALDA calculation (blue diamond), and renormalized ALDA calculation (red diamond). Where reciprocal lattice unit (r.l.u.) = 0.43 $Å^{-1}$.

We now turn our attention to the TDDFT calculation curve in figure 3.3. As we can see, the calculation (blue spots) predicts a stronger blue shift of 300 meV (across 0.5 $Å^{-1}$) than the observation in the experiment (gray curve). There are two factors that contribute to theory overestimation: the ALDA overestimates the bandwidth in TMO and the choice of exchange-correlation. In order to compensate for the effects of overestimation, the bandwidth is reduced by a factor of 1.5 [55], and the renormalized curve is shown in red. The energy dispersion of the renormalized curve agrees perfectly with the experimental data, confirming that the V-3*d* band dispersion is at the origin of the weak plasmonic energy dispersion. Additionally, a good match has been obtained with a band renormalization that is smaller than the value often suggested by dynamical mean-field theory calculations of the quasiparticle band in SVO [15].

## 3.3 Numerical simulation: Finite-difference time-domain (FDTD) method

### 3.3.1 Localized surface plasmon (LSP)

Since we observed the intense bulk and surface plasmons in the quasi-infinite SVO slabs with different thicknesses (section 3.2), we are interested in the behavior of these LSP for nanostructures and their possible performance. The LSP can be considered as surface charges of nanostructures excited by an electromagnetic wave, such as an electric field caused by an electron beam, and surface charges exhibit damped harmonic oscillators. Figure 3.4 shows that the gold nanorod is excited by fast electrons and causes oscillations of the surface charges, thus allowing the LSP modes to be revealed in the frequency domain [47]. That is to say, we can observe the LSP modes by EELS [56]. A considerable number of plasmonic materials have been reported with excellent LSPs, such as gold [47], silver [57, 58], and copper [59]. It is not only conventional noble metals that are capable of LSPs, but there are more and more studies concerning potential alternative materials as well [44, 45, 46]. Additionally, the energy of the LSP modes strongly depends on the shape and size of nanostructures, such as nanorod [60] and nanotube [61], even the more complex structures have been reported [47, 62]. We will discuss the geometric effect on LSP in section 3.4.

The EELS is an appropriate technique to investigate the LSP of nanostructures, thanks to the spatial-resolved EELS spectrum imaging at nanometric resolution. Nevertheless, a numerical simulation also plays an indispensable role in interpreting the behaviors of LSP on different nanostructures. Several techniques have been established for calculating the LSP, such as photonic local density of state (LDOS) [63], boundary element method (BEM), discrete dipole approximation (DDA), finite element method (FEM) and finite-difference time-domain method (FDTD) [64, 65, 66, 67, 68]. Here, we simulate the EELS spectrum by the FDTD method [64, 69], and the basic principles of EELS spectrum calculation are briefly presented step by step in this section.

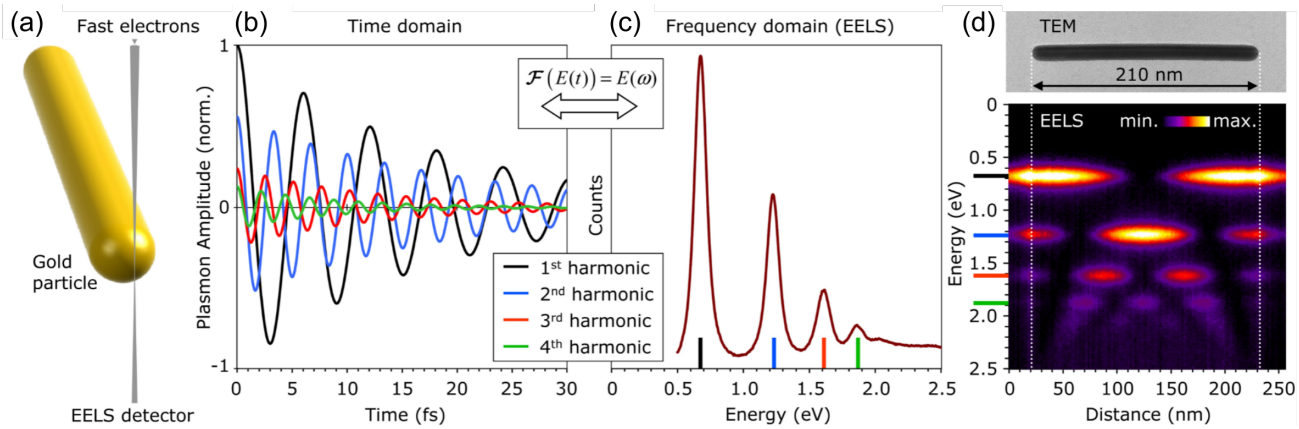


**Figure 3.4:** (**a**) The fast electrons excite the surface charges of the gold nanorod and cause the surface charges to oscillate. Localized surface plasmon (LSP) resonances are shown in (**b**) time and (**c**) frequency domains, which can be transformed by Fourier transformation. (**d**) The EELS spectrum imaging reveals the LSP resonance with spatial resolution. For instance, a dipolar LSP mode is clearly visible at 0.7 eV with two maxima of intensity at both tips of the nanorods. Reproduced from ref. [47].

### 3.3.2 Electron energy loss probability

First, a fast electron with velocity $\mathbf{v} = v\hat{z}$ passes through near an object along the $z$-axis, and the position of the electron in the time domain can be described as $\mathbf{r}(t) = \mathbf{r}_0 + \mathbf{v}t$, where $\mathbf{r}_0$ is the initial position of the electron. The electric field of the electron interacts with the object, and the object responds to an induced electric field $\mathbf{E}^{\text{ind}}$, and then this induced electric field acts back to the moving electron, causing energy loss. This energy loss of the electron can be written as the work due to the forces along the electron trajectory:

$$\Delta E = e\int \mathbf{v}\cdot\mathbf{E}^{\text{ind}}(\mathbf{r},t)dt = \int_0^\infty \hbar\omega\Gamma_{\text{EELS}}(\omega)d\omega \tag{3.3.1}$$

where negative electron charge -$e$ has been included (i.e., $\Delta E > 0$), and $\Gamma_{\text{EELS}}(\omega)$ is the energy loss probability of EELS. The time-domain induced electric field $\mathbf{E}^{\text{ind}}(\mathbf{r},t)$ can be transformed to the frequency domain by Fourier transform:

$$\mathbf{E}^{\text{ind}}(\mathbf{r},t) = \frac{1}{\pi}\int_0^\infty e^{-i\omega t}\mathbf{E}^{\text{ind}}(\mathbf{r},\omega)d\omega \tag{3.3.2}$$

and the energy loss probability of EELS in the frequency domain is written as

$$\Gamma_{\text{EELS}}(\omega) = \frac{e}{\pi\hbar\omega}\int Re\left[e^{-i\omega t}\mathbf{v}\cdot\mathbf{E}^{\text{ind}}(\mathbf{r},\omega)\right]dt \tag{3.3.3}$$

Up until now, according to the equation 3.3.3, the induced electric field is the key point of this calculation. A schematic diagram of the energy loss probability calculation process is shown in figure 3.5.

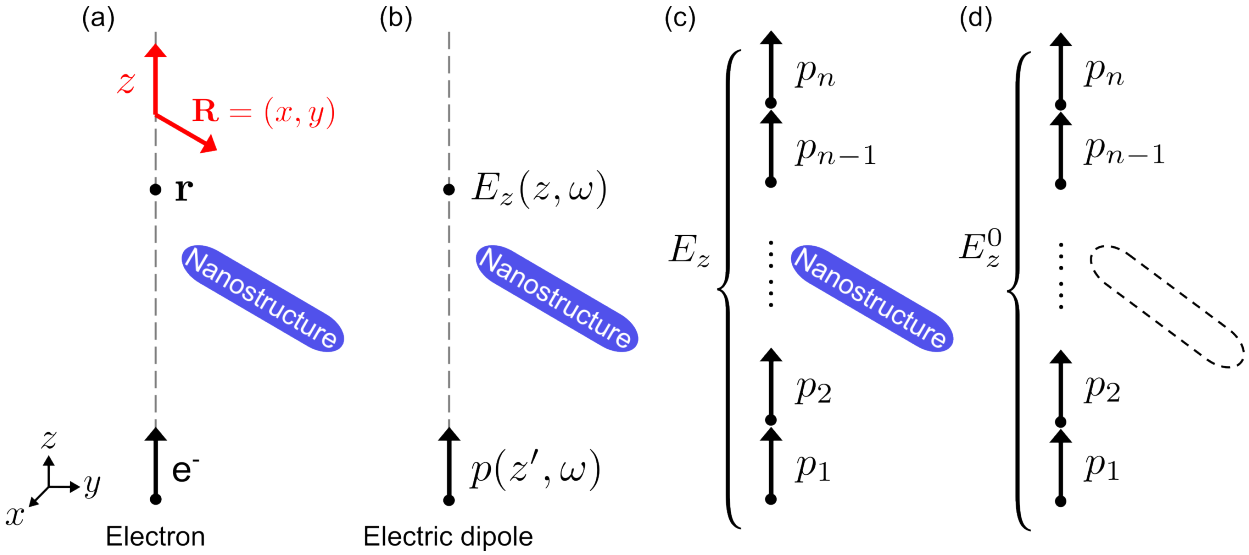


**Figure 3.5:** Schematic diagram of the electron energy loss probability calculation process. **(a)** A fast electron travels along the positive $z$-axis. The coordinate system is employed by $\mathbf{r} = (\mathbf{R}, z)$ with $\mathbf{R} = (x, y)$. **(b)** Substituting the electron for an electric dipole $p(z', \omega)$, and $E_z(z, \omega)$ represents the $z$-component of electric field generated by the electric dipole. **(c)** The electron beam can be considered as a series of electric dipoles ($p_1$ to $p_n$) placed along the $z$-axis electron trajectory, and the integration of the electric field generated by all the electric dipoles is $E_z$. **(d)** With a similar approach with $E_z$, but the electric field $E_z^0$ is calculated without the nanostructure, i.e., the background electric field. The induced electric field $E_z^{\text{ind}}$ is described as the electric field calculated in (c), deducting the electric field calculated in (d).

Let's now consider the moving electron along the $z$-axis trajectory by its electron charge density $\rho(\mathbf{r}, \omega)$

$$\rho(\mathbf{r}, \omega) = -e \int e^{i\omega t} \delta[\mathbf{r} - (\mathbf{r}_0 + \mathbf{v}t)] dt \tag{3.3.4a}$$

$$= -\frac{e}{v} \delta(\mathbf{R} - \mathbf{R}_0) e^{i\omega(z - z_0)/v} \tag{3.3.4b}$$

where $\mathbf{r} = (\mathbf{R}, z)$, with $\mathbf{R} = (x, y)$ representing the impact parameter on the $x$-$y$ plane, and the initial position $\mathbf{r}_0 = (\mathbf{R}_0, z_0)$. The external current density $\mathbf{j}(\mathbf{r}, \omega) = \mathbf{v} \cdot \rho(\mathbf{r}, \omega)$ can be substituted by the electron charge density in equation 3.3.4b and then the external current density becomes:

$$\mathbf{j}(\mathbf{r}, \omega) = -e\delta(\mathbf{R} - \mathbf{R}_0) e^{i\omega(z - z_0)/v} \hat{z} \tag{3.3.5}$$

The electric field generated by this external current density can be rewritten by Green tensor $\mathbf{G}(\mathbf{r}, \mathbf{r}', \omega)$ as:

$$\mathbf{E}(\mathbf{r}, \omega) = -4\pi i\omega \int \mathbf{G}(\mathbf{r}, \mathbf{r}', \omega) \cdot \mathbf{j}(\mathbf{r}', \omega) d\mathbf{r}' \tag{3.3.6}$$

where the Green tensor satisfies the solution of the inhomogeneous Helmholtz equation as follows:

$$\nabla \times \nabla \times \mathbf{G}(\mathbf{r}, \mathbf{r}', \omega) - (\frac{\omega}{c})^2 \varepsilon(\mathbf{r}, \omega)\mathbf{G}(\mathbf{r}, \mathbf{r}', \omega) = -\frac{1}{c^2}\delta(\mathbf{r} - \mathbf{r}') \tag{3.3.7}$$

where $\varepsilon(\mathbf{r}, \omega)$ is the permittivity of the medium. The energy loss probability of EELS (equation 3.3.3) can be rewritten by substituting the external current density (equation 3.3.5) and the electric field (equation 3.3.6):

$$\Gamma_{\text{EELS}}(\omega) = \frac{4e^2}{\hbar} \int \int_{-\infty}^{\infty} cos[\frac{\omega(z - z')}{v}] \times Im[-G_{zz}^{\text{ind}}(z, z', \omega)]dzdz' \tag{3.3.8}$$

where $G_{zz}^{\text{ind}}(z, z', \omega)$ is $z$-component of the induced Green tensor. The induced Green tensor $\mathbf{G}^{\text{ind}}$ can be considered as a Green tensor $\mathbf{G}$ removing the background contribution; in other words, the Green tensor in vacuum $\mathbf{G}^0$ needs to be taken away. The induced Green tensor is written as:

$$\mathbf{G}^{\text{ind}}(z, z', \omega) = \mathbf{G}(z, z', \omega) - \mathbf{G}^0(z, z', \omega) \tag{3.3.9}$$

Then, according to equation 3.3.8, only $z$-component term of the induced Green tensor $\mathbf{G}^{\text{ind}}$ needs to be considered. The $z$-component of the induced Green tensor can be written as $G_{zz}^{\text{ind}} = \hat{z} \cdot \mathbf{G}^{\text{ind}} \cdot \hat{z}$, therefore, the $z$-component of the induced Green tensor is

$$G_{zz}^{\text{ind}}(z, z', \omega) = \hat{z} \cdot [\mathbf{G}(z, z', \omega) - \mathbf{G}^0(z, z', \omega)] \cdot \hat{z} \tag{3.3.10}$$

The $z$-component of Green tensor $G_{zz}^{\text{ind}}(z', z, \omega)$ can also be described by the $z$-component induced electric field $E_z^{\text{ind}}(z, \omega)$ and the electric dipole $p(z', \omega)$ located at $z'$ along the electron trajectory:

$$G_{zz}^{\text{ind}}(z, z', \omega) = -\frac{1}{4\pi\omega^2} \frac{E_z^{\text{ind}}(z, \omega)}{p(z', \omega)} \tag{3.3.11}$$

Finally, substituting the $z$-component of the induced Green tensor of equation 3.3.11 into equation 3.3.8, allows us to simplify the energy loss probability of EELS as follows:

$$\Gamma_{\text{EELS}}(\omega) = \frac{e^2}{\pi\hbar\omega^2} \int \int_{-\infty}^{\infty} cos[\frac{\omega(z - z')}{v}] \times Im[\frac{E_z^{\text{ind}}(z, \omega)}{p(z', \omega)}]dzdz' \tag{3.3.12}$$

It is interesting to note that in order to calculate the energy loss probability of EELS by a fast electron (figure 3.5(a)), we only need to take into account the $z$-component of the induced electric field, which is produced by the electric dipoles along the electron trajectory (figure 3.5(b)).

In practice, the loss function calculation requires a numerical estimation of this double integration along $z$, $z'$. One needs first to sum the $E_z^{\text{ind}}(z,\omega)$ over all $z$ positions for a given dipole positioned at $z'$, as shown in figure 3.5(c). Then, the second integration corresponds to the sum when the position of the dipole is shifted along the electron trajectory, as shown in figure 3.5(d). An integrand is mainly weighed by the cosine term, which considers the distance between the electric dipole and the induced electric field. The $E_z^{\text{ind}}(z,\omega)$ can be numerically computed through the FDTD method.

### 3.3.3 FDTD algorithm

The next step is to calculate the induced electric field in order to reproduce the energy loss probability of EELS (based on equation 3.3.12). The FDTD method is a powerful approach for solving time-dependent Maxwell's equations in complex nanostructure geometries. The advantage of this time-domain method is that it provides a spectrum with a wide range of frequencies within a single simulation.

FDTD algorithm starts from time-dependent Maxwell's equations:

$$\nabla \times \mathbf{H} = \varepsilon \frac{\partial \mathbf{E}}{\partial t} \tag{3.3.13a}$$

$$\nabla \times \mathbf{E} = -\mu \frac{\partial \mathbf{H}}{\partial t} \tag{3.3.13b}$$

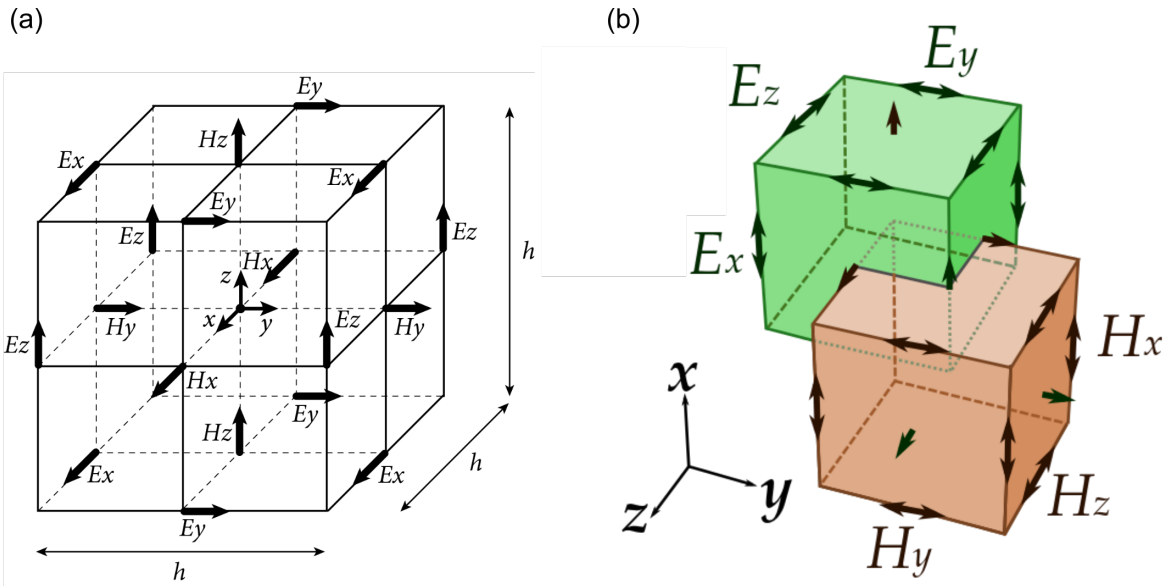


**Figure 3.6:** (**a**) A *Yee cell* in three-dimensional real space. $H_x, H_y, H_z$ and $E_x, E_y, E_z$ are $x$-, $y$-, and $z$-component of magnetic and electric fields respectively. Where $h$ is the grid spacing. (**b**) The *Yee cells* in time evolution. The primary (green) and secondary *Yee cells* (orange) show their intertwined magnetic and electric fields.

To drive time-dependent Maxwell's equations, K. Yee proposed the *Yee cell* that discretizes the equations in both space and time with a uniform grid that spatially staggered the magnetic and electric fields [70]. The magnetic and electric fields in three-dimensional spatial space can be described by the following equations, and the schematic is shown in figure 3.6(a):

$$\begin{aligned} H_x &= \mathbf{H}[(x+\frac{h}{2}, y, z), t-\frac{\Delta t}{2}], & E_x &= \mathbf{E}[(x, y+\frac{h}{2}, z+\frac{h}{2}),\ t] \\ H_y &= \mathbf{H}[(x, y+\frac{h}{2}, z), t-\frac{\Delta t}{2}], & E_y &= \mathbf{E}[(x+\frac{h}{2}, y, z+\frac{h}{2}),\ t] \\ H_z &= \mathbf{H}[(x, y, z+\frac{h}{2}), t-\frac{\Delta t}{2}], & E_z &= \mathbf{E}[(x+\frac{h}{2}, y+\frac{h}{2}, z),\ t] \end{aligned} \tag{3.3.14}$$

where $h$ is the grid spacing, and $\Delta t$ is a time-step. The discretized time components of the magnetic and electric fields are notated as $\mathbf{H}(t) \rightarrow \mathbf{H}^{n+\frac{1}{2}}$ and $\mathbf{E}(t) \rightarrow \mathbf{E}^n$, where superscript represents the time term ($n$ is an integer $\geq 0$).

The electric and magnetic fields can be rewritten in the time evolution form by equation 3.3.13 and finite difference equation, then we have

$$\mathbf{H}^{n+\frac{1}{2}} = \mathbf{H}^{n-\frac{1}{2}} - \frac{\Delta t}{\mu}\nabla \times \mathbf{E}^n \tag{3.3.15a}$$

$$\mathbf{E}^{n+1} = \mathbf{E}^n + \frac{\Delta t}{\varepsilon}\nabla \times \mathbf{H}^{n+\frac{1}{2}} \tag{3.3.15b}$$

The magnetic and electric field updates are staggered in time evolution, i.e., the magnetic field update is followed by succeeding electric field updates (shown in figure 3.6(b)), and conversely. Consequently, with the initial conditions of $\mathbf{H}^{-\frac{1}{2}} = 0$ and $\mathbf{E}^0 = 0$, we can calculate magnetic and electric fields in the order of time evolution:

$$(\mathbf{H}^{-\frac{1}{2}}, \mathbf{E}^0) \rightarrow \mathbf{H}^{\frac{1}{2}} \rightarrow \mathbf{E}^1 \rightarrow \mathbf{H}^{\frac{3}{2}} \rightarrow \mathbf{E}^2 \rightarrow \mathbf{H}^{\frac{5}{2}} \rightarrow \cdots \tag{3.3.16}$$

By iteratively calculating the electric field, a convergent field can be substituted into equation 3.3.12.

### 3.3.4 Lumerical FDTD simulator

Here, we use the Lumerical software to achieve the calculation of the electric field. The Lumerical software is a state-of-art software for optoelectronic simulation and photonic circuit design. The FDTD solver package of the Lumerical software is an easy and reliable tool to solve Maxwell's equations by the FDTD method in a friendly operational environment. The setup for the calculation is briefly described in this subsection.

**Description of nanostructure (geometry and permittivity)**

Initially, an arbitrary three-dimensional object needs to be designed, and the corresponding complex relative permittivity is imported to describe the material (relative permittivity of SVO is shown in figure 3.7). Nevertheless, the discrete values of the relative permittivity cannot be used directly in the simulation; an analytic material model should be used instead. In order to obtain the most accurate fit, we can modify several parameters, including the fit tolerance, the maximum coefficients, and the imaginary weight. Finally, the RMS (root-mean-square) error is 0.16 when the wavelength range of the relative permittivity is from 500 nm to 12000 nm (i.e., from 2.48 eV to 0.1 eV). With a frequency point of 300, the spectrum has an energy dispersion of 8 meV per channel.

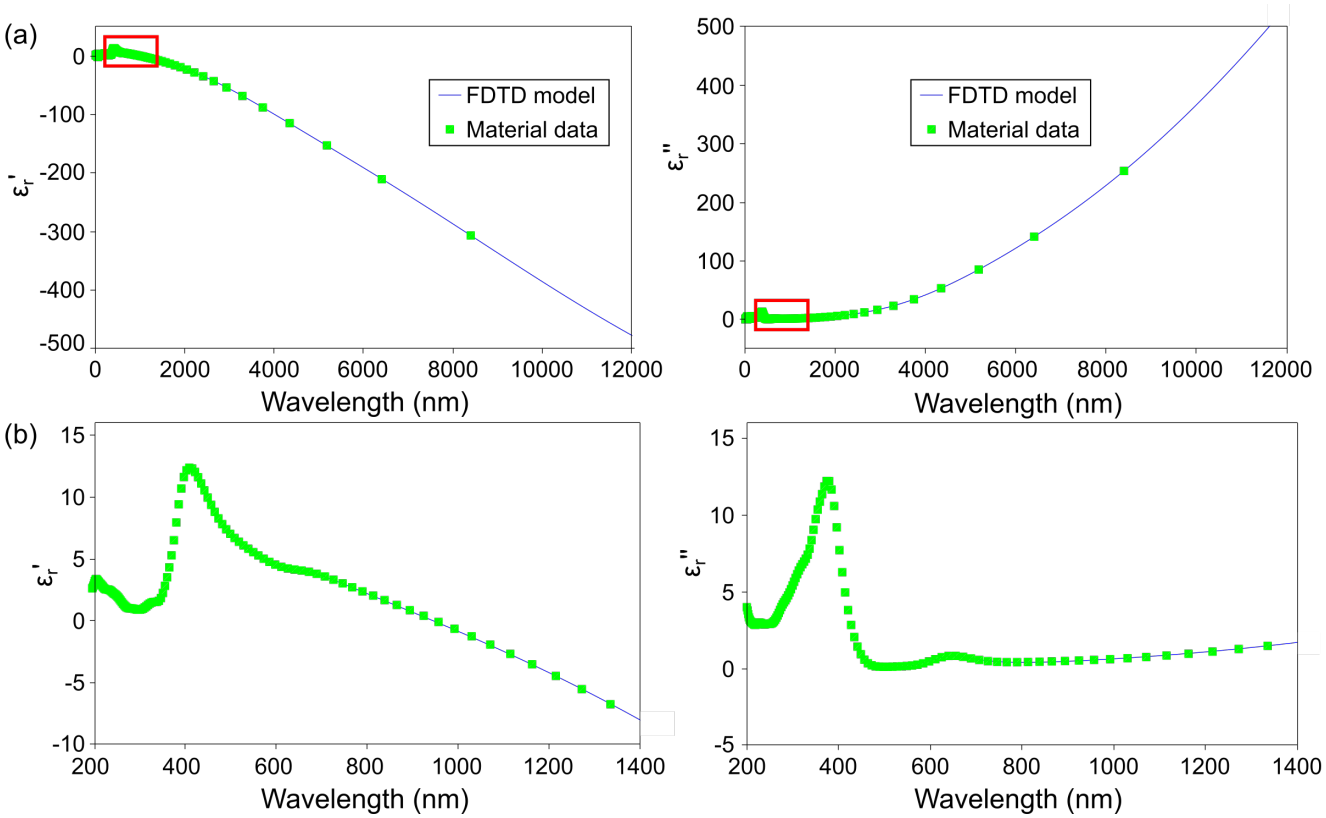


**Figure 3.7:** (**a**) The real and imaginary parts of the SVO relative permittivity. The discrete values of relative permittivity are shown as green spots and the fitting curve by Lumerical software is shown as blue curves. (**b**) Extracted visible and near-infrared portions of the SVO relative permittivity (marked as red boxes in (a)).

**Source - electric dipole**

A series of electric dipoles are placed along the $z$-axis electron trajectory, and these electric dipoles can be regarded as a continuous electron beam (according to the integral for all the electric dipoles in equation 3.3.12). A finite number of electric dipoles is sufficient to represent an electron beam since the contribution of electron energy loss by the dipoles further away from the object can be ignored. We place equally spaced 10 electric dipoles (an amplitude of $7.78\times10^{-31}$ C·m; a pulse length of 3.3 fs; a frequency of 312 THz) between $z = \pm125$ nm along $z$-axis. These parameters are for a 100 nm thick object, balancing the number of electric dipoles and computation time. In order to calculate the spatial-resolved LSP, we adjust the impact parameter of the electric dipoles, and the electric dipole is located at 2 nm from the surface of the object, like the aloof beam mode. Since we focus on the LSP in our case, we do not take into account the plasmon response inside the object, and a modification of the equation is required if the electron beam penetrates the object [64].

**Boundary conditions**

The boundary conditions have to be optimized in order to avoid spurious effects such as the reflection of electromagnetic waves from the box wall. Perfectly matched layers (PMLs) are defined as boundary conditions that absorb all reflections from exterior boundaries. The mesh type of PMLs is *auto non-uniform*, where the mesh cell in the FDTD algorithm is set as a graded rectangular cell whose size is a function of position. The software automatically optimizes mesh size (minimum mesh of 0.25 nm) to minimize artifacts from numerical dispersion, using the finer mesh near the interface or curved surface. *Auto non-uniform* mesh setting gives higher precision than uniform mesh and requires less computation time and memory, due to computation time being proportional to $(1/dx)^4$ for a three-dimensional structure, where $dx$ is the size of a mesh.

In order to improve the convergence of calculation, we defined an override mesh to specify the object; the override mesh of the object consists of uniform 4 $nm^3$ unit cells. The override mesh extends 2 nm outward from the object's surface. Additionally, a one-dimensional monitor is used for recording the $z$-component of the electromagnetic field, and another override mesh grid covers the monitor to improve convergence.

Additionally, the simulation time of 100 fs is the maximum duration of the simulation. The *auto-shutoff* value of $10^{-5}$ ensures that the simulation will end when the ratio of total energy to maximum injected energy drops below this value.

**Induced electric field**

The calculation for the induced electric field needs to operate twice: the first time, we calculate the electric field with the object and obtain the $E_z(z,\omega)$; the second time, we calculate the electric field without the object (i.e., in the vacuum) and obtain the $E_z^0(z,\omega)$. By subtracting $E_z^0(z,\omega)$ from $E_z(z,\omega)$, we can obtain the induced electric field $E_z^{\text{ind}}(z,\omega)$, similar concept to equation 3.3.9 and figure 3.5(c,d). Furthermore, using a Matlab script, which is doing the double integral to all the induced electric fields according to equation 3.3.12 can achieve the EELS spectrum calculation.

## 3.4 $SrVO_3$ nanostructures

### 3.4.1 Presence of LSP on slabs

We are intrigued by the possibility of SVO nanostructures supporting LSPs. In this study, we measured the EELS spectra of SVO slabs a few tens of nanometers away from the edge. Firstly, a HAADF image of a slab with a thickness of ∼100 nm and its EELS spectra are shown in figure 3.8(a, c), respectively. Impact parameters from 2 nm to 100 nm correspond to dark blue to light blue curves in the spectrum. The surface plasmon peak (peak-$\omega_B$) and the edge state peaks (peak-$\omega_{A,1}$ and $\omega_{A,2}$) are visible; in addition, they are still able to survive at a far distance from the edge (more than 100 nm). The intensity of the edge state peak increases with moving away from the surface, while the intensity of the surface plasmon peak decreases. The FDTD calculation of the similar slab (the model in figure 3.8(b) and corresponding spectrum in figure 3.8(d)) can roughly describe the intensity trends of surface plasmon and edge states. However, the single peak-$\omega_A$ of the calculation rather than the two peaks of the experiment is probably due to the approximation in the slab shape model.

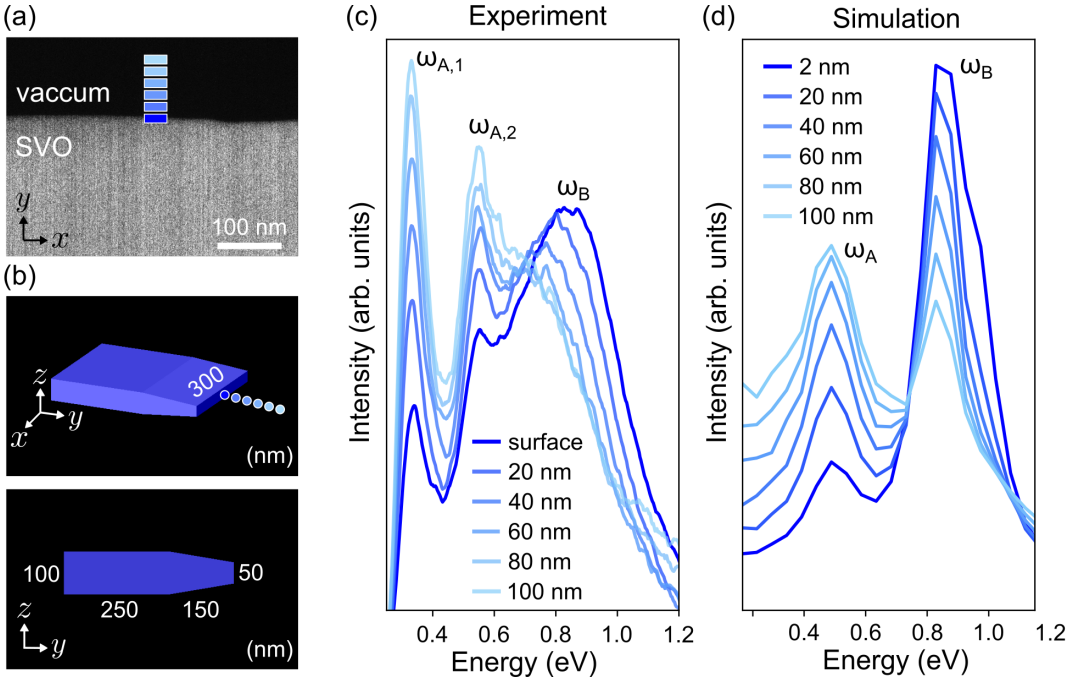


**Figure 3.8:** A comparison between the (**a,c**) experimental and (**b,d**) simulated EELS spectra by the FDTD method of the SVO slab with a thickness of ∼ 100 nm. (**a**) The HAADF image of the SVO slab and (**b**) correspondent three-dimensional model of the SVO slab created by Lumerical software. (**c,d**) The spatial dependence EELS spectra with impact parameters from 2 nm (dark blue) to 100 nm (light blue). The spectrum is taken from the position indicated by the corresponding color in (a,b).

Since we calculated the slab with simple geometry (figure 3.8), a more complex slab has also been investigated. Figure 3.9(a,c) show the HAADF image and spectrum of the three-step slab with a gradient thickness from 50 nm to 100 nm. In figure 3.9(c), the intensity ratio of the surface plasmon (ca. 0.7-0.9 eV) and edge state peaks (below 0.6 eV) depends on the impact parameters; surface plasmon peaks weaken as they move away from the surface, while edge state peaks become stronger. We extracted the spectrum from several positions, which are marked in A, B, and C in figure 3.9(a), and the corresponding spectrum is displayed from top to bottom in figure 3.9(c), respectively. Nevertheless, trends are also captured by the FDTD calculation of a similar structure, whose model and spectrum are shown in figure 3.9(b,d), respectively.

From these results of SVO slabs, we can confirm that the SVO has mostly LSP modes located in a range from 0.4 to 1.2 eV, which strongly depends on the geometries of nanostructures. Additionally, the FDTD calculation can effectively investigate the trend of LSP with varying geometrical structures.

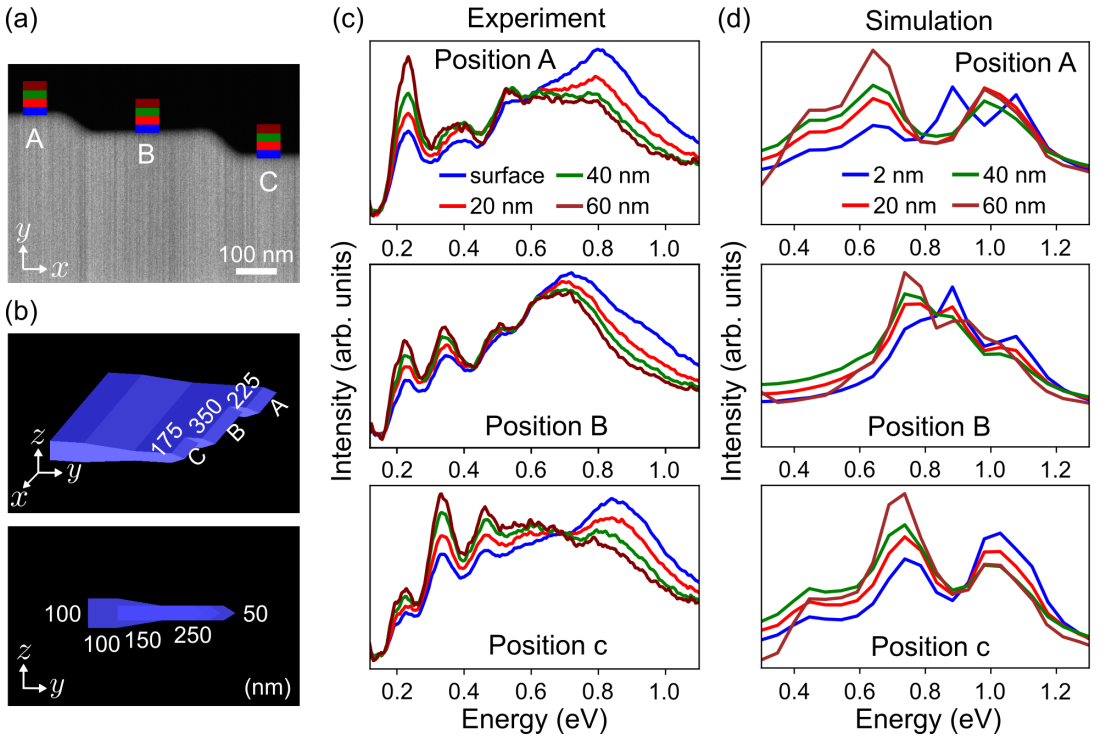


**Figure 3.9:** A comparison between the (**a,c**) experimental and (**b,d**) simulated EELS spectra by the FDTD method of the SVO step-like slab with a thickness of $\sim$ 100 nm. (**a**) The HAADF image and (**b**) correspondent three-dimensional model of the SVO step-like slab created by Lumerical software. (**c,d**) The spatial dependence EELS spectra with impact parameters of 2 nm (blue), 20 nm (red), 40 nm (green), and 60 nm (brown). In (c,d), from the top to bottom row correspond the spectra of positions A, B, and C, respectively.

### 3.4.2 LSP of rod-like nanostructures

As a result of the LSPs observed in SVO quasi-infinite slabs, several geometric models also show them; for instance, nanoparticles and nanowires are widely investigated [71, 72]. The rod-like nanostructures are more accessible to control than complex nanostructures; in addition, the rod-like nanostructures have the possibility to display Fabry-Perrot type LSP. Here, we will discuss how the LSP behaves on different nanostructures, such as half-rod and slit.

Figure 3.10 shows the low magnification STEM images of SVO nanostructures fabricated from a single crystal by the focused ion beam (FIB). A shorter (0.85 μm), a longer (2.5 μm), and a triple neighboring half-rod (2.5 μm) are shown in figure 3.10(a); slits of 2.5 μm length with different widths are shown in figure 3.10(b). Aspect ratios can be used to quantify the geometric shapes of these nanostructures, and we will demonstrate the performance of LSP on these SVO nanostructures.

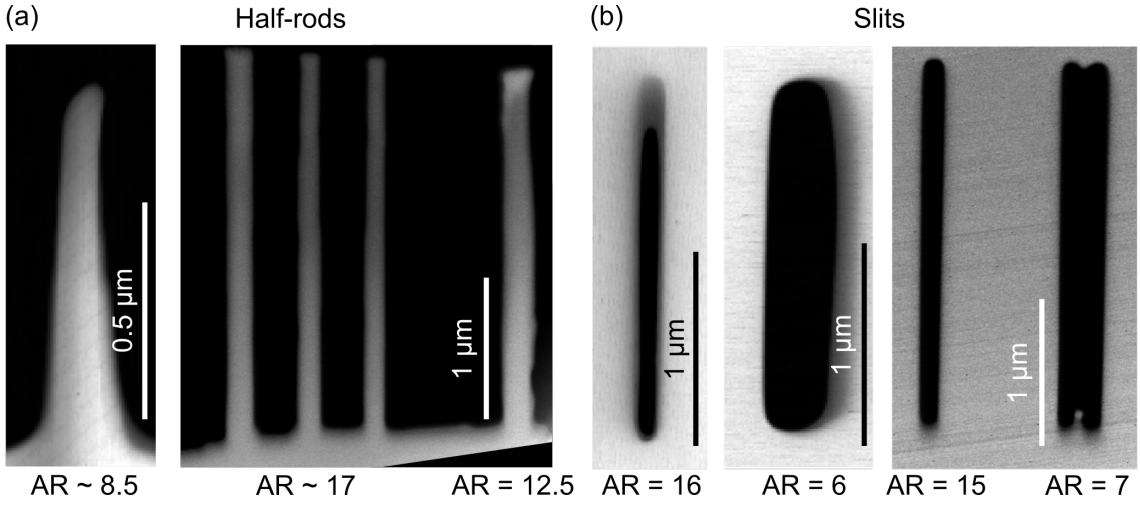


**Figure 3.10:** The SVO nanostructures of (**a**) half-rods and (**b**) slits fabricated by the focused ion beam. The aspect ratio (AR) is calculated by dividing the length by the width of a nanostructure.

**Half-rods**

First, the EELS measurements of an isolated 850 nm half-rod are shown in figure 3.11(a,b). Spectra are extracted from different spatial positions, which correspond to the color-matching spots in the HAADF image, and several LSP peaks are observed. The energy-filtered STEM-EELS maps in figure 3.11(b) reveal the spatial distribution of these LSP modes, whose energy windows correspond to 240, 510, and 740 meV with a 100 meV energy range, respectively. Furthermore, figure 3.11(c) demonstrates the simulated FDTD model, consisting of a 0.85 μm × 0.1 μm rod connected to a 2.5 μm × 1.5 μm substrate with 0.1 μm thickness, whose structure roughly corresponds to the experiment in figure 3.11(a). There are also several LSP peaks visible in the spectra. Figure 3.11(d) shows the two-dimensional simulated EELS map, which clearly identifies the first-order to fourth-order LSP modes. Figure 3.11(b,d) are comparable with their LSP spatial distribution at each

mode; notably, the tip of the rod consistently exhibits the LSP as we expected for the rod-like structure. However, since the experimental sample does not have the exact shape of the simulated model, differences in nanostructure geometries can significantly affect the energy and spatial location of LSP modes, and we will discuss this phenomenon later.

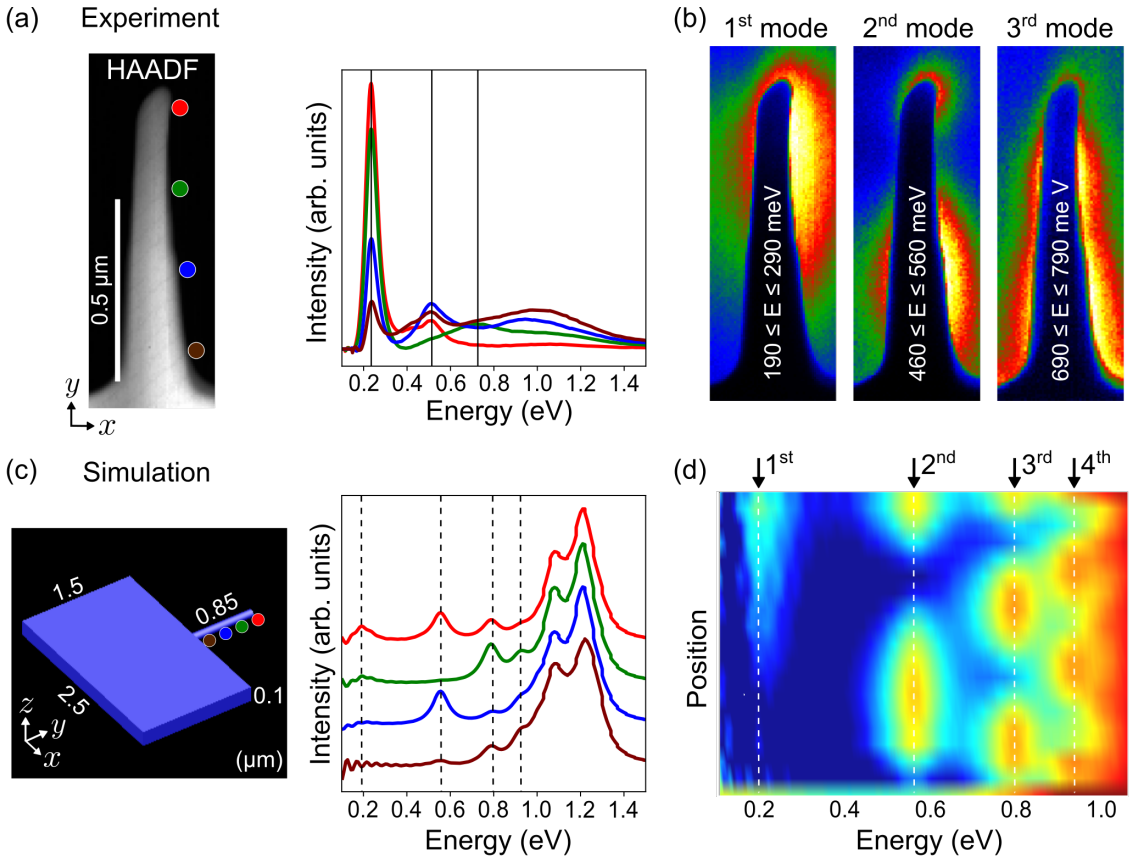


**Figure 3.11:** (**a**) HAADF image of the 850 nm length half-rod and the zero-loss-peak subtracted EELS spectra, which are extracted from the positions in matching color in the HAADF image. The black solid lines highlight the energy of LSP modes. (**b**) Several LSP modes can be presented by energy-filtered STEM-EELS maps, with energy-selecting windows of 100 meV. (**c**) The correspondent three-dimensional model of the SVO half-rod and the simulated EELS spectra extracted from the positions in matching color in the model. The black dashed lines highlight the energy of simulated LSP modes. (**d**) A two-dimensional simulated EELS map indicates the spatial distribution of the LSP modes.

Figure 3.12(a,b) show energy-filter STEM-EELS images and a two-dimensional simulated EELS map of a 2.5 μm length half-rod. In comparison with the shorter half-rod, the LSP energy peaks shift to lower energy (first-order to third-order modes are observed below 0.5 eV), and the intervals between different LSP modes decrease. Therefore, more nodes are revealed for higher-order LSP modes. Additionally, the LSPs have an asymmetric spatial distribution due to the asymmetric geometry of the half-rod.

Figure 3.12(c) reveals the LSP modes for triple neighboring half-rods. The geometry of each rod is not identical (with slightly different widths) as the result of the spatial shifting of the LSP, confirming that slight variations in aspect ratios can significantly affect the position and energy of LSP.

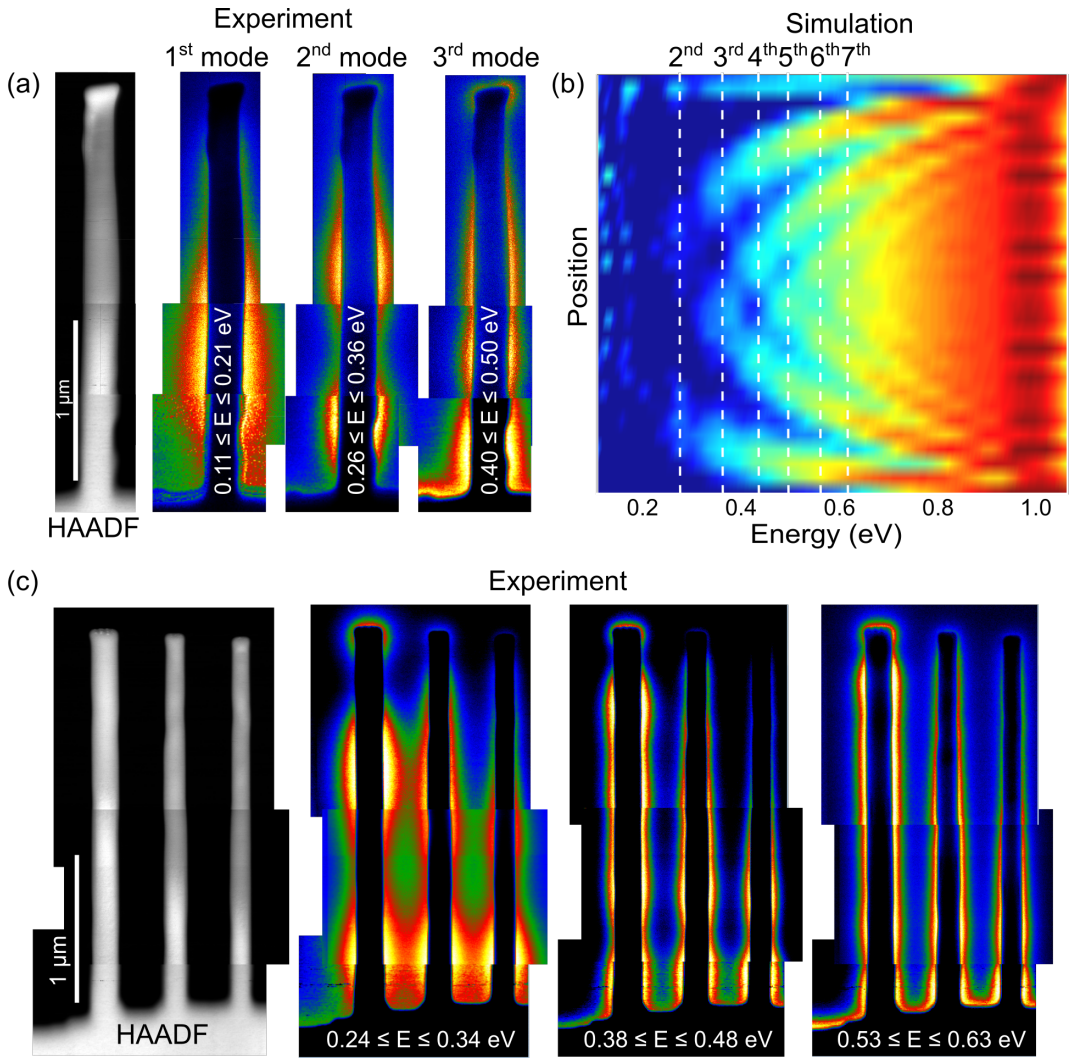


**Figure 3.12:** (**a**) HAADF image and the energy-filtered STEM-EELS maps and (**b**) two-dimensional simulated EELS map of the 2.5 μm length half-rod. The white dashed lines highlight the energy of simulated LSP modes. (**c**) HAADF image and the energy-filtered STEM-EELS maps of the 2.5 μm length triple neighboring half-rods.

**Slits**

Lastly, a result of the 2.5 μm length slit is shown in figure 3.13, where both experimental (figure 3.13(a)) and simulated results (figure 3.13(b)) show several LSP modes. As expected from the Babinet principle, which predicts the plasmonic response of two complementary structures [73, 71, 72], the lowest LSP mode is not at the tip but rather at the center of the slit. Additionally, for the FDTD simulation, the closed structure enhances the reflection of the electromagnetic wave inside the slit, causing small ripples in the low energy range (below 0.3 eV). Since we confirmed that the geometric effect plays a significant role in LSP mode, we then simulate LSP in different geometries.

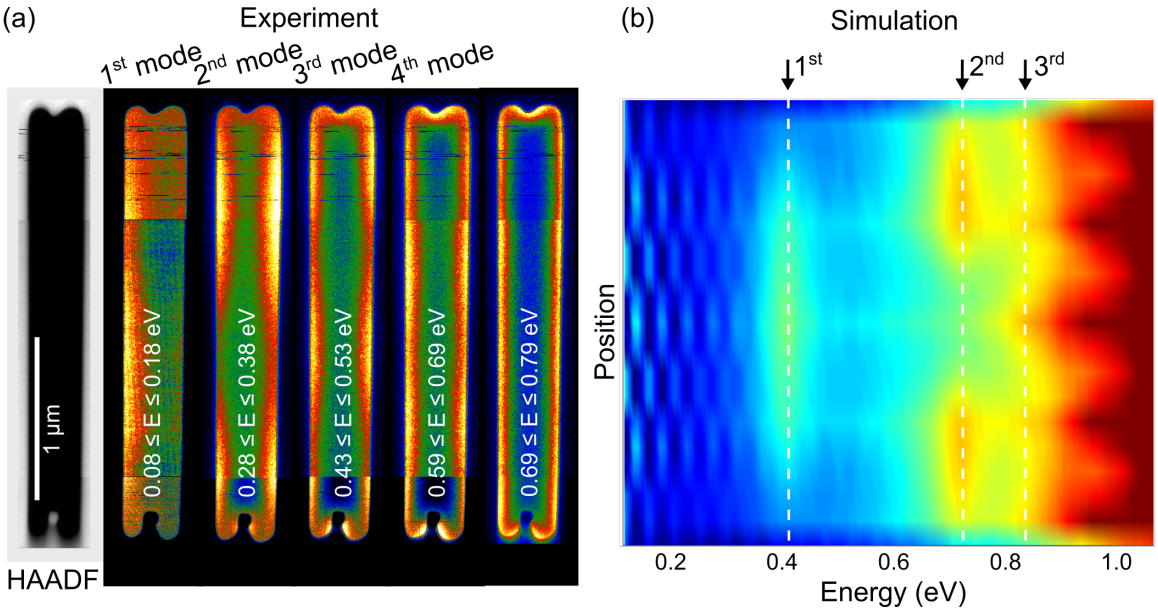


**Figure 3.13:** (**a**) HAADF image and the energy-filtered STEM-EELS images and (**b**) two-dimensional simulated EELS map of the 2.5 μm length slit. The white dashed lines highlight the energy of simulated LSP modes.

### 3.4.3 A series of rod-like nanostructures with different aspect ratios

Further, a comparison of the two-dimensional simulated EELS map between the LSPs of the rods, slits, and half-rods is shown in figure 3.14. With increments of the length $l$ and the fixed-width $d$, the aspect ratios ($AR = l/d$) of nanostructures can be turned from 20 to 80. Obviously, the rods (first row) and the slits (middle row) exhibit complementary LSP patterns that match Babinet's principle well. The half-rods (bottom row) have asymmetric patterns due to the effect of the substrate. In this way, we are able to understand how LSPs are spatially distributed based on different geometries. Moreover, there is a larger energy dispersion ($> 0.5$ eV) by geometry effect than energy-momentum dispersion ($\sim 0.2$ eV).

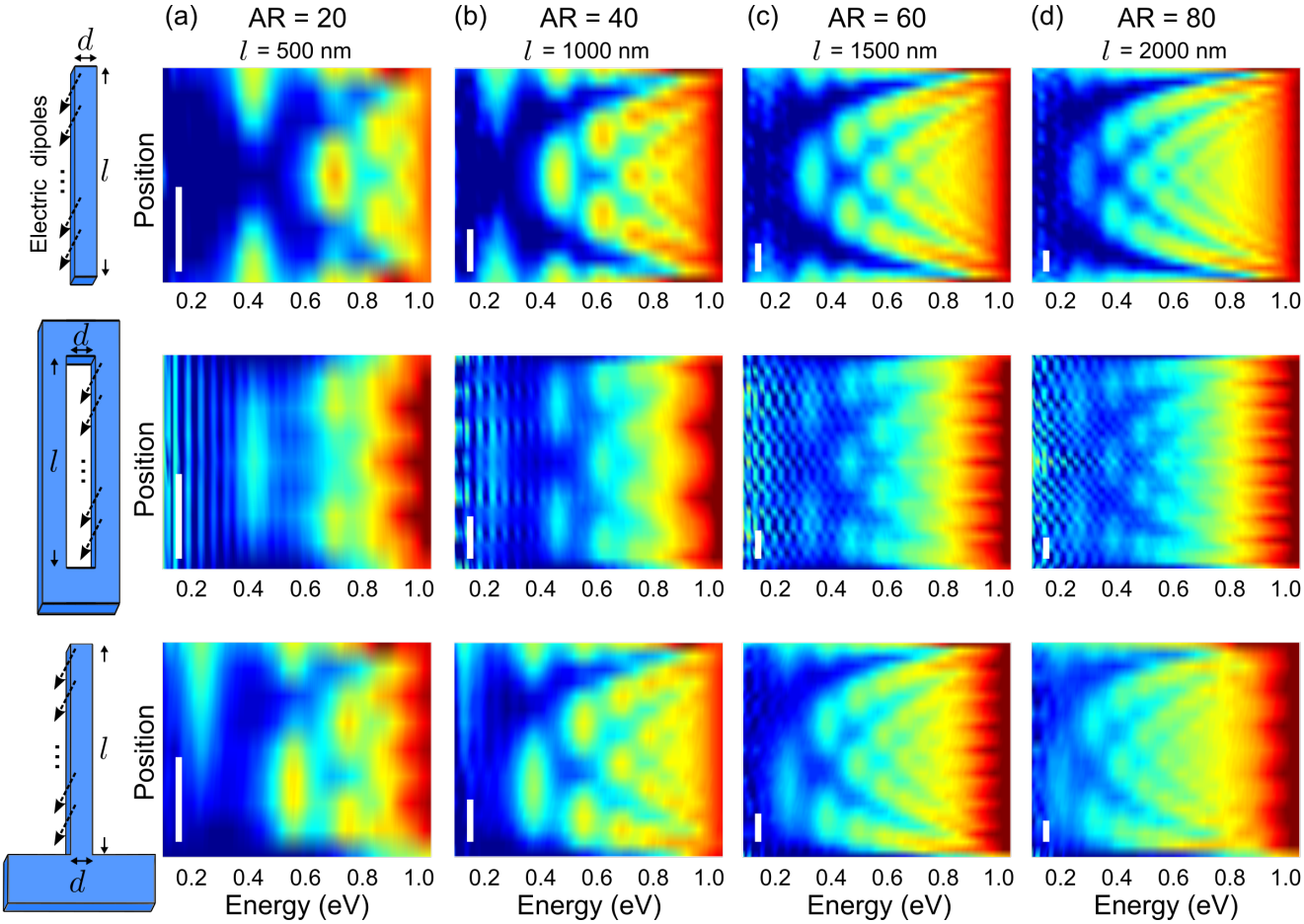


**Figure 3.14:** Two-dimensional simulated EELS maps of different types of nanostructures with a series of aspect ratios ($AR = l/d$). The sizes of the rods (upper row), the slits (middle row), and the half-rods (bottom row) are **(a)** $l = 500$ nm, $d = 25$ nm ($AR = 20$); **(b)** $l = 1000$ nm, $d = 25$ nm ($AR = 40$); **(c)** $l = 1500$ nm, $d = 25$ nm ($AR = 60$) and **(d)** $l = 2000$ nm, $d = 25$ nm ($AR = 80$). The values of $l$ and $d$ are the same in each column, and all the scale bars are 200 nm.

### 3.4.4 Quality factor of LSP

In order to evaluate the quality of the LSPs on these nanostructures, we estimated the quality factor of each LSP mode. In figure 3.15(a), the quality factors of the LSPs are plotted as a function of plasmon energy and FWHM. The quality factor $Q$ can be derived from the damped harmonic oscillators [47], and be written as:

$$Q \approx \frac{\omega_p}{\Gamma} \tag{3.4.17}$$

where $\omega_p$ is the energy of the LSP mode, and $\Gamma$ corresponds to its FWHM. Several LSP modes exhibit FWHM below 100 meV, and SVO has quality factors around 2-5 in a range of 0.2 to 0.9 eV. A clear feature of three LSP modes can be seen in the EELS spectrum of the slit in figure 3.15(b). Without deconvolution of the EELS spectrum, the quality factor estimation is rather conservative due to an energy broadening of approximately 40 meV in the zero-loss peak (ZLP). Nevertheless, these quality factors almost reach those of known metallic oxides. For instance, indium tin oxide (ITO) nanostructures exhibit LSP excitations between 150 and 550 meV with an FWHM of around 150 meV, resulting in quality factors of 1-3 [44]. The cerium-doped indium oxide (Ce:$In_2O_3$) nanocrystal has been reported to exhibit a LSP peak at 313 meV with a narrow FWHW of 77 meV, indicating its quality factor of $\sim 4$ [74]. La-doped $BaSnO_3$ nanoparticles have also been reported that the LSPs below 0.8 eV with quality factors of 3-5 [45]. Compared to doped semiconducting oxides, SVO has a different electronic structure that provides a possibility for alternative plasmonic materials.

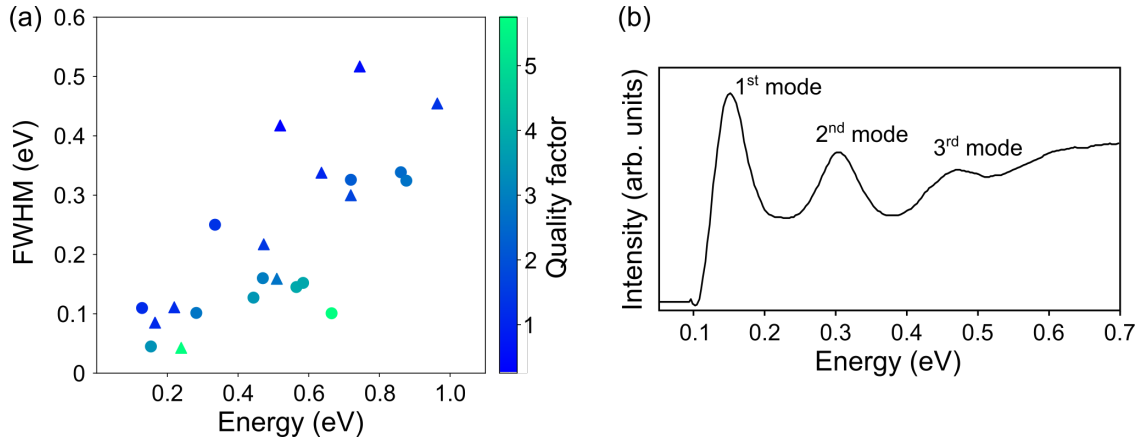


**Figure 3.15:** (**a**) Quality factors of the SVO LSP modes for the half-rods (triangle symbol) and slits (circle symbol) as a function of plasmon energy and full width at half maximum (FWHM). Their peak energy and FWHM are fitted by the Lorentzian function. (**b**) The zero-loss-peak subtracted EELS spectrum of the slit shows three LSP modes.

## 3.5 A possible alternative plasmonic material

More alternative plasmonic materials have been developed [75, 76, 77, 78, 79], focusing on lower loss materials to expand plasmonic applications from the near-infrared to the ultraviolet range. Figure 3.16(a) compares the relative permittivity of potential plasmonic materials, whereas the relative permittivity of SVO is shown separately in figure 3.16(b). Additionally, several materials show high potential to be candidates but unavoidably suffer some drawbacks (see appendix A).

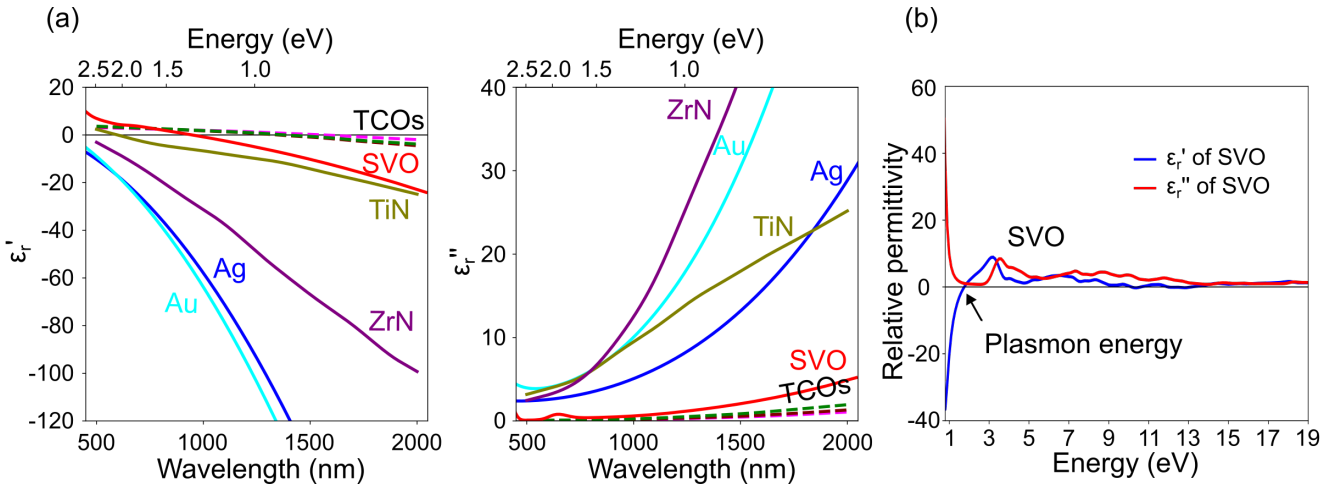


**Figure 3.16:** Summary of the optical properties of various plasmonic materials. (**a**) the real and imaginary parts of their relative permittivity ($\varepsilon_r = \varepsilon_r' + i\varepsilon_r''$), where TCOs include AZO, GZO, and ITO. Data of Ag and Au are reproduced from ref. [80]; TiN and ZrN are reproduced from ref. [79]; TCOs are reproduced from ref. [81]. The relative permittivity of SVO calculated by the renormalized ALDA for the linear-response TDDFT at $q = 0.136$ Å$^{-1}$ is presented separately in (**b**). Additionally, plasmon energy is defined as the real part of the permittivity at zero. The relative permittivity of SVO is provided by our collaborators.

The relative permittivity of different plasmonic materials (figure 3.16(a)) can be used to estimate their quality factors. Two types of geometries are used as models for estimation [76]. The quality factor of a spherical nanoparticle can be written as:

$$Q_{\text{sphere}} = \frac{-\varepsilon_r'(\omega)}{\varepsilon_r''(\omega)} \tag{3.5.18}$$

and for the cigar-shaped spheroid nanoparticle, the form of quality factor changes into:

$$Q_{\text{spheroid}} = \frac{\varepsilon_r'(\omega)^2}{\varepsilon_r''(\omega)} \tag{3.5.19}$$

Figure 3.17(a,b) are the quality factors of various plasmonic materials calculated by two kinds of formulas (equation 3.5.18 and 3.5.19, respectively). The noble metals (Ag and Au) have the highest quality factor as expected; the transparent conductive oxides (TCOs), such as ITO, GZO, and AZO are the lowest; the transition metal nitrides (TiN, ZrN) are in between. From our earlier discussion, SVO shows comparable quality factors on nanostructures, suggesting a high potential as a plasmonic material.

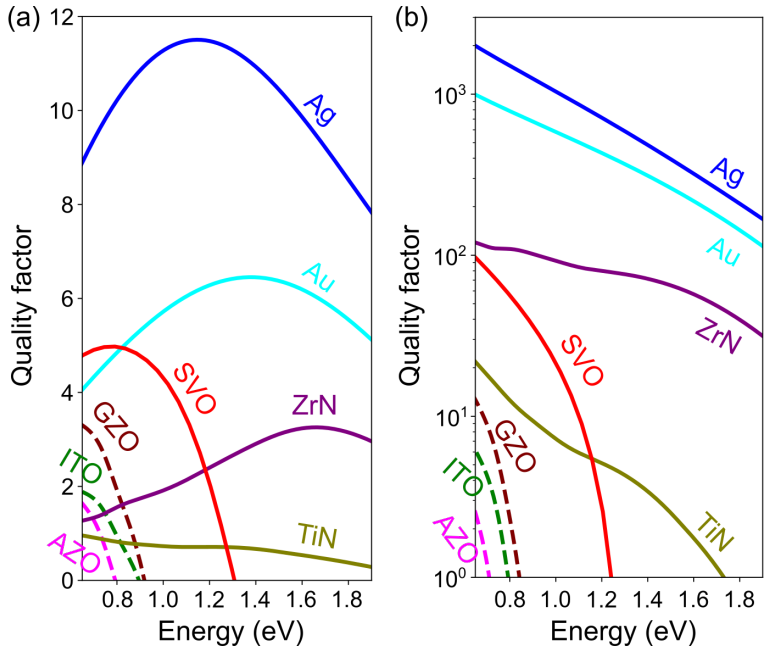


**Figure 3.17:** Estimation of the quality factor of the LSP for various plasmonic materials using the formulas of **(a)** $-\varepsilon_r'/\varepsilon_r''$ and **(b)** $\varepsilon_r'^2/\varepsilon_r''$. The database of relative permittivity is based on ref. [79, 80, 81].

## 3.6 Retrieving bulk properties from nanostructure

The presence of strong *d-d* surface plasmon excitations in nanostructures is of interest from an optical point of view. Unfortunately, such a surface contribution may energy shift the measured plasmon or even dampen the bulk contribution. On the other hand, a "true" measurement of the bulk plasmon will be of interest for investigating with high spatial resolution the electronic structure evolution, such as in the case of MIT in correlated oxide.

Here, we retrieve the bulk-type plasmon on the nanostructure at the nanometric scale under dipole and non-dipole conditions. The dipole ($q < 0.1$ Å$^{-1}$) and non-dipole ($q = 0.2$ Å$^{-1}$) EELS measurements at the tip of a 2.5 μm half-rod are demonstrated in this section. Under the momentum-resolved EELS experiment, the collection angle of the STEM dark-field image is restricted within a small range (4-8 mrad), so the dark-field image in figure 3.18(a) exhibits diffraction contrast (similar to the MAADF image). In figure 3.18(b), the energy-filtered STEM-EELS map under the dipole condition with an energy filter window at 0.2-0.3 eV shows the LSP pattern. On the other hand, in figure 3.18(c), the energy-filtered STEM-EELS map under the non-dipole condition with an energy filter window at 1.4 eV presents the bulk-type plasmon in the central part of the nanorod. Figure 3.18(d,e) compare the dipole and non-dipole EELS spectrum between different spatial positions near the tip of the nanorod. The bulk-type plasmon is invisible under the dipole condition in figure 3.18(d), while the surface plasmons (the peak below 1 eV) are observed everywhere. In contrast, the spectrum under the non-dipole condition in figure 3.18(e) displays strong bulk-type plasmon (*d-d* excitation) at the central part of the nanorod and up to $\sim$ 30 nm from the surface (cyan and red curves) and eventually vanishing in the vacuum (blue curve).

Figure 3.18(f,g) reveal the electronic structures of the core (blue) and shell (brown) areas of the nanorod, indicating the difference between their V-$L_{2,3}$ edge (521 and 513 eV, respectively) and O-*K* edge (532 eV). Their V-*L* and O-*K* edges exhibit different fine structures, which are indicative of their different electronic structures, and even small changes in the electronic structure can have significant effects. For the shell area, the V-*L* edge exhibit more resolved multiplet peaks, and the splitting of the O-*K* pre-edge ($\sim$ 527-530 eV) is reduced and accompanied by a blue shift of 0.8 eV. This phenomenon is a result of sample preparation by the FIB damaging the shell area and causing a more amorphized SVO area. The splitting of the oxygen pre-edge is partially affected by the crystal field since amorphous oxides are expected to have a weaker crystal field than typical perovskite unit cells. It might be evidence that the band gap has opened in the shell area. It is noted that disordered and ultra-thin SVO thin films are reported to undergo an MIT [48, 82]. Further, figure 3.18(h) compares the core and shell areas within the non-dipole condition ($q = 0.2$ Å$^{-1}$). In the shell area, the bulk *d-d* plasmon excitation has disappeared, and the *p-d* excitation (the energy difference between O-2*p* and V-3*d*) exhibits an edge shift of 0.8 eV, which matches perfectly with the shift of the O-*K* pre-edge. That is also evidence that the

amorphized shell area exhibits a different electronic structure compared to the bulk SVO, which is likely to be associated with MIT.

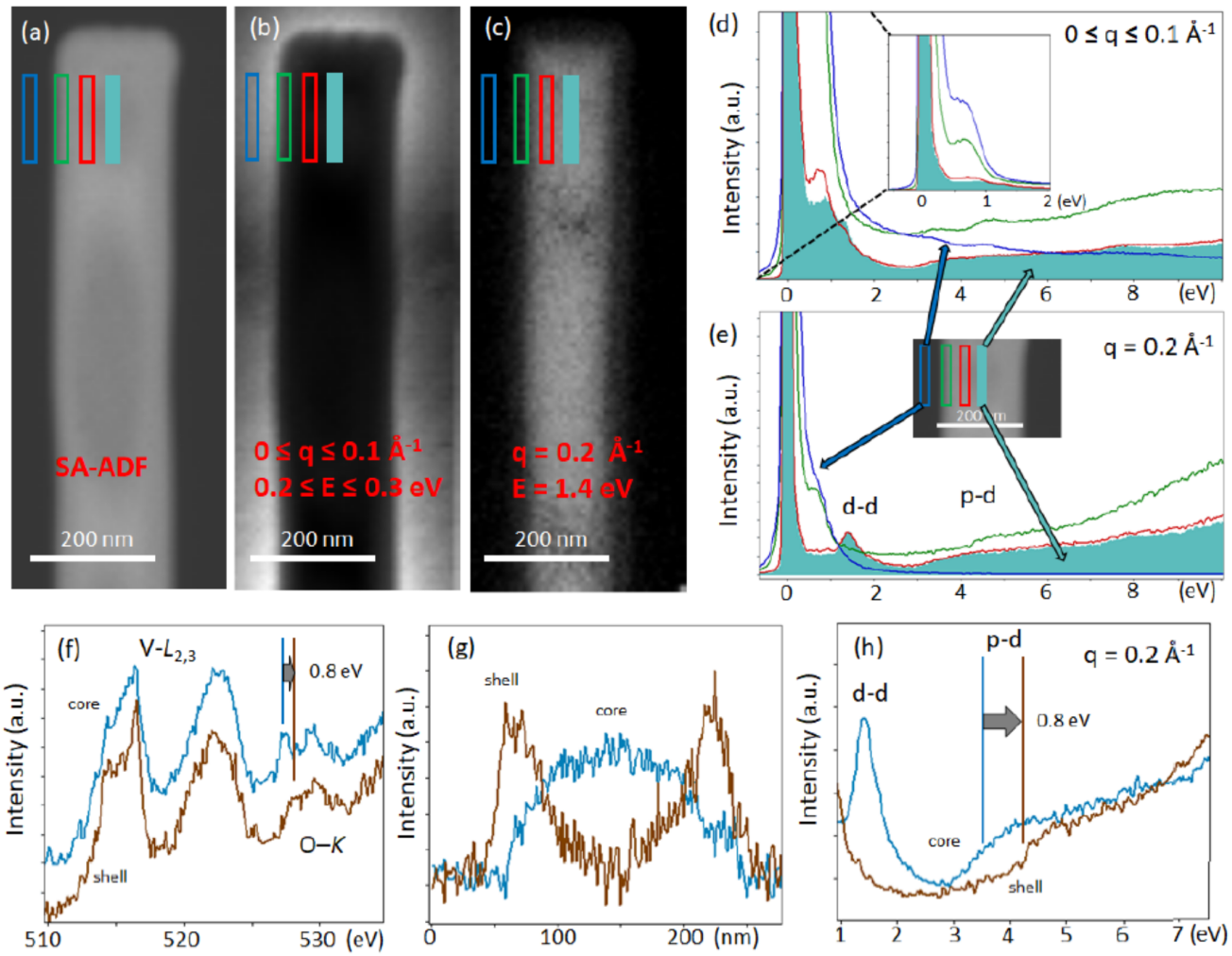


**Figure 3.18:** (**a**) Small-angle annular dark-field (SAADF) image of the tip of a 2.5 µm length half-rod (one of the triple neighboring half-rods, shown in figure 3.10(a)). Energy-filtered STEM-EELS maps under (**b**) dipole ($0 < q < 0.1$ Å$^{-1}$) and (**c**) non-dipole ($q = 0.2$ Å$^{-1}$) conditions indicate the surface plasmon at a range 0.2-0.3 eV and bulk plasmon at 1.4 eV, respectively. (**d,e**) The spectra are extracted from the different positions marked in the images in (b,c), respectively. (**f**) EELS spectra of the V-*L* and O-*K* edges are measured at the core (blue) and shell (brown) areas, and the corresponding fitting weight profiles for the core and shell areas of the tip are shown in (**g**). (**h**) EELS measurements under the non-dipole condition ($q = 0.2$ Å$^{-1}$) at the core and shell areas, indicating their *d*-*d* and *p*-*d* transitions.

## 3.7 Summary

This chapter investigated the plasmonic excitations of SVO bulk and nanostructures. First, the *ab-initio* calculations revealed an electronic excitation at 1.35 eV in the infrared region, corresponding to the bulk plasmon excitation of SVO, then providing the quantitative plasmon energy and energy dispersion at dipole and non-dipole conditions and agreeing well with the experimental results. Additionally, LSPs have been observed in SVO nanostructures, and slabs, half-rods, and slits exhibit Fabry-Perot-type LSP modes that are comparable to FDTD simulations by Lumerical software. Comparing the quality factor of SVO with other known plasmonic materials suggests that SVO can be further applied to plasmonics. Finally, the nanorod demonstrated bulk-type plasmon under non-dipole conditions, confirming that the non-dipole EELS measurement can probe bulk-type electronic excitation, even in the nanostructure. The difference in electronic structures between the core and shell areas of the nanorod probably relates to MIT.

Considering that the nanostructure suggests the occurrence of MIT and the coupling between electronic structure and interfacial effects, the coupling between ferroelectric thin film heterostructures and TMO, associated with MIT, is presented in the next two chapters.

# Chapter 4

# Domain engineering of ferroelectric $PbTiO_3$ heterostructure with $SrRuO_3$ electrodes

**Contents**



## 4.1 Introduction: Ferroelectric thin films with electrodes

Ferroelectric material involves the coupling of charge and lattice degrees of freedom, exhibiting spontaneous and switchable electric polarization, accompanied by ferroelectric domains with uniform polarization directions. Ferroelectric domain configurations, especially in thin film heterostructures, are highly influenced by mechanical and electrostatic boundary conditions, resulting in the development of various domain configurations with distinctive properties.

Figure 4.1 gives a schematic representation of ferroelectric thin-film capacitors. In the case in figure 4.1(a), one considers a ferroelectric thin film in a vacuum, where the noted charges in figure 4.1(a) are bound charges, which are dependent on the ferroelectric dipole ($P_{ferro}$) within the material. These uncompensated polarization charges at both

surfaces give rise to a so-called depolarization field ($E_{depolar}$). The inner field and its energy cost will, however, hinder ferroelectricity's development. As a result, the case presented in figure 4.1(b) is a striped domain configuration, which is a possibility to avoid or reduce the depolarization field and minimize electrostatic energy. Figure 4.1(c) is a ferroelectric thin film with short-circuited perfect electrodes, that will null the depolarization field by having mobile charges at the interfaces, and will not form a ferroelectric domain. The coexistence of several effects is common in many cases. For instance, in figure 4.1(d), a ferroelectric thin film with short-circuited imperfect electrodes will still have a residual depolarization field, possibly combined with ferroelectric domains, which can form more complex ferroelectric domains.

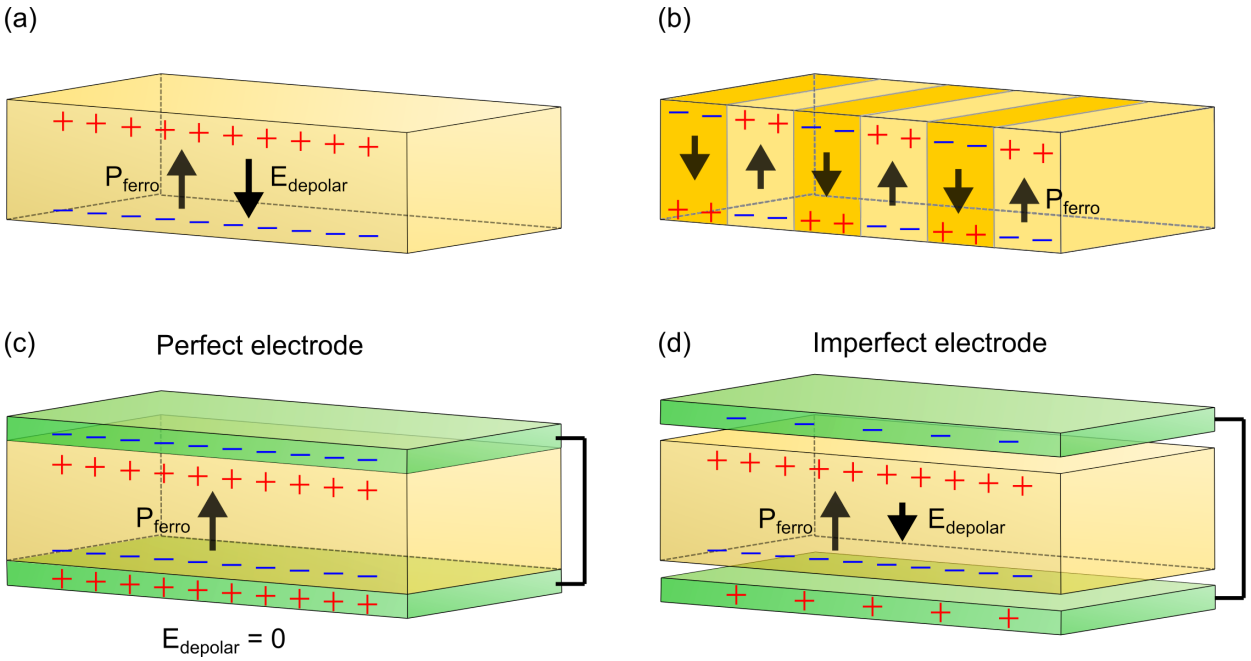


**Figure 4.1:** A schematic of ferroelectric thin-film capacitors. (**a**) A ferroelectric thin film in a vacuum. The ferroelectric dipole ($P_{ferro}$) causes the bound charges close to the surfaces, and the uncompensated polarization charges at both surfaces induce a depolarization field ($E_{depolar}$). (**b**) The thin film forms a striped domain structure to avoid or reduce the depolarization field, and minimize electrostatic energy. (**c**) A thin film with short-circuited perfect electrodes, in which the depolarization field is zero and has no ferroelectric domain. (**d**) A thin film with short-circuited imperfect electrodes, in which the depolarization field is reduced.

These schemes are rather a simplified description of a ferroelectric thin film. For instance, ferroelectric thin films exhibit different ferroelectric domain configurations as a function of temperature and epitaxial strain. In addition, the phase diagrams have also been theoretically predicted [83, 84].

Since the continuous electric dipole rotational behavior in ferroelectric thin film was observed [85], increasing research has been conducted on complex ferroelectric domain configurations, such as flux-closure [16], vortices [17], and skyrmions polar domains [86]. Nowadays, scientists can manipulate various polar domain structures through the thickness effect and external electric field [18, 87]. For instance, figure 4.2 shows that

the $PbTiO_3(n)/SrTiO_3(10)$ multilayer films with gradient thickness of $PbTiO_3$ (n = 1-21) exhibit domain configuration evolving from $a/c$ domain to polar wave, vortices, and eventually flux-closure state with increasing thickness of ferroelectric $PbTiO_3$ layer.

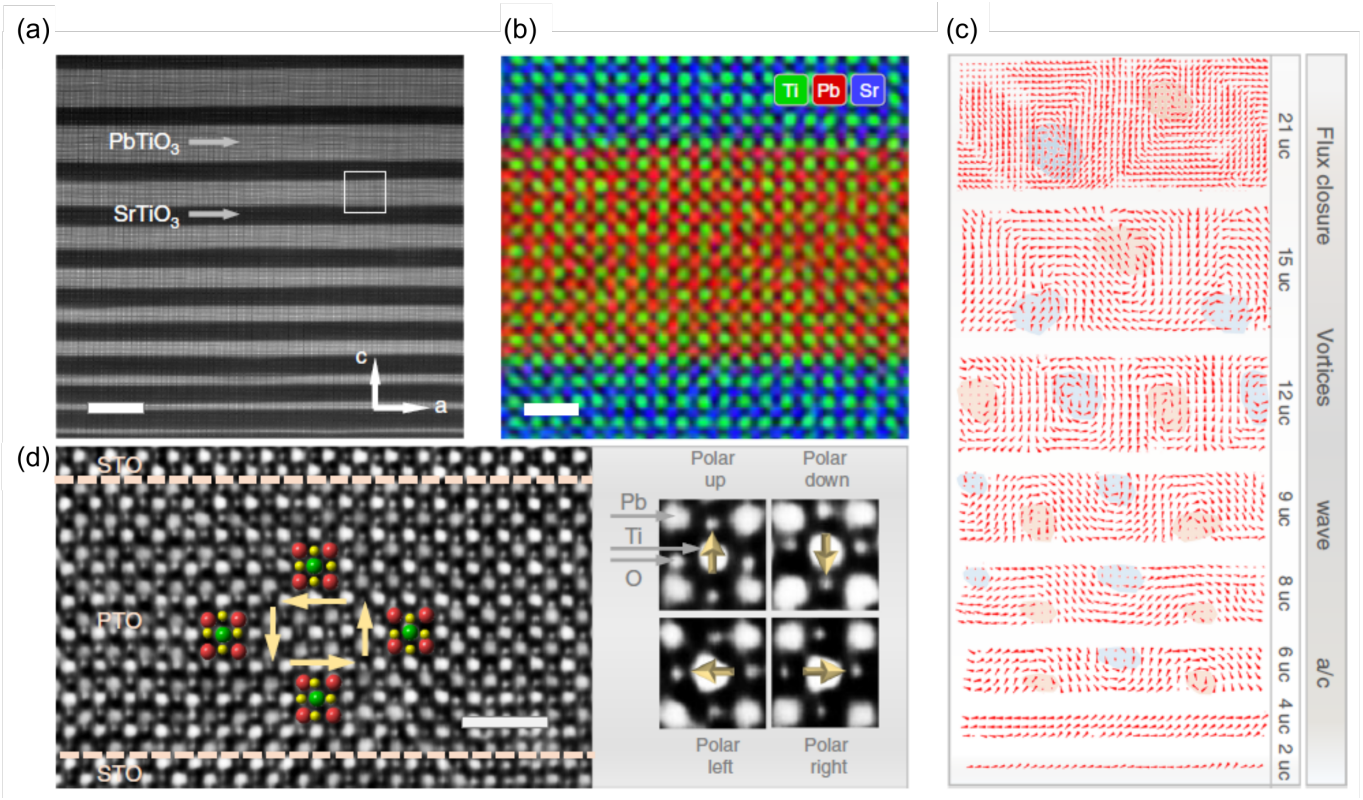


**Figure 4.2:** Structural characterization of the $PbTiO_3(n)/SrTiO_3(10)$ multilayer, where n = 1-21. (**a**) STEM image with a scale bar of 10 nm. (**b**) EDS-mapping[1]shows that the interfaces of PTO/STO are well-defined. (**c**) Ti atomic displacement maps of the PTO thin film with different thicknesses. The ferroelectric domain evolves from $a/c$ to wave, vortices, and finally flux-closure type domain configuration, with increasing the PTO thickness. (**d**) iDPC-STEM[2]image shows atomic displacements of Ti (green) and O (yellow), which correspond to the polarization direction. Reproduced from ref. [18].

Furthermore, electrostatic boundary conditions according to adjacent layers, which can be insulators or electrodes, are able to affect the domain configuration of ferroelectric thin films significantly [20, 88, 89, 90]. In principle, the electrode and the presence of a screening charge tend to reduce the depolarization field and may favor larger or more simple polar domain configurations. However, $PbTiO_3$ superlattices with an electrode of $SrRuO_3$ exhibit ordered arrays of polar nano-domains in the ferroelectric layers [19], and $Co/PbTiO_3/(La,Sr)MnO_3$ ferroelectric tunnel junction whose $PbTiO_3$ layer is sandwiched by electrodes present the flux-closure polar domains in the ferroelectric layer [91]. It has not been reported how the ferroelectric domains are affected by the electrodes, and the

[1]Energy dispersive X-ray spectroscopy (EDS) can be used to analyze elemental identity and reveal chemical composition maps at atomic resolution.

[2]The integrated differential phase contrast-STEM (iDPC-STEM) image technique directly uses atomic electrostatic potentials to measure atomic positions, and its image contrast is linearly correlated with the atomic number.

role of the electrode remains unclear. There are a number of open questions that remain to be addressed.

We then investigated a series of $PbTiO_3$ (PTO) thin film heterostructures sandwiched by $SrRuO_3$ (SRO) electrodes of 55 unit cells (uc), grown on $(110)_o$-oriented $DyScO_3$ (DSO) substrate, and the PTO thin film thickness varies from 23 to 133 uc. This investigation has been done in collaboration with the group of Prof. Jean-Marc Triscone from the department of quantum matter physics (DQMP) at the University of Geneva. In particular, I would like to express my gratitude to Dr. Céline Lichtensteiger, as well as Dr. Marios Hadjimichael and Ludovica Tovaglieri, for providing this series of PTO samples and the measurements of atomic force microscopy (AFM), X-ray diffraction (XRD), and scanning X-ray nanodiffraction microscopy (SXDM) at synchrotron, which present systematic analyses of the ferroelectric domain periodicities and possible ferroelectric domain configurations.

In conjunction with the AFM and X-ray analyses, we further investigate these PTO ferroelectric domains from a microscopic perspective by STEM technique. This chapter aims to answer the following questions:

- What kind of PTO ferroelectric domain configurations are present in these thin film heterostructures as a function of PTO thickness, especially when we observe them at the nanometric scale?
- What is the structural difference between the top and bottom SRO electrodes, and how do they associate with the PTO ferroelectric domains? Can we control or engineer the structure of electrodes via the ferroelectric domain?

## 4.2 Parameters of thin film heterostructures

A series of PTO thin films have been grown on $(110)_o$-oriented DSO substrates, with bottom and top SRO electrodes of 55 uc, and PTO film thickness of 23, 45, 51, 76, 90, 101, and 127 uc. All the samples were deposited using an off-axis radio-frequency magnetron sputtering system, equipped with three different guns allowing the deposition of heterostructures and solid solutions of high crystalline quality. PTO thin films are typically deposited around 560 °C and 580 °C, in 180 mTorr of a 20:29 $O_2/Ar$ mixture using a power of 60 W and a $Pb_{1.1}TiO_3$ target with 10% excess of Pb to compensate for its volatility. SRO electrodes were deposited *in situ* from a stoichiometric target at 640 °C in 100 mTorr of $O_2/Ar$ mixture of ratio 3:60 using a power of 80 W.

The DSO substrate has an orthorhombic structure (space group of *Pbnm*, No. 62) with the lattice parameters $a_o = 5.443$ Å, $b_o = 5.717$ Å, and $c_o = 7.901$ Å [92]. The orthorhombic unit cell is often described as a pseudo-cubic unit cell with the lattice parameters $a_{pc} = b_{pc} = \frac{\sqrt{a_o^2+b_o^2}}{2} = 3.947$ Å, $c_{pc} = c_o/2 = 3.951$ Å, and $\alpha_{pc} = \beta_{pc} = 90°$, $\gamma_{pc} = 2\arctan(a_o/b_o) = 87.187°$, where the subscripts "o" and "pc" refer to the orthorhombic and pseudo-cubic

unit cells, respectively. For $(110)_o$-oriented DSO substrate, the out-of-plane direction of $[001]_{pc}$ parallels to $[110]_o$, and the in-plane direction of $[010]_{pc}$ and $[100]_{pc}$ parallel to $[001]_o$ and $[\bar{1}10]_o$, respectively.

The metallic TMO of SRO is often used as an electrode in ferroelectric oxides. SRO has been reported to show metallic conductivity and have a phase transition from paramagnetic to ferromagnetic at 160 K. SRO has an orthorhombic structure (space group of *Pbnm*) with lattice parameters $a_o = 5.567$ Å, $b_o = 5.530$ Å, and $c_o = 7.845$ Å, which also can be described as a pseudo-cubic unit cell with the lattice parameters $a_{pc} = b_{pc} = 3.924$ Å, $c_{pc} = 3.923$ Å, and $\alpha_{pc} = \beta_{pc} = 90°$, $\gamma_{pc} = 90.382°$. Furthermore, SRO is found in six different possible orientations when grown on a substrate [93]. Figure 4.14 provides a detailed schematic diagram of the relation between pseudo-cubic and orthorhombic unit cells, as well as possible SRO orientations.

Ferroelectric PTO has a tetragonal structure (space group of *P4mm*, No. 99) with lattice parameters $a = b = 3.904$ Å and $c = 4.152$ Å at room temperature. Growing on a DSO substrate results in a tensile strain in the PTO.

Throughout this chapter, the pseudo-cubic notation "pc" is primarily used, and the orthorhombic notation "o" is mainly used in the further analysis of orthorhombic structure in section 4.4.5. The lattice parameters of each component in thin film heterostructures are listed in table 4.1.

| Material | Space group | Lattice parameters | | | Pseudo-cubic lattice parameters | | |
|---|---|---|---|---|---|---|---|
| | | $a$ (Å) | $b$ (Å) | $c$ (Å) | $a_{pc}$ (Å) | $b_{pc}$ (Å) | $c_{pc}$ (Å) |
| $DyScO_3$ | Orthorhombic (*Pbnm*) | 5.443 | 5.717 | 7.901 | 3.947 | 3.947 | 3.951 |
| $SrRuO_3$ | Orthorhombic (*Pbnm*) | 5.567 | 5.530 | 7.845 | 3.924 | 3.924 | 3.923 |
| $PbTiO_3$ | Tetragonal (*P4mm*) | 3.904 | 3.904 | 4.152 | - | - | - |

**Table 4.1:** The crystal structure and lattice parameters of each component in thin film heterostructures. The corresponding pseudo-cubic lattice parameters are calculated as: $a_{pc} = b_{pc} = \sqrt{a^2 + b^2}/2$, $c_{pc} = c/2$ for *Pbnm* orthorhombic.

## 4.3 AFM and X-ray analyses

### 4.3.1 Periodic patterns at the surface

In the beginning, AFM is a typical surface analysis technique to obtain topographic surface maps, providing surface information, such as surface texture. The topography images of a series of samples with PTO thickness varying from 23 uc to 127 uc are shown in figure 4.3(a), performed by our collaborators at the University of Geneva.

For the thinner samples (23 uc and 45 uc), only homogeneous topography patterns are observed, while periodic patterns (trench patterns) are noticeable as the PTO thickness increases. By observing the topography images of the thicker samples (above 51 uc), the trench patterns parallel to $[010]_{pc}$ and $[100]_{pc}$ exhibit anisotropic features, and those along $[010]_{pc}$ are longer and deeper than those along $[100]_{pc}$. In order to reveal the periods of these trench patterns, an autocorrelation analysis is used, which is more sensitive to periodic patterns than a direct Fourier transformation of the topography image [94]. The process of estimating the period of the 90 uc PTO using the autocorrelation technique is illustrated in figure 4.3(b-e). Two periodic peaks along $[010]_{pc}$ are revealed (red curve), while a single periodic peak exhibits along $[100]_{pc}$ (blue curve). More precisely, for the 90 uc PTO, the autocorrelation analysis reveals periods of 75 nm and 259 nm along the $[010]_{pc}$, and 347 nm along the $[100]_{pc}$. The measured periods of all the samples will be compared in section 4.5.

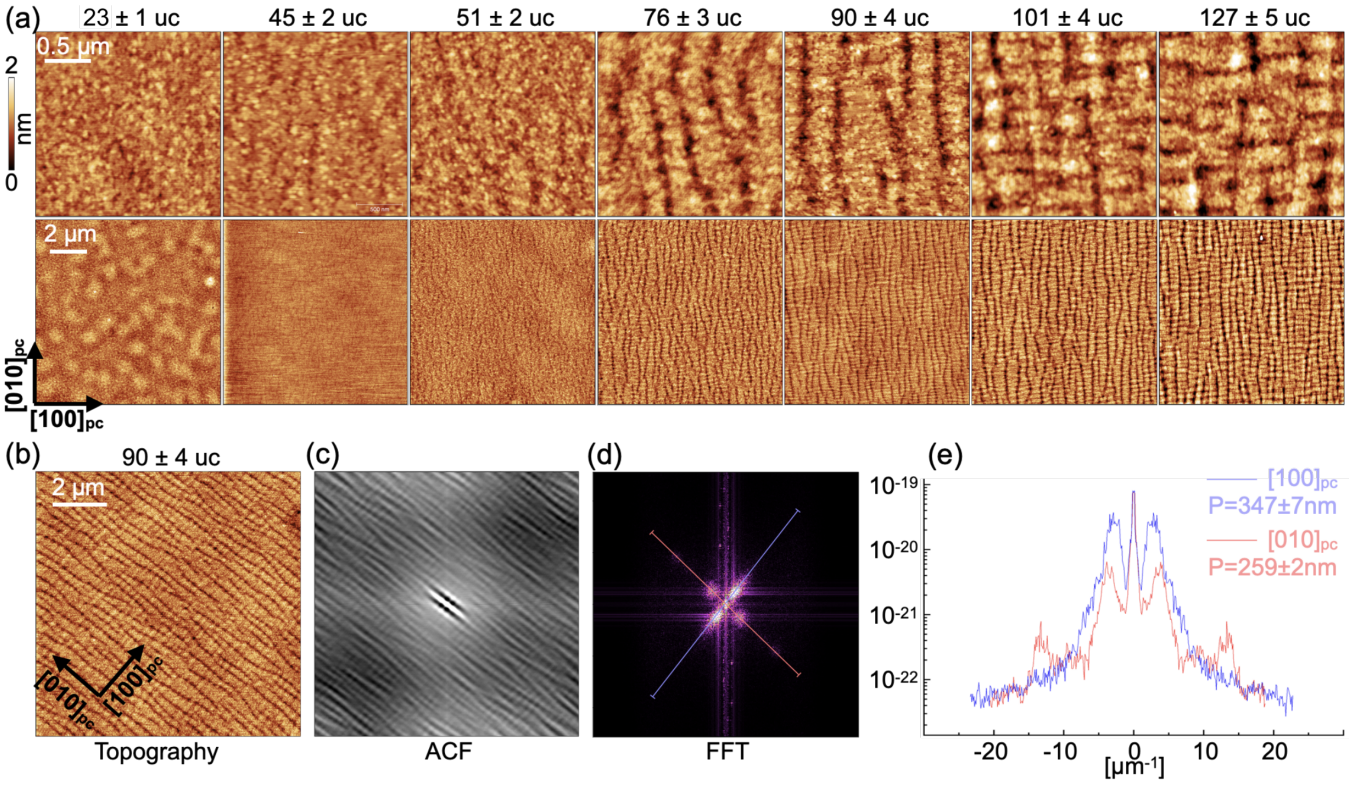


**Figure 4.3:** (**a**) AFM topography images of a series of PTO thin films sandwiched by SRO electrodes grown on $(110)_o$-oriented DSO substrate. The scan area of the top row and bottom row are 2x2 µm$^2$ and 10x10 µm$^2$, respectively. (**b-e**) Autocorrelation analysis on the 90 uc PTO sample. Starting from the topography image in (**b**), the autocorrelation function (ACF) gives the result in (**c**), and the Fast Fourier transformation (FFT) of this image is shown in (**d**). (**e**) The intensity profiles along $[100]_{pc}$ (blue) and $[010]_{pc}$ (red) are extracted from the FFT image, revealing the periodic peaks.

### 4.3.2 Ferroelectric domain periodicities

As the domains of topography images are revealed by AFM analysis, we then used XRD techniques to identify periodic ordered phases and domains in this series of samples. These XRD measurements were performed by our collaborators at the University of Geneva using a *Panalytical X'Pert* diffractometer with Cu K$\alpha_1$ radiation (1.5405980 Å) equipped with a 2-bounce Ge(220) monochromator and a triple axis detector at the University of Geneva.

The reciprocal space maps (RSM) around the $(001)_{pc}$ peak are projected onto $Q_{[001]_{pc}}$-$Q_{[100]_{pc}}$ plane (figure 4.4(a)) and $Q_{[001]_{pc}}$-$Q_{[010]_{pc}}$ plane (figure 4.4(b)), and the corresponding intensity profiles shown below are from intensity cut at $Q_{[001]_{pc}} = 1.55$ Å$^{-1}$ (marked by white dashed lines in figure 4.4(a,b)), corresponding to a lattice parameter of $2\pi/Q_{[001]_{pc}}$ $\sim 4.05$ Å. By observing the RSM, the thicker PTO samples (76 uc and higher) exhibit the *butterfly* shape, which comes from the tilts in *a*- and *c*-domains [95] (orientations of these tilts will be defined in section 4.3.3). Further, satellite peaks along $[010]_{pc}$ (figure 4.4(b)) are found, while periodic peaks along $[100]_{pc}$ are invisible; hence we pay more attention to the periodicity along $[010]_{pc}$. The intensity profiles along $[010]_{pc}$ are extracted to figure 4.4(c), and their periods as a function of thickness are shown in figure 4.4(d). Moreover, the additional peaks in thicker samples (76 uc and higher) have been observed, which are marked with the green stars in figure 4.4(c), indicating the appearance of a longer period.

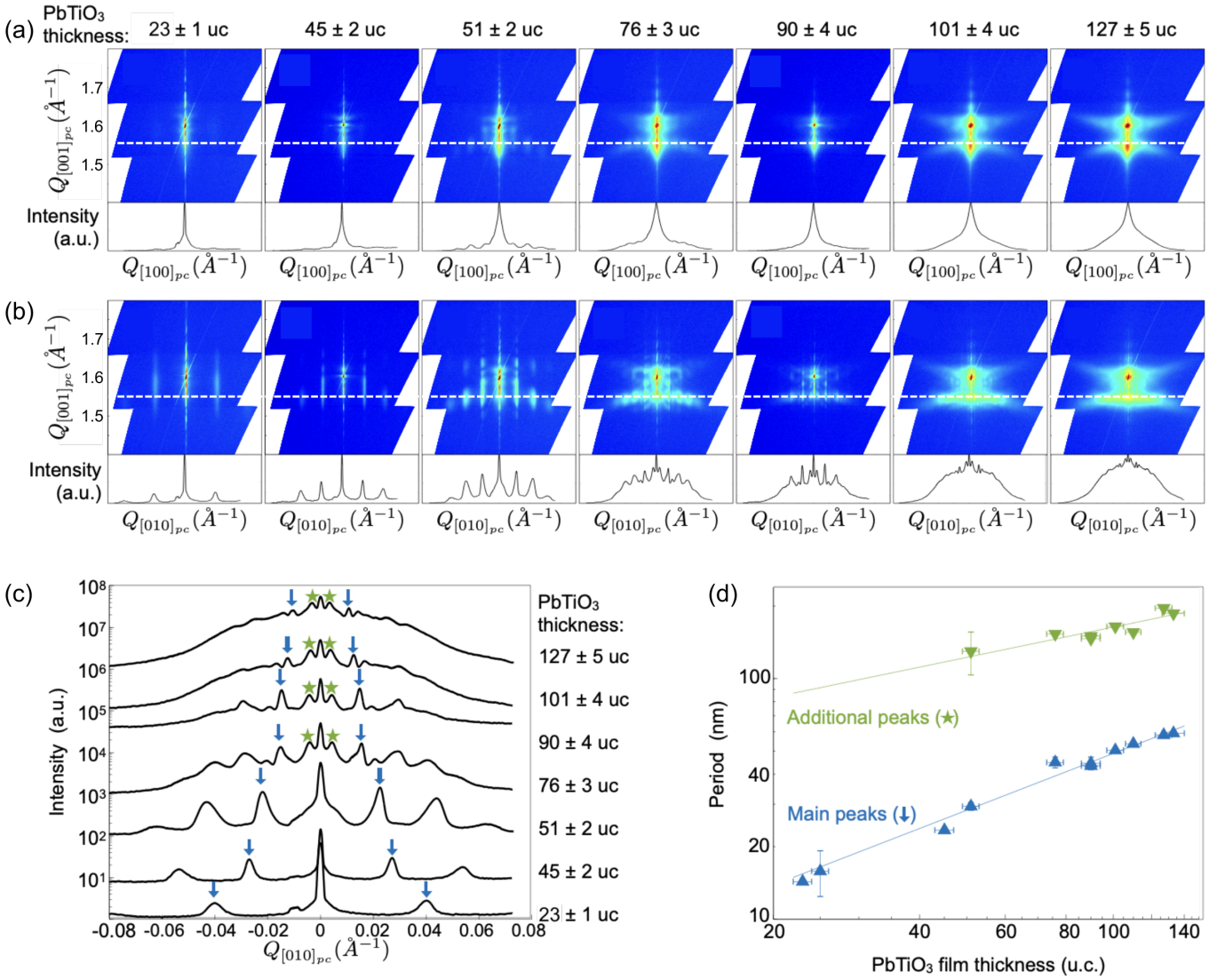


**Figure 4.4:** Reciprocal space maps (RSM) of a series of the PTO samples with different thicknesses. The $(001)_{pc}$ peak projects in $Q_{[001]_{pc}}$-$Q_{[100]_{pc}}$ plane shown in (**a**) and $Q_{[001]_{pc}}$-$Q_{[010]_{pc}}$ plane shown in (**b**). The $Q_{[100]_{pc}}$ and $Q_{[010]_{pc}}$ vary from -0.1 Å$^{-1}$ to 0.1 Å$^{-1}$, and the $Q_{[001]_{pc}}$ varies from 1.4 Å$^{-1}$ to 1.8 Å$^{-1}$. The intensity profiles below are obtained from a cut at $Q_{[001]_{pc}}$ = 1.55 Å$^{-1}$ (marked white dashed lines). The summary of these samples is shown in (**c**) for the peak profiles from (b), and (**d**) for the corresponding domain periods.

### 4.3.3 Tilts in ferroelectric *a*- and *c*-domains

The 90 uc thick PTO sample was specifically examined using scanning X-ray diffraction microscopy (SXDM), which was performed by our collaborators at the University of Geneva. SXDM is able to investigate localized regions and allows a more detailed investigation than the ensemble average of previous XRD measurements. As we will see later, SXDM is strongly complementary to STEM analysis, and we have decided to present them in this manuscript before discussing our electron microscopic investigation. In particular, both techniques enable real space mapping of the crystallographic or ferroelectric domains by filtering different regions of interest in the reciprocal space.

This SXDM is equipped on the ID01 beamline at the European Synchrotron Radiation Facility (ESRF) [96]. An incident X-ray energy of 9.5 keV was selected using a Si(111) double crystal monochromator with resolution $\Delta\lambda/\lambda = 10^{-4}$. A 0.7 µm-thick tungsten Fresnel zone plate with 300 µm diameter and 20 nm outer zone width was used to focus the X-ray beam down to a spot size of $\sim 30 \times 30$ nm$^2$ FWHM.

For 90 uc PTO sample, two projections onto $Q_{[001]_{pc}}$-$Q_{[100]_{pc}}$ and $Q_{[001]_{pc}}$-$Q_{[010]_{pc}}$ planes from the 3D-RSM of SXDM measurements are shown in figure 4.5(a,c). They exhibit a similar *butterfly* shape as observed in the XRD results. The areas with a larger value in $Q_{[001]_{pc}}$ (corresponding to out-of-plane lattice parameter) represent the ferroelectric *a*-domains, which have smaller out-of-plane lattice parameters. On the other hand, the areas with a smaller value in $Q_{[001]_{pc}}$ represent the ferroelectric *c*-domains, which have larger out-of-plane lattice parameters.

The *butterfly* shape indicates that the *a*- or *c*-domain has the possibility of being tilted in one of the four directions: $[100]_{pc}$, $[\bar{1}00]_{pc}$, $[010]_{pc}$, or $[0\bar{1}0]_{pc}$. For instance, on $Q_{[001]_{pc}}$-$Q_{[010]_{pc}}$ plane (figure 4.5(c,d)), four corners clockwise from top left correspond to $a^{[0\bar{1}0]_{pc}}$, $a^{[010]_{pc}}$, $c^{[010]_{pc}}$, and $c^{[0\bar{1}0]_{pc}}$, respectively. The spatial distribution maps of the tilted *a*- and *c*-domains are shown in figure 4.5(b,d), which come from the color-matching boxes in figure 4.5(a,c), correspondingly. Moreover, examining the figure 4.5(d) in more detail, for *a*- and *c*-domains tilting in $[010]_{pc}$ or $[0\bar{1}0]_{pc}$ direction, $a^{[0\bar{1}0]_{pc}}$ and $c^{[010]_{pc}}$, as well as $a^{[010]_{pc}}$ and $c^{[0\bar{1}0]_{pc}}$ display similar patterns, respectively. Therefore, the clear correlations of domain bundles of $a^{[0\bar{1}0]_{pc}}/c^{[010]_{pc}}$ and $a^{[010]_{pc}}/c^{[0\bar{1}0]_{pc}}$ are revealed. Additionally, figure 4.5(e) shows the topography image of the 90 uc PTO sample with the same scale, and its periodic trench pattern is comparable with the spatial distribution maps in figure 4.5(d), indicating the period measured by topography images in figure 4.3 are related to the domain bundles of *a*- and *c*-domains.

Since the clear domain bundles ($a^{[0\bar{1}0]_{pc}}/c^{[010]_{pc}}$ and $a^{[010]_{pc}}/c^{[0\bar{1}0]_{pc}}$) are revealed, and the XRD results (figure 4.4(b)) only exhibit satellite peaks along $[010]_{pc}$, our attention is drawn to the behavior of the ferroelectric domain along $[010]_{pc}$.

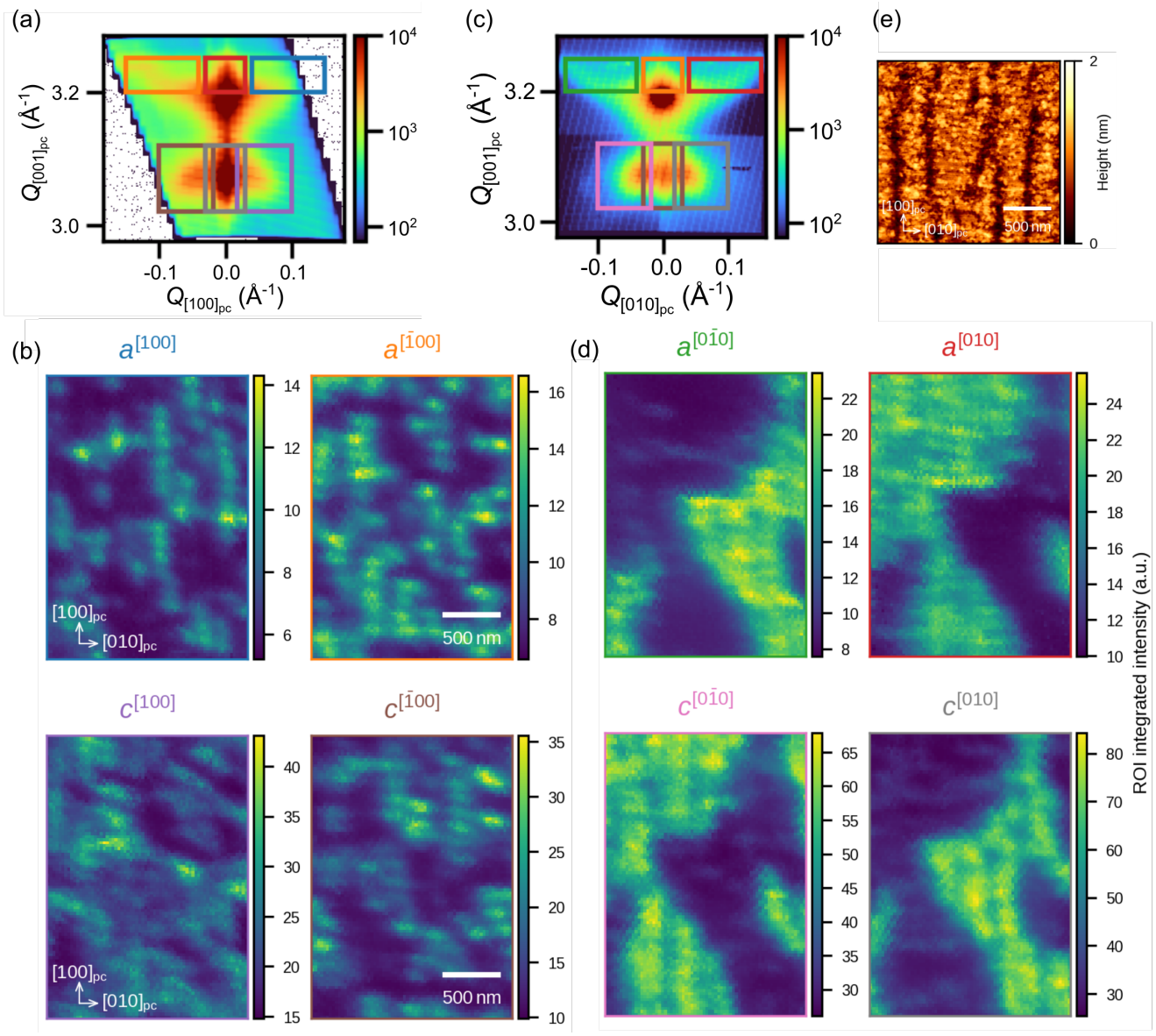


**Figure 4.5:** Scanning X-ray diffraction microscopy (SXDM) results of the 90 uc PTO sample. The projections of (**a**) $Q_{[001]_{pc}}$-$Q_{[100]_{pc}}$ and (**c**) $Q_{[001]_{pc}}$-$Q_{[010]_{pc}}$ planes cut from the 3D-RSM. (**b,d**) The spatial distribution maps of different orientations of the *a*- and *c*-domains, which are extracted from the color matching boxes defined in (a) and (c), respectively. (**e**) The topography image of the AFM result at the same scale, whose domain period is comparable to the patterns in (d).

## 4.4 Microscopic investigations through STEM

### 4.4.1 STEM images

According to the AFM and X-ray analyses presented in the preceding section, we have a first understanding of the domain periods and tilting of the *a*- and *c*-domains of this series of PTO samples, notably in the 90 uc PTO sample. However, there are still some puzzling questions; for instance, what is the ferroelectric domain configuration on each sample? And why do the samples with lower PTO thicknesses have fewer periodicities in X-ray measurements and no super-periodicity in topography images? What is the role of the SRO electrodes, and are they associated with the PTO domain? Our goal is to control TMO properties with the ferroelectric proximity-induced effect, which implies at least some interfacial couplings. In this section, we continue to investigate using STEM techniques, such as different types of STEM images, geometric phase analysis (GPA), atomic-resolved images, and fast Fourier transform (FFT) analysis, allowing us to examine the microscopic details of these samples.

Among this series of PTO thin films, we chose three representative samples: 90 uc, 45 uc, and 23 uc PTO samples. The differences have been observed between the 90 uc and 23 uc PTO samples, not merely the trench patterns in the topography images (section 4.3.1) but also in the behaviors of periodic peaks in the RSM (section 4.3.2). These two distinct behaviors might mix in the 45 uc PTO sample. Additionally, we prepared STEM cross-section lamellas of these three samples by focused ion beam (FIB), and we observed them on the $Q_{[001]_{pc}}$-$Q_{[010]_{pc}}$ plane (along $[010]_{pc}$), which shows more interesting phenomena as discussed earlier.

From the STEM images shown in figure 4.6(a-c), the high-angle annular dark-field (HAADF) images barely observe the ferroelectric domain (discussed in figure 2.4), while both middle-angle annular dark-field (MAADF) and bright-field (BF) images are able to demonstrate clearer contrasts of the ferroelectric domain configurations in the PTO layers. As the PTO thickness decreases, the domain contrast transforms from a typical ferroelectric $a/c$ pattern into a flux-closure-like pattern (figure 4.6(d)). Further, we extracted the periods of these PTO domains using FFT analysis (detailed in section 4.4.4), and found the period of 46 nm $\pm$ 3 nm for the 90 uc PTO, 26 nm $\pm$ 1 nm for the 45 uc PTO, and 13 nm $\pm$ 1 nm for the 23 uc PTO. These periods are in perfect agreement with the XRD results and it confirms that the main peaks in figure 4.4(d) is associated with the PTO ferroelectric domain.

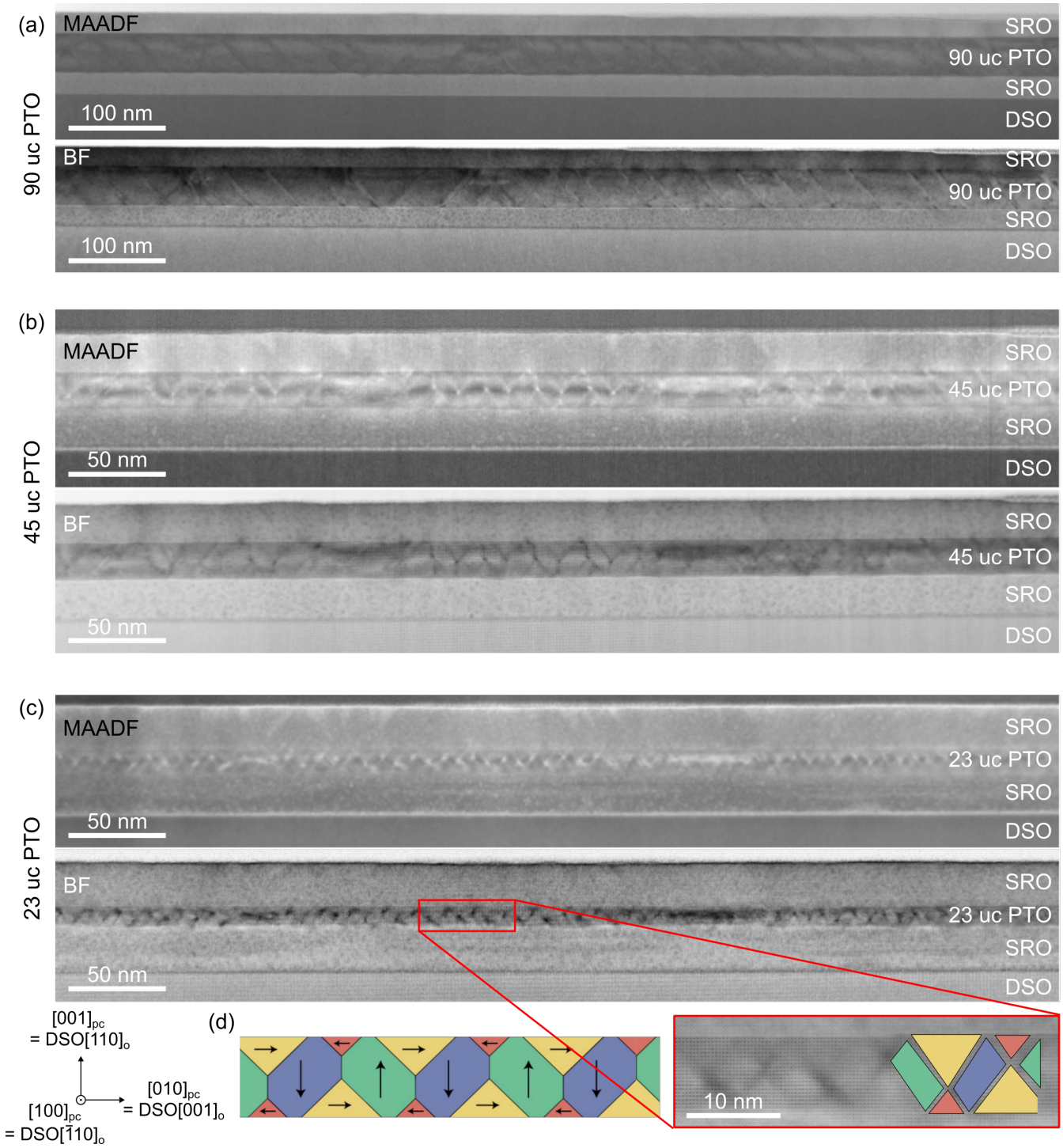


**Figure 4.6:** The MAADF (collection angles of 15-30 or 30-60 mrad) and BF (collection angle of 0-15 mrad) STEM images of (**a**) 90 uc, (**b**) 45 uc, and (**c**) 23 uc PTO samples. (**d**) A flux-closure-like ferroelectric domain configuration (reproduced from supplementary information of ref. [19]) is comparable with the domain contrast of the enlarged image of (c).

### 4.4.2 Ferroelectric polarization configurations

The HAADF images reveal poor domain contrast, while it is a powerful tool to directly observe atomic displacement and unit cell crystal structure distortion, which relate to ferroelectric polarization direction and domain wall reconstruction. In the case of tetragonal PTO, the atomic displacement of the titanium determines the ferroelectric polarization direction (discussed in figure 2.5).

Figure 4.7 and 4.8 shows the atomic-resolved HAADF images of the 90 uc, 45 uc, and 23 uc PTO samples. The 90 uc PTO sample (figure 4.7) exhibits typical $a/c$ domains as discussed earlier, and the corresponding polarization directions can be further confirmed in this part. First, the ferroelectric domain wall of the *a*- and *c*-domain can be easily identified and are marked in the red lines in figure 4.7, according to atomic distortions (the columns of atoms rotate at a certain angle when crossing a domain wall). Second, we found that there are two kinds of *a*-domains with opposite inclined directions (the left and right in figure 4.7), both of their polarization directions always point to the right with respect to the substrate at the bottom. On the other hand, the polarization directions of the *c*-domains always point toward the bottom. This is a bit intriguing since it gives different types of the domain wall, notably distinct charge distributions near the domain wall, exhibiting head-to-head or tail-to-tail polarization for the *a*-domain on the left, and head-to-tail polarization for the *a*-domain on the right.

The polarization arrow map, whose working principles were discussed in section 2.3.3, can effectively quantify ferroelectric polarization in localized areas. The polarization arrow map of the 45 uc PTO sample is shown in figure 4.8(a). The PTO layer has two opposite polarizations: the upper area with a polarization pointing toward the top; and the lower area with a polarization pointing toward the bottom. The center area of the PTO layer with slight in-plane polarization roughly separates the PTO layer into two regions. Additionally, there is the possibility of presenting some *incomplete a*-domains, which only exist in the upper or lower half of the PTO. Finally, in figure 4.8(b), the 23 uc PTO sample shows the polarizations pointing to the top and bottom and a wave-like region with slight in-plane polarization at the center, which is similar to the 45 uc PTO sample.

The 45 uc and 23 uc PTO samples have complex flux-closure type polarization configurations, and their driving mechanism remains unclear. We tried to match the observed MAADF contrast that resembles a typical flux-closure type contrast to the HAADF arrow maps, but we were not able to obtain a non-ambiguous distribution of the ferroelectric domain. In particular, in the case of the 23 uc, the observed domain is not compatible with a flux-closure type domain as shown in figure 4.6(d) and the measurements done by M. Hadjimichael [19]. A major difference is that the ferroelectric polarizations close to the interface are in the majority pointing toward the interface while a pure flux-close type tends to have the ferroelectric polarizations lying within the planes near the surfaces or interfaces. This is comprehensible since the SRO electrodes can provide screening charges.

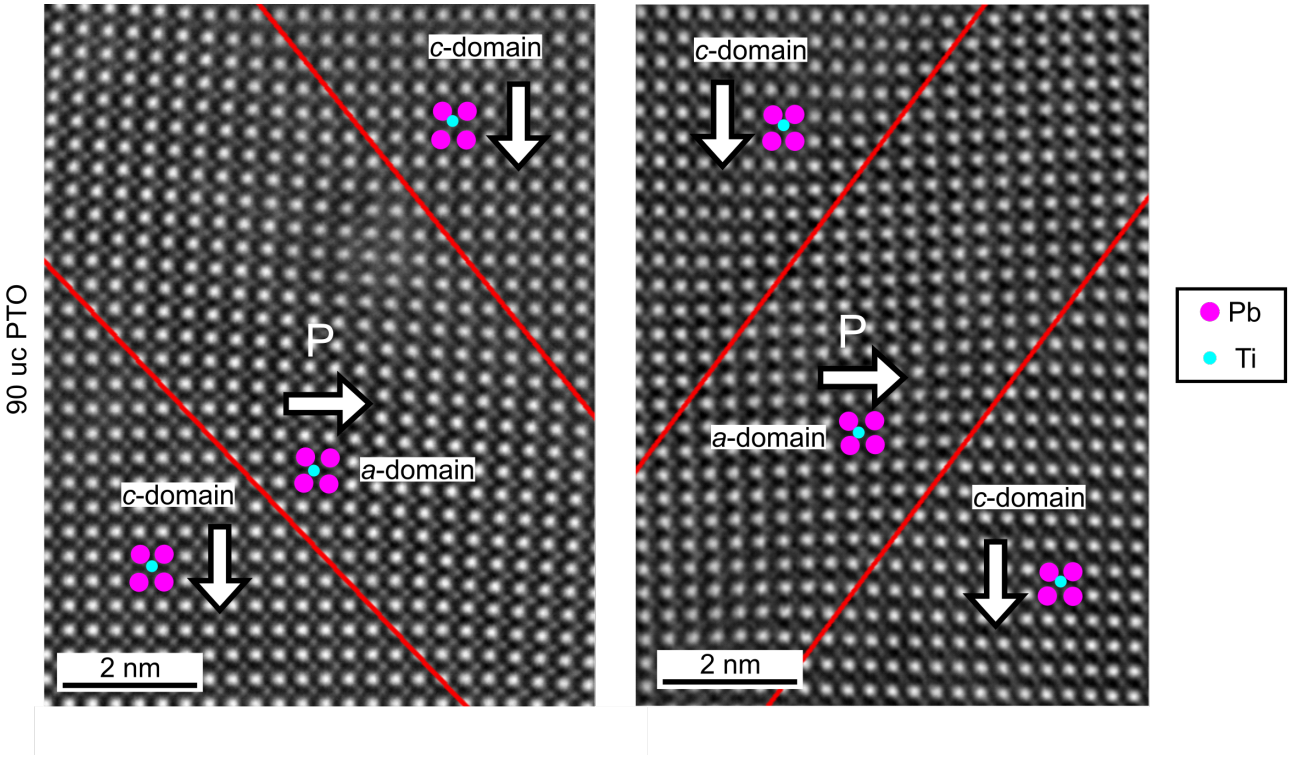


**Figure 4.7:** The atomic-resolved HAADF images of 90 uc PTO sample. The two kinds of ferroelectric $a/c$-domains with opposite inclined directions are found; in addition, the polarizations of the $a$-domains always point to the right, and the polarizations of the $c$-domains always point to the bottom, with respect to the substrate.

In the 45 uc, the ferroelectric polarizations also often point within the electrodes, but a nascent $c/a$ type domain is also present near the top interface. It has already been reported that, as the ferroelectric layer thickness decreases, the typical ferroelectric domain turns into complex domain structures, which might be the result of the incomplete screening of depolarizing field due to the electrode [97], the instability of the ferroelectric properties in ultrathin films [89], or topological defects [98].

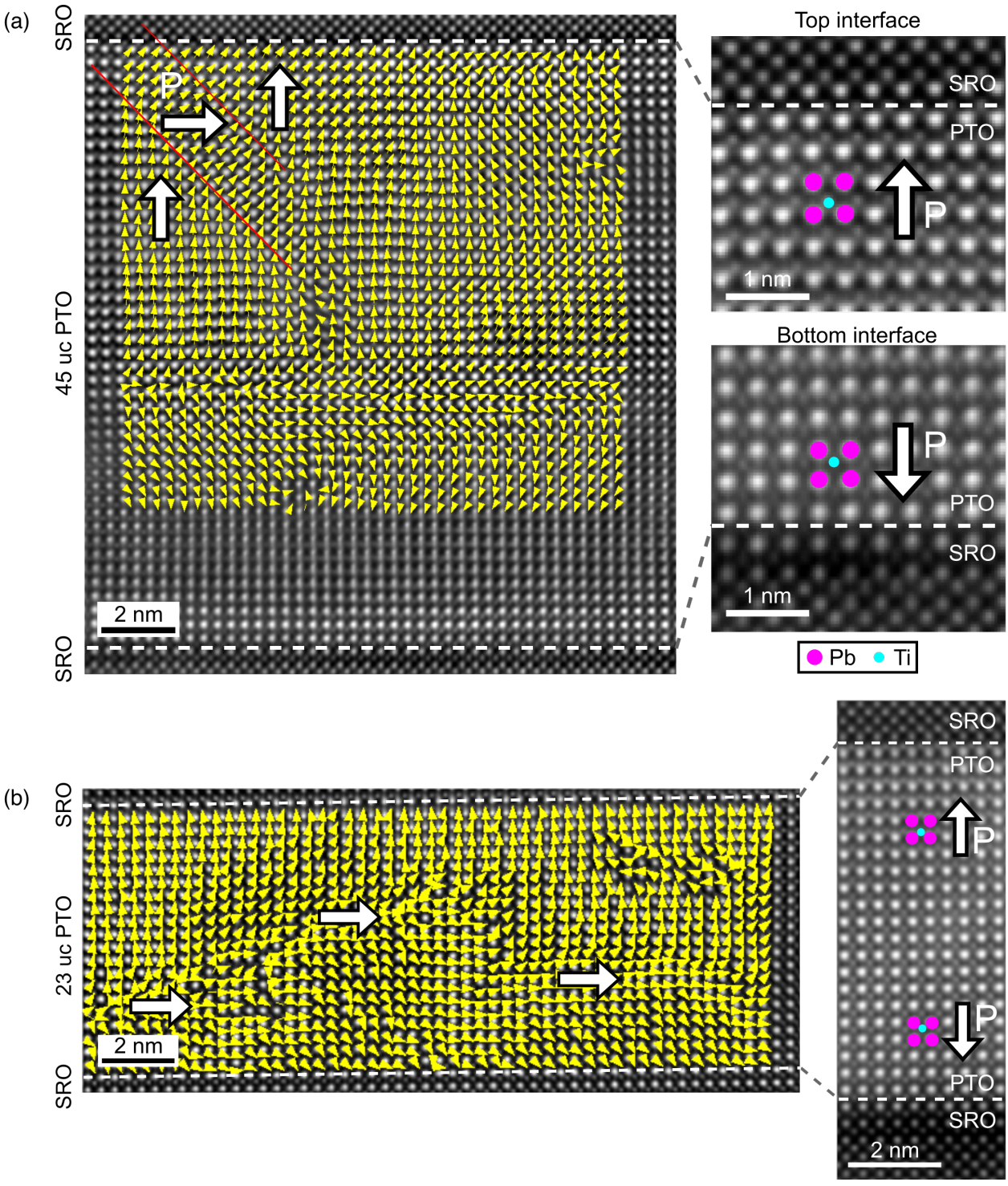


**Figure 4.8:** The atomic-resolved HAADF images of (**a**) 45 uc and (**b**) 23 uc PTO samples. (**a**) The polarization arrow map shows the PTO layer has opposite out-of-plane polarizations (tail-to-tail polarization) in the upper and lower areas, which are shown in the enlarged images on the right, and a slight in-plane polarization in the middle. Moreover, some *incomplete a*-domains are found (the domain walls are marked in red lines). (**b**) The polarization arrow map shows the PTO layer has opposite polarization in the upper and lower areas, similar to the case of the 45 uc PTO sample, but a wave-like area with in-plane polarization in the middle.

### 4.4.3 Strain analysis

The epitaxial strain is an essential parameter in the thin film heterostructure, and the strain pattern provides another method of identifying the ferroelectric domain structures [20, 99]. The strain maps of 90 uc, 45 uc, and 23 uc PTO samples are shown in figure 4.9(a-c), respectively; the columns from left to right correspond to the out-of-plane strain, in-plane strain, shear strain, and rotation map, respectively.

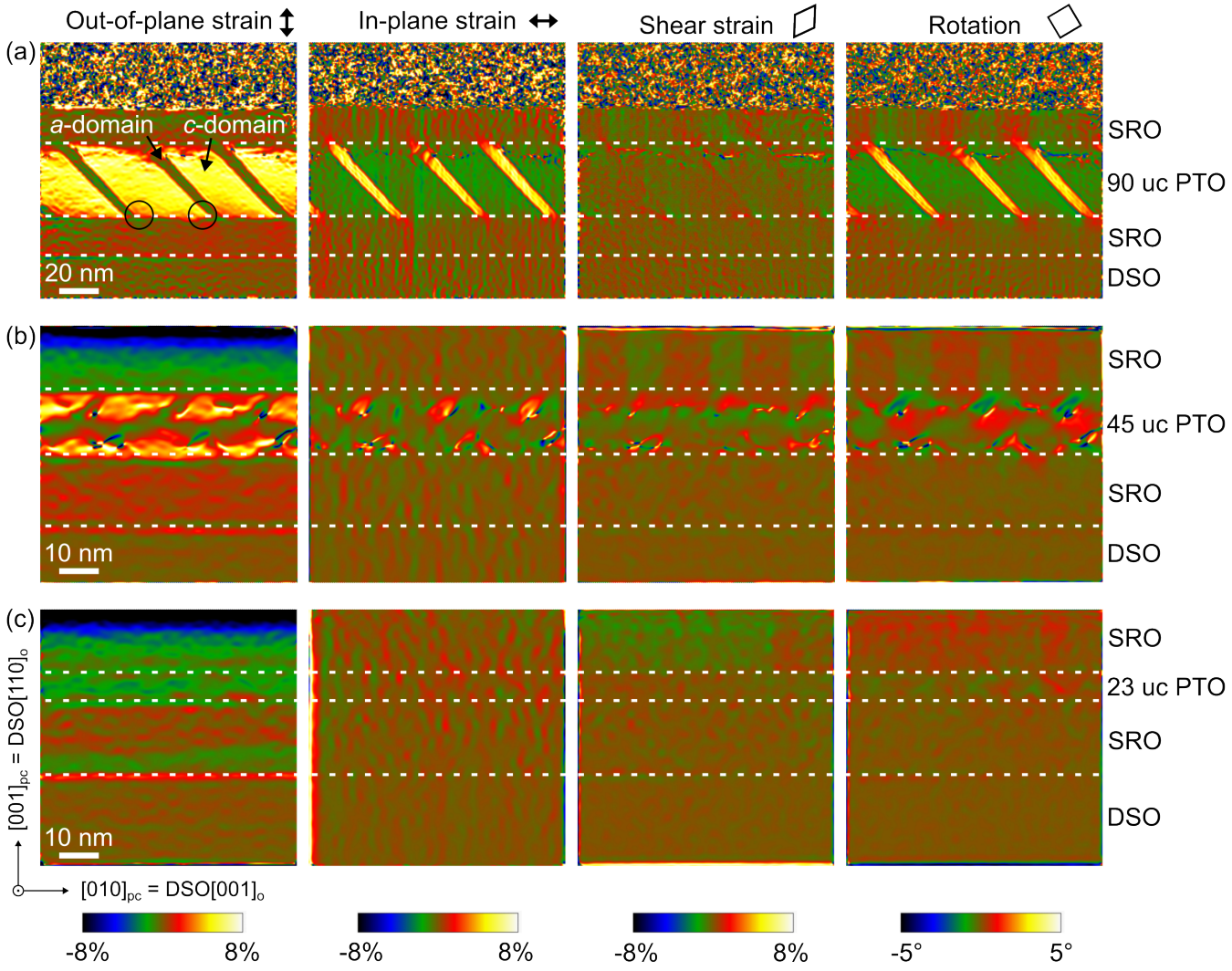


**Figure 4.9:** Strain maps for the (**a**) 90 uc, (**b**) 45 uc, and (**c**) 23 uc PTO samples. The patterns from left to right correspond to the out-of-plane strain, in-plane strain, shear strain, and rotation, respectively. All the strain maps are at the same color intensity scale from -8% to 8%, while the rotation map is from -5° to 5° (anticlockwise positive). In the out-of-plane strain map in (a), two black circles indicate acute and obtuse corners that have different out-of-plane expansions. As a result of this gradient of strain, horizontal flexoelectricity is involved.

For the 90 uc PTO, the regions with lower out-of-plane strain and higher in-plane strain indicate the ferroelectric *a*-domain (in-plane polarization); the other regions correspond to the *c*-domain (out-of-plane polarization), confirming that this sample exhibits typical ferroelectric $a/c$ domains. Shear strain and rotation maps indicate that the ferroelectric domain walls exhibit slight shear behavior and atomic rotation.

Further, taking a closer look at the out-of-plane strain map at the bottom of the PTO layer, showing the horizontal strain gradient (the obtuse corner has a lower strain value than the acute corner, and the corners are marked in black circles). The strain gradient between the obtuse and acute corners can induce a horizontal flexoelectric polarization [100]. From the GPA results, we can estimate the gradient of out-of-plane strain $\Delta\varepsilon_{yy}$, which spans from 1.5% to 3% between the obtuse and acute corners, and the relaxation length $w$ (i.e., the width of *c*-domain) is 15-25 nm. With the typical flexoelectric coefficient $\mu$ of PTO $\approx$ 200 nC·m$^{-1}$, the horizontal flexoelectric polarization $P_{x(flexo)}$ can be estimated as $\mu(\Delta\varepsilon_{yy}/w) \approx$ 20-25 μC·cm$^{-2}$. Regarding the typical ferroelectric polarization of PTO with 40-60 μC·cm$^{-2}$, this value of flexoelectric polarization is not negligible. Therefore, horizontal flexoelectric polarization could affect ferroelectric domains, and the charge might be removed from or injected into the domain walls as a result. It might be one of the reasons why different polar domain walls, such as head-to-head, tail-to-tail, and head-to-tail domain walls, can be observed. The horizontal flexoelectricity reduces the energy cost difference by reducing the charge differences at the domain wall. The possible ferroelectric domain configurations are shown in figure 4.10). In the case of figure 4.9(a), compared with the two kinds of left-inclined *a*-domains in figure 4.10(a,b), the flexoelectric polarization effect tends to reduce rather than increase the charge in the domain wall; therefore, the configuration in figure 4.10(a) is observed.

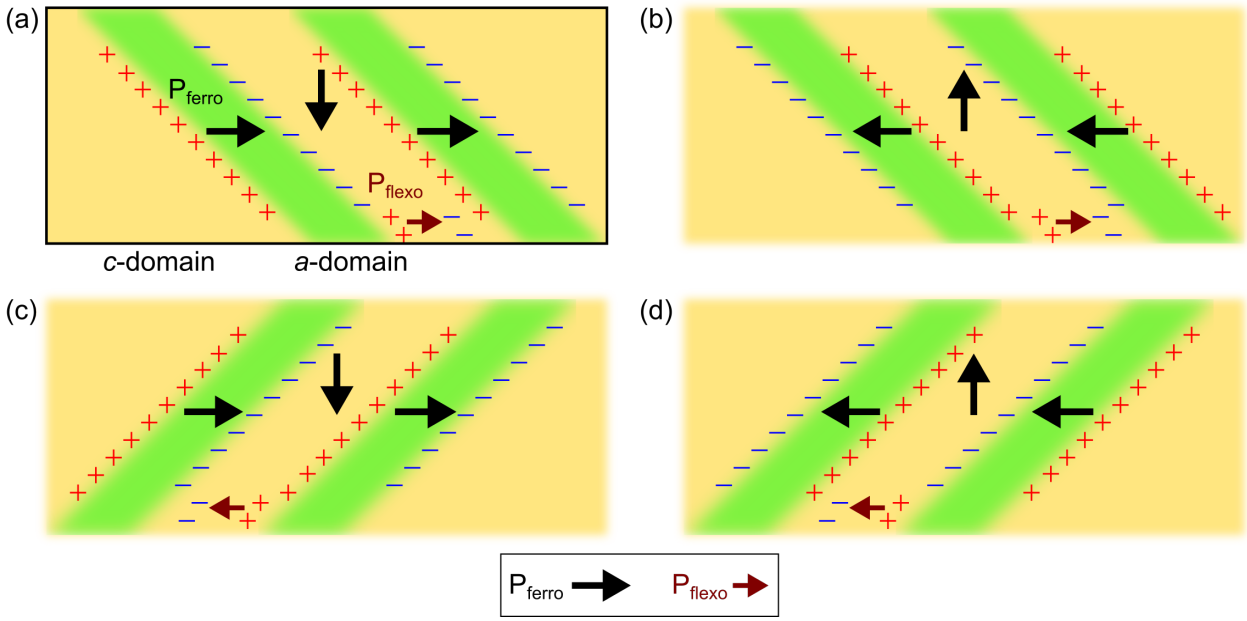


**Figure 4.10:** The possible ferroelectric domain configurations. The PTO layers with (**a,b**) left-inclined *a*-domains, and (**c,d**) right-inclined *a*-domains. In our case, the domain configuration in (a) is observed.

For the 45 uc PTO, the strain maps show much more complex patterns, a reduced strain area at the center of the PTO layer, and intense out-of-plane or in-plane strain near the top and bottom interfaces of the PTO layer. According to these strain behaviors, sole flux-closure type domain configurations might not be accepted. In fact, the GPA confirms that an out-of-plane expansion is dominating near the bottom and top interface of the PTO layers which is in agreement with ferroelectric vectors pointing toward the electrodes. In the case of the 45 uc, the nascent $a/c$ domain configuration is visible, with the presence of a small tilted $a$ domain near the top interface. For the 23 uc PTO, the strain maps show homogeneous patterns, and no visible ferroelectric domain contrast can be identified in the PTO layer from this GPA measurement. The domain configurations of the 45 uc and 23 uc PTO samples are not able to be directly determined at this moment. Moreover, the top SRO layers of the 90 uc and 45 uc PTO samples exhibit periodic patterns associated with the PTO domains, and these findings will be discussed in section 4.4.5.

### 4.4.4 FFT analysis

Through the use of FFT analysis, more information is uncovered in reciprocal space. Figure 4.11(a) shows the reconstructed colored FFT images from the HAADF image of the 90 uc PTO sample, and figure 4.11(b) shows the corresponding MAADF image to illustrate where the domains are, due to the domain contrast of the HAADF image being hardly visible. The *butterfly* pattern around $(001)_{pc}$ peak can be defined by four orientations of the *a*- and *c*-domain, according to the result of SXDM in section 4.3.3. The reconstructed colored FFT image highlights two kinds of the $a/c$-domains in different colors. The green pattern results from the $a/c$-domains, which slope from top-left to bottom-right; the red pattern results from the $a/c$-domains, which slope from top-right to bottom-left; both of them can be observed in figure 4.11(b). Additionally, the satellite peaks in the FFT image indicate a periodic phase, and we can estimate the corresponding period of the domain. However, the satellite peaks are barely visible in this *butterfly* pattern, which only consists of a small number of $a/c$ domains and is not enough to display clear satellite peaks. Further, a zoomed part in the upper right corner of the figure 4.11(a) shows the satellite peaks of the $a^{[010]_{pc}}$ domain, which comes from the other region consisting of more than 15 $a^{[010]_{pc}}$ domains, giving an apparent period of $\sim 46$ nm.

Then, we select four corners of the *butterfly* pattern in the FFT image and reveal their spatial distribution maps through inverse FFT in a similar manner as it was reported by SXDM in figure 4.5. The FFT-filtered patterns, which are filtered by the cyan and orange boxes in the FFT image, are presented in figure 4.11(c,d), respectively. In figure 4.11(c), it is evident that the colored areas correspond to the *a*-domains ($a^{[010]_{pc}}$ in green and $a^{[0\bar{1}0]_{pc}}$ in red); and in figure 4.11(d), the colored areas correspond to the *c*-domains ($c^{[0\bar{1}0]_{pc}}$ in green and $c^{[010]_{pc}}$ in red). The $a^{[010]_{pc}}$ and $c^{[0\bar{1}0]_{pc}}$ are always present together, as well as $a^{[0\bar{1}0]_{pc}}$ and $c^{[010]_{pc}}$. As a result, the domain bundles of $a^{[010]_{pc}}/c^{[0\bar{1}0]_{pc}}$ (green) and $a^{[0\bar{1}0]_{pc}}/c^{[010]_{pc}}$ (red) are consistent with the result of the SXDM.

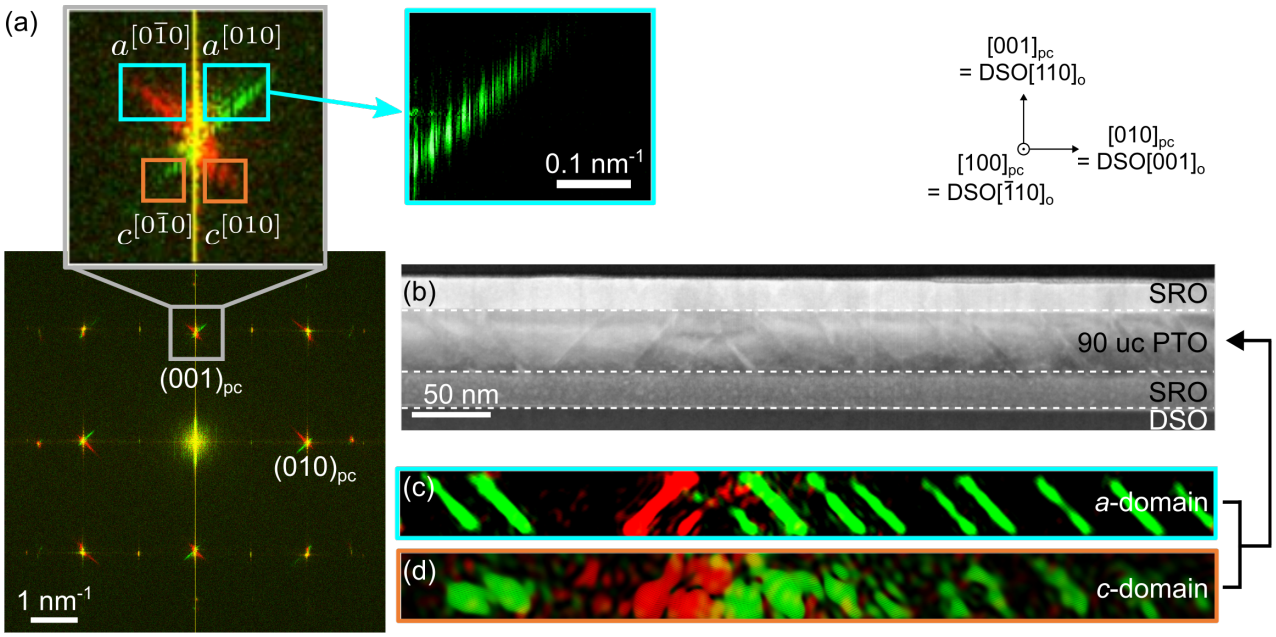


**Figure 4.11:** FFT analysis of the 90 uc PTO sample. (**a**) The reconstructed colored FFT image highlights the different orientations of $a/c$ domain. The green and red patterns correspond to the left-inclined $a/c$-domain and right-inclined $a/c$-domain, respectively. The *butterfly* shape of $(001)_{pc}$ peak is defined as four orientations, $a^{[0\bar{1}0]_{pc}}$, $a^{[010]_{pc}}$, $c^{[010]_{pc}}$, and $c^{[0\bar{1}0]_{pc}}$. A zoomed part in the upper right corner of (a) shows the satellite peaks of the $a^{[010]_{pc}}$ domain, which comes from the other region consisting of more than 15 $a^{[010]_{pc}}$ domains, giving an apparent period of $\sim$ 46 nm. (**b**) The MAADF image, where the FFT analysis has been done, illustrates the position of the domain. (**c,d**) The FFT-filtered patterns, which are filtered by the cyan and orange boxes in the FFT image, correspond to the $a$-domain and $c$-domain, respectively.

The FFT image of the 45 uc PTO sample is shown in figure 4.12(a). The $(001)_{pc}$ peak shows the satellite peaks of PTO and indicates a period of $\sim$ 26 nm, which can be observed by the MAADF image in figure 4.12(b). The *butterfly* pattern in the FFT image is not clearly identified the four orientations of *a*- and *c*-domains, and it might associate with *incomplete* *a*-domains, which is presented in figure 4.8(a) and figure 4.9(b). The FFT-filtered pattern is shown in figure 4.12(c) in a similar manner as in figure 4.11(c,d).

Finally, for the 23 uc PTO sample, the FFT image is shown in figure 4.13(a); from the $(001)_{pc}$ peak, only the satellite peaks of the PTO can be observed, and the *butterfly* pattern is invisible. The satellite peaks indicate a period of $\sim$ 13 nm, which can be observed by the MAADF image in figure 4.13(b). The FFT-filtered pattern of PTO is shown in figure 4.13(c).

Consequently, the diffraction patterns of the 45 uc and 23 uc PTO samples do not exhibit the visible *butterfly* shape, making it difficult to determine the orientations of the *a*- and *c*-domains. This phenomenon could be associated with complex polarization configurations. In general, the periodicities of all these samples agree well with the results of the X-ray analysis, and we will compare them in section 4.5.

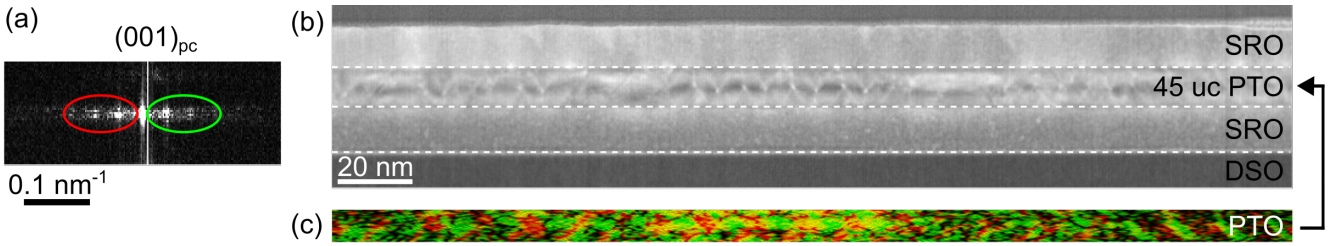


**Figure 4.12:** FFT analysis of the 45 uc PTO sample. (**a**) The $(001)_{pc}$ peak of FFT images. (**b**) The MAADF image, where the FFT analysis has been done, illustrates the position of the domain. (**c**) The FFT-filtered pattern by filtering the colored areas marked in (a).

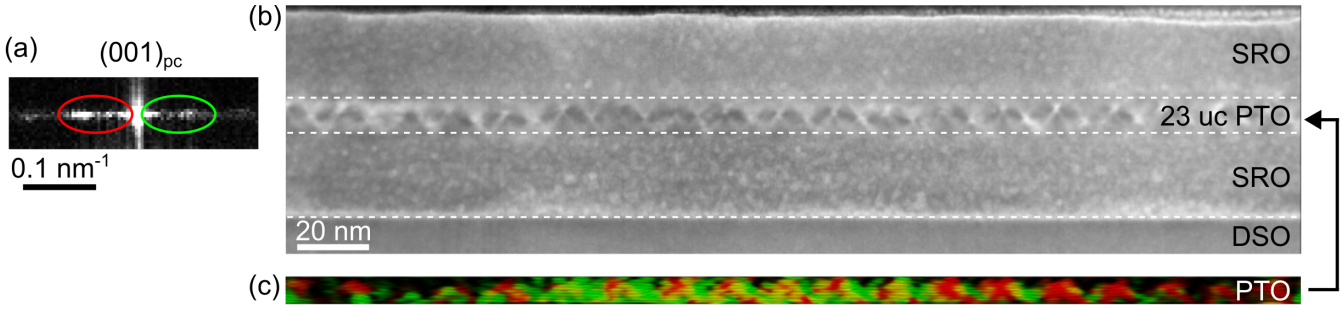


**Figure 4.13:** FFT analysis of the 23 uc PTO sample. (**a**) The $(001)_{pc}$ peak of FFT images. (**b**) The MAADF image, where the FFT analysis has been done, illustrates the position of the domain. (**c**) The FFT-filtered pattern by filtering the colored areas marked in (a).

### 4.4.5 Domains of the $SrRuO_3$ electrodes

Recalling the GPA result in figure 4.9, the strain contrast modulations of the top SRO layers are visible by observing the shear strain and rotation maps of the 90 uc and 45 uc PTO samples. Additionally, these strain contrast modulations are coupled with ferroelectric domains in PTO with the same period, indicating another domain in the top SRO. Therefore, we examine the neighboring SRO layers to identify what types of domains exist in them, and how they correlate with the ferroelectric PTO domains.

Since the lattice parameters $a_o$ and $b_o$ of SRO are not identical ($a_o = 5.567$ Å and $b_o = 5.530$ Å), its pseudo-cubic unit cell can be observed a slight distortion angle of either $\sim 90.4°$ and $\sim 89.6°$ (see figure 4.14(a)). Six possible orthorhombic orientations grown on STO substrate have been first reported by J. C. Jiang [93, 101], and the schematic diagram is shown in figure 4.14(b). According to the direction of orthorhombic *c*-axis, they can be defined as **X**-, **Y**-, **Z**-orientation; since there are two distortion angles (90.4° and 89.6°), there are **X**′-, **Y**′-, **Z**′-orientation as well.

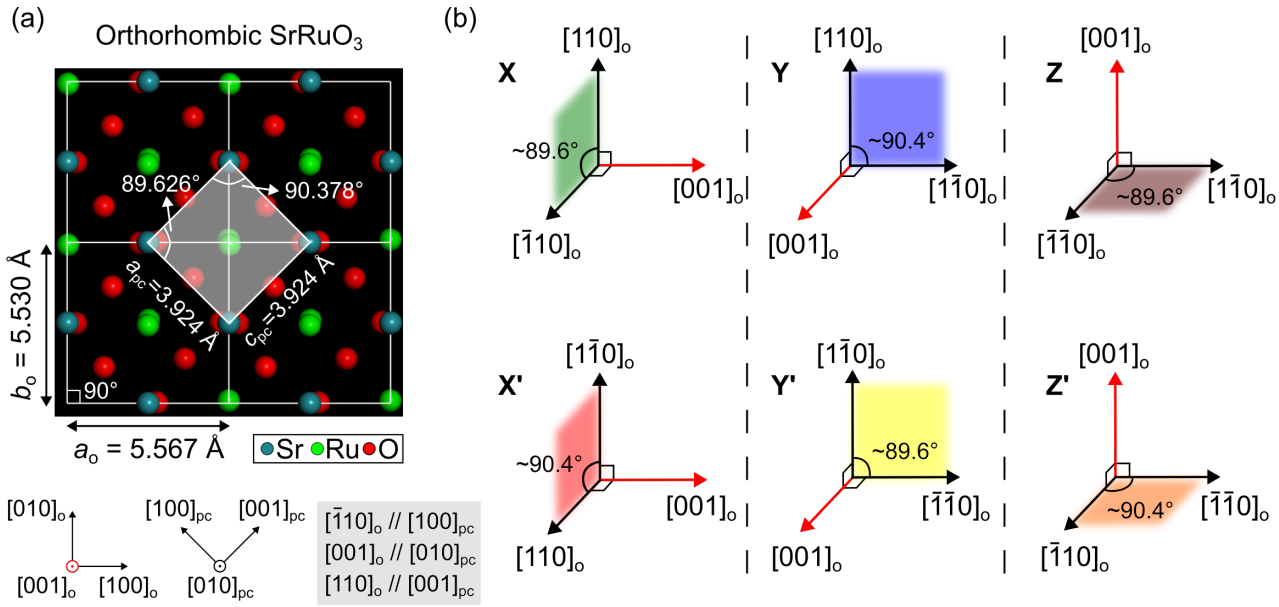


**Figure 4.14:** (**a**) The crystal structure of orthorhombic SRO projected along $[001]_o$(i.e., $[010]_{pc}$), showing the distortion angles (90.4° and 89.6°) in the pseudo-cubic unit cell. (**b**) Schematic diagram showing six possible orientations of SRO thin film grown on a substrate. The red axis refers orthorhombic *c*-axis, and the colored planes highlight the plane where two axes are not orthogonal. Reproduced from ref. [93].

According to our analysis, the SRO layers exhibit different orientations, and the FFT images are shown in figures 4.15(a,b). Figure 4.15(a) shows the superstructures of $\{111\}_o$ family (i.e., $(1\,1\,1)_o$, $(\bar{1}\,\bar{1}\,1)_o$, $(\bar{1}\,\bar{1}\,\bar{1})_o$, and $(1\,1\,\bar{1})_o$, encircled in dark yellow), corresponding the orthorhombic *c*-axis SRO$[001]_o$ parallels to DSO$[001]_o$, defined as **X**-orientation. On the contrary, figure 4.15(b) shows the superstructures of $\{100\}_o$ (i.e., $(100)_o$ and $(\bar{1}00)_o$) and $\{010\}_o$ families (i.e., $(010)_o$ and $(0\bar{1}0)_o$, encircled in cyan), corresponding to the orthorhombic *c*-axis SRO$[001]_o$ parallels to DSO$[\bar{1}10]_o$, defined as **Y**-orientation. Further-

more, filtering the superstructures of **X**-orientation (dark yellow circles in figure 4.15(a)) and **Y**-orientation (cyan circles in figure 4.15(b)), the matching colored FFT-filtered patterns of the 23 uc, 45 uc, and 90 uc PTO samples are shown in figure 4.15(c-e), respectively. For the bottom SRO, all samples exhibit the same **X**-orientation, probably pinned by the interfacial continuity imposed by the $(110)_o$-DSO substrate (**X**-orientation). For the top SRO, the 23 uc and 45 uc PTO samples have only **Y**-orientation, while the 90 uc PTO sample exhibits a mixture of both **X**- and **Y**-orientations.

When observing the **X**- and **Y**-orientation along DSO$[\bar{1}10]_o$, it is noted that the **X**- and **X**′-orientations cannot be identified; therefore, **X**-orientation is used to refer to either **X**- and **X**′-orientations in this section. On the other hand, the structural difference between the **Y**- and **Y**′-orientations is visible from our observation axis (see the colored plane in figure 4.14(b)), and they can be distinguished through the Bragg peaks of the FFT image and atomic-resolved image as well.

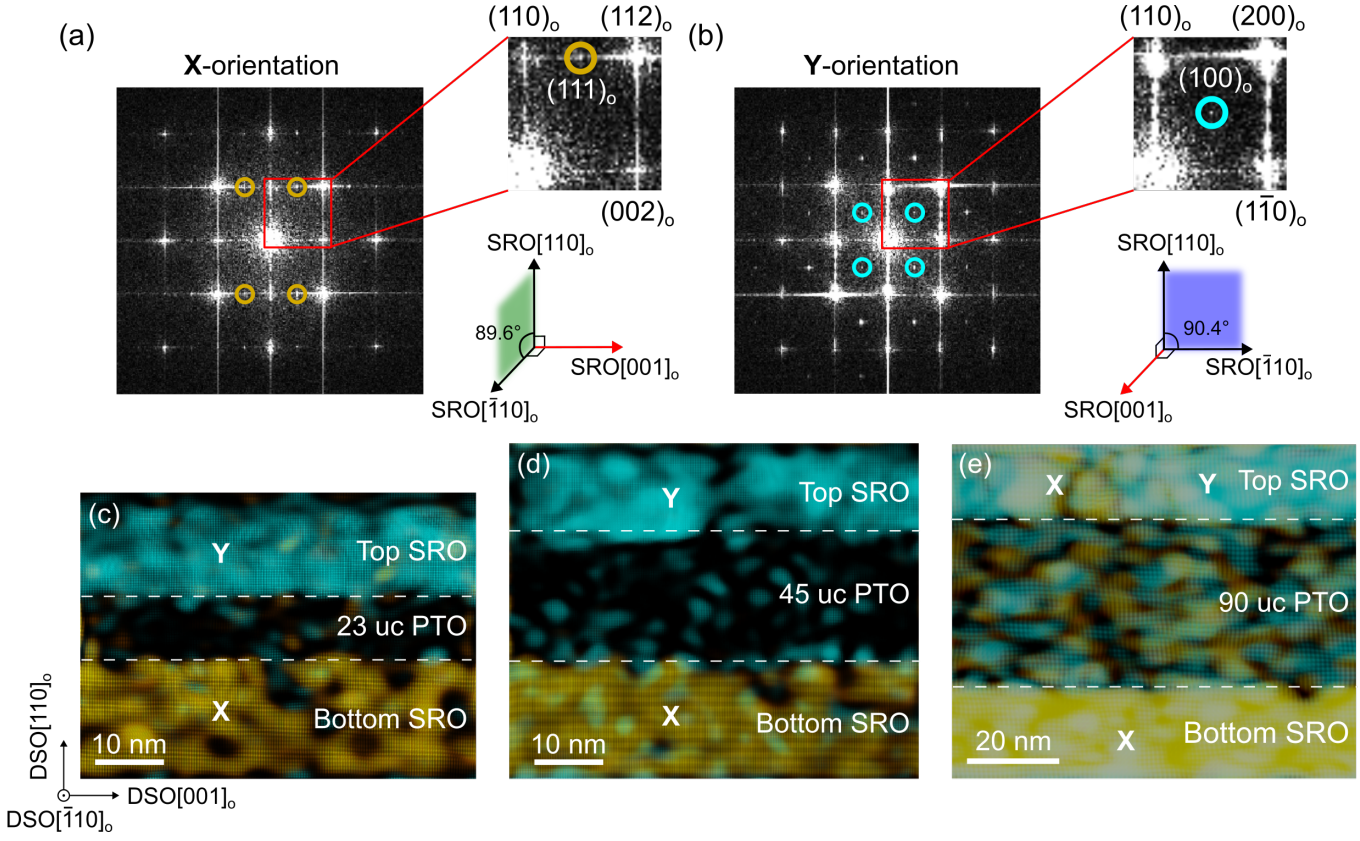


**Figure 4.15:** FFT analysis of the top and bottom SRO electrodes of the 23 uc, 45 uc, and 90 uc PTO samples. (**a,b**) FFT images correspond to two families of SRO orthorhombic orientations, in which the superstructures are marked. (a) corresponds to**X**-orientation due to the superstructures of $\{111\}_o$ family, and (b) corresponds to**Y**-orientation due to the superstructures of $\{100\}_o$ and $\{010\}_o$ families. (**c-e**) FFT-filtered patterns of the 23 uc, 45 uc, and 90 uc PTO samples, respectively. The dark yellow and cyan areas correspond to the **X**- and **Y**-orientations, respectively.

The GPA results of 90 uc and 45 uc PTO show their top SRO layers have periodic shear strain and rotation, which are extracted into figure 4.16(a,d). It is evident that their top SRO exhibit two types of domains (marked in black boxes). The FFT images from these two regions in black boxes in figure 4.16(a,d) are colored and overlapped in figure 4.16(b,e), respectively. In order to emphasize the slight shift between the Bragg peaks of the red and green FFT images, the corresponding schematic diagrams are displayed in figure 4.16(c,f), whose distortion angles have been enlarged by five times, due to the difference in the angular distortion being smaller than 0.8°. First, for the 45 uc PTO, the $\{100\}_o$ and $\{010\}_o$ peaks exhibit shear behavior, while the $\{220\}_o$ peaks exhibit rotational behavior, corresponding to the shear strain and rotation maps of the GPA measurements. Therefore, they correspond to the $\mathbf{Y}$- and $\mathbf{Y}'$-orientations. Second, the 90 uc PTO exhibits a similar FFT pattern as the 45 uc PTO, showing the $\mathbf{Y}$- and $\mathbf{Y}'$-orientations as well. Additionally, the interface between the $\mathbf{Y}$- and $\mathbf{Y}'$-orientations of the 90 uc PTO is not well defined, resulting in a small rotation of all $\{220\}_o$ peaks.

We enlarge the interface of $\mathbf{Y}$- and $\mathbf{Y}'$-orientations to examine their crystal structures by atomic-resolved HAADF image. A HAADF image of the 45 uc PTO is shown in figure 4.17(a). In fact, the interface of PTO and top SRO has a zigzag distorted behavior due to the presence of small ferroelectric *a*-domain near the top PTO layer, inducing SRO *twinning* $\mathbf{Y}$- and $\mathbf{Y}'$-crystal domains. Both the SRO crystal domain and PTO ferroelectric domain have roughly the same periodicity ($\sim$ 26 nm), sharing interface connectivity. In addition, the measured distortion angle matches the ideal crystal structure of $\mathbf{Y}$- and $\mathbf{Y}'$-crystal domains in figure 4.17(b), which overlaps the $\mathbf{Y}$- and $\mathbf{Y}'$-crystal domains. This finding demonstrates the ferroelectric $c/a$ domain near the top PTO layer imposes the crystallographic domain distribution in the top SRO layer.

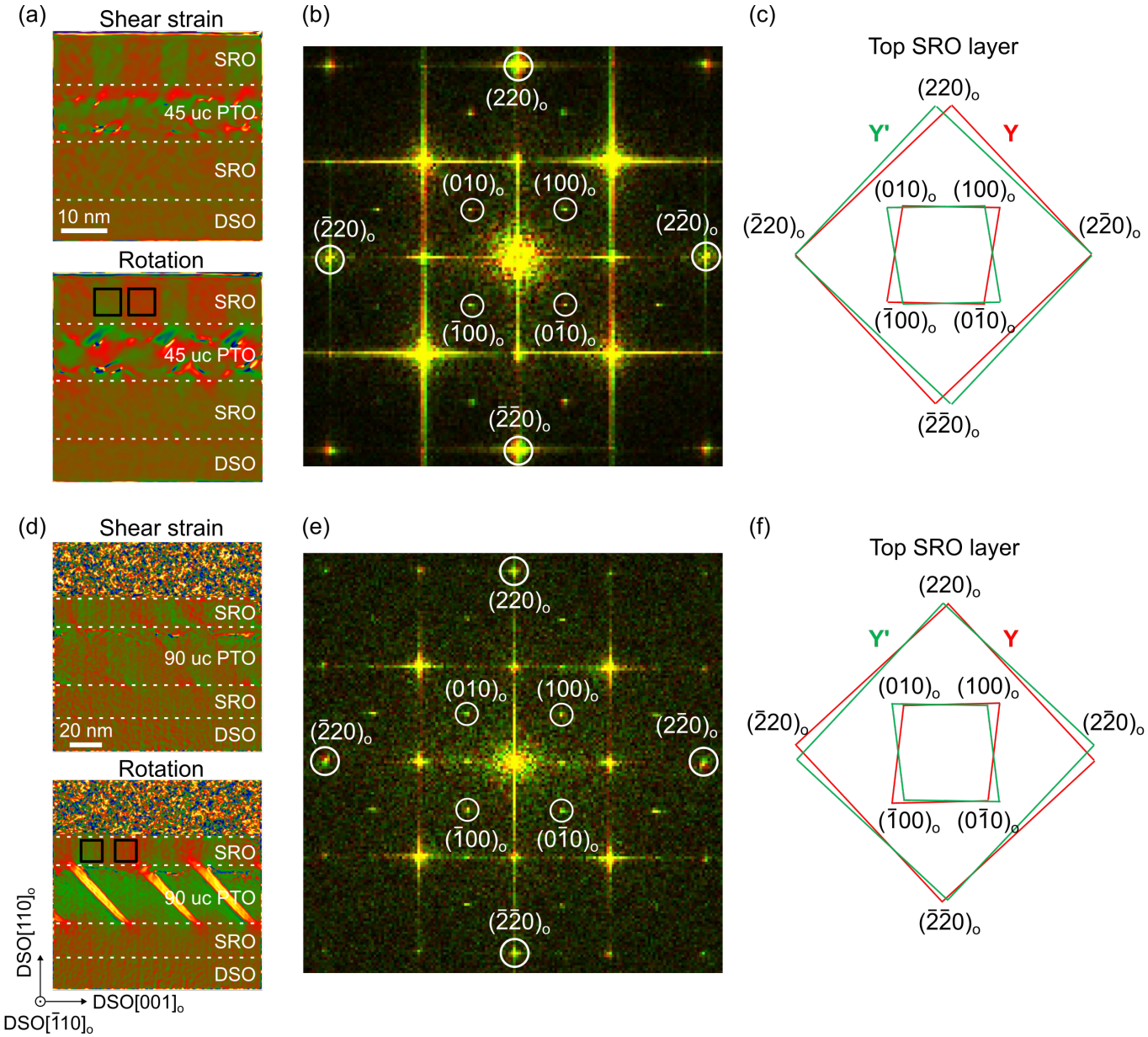


**Figure 4.16:** A comparison of the top SRO layers in (**a-c**) 45 uc and (**d-f**) 90 uc PTO samples. (**a,d**) The shear strain and rotation maps are extracted from figure 4.9(b,a), respectively. (**b,e**) The FFT images from two regions of interest (enclosed with black boxes in (a,d)) in the top SRO layers are colored and overlapped. These two regions represent the **Y**- and **Y**′-orientations. (**c,f**) The corresponding schematic diagrams, whose distortion angles have been enlarged by five times, due to the difference in the angular distortion being smaller than 0.8°. The $\{100\}_o$ and $\{010\}_o$ peaks exhibit shear behavior, while the $\{220\}_o$ peaks exhibit rotational behavior.

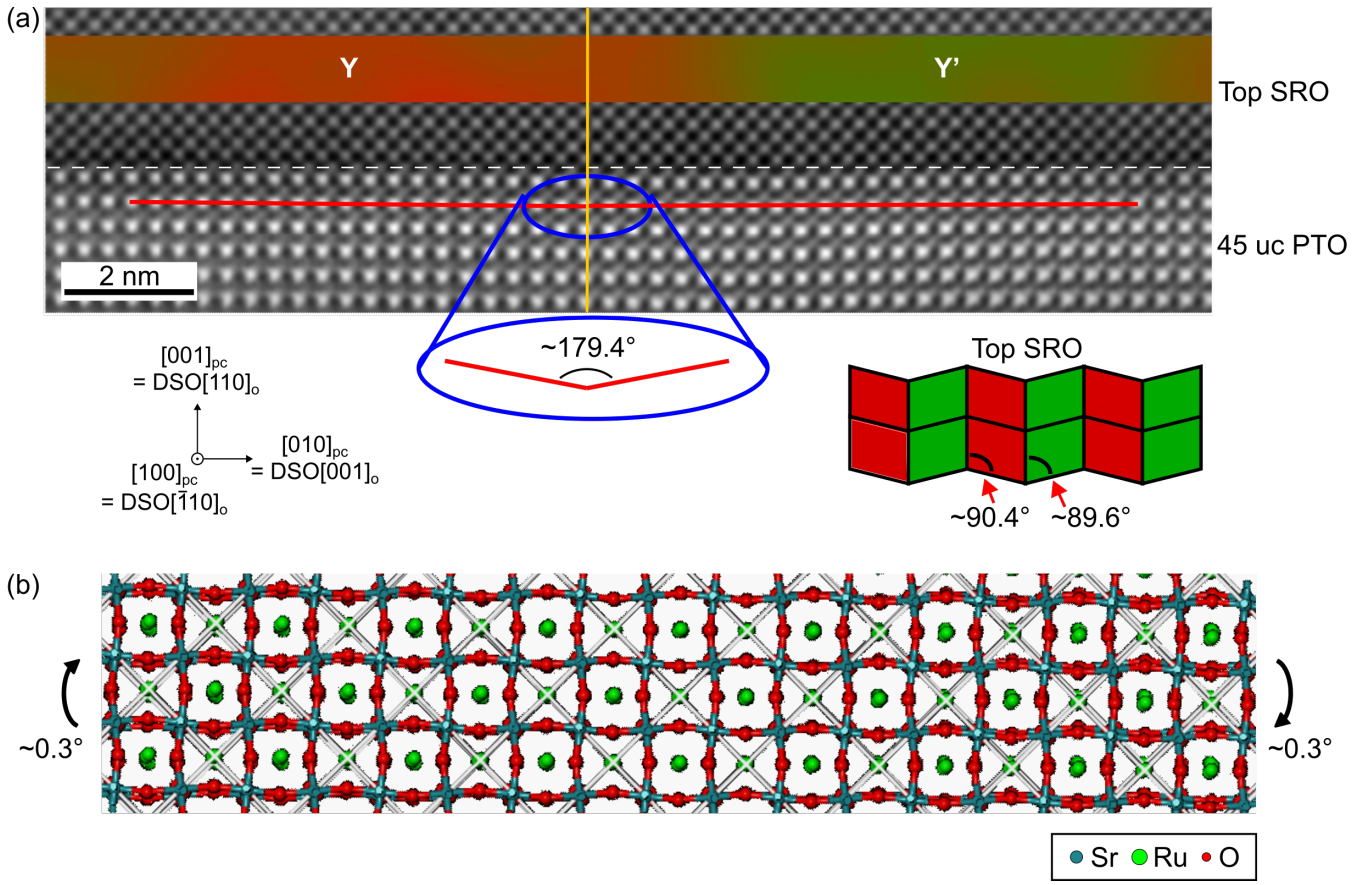


**Figure 4.17:** (**a**) High-resolution HAADF image of the 45 uc PTO sample. The red lines highlight the distorted atomic layers, showing a small angular difference near the interface of the PTO and SRO layers. The corresponding rotation map of the GPA result overlays the image. (**b**) The overlapping of the crystal structure of the $\mathbf{Y}$- and $\mathbf{Y}'$-orientations. It reveals the continuity of cation along $[110]_o$ and a slight clockwise or counterclockwise rotation.

## 4.5 Domain period as a function of $PbTiO_3$ film thickness

The periodicities of this series of PTO samples measured by the topography images of AFM, RSM of XRD, and FFT analysis of STEM images are summarised in figure 4.18. According to our investigations, this series of samples can be divided into two regions in terms of thickness that exhibit distinct behaviors. The first region (region I) consists of samples with a thinner PTO layer than 50 uc, in which trench patterns in topography images are not visible, and the additional peaks in RSM cannot be observed. The PTO layers exhibit complex domain configurations and a null or weak connection to the top SRO electrode. On the other hand, the second region (region II) consists of samples with a thicker PTO layer than 50 uc, in which trench patterns are apparent in topography images, and the additional peaks are displayed in RSM. Moreover, the PTO in this region has well-defined ferroelectric $a/c$ domains and is strongly correlated to the top SRO electrode.

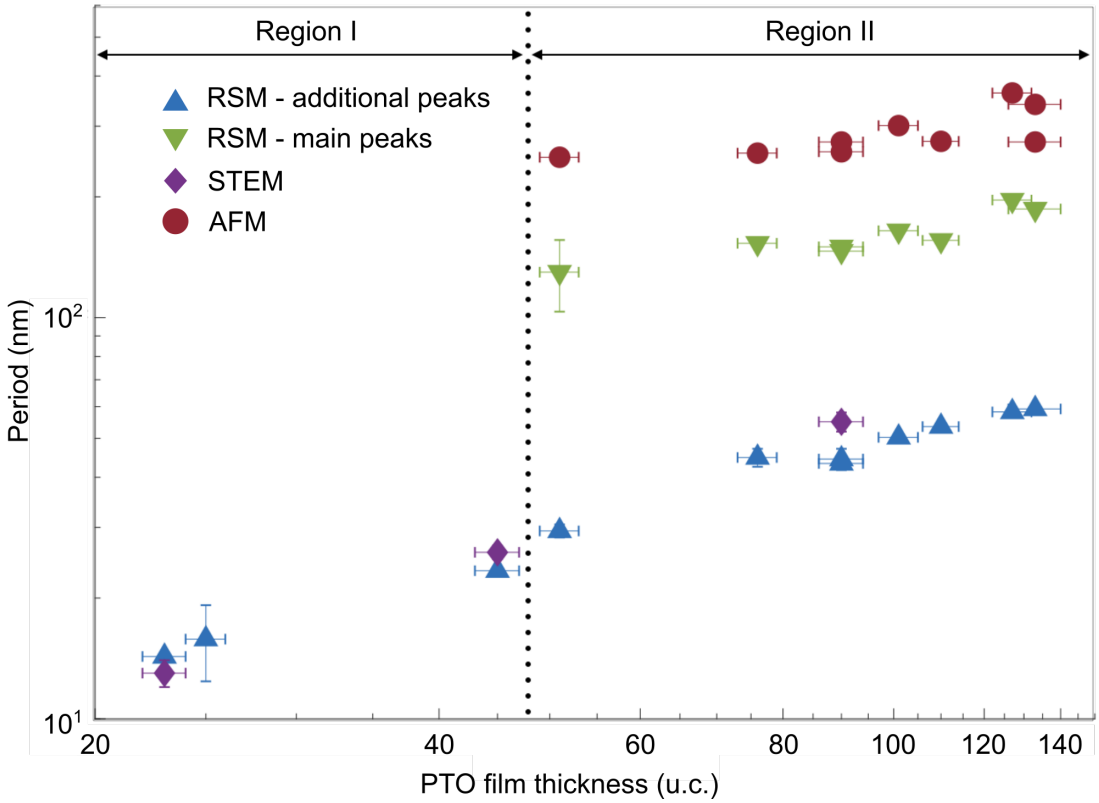


**Figure 4.18:** Summary of the period along $[010]_{pc}$ as a function of PTO thickness. The values are obtained from the topography images of AFM (red dots), RSM of XRD (blue and green triangles correspond to the additional period and primary period, respectively), and FFT analysis of STEM images (purple diamonds). Two different regions are defined: region I for the samples with a PTO thickness of less than 50 uc; region II for the samples with a PTO thickness of more than 50 uc.

According to our observations of the period of PTO ferroelectric domains as a function of film thickness, the period $p$ decreases with decreasing film thickness $t$ as a function of $p \propto t^n$ with $n = 0.8 \pm 0.1$. Similar results were reported in a series of PTO thin film heterostructures, giving the exponent $n = 0.68 \pm 0.3$ [94].

The sample in region II exhibits typical $a/c$ ferroelectric domains with the expected periods. As the film thickness reduces, in the region I, we expect to observe $c^+$ and $c^-$ ferroelectric domains [102]. Instead, we observed the complex polarization configurations and strain patterns that might associate with the energies between ferroelectricity and ferroelasticity [103], and the behavior of our samples in region I could be determined by the complex interaction between strain and electrostatic boundary conditions.

## 4.6 Summary

This chapter examines the evolution of the ferroelectric domain through PTO thin film heterostructures with various PTO film thicknesses. A series of PTO thin films sandwiched by SRO electrodes was investigated through a combination of AFM, XRD, SXDM, and STEM analyses, revealing their periodicities, $a/c$ domain with tilted orientations, and ferroelectric domain configurations. Increasing the PTO thin film thickness results in the domain configuration evolving from a complex flux-closure-like state into the typical ferroelectric $a/c$ domain. Nevertheless, all the samples have periodic domain configurations, and can be divided into two regions exhibiting distinct structural behaviors according to thickness. The influence of film thickness on ferroelectric domain configurations is revealed.

Furthermore, anisotropic strain and structural distortion in the PTO layers are correlated with the top SRO electrode and result in a reorientation of the crystal structure of the SRO. This finding indicates the possibility of affecting the properties of neighboring layers through the ferroelectric effects.

Subsequently, the investigation regarding nickelate's structural and electronic properties modulated through the ferroelectric effect is presented in the next chapter.

# Chapter 5

# Controlling the properties of $NdNiO_3$ thin films through ferroelectricity

**Contents**

## 5.1 Introduction: Structural and electronic properties of $RNiO_3$ nickelates

The coupling between lattice and charge degrees of freedom, which are associated with ferroelectricity, is discussed in chapter 4. Following the investigation of ferroelectric materials, this chapter investigates how the electronic and structural properties of TMOs, such as the metal-insulator transition (MIT), are controlled by ferroelectric materials.

There is an essential topic among TMOs regarding the $RNiO_3$ perovskite nickelates (where $R$ is the rare-earth element, e.g., La, Pr, Nd), which are characterized by their extraordinary structural and physical properties [104, 105]. Figure 5.1 shows a phase diagram of the $RNiO_3$ family with different $R$ cations. With increasing the size of the $R$ cation (except for $R$ = La), the MIT temperature decreases according to the structural distortion of Ni-O-Ni bond angles [106], which couples with the charge and orbital degrees of freedom. As a result, there are a variety of parameters that can be modulated in order to alter the physical properties of nickelates.

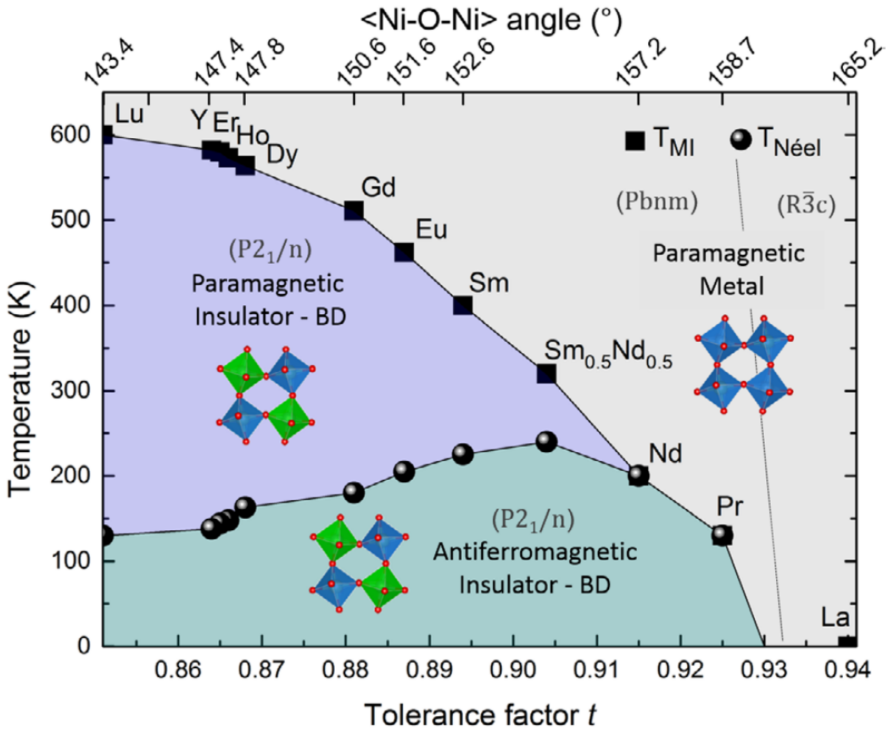


**Figure 5.1:** Phase diagram of $RNiO_3$ nickelate family. The evolution of crystal structure, metal-insulator transition and Néel transition temperatures as a function of Goldschmidt tolerance factor $t$ (values are calculated from experimental measurements of the $R$-O and Ni–O distances), and Ni-O-Ni bond angle. BD represents the bond disproportionated state. Reproduced from ref. [104].

In recent years, there has been an increasing interest in $RNiO_3$ thin films and their heterostructures [107]. As the thin film is easier to distort within a few unit cells, interface-driven effects have the potential to enhance the physical properties or generate novel functionalities with promising rich applications [108].

For instance, the performance of nickelate strongly depends on the epitaxial strain by selecting different substrates [104, 109, 110]. Nickelate thin films under compressive or tensile strain are often associated with the presence of Ruddlesden-Popper (RP) fault [111, 112], which can involve MIT [113]. Additionally, nickelate thin film heterostructures usually exhibit structural phase transitions, such as oxygen octahedra tilting and distortion [114, 115, 116], which can cause charge disproportionation [117]. The $NiO_6$ octahedral exhibits breathing distortion resulting in inequivalent Ni-O bonds and symmetry breaking [118]. This bond modulation induces charge disordering due to the Ni-3$d$ band lying close to the ligand oxygen-2$p$ band, the electron can hop from the 2$p$ band to the 3$d$ band and create a ligand hole $\underline{L}$ in the oxygen band (i.e., $3d^7 \rightarrow 3d^8\underline{L}^1$) [119]. Moreover, as a result of the bond disproportionation, the nickel-$3d^8\underline{L}^1$ can split into two different Ni sites $3d^8\underline{L}^0$ and $3d^8\underline{L}^2$, that is to say, $3d^8\underline{L}^1 + 3d^8\underline{L}^1 \rightarrow 3d^8\underline{L}^0 + 3d^8\underline{L}^2$. The superposition of $3d^8\underline{L}^0$ and $3d^8\underline{L}^2$ state indicate the $Ni^{2+}$ and $Ni^{4+}$ valence states rather than the nominal $Ni^{3+}$ valence state. Consequently, the self-doped oxygen-2$p$ ligand hole causes a rocksalt-type distortion of the $NiO_6$ octahedral, which can be described as compressed $3d^8\underline{L}^2$ and expanded $3d^8\underline{L}^0$ octahedra [120].

In this chapter, we will report the investigation of $NdNiO_3$ (NNO) nickelate thin films in contact with Pb(Zr,Ti)$O_3$ (PZT) ferroelectric thin films. The interest of such heterostructures resides in the possibility to engineer the properties of the NNO, such as the MIT temperature, the magnetic transition, and control of the charge disproportion by the neighboring ferroelectric effects. This work was done in collaboration with Dr. Daniele Preziosi, who focused on the growth of oxide thin films and the study of their magneto-transport and electronic properties at the Strasbourg Institute of Material Physics and Chemistry (IPCMS) at the University of Strasbourg (UNISTRA), France. My gratitude also goes to Guillaume Krieger and Dr. Nathalie Viart, from the same group, for their help and their participation in this motivating collaboration. Nickelate thin films were prepared by our collaborators, then analyzed by them using X-ray diffraction (XRD), piezoresponse force microscopy (PFM), and transport measurements. Different parameters of the heterostructures were changed, such as the nature of buffer layers (a very thin film next to the substrate) or the thickness of the ferroelectric films.

This chapter is divided into two parts. The first part discusses the 20/80 PZT (i.e., $Pb(Zr_{0.2},Ti_{0.8})O_3$) ferroelectric heterostructures growth with different TMO-based buffer layers on a $SrTiO_3$ substrate. We will show that the NNO and $LaMnO_3$ (LMO) buffer layers result in ferroelectric layers with opposite directions for ferroelectric polarization. On top of this ferroelectric layer is grown an additional NNO film that is then in contact with differently polarized ferroelectric layers. Such control of the ferroelectric by a buffer layer could be useful, but its origin is unclear, and we will try to elucidate its origin. The second part focuses on the NNO-buffered PZT heterostructures with different PZT thicknesses. Different thicknesses result in different ferroelectric polarization configurations, accompanied by different physical properties of the nickelate, such as the $NiO_6$ octahedra distortions, which are reported by X-ray absorption spectroscopy (XAS) by the Strasbourg's team.

However, both PFM and XRD analysis can be used to determine the average properties, such as the general polarization direction of the ferroelectric layer and lattice parameters of each layer; they hardly reveal local information. For instance, the evolution of the $NiO_6$ octahedral distortions only occurs over a few unit cells at interfaces, and the strain relaxation could play a crucial role. To understand the physical properties of such heterostructures, we must examine their strains, defects, and structural distortions, with the challenging constraint of nanometric resolution. Thus, we aim to investigate how the ferroelectric layers affect the structural and electronic properties of the NNO layers using the STEM-EELS technique, including atomic-resolved STEM images, GPA, FFT analysis, and fine structures of the EELS spectrum. In conjunction with the microscopic investigations, we hope to be able to carry out a more comprehensive analysis of these samples.

# PART I

## 5.2 Modulation of ferroelectric properties with different buffer layers

### 5.2.1 PFM and X-ray analyses of $NdNiO_3/Pb(Zr,Ti)O_3/(LaMnO_3$ or $NdNiO_3)$ heterostructures

In the beginning, the PFM and XRD investigations of the sandwiched heterostructures of 60 nm PZT with 5 nm NNO or LMO buffer layer grown on STO substrate were performed by our collaborators at the University of Strasbourg.

The PFM gives an overview of the polarization behavior of the PZT ferroelectric layers in these two thin film heterostructures. Observing the topography and PFM phase images in figure 5.2, either as-grown or switched by a negative (-5 V) and positive (+5 V) tip bias on these thin films, the PFM phase image of the LMO-buffered PZT sample (figure 5.2(a)) has an intense upward polarization (pointing to the surface). On the other hand, the PFM phase image of the NNO-buffered PZT sample (figure 5.2(b)) shows a majority of downward polarization (pointing to the substrate). The PFM phase image of this sample does not show an entirely coherent downward polarization, therefore, the other ferroelectric domain configuration is expected to exist in this PZT layer. In any case, as a result of the different buffer layers, these two samples exhibit nearly opposite polarizations.

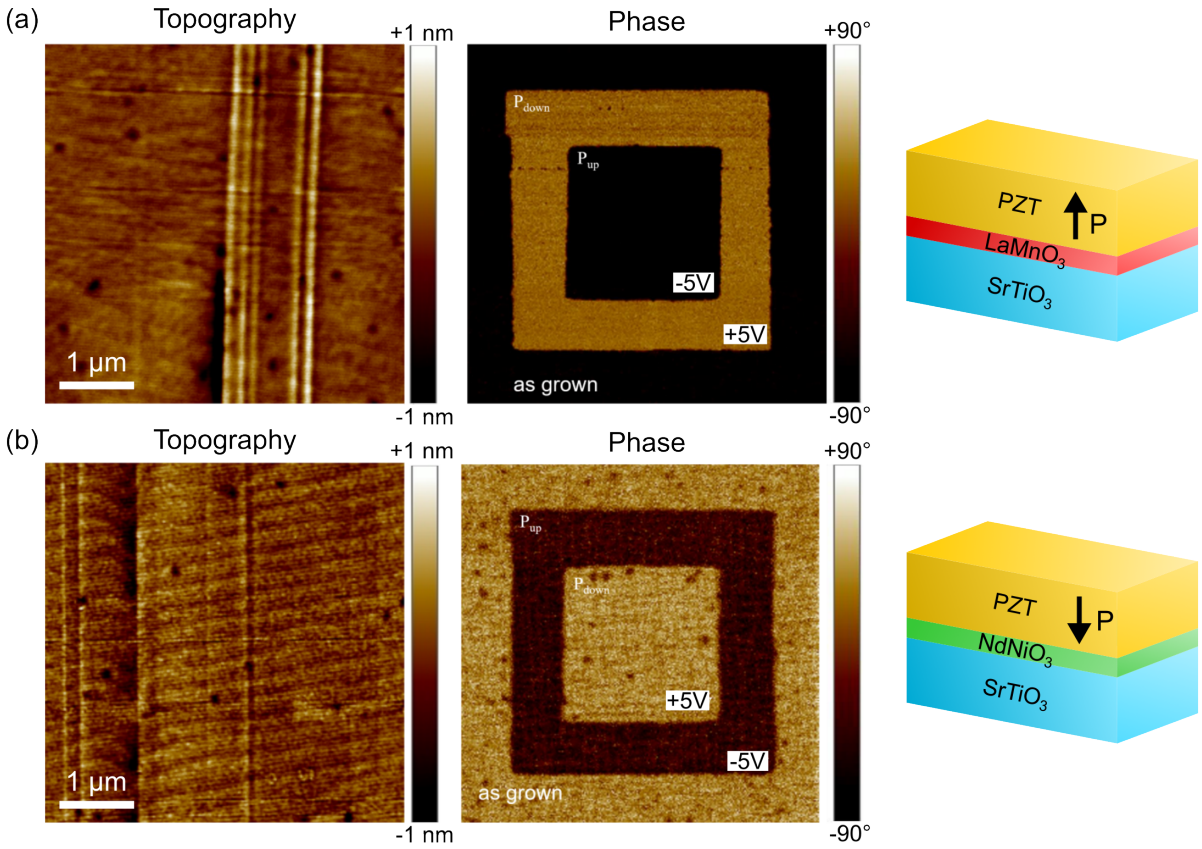


**Figure 5.2:** Topography and PFM phase images of the thin film heterostructures, which are composed of 60 nm PZT with 5 nm LMO or NNO buffer layer grown on a STO substrate. After switching a negative (-5 V) and positive (+5 V) tip bias, (**a**) LMO-buffered and (**b**) NNO-buffered PZT show as-grown upward and downward ferroelectric polarizations, respectively. This figure is reproduced courtesy of D. Preziosi at IPCMS, University of Strasbourg.

The XRD analysis of these two samples is shown in figure 5.3. After the incident X-ray irradiates the thin films, the intensity and scattering angle of the scattered X-ray reveal the crystallographic structure and the lattice parameters of each component. From measuring the scattering angles of the characteristic peaks of the PZT, one can find that the *c*-axis (out-of-plane) lattice parameters of the PZT in these samples are not identical: 4.23 Å for the LMO-buffered PZT (red curve) and 4.14 Å for the NNO-buffered PZT (green curve). This difference in the lattice parameter indicates that these PZT layers do not grow with the same strain on the LMO and NNO buffer layers, and behave differently during strain relaxation. Compared to LMO-buffered PZT, the lattice parameter of NNO-buffered PZT is much smaller and it is evidencing a possible stronger strain relaxation in the PZT ferroelectric layer.

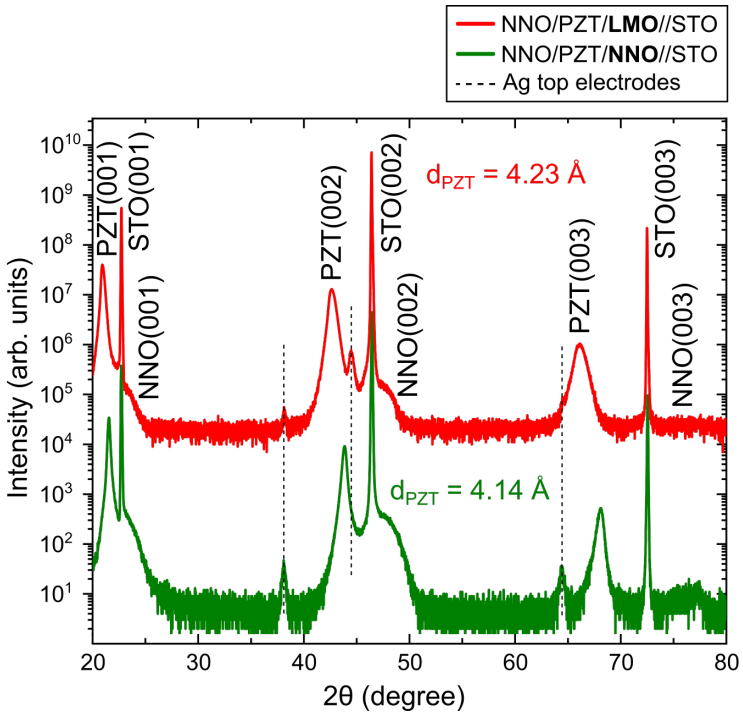


**Figure 5.3:** XRD pattern of the LMO-buffered (red) and NNO-buffered (green) samples, indicating the out-of-plane lattice parameter of 4.23 Å for the LMO-buffered PZT and 4.14 Å for the NNO-buffered PZT. This figure is reproduced courtesy of D. Preziosi at IPCMS, University of Strasbourg.

### 5.2.2 Strain relaxation caused by different buffer layers

The analyses by PFM and XRD in the previous subsection revealed that different buffer layers can manipulate the polarization directions of the neighboring PZT ferroelectric layers, and strain relaxation issues could play a role in this system. Here, we examine the differences between these two samples in structural properties by STEM-EELS to understand why the PZT ferroelectric layers behave differently depending on the buffer layers.

First, the LMO and NNO buffer layers grown epitaxially are under different strains due to the lattice-mismatched STO substrate, and then the electronic properties could be significantly affected by epitaxial strain [110]. The lattice parameters of each layer in thin film heterostructure and corresponding pseudo-cubic (pc) lattice parameters are listed in table 5.1. The LMO thin film has been reported as rhombohedral [121] and orthorhombic crystal structures [122], and their pseudo-cubic lattice parameters ($a_{pc} = b_{pc} = c_{pc} = 3.905$ Å for rhombohedral; $a_{pc} = b_{pc} = 3.974$ Å and $c_{pc} = 3.859$ Å for orthorhombic) resemble of the STO substrate ($a = b = c = 3.905$ Å), causing a weakly strained LMO layer. More precisely, the LMO layer with the rhombohedral-type lattice parameters is strain-free; the LMO layer with the orthorhombic-type lattice parameters can have a (3.974 - 3.905)/3.905 = 1.8% compressive bi-axial strain ($c_{pc}$-axis lies in the out-of-plane direction) or a mixed compressive and (3.859 - 3.905)/3.905 = -1.2% tensile strain ($c_{pc}$-axis lies in the in-plane direction), which could compensate each other and create a nearly strain-free LMO layer. On the other hand, the pseudo-cubic lattice parameters of orthorhombic NNO ($a_{pc} = b_{pc}$ = 3.808 Å and $c_{pc} = 3.805$ Å) are both smaller than the STO substrate, causing NNO with typically (3.808 - 3.905)/3.905 = -2.5% tensile strain. Therefore, weakly strained LMO and tensile strained NNO buffer layer is the first difference that could cause the neighboring PZT layers to relax their strains in different manners.

| Material | Space group | Lattice parameters | | | Pseudo-cubic lattice parameters | | |
|---|---|---|---|---|---|---|---|
| | | $a$ (Å) | $b$ (Å) | $c$ (Å) | $a_{pc}$ (Å) | $b_{pc}$ (Å) | $c_{pc}$ (Å) |
| $LaMnO_3$ | Rhombohedral ($R\bar{3}c$) [121] | 5.523 | 5.523 | 13.324 | 3.905 | 3.905 | 3.905 |
| | Orthorhombic ($Pbnm$) [122][1] | 5.539 | 5.699 | 7.718 | 3.974 | 3.974 | 3.859 |
| $NdNiO_3$ | Orthorhombic ($Pbnm$) [123] | 5.387 | 5.383 | 7.609 | 3.808 | 3.808 | 3.805 |
| $Pb(Zr_{0.2}Ti_{0.8})O_3$ | Tetragonal ($P4mm$) [124] | 3.950 | 3.950 | 4.150 | - | - | - |
| $SrTiO_3$ | Cubic ($Pm\bar{3}m$) | 3.905 | 3.905 | 3.905 | - | - | - |

**Table 5.1:** The crystal structure and lattice parameters of each component in thin film heterostructures. The corresponding pseudo-cubic lattice parameters are calculated as: $a_{pc} = b_{pc} = c_{pc} = a/\sqrt{2}$ for rhombohedral; $a_{pc} = b_{pc} = \sqrt{a^2 + b^2}/2$, $c_{pc} = c/2$ for $Pbnm$ orthorhombic.

[1] Ref. [122] using $Pnma$ as the coordinates, and the lattice parameters "$abc$" of $Pnma$ correspond to "$bca$" of $Pbnm$.

The GPA technique is used to analyze the strain distributions of the thin film heterostructures and investigate how their strains are relaxed. Figure 5.4 shows the GPA strain maps of the LMO- and NNO-buffered PZT samples, from left to right representing the HAADF image, out-of-strain strain, in-plane strain, shear strain, and rotation map, respectively.

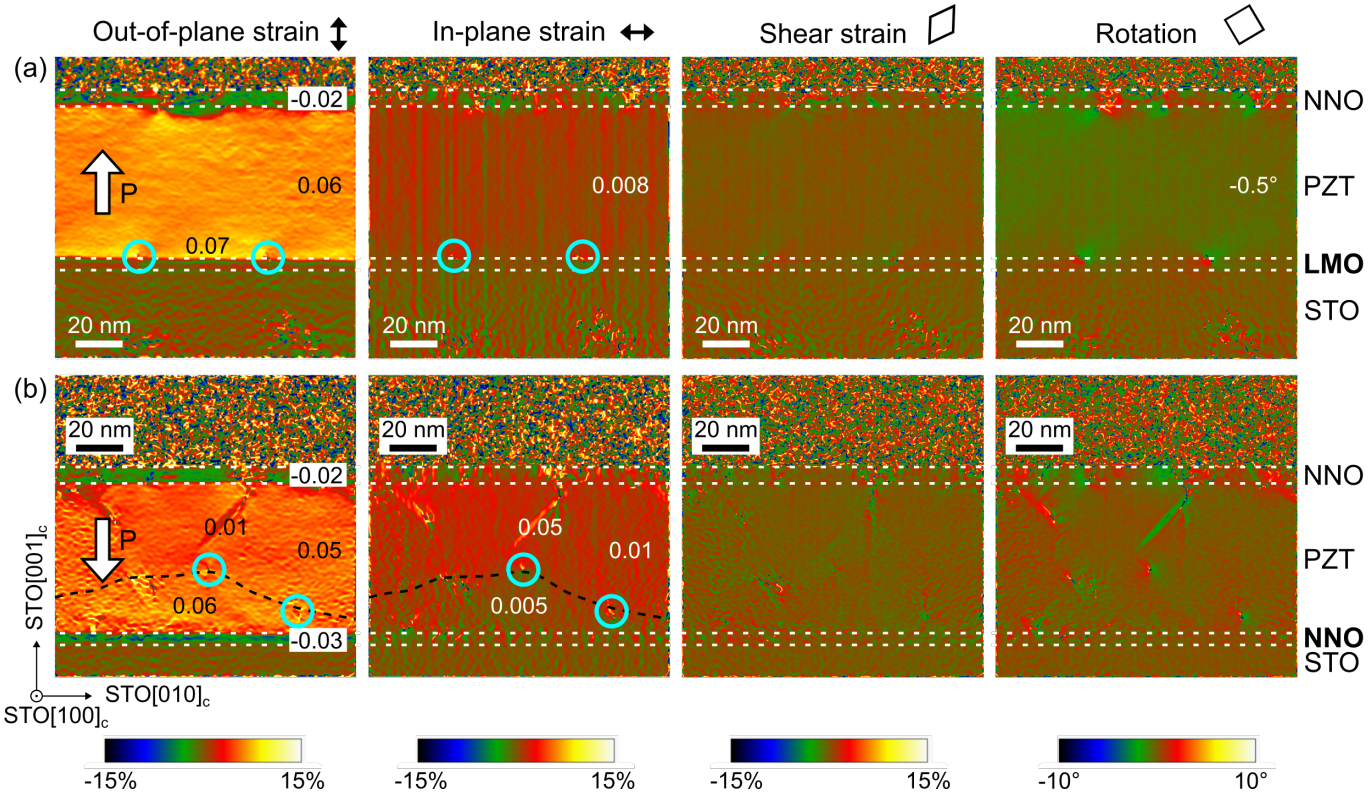


**Figure 5.4:** Strain maps for the (**a**) LMO-buffered and (**b**) NNO-buffered samples. The patterns from left to right correspond to the out-of-plane strain, in-plane strain, shear strain, and rotation, respectively. All strain maps are at the same color intensity scale from -15% to 15%, while the rotation map is from -10° to 10° (anticlockwise positive). The dislocations are marked with cyan circles.

For the LMO-buffered PZT sample (figure 5.4(a)), the LMO buffer layer shows homogeneous out-of-plane and in-plane strain patterns with values close to zero, revealing the weakly strained LMO layer as expected. The dislocations at the interface between the PZT and LMO layer (marked by cyan circles), one of which is enlarged in figure 5.5, relax the strain caused by the lattice mismatch between PZT and LMO; therefore, a homogeneous in-plane strain map of PZT is observed.

Then, the neighboring PZT layer exhibits out-of-plane strain (6-7%) and in-plane strain ($\sim$ 0.8%) with respect to the STO substrate. Therefore, the in-plane lattice parameter of the PZT is about 3.936 Å, corresponding to a 0.35% in-plane strain with respect to the bulk PZT (3.950 Å). According to the hypothesis of a Poisson ratio of 0.3, the ideal relaxed lattice parameter of the PZT is 4.154 Å (i.e., 6.4% out-of-plane strain with respect to the STO), which is close to the GPA measurement (6-7%). Additionally, the out-of-plane strain map shows slightly larger lattice expansion in the bottom region of the PZT layer

(below the black dashed line) than in the top region, in relation to these defects, but it can be considered that the strain of the PZT is homogeneously relaxed within about 20 nm.

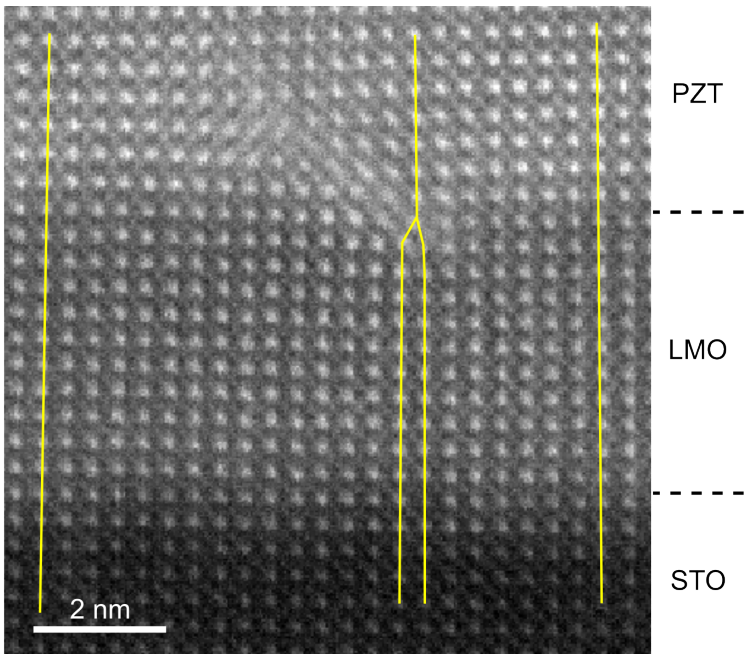


**Figure 5.5:** Dislocations in the LMO-buffered sample are located at the interface between LMO and PZT layers, as indicated by the cyan circles in 5.4.

For the NNO-buffered PZT sample (figure 5.4(b)), the NNO buffer layer is expected to have a -2.5% tensile strain; as a result, its out-of-plane lattice parameter shrinks by at least 3% with respect to the STO substrate in accordance with the GPA map observation.

Then, the neighboring PZT layer presents a minor out-of-plane strain (5-6%) than the previous sample, and with a noticeable absence of dislocations at the interface between the PZT and NNO layer. However, the strain needs to be relaxed in another way, leading to the generation of ferroelectric *a*-domains in the upper region of the PZT layer and some dislocations in the middle of the PZT layer (marked by cyan circles) providing more strain relaxation.

Indeed, the weakly strained LMO buffer layer generates dislocations at the interface between LMO and PZT, allowing a partial but rather homogeneous relaxation of the PZT layer. In contrast, the tensile-strained NNO buffer layer does not seem to relax the PZT layer at the interface, and the dislocations and ferroelectric *a*-domains are induced to later relax the strain. This is very much in accordance with the XRD results in figure 5.3, the lattice parameter of the NNO-buffered PZT (4.14 Å) being smaller than the LMO-buffered PZT (4.23 Å), resulting in a more relaxed PZT.

### 5.2.3 Flexoelectric effect

The NNO-buffered PZT exhibits relatively complex out-of-plane and in-plane strain patterns, and the inhomogeneous strain, such as strain gradient, can lead to flexoelectric effect [125, 126, 127]. The profiles of the out-of-plane and in-plane strains of the LMO-buffered (red) and NNO-buffered (green) PZT layers are shown in figure 5.6(a,b). The out-of-plane strains (figure 5.6(a)) of both samples are generally homogeneous throughout the PZT layer, while the top area of the NNO-buffered PZT has the appearance of the ferroelectric *a*-domains, causing the average strain to slightly decrease. However, the in-plane strain (figure 5.6(b)) of both LMO-buffered and NNO-buffered PZT layers exhibits an obvious strain gradient in the bottom area, indicating a toward-up flexoelectric polarization (pointing from the region with lower strain to higher in-plane strain), and a schematic diagram is shown in figure 5.6(c). The flexoelectric polarization can be estimated in a similar manner as in section 4.4.3. In the case of NNO-buffered PZT, the in-plane strain spans from 0.5% to 1.5% (i.e., $\Delta\varepsilon_{xx} = 0.01$) within 30 nm (i.e., $w = 30$ nm), and the strain gradient $\Delta\varepsilon_{xx}/w \approx 0.01/30\ \text{nm} = 3.3 \times 10^5\ \text{m}^{-1}$. The flexoelectric coefficient of PZT $\mu_{PZT}$ is roughly 1.4 $\mu\text{C}\cdot\text{m}^{-1}$ [128], which is seven times larger than the flexoelectric coefficient of PTO. The flexoelectric polarization $P_{flexo} = \mu_{PZT} \cdot (\Delta\varepsilon_{xx}/w) \approx 46\ \mu\text{C}\cdot\text{cm}^{-2}$. Compared with the typical PZT spontaneous polarization of $\sim 80\ \mu\text{C}\cdot\text{cm}^{-2}$, this flexoelectric polarization has a certain effect on the polarization of PZT but is not able to change the overall polarization direction.

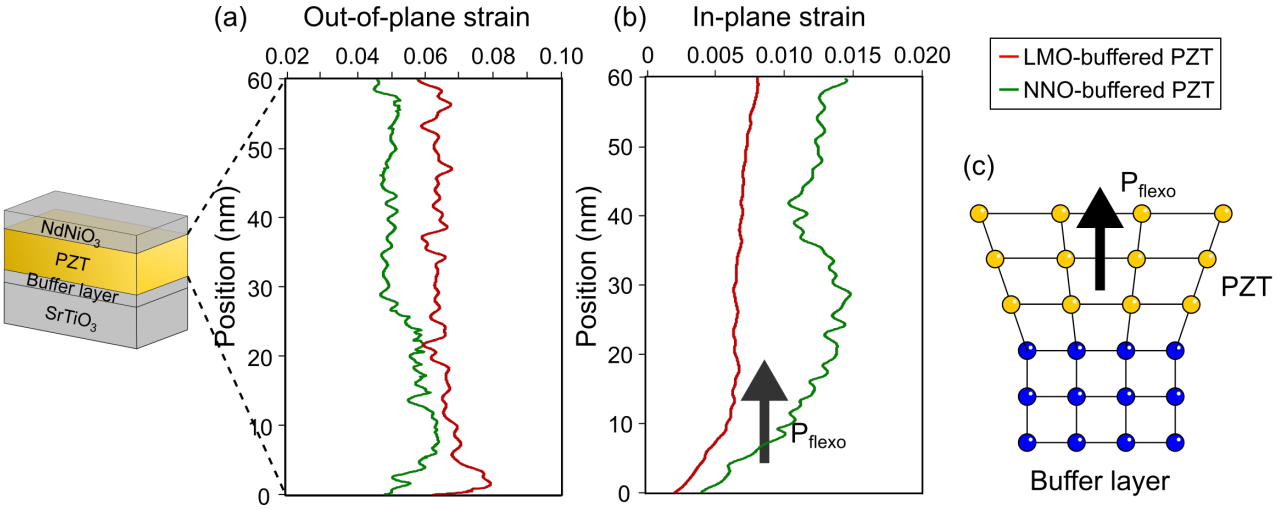


**Figure 5.6:** (**a**) out-of-plane strain and (**b**) in-plane strain intensity profiles of the LMO-buffered (red) and NNO-buffered (green) PZT layers. (**c**) Schematic diagram of the in-plane strain gradient that generates an upward flexoelectric polarization ($P_{flexo}$) within the PZT layers.

### 5.2.4 Ferroelectric polarization

Finally, in order to determine the overall polarization in the PZT layer, spontaneous ferroelectric polarization needs to be considered. The direction and intensity of ferroelectric polarization are associated with the atomic displacements of the *B* cation (Zr/Ti, in the case of PZT) and oxygen. The ferroelectric polarization of these two samples can be estimated by analyzing atomic-resolved HAADF images, which allowed us to determine the atomic displacement of each atom and calculate the polarization direction and the value accordingly. The atomic displacements and corresponding ferroelectric polarization direction of the LMO-buffered PZT are shown in figure 5.7(a-c) and NNO-buffered PZT in figure 5.7(d-f)). Figure 5.7(a,d) are HAADF images of these two samples, and the extractions of a small part of the PZT layer are displayed in figure 5.7(b,e), revealing the *B* cations (marked in cyan) have opposite atomic displacements between these two samples; more precisely, the Zr/Ti atoms of LMO-buffered PZT have downward displacements, and the Zr/Ti atoms of NNO-buffered PZT have upward displacements. The yellow arrows in figure 5.7(c,f) represent the polarization direction of the PZT layers, whose directions are opposite to the atomic displacements of *B* cations. Then the ferroelectric polarization can be estimated by $P_{\text{ferro}} = \kappa \cdot \delta_{\text{B-O}}$ [129, 130], where $\kappa$ is an elastic constant associated with the ferroelectric polarization and it is in a range from 2500 to 2900 $\mu C \cdot cm^{-2} \cdot nm^{-1}$ for PZT [130], and $\delta_{\text{B-O}}$ is the average atomic separation between *B* cation and oxygen. By measuring atomic-resolved HAADF images in figure 5.7(b,e), the average $\delta_{\text{B-O}}$ of the LMO-buffered PZT is about +0.2 Å and the $\delta_{\text{B-O}}$ of the NNO-buffered PZT is about -0.3 Å, where positive value represents the upward direction, which gives the ferroelectric polarization of LMO- and NNO-buffered PZT of +55 and -80 $\mu C \cdot cm^{-2}$, respectively.

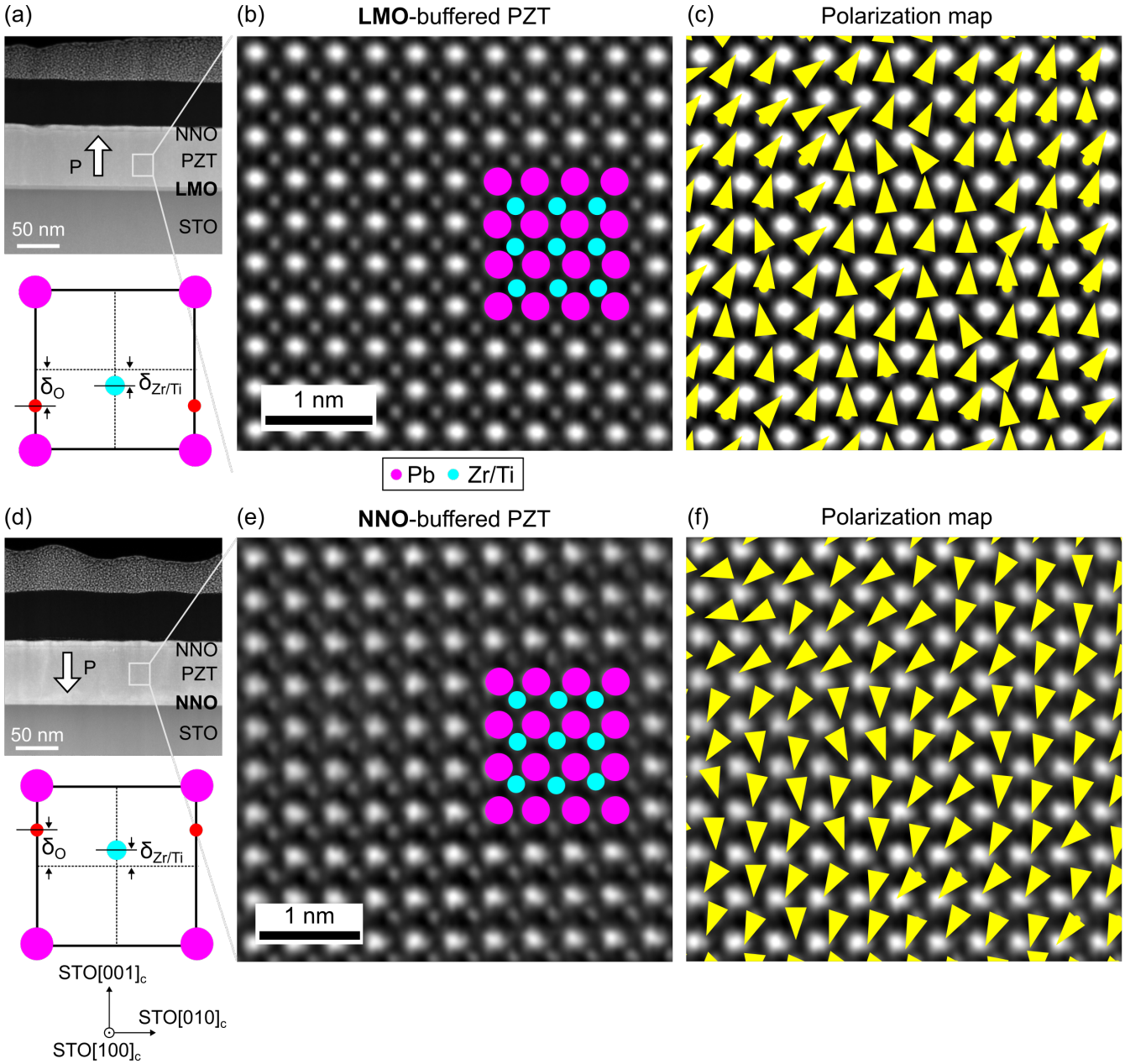


**Figure 5.7:** The HAADF images of (**a-c**) LMO-buffered and (**d-f**) NNO-buffered samples reveal atomic displacements and corresponding ferroelectric polarizations, in accordance with the concept discussed in figure 2.5. (**a,d**) Low-magnification HAADF images observed along STO$[100]_c$ axis, and their enlarged atomic-resolved HAADF images of the PZT layers are shown in (**b,e**), respectively. The atomic displacements of *B* cation (i.e., Zr/Ti, cyan), with respect to *A* cation (i.e., Pb, magenta), are shown as downward in (b) and upward in (e). (**c,f**) The polarization maps of the PZT layers, whose directions are opposite to the atomic displacements of the *B* cations, indicate an upward ferroelectric polarization for the LMO-buffered PZT and a downward ferroelectric polarization for the NNO-buffered PZT.

As a result of combining ferroelectric polarization and flexoelectric polarization, the overall polarization in the PZT can be revealed. The LMO-buffered PZT layer shows an upward ferroelectric polarization (+55 $\mu C \cdot cm^{-2}$) with also an upward flexoelectric effect; on the other hand, the NNO-buffered PZT exhibits a downward ferroelectric polarization (-80 $\mu C \cdot cm^{-2}$) and an upward flexoelectric polarization (+46 $\mu C \cdot cm^{-2}$), but the PZT still maintains a downward polarization.

According to the PFM phase images, the sharp contrast of the LMO-buffered PZT (figure 5.2(a)) indicates the unique ferroelectric polarization direction. The LMO-buffered PZT displays an inhomogeneous pattern (figure 5.2(b)), which is a strong indication of the presence of inverse flexoelectric polarization contribution and ferroelectric *a*-domains. As a result, the PFM results are in good agreement with our STEM measurements.

## 5.3 Structural differences between the buffer layers

### 5.3.1 Interface termination

Several mechanisms have been reported that can modulate the ferroelectric polarization direction, such as the termination layer of the interface [131], thickness-dependent interfacial charge screening [132], surface reconstruction [133], and breaking of orbital degeneracy [10, 11]. This section will take into account the difference in structural parameters between these two buffer layers, focusing on the interface termination, and crystal orientation.

First, the interface termination of each layer can be determined using energy-filtered STEM-EELS map, which reveals the distribution of chemical compositions in each atomic layer. The EELS chemical composition maps of the LMO buffer layer are shown in figure 5.8(a). EELS chemical composition maps are obtained by selecting characteristic edge peaks with an energy-selecting window of $\sim$ 5 eV width. For instance, the distribution of lanthanum, manganese, and titanium is mapped by La-$M_{4,5}$ ($\sim$ 849 eV), Mn-$L_{2,3}$ ($\sim$ 640 eV), and Ti-$L_{2,3}$ ($\sim$ 462 eV) edges, corresponding to red, green, and cyan patterns, respectively. In figure 5.8(c), the profiles of La (red) and Mn (green) indicate the LMO buffer layer has both LaO-terminated atomic layers at the bottom (between LMO and STO substrate) and top interface (between LMO and PZT).

On the other hand, the EELS chemical composition maps of the NNO buffer layer are shown in figure 5.8(b). An energy-selecting window selects the Nd-$M_{4,5}$ ($\sim$ 978 eV) and Ni-$L_{2,3}$ ($\sim$ 855 eV) edges to map the distributions of neodymium (red) and nickel (green). In figure 5.8(d), the NNO buffer layer has both NdO-terminated atomic layers at the bottom and top interfaces.

Both buffer layers have the interface termination of the $A$ cation (LaO or NdO) at the bottom and top interfaces. Additionally, both LMO and NNO components have the same valence, i.e. $(LaO)^{+1}/(MnO_2)^{-1}$ and $(NdO)^{+1}/(NiO_2)^{-1}$, when they are in contact with the charge-neutral interface termination of the STO substrate ( $(SrO)^0/(TiO_2)^0$) at the bottom, and also the charge-neutral interface termination of the PZT layer ( $(PbO)^0/[(Zr,Ti)O_2]^0$) at the top, causing a similar interfacial dipolar discontinuity.

It has been demonstrated the important role, and even the possibility of controlling the ferroelectric polarization by inverting the interface termination in perovskite with charged planes (within an ionic description of the charges, eg., $(LaO)^{+1}/(MnO_2)^{-1}$ termination) [131]. NNO and LMO are different materials, and the potential discontinuity is not only controlled by the interface sequences, but also work function or mean inner potential of the bulk materials. Nevertheless, interface terminations have also been demonstrated to strongly control, for instance, the work function of such perovskite when a polar surface is formed [134]. Therefore, due to the similarity in the plane sequences, it is reasonable to consider that interface termination should not have a dominant effect on the polarization direction of the ferroelectric layer.

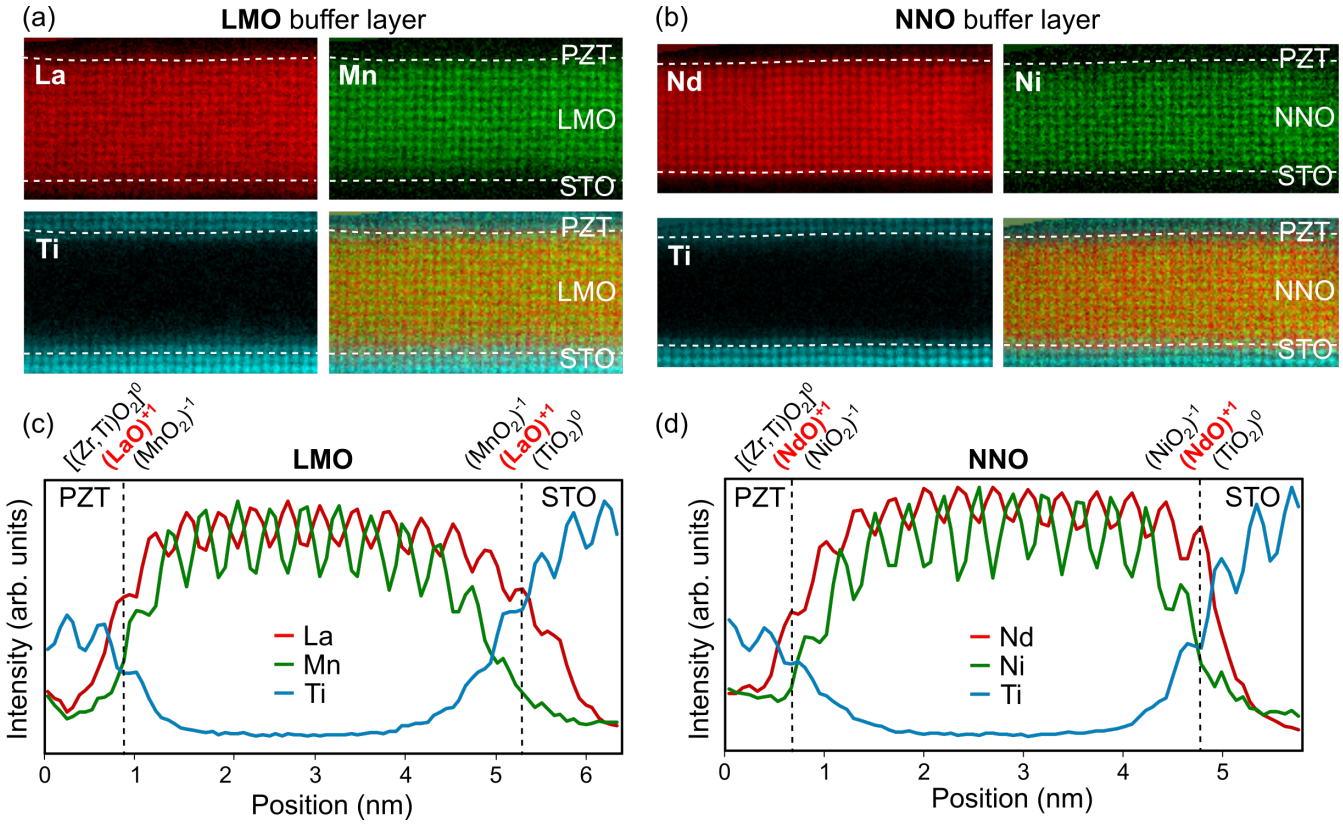


**Figure 5.8:** The EELS chemical composition maps of (**a**) the LMO buffer layer and (**b**) the NNO buffer layer. The La-$M_{4,5}$ ($\sim$ 849 eV), Mn-$L_{2,3}$ ($\sim$ 640 eV), Ti-$L_{2,3}$ ($\sim$ 462 eV), Nd-$M_{4,5}$ ($\sim$ 978 eV), and Ni-$L_{2,3}$ ($\sim$ 855 eV), edges were used for mapping the chemical compositions. (**c,d**) The intensity profiles obtained from the patterns in (a,b) illustrate chemical composition distributions at each atomic layer, with the black dashed lines representing the interfaces. Both interfaces of the LMO (NNO) buffer layer are terminated by LaO (NdO).

### 5.3.2 Crystal orientation of $LaMnO_3$ and $NdNiO_3$ buffer layers

Second, the crystal orientation of the buffer layers might be another parameter to tune the properties of the neighboring layer, such as strain relaxation. LMO thin film has been reported that the crystal orientation can be controlled by the oxygen concentration of growth, which can modify the out-of-plane lattice parameter and thus affect strain [135]. Additionally, orthorhombic thin films with *Pbnm* structure have been reported to be composed of multiple crystal domains, such as LMO [136], $YMnO_3$ [137], and $SrRuO_3$ [93]; the orthorhombic *c*-axis can lie in the in-plane, or out-of-plane directions. As a result of multiple domains, it is challenging to investigate oxygen octahedrons on these orthorhombic thin films.

The FFT images of the LMO buffer layer are displayed in figure 5.9(a,b), illustrating two possible crystal orientations of the LMO. The crystal orientation can be identified by the superstructure Bragg peaks in the FFT images (marked by red and green circles), revealing that LMO has the orientation of $[110]_o$ (figure 5.9(a)) and $[001]_o$ (figure 5.9(b)). HAADF images inserted on the right of the FFT images demonstrate that misaligned La atoms (the cyan line in the magnified HAADF image), which can be observed along the $[110]_o$ orientation. It is noticed that the La atom has an elliptical shape, observed along the $[001]_o$ orientation, owing to the overlap of two La atoms. The $[110]_o$ and $[001]_o$ orientations of the LMO indicate that the orthorhombic *c*-axis always lies in the in-plane direction (perpendicular to the growth direction). The presence of these two orientations is probably normal since the STO symmetry does not induce a preferential direction and such "texturization" will reduce the strain and its asymmetry. Additionally, a more detailed description of the orthorhombic diffraction patterns and corresponding crystal structures in real space are given in appendix B.

For the other sample, the NNO buffer layer shows a unique orientation of $[110]_o$ in figure 5.9(c); however, it rotated 90° compared to the LMO$[110]_o$ orientation (figure 5.9(a)), indicating the orthorhombic *c*-axis lies in the out-of-plane direction (parallel to the growth direction).

It has been found that the interfacial oxygen octahedral coupling has the capability to switch the growth orientation in orthorhombic structures [136]. For instance, the LMO thin film has rotated $MnO_6$ octahedra with an Mn-O-Mn angle of 155° (observed the bulk LMO along $[010]_o$) [136], when the rotating $MnO_6$ octahedron of the LMO layer is coupled with a nonrotating $TiO_6$ octahedron of the STO substrate, the octahedral rotation of the LMO is slightly suppressed, inducing the orthorhombic *c*-axis to lie in-plane direction. On the other hand, for the NNO buffer layer, the tensile strain can restrict the orthorhombic *c*-axis to grow only along the out-of-plane direction [138].

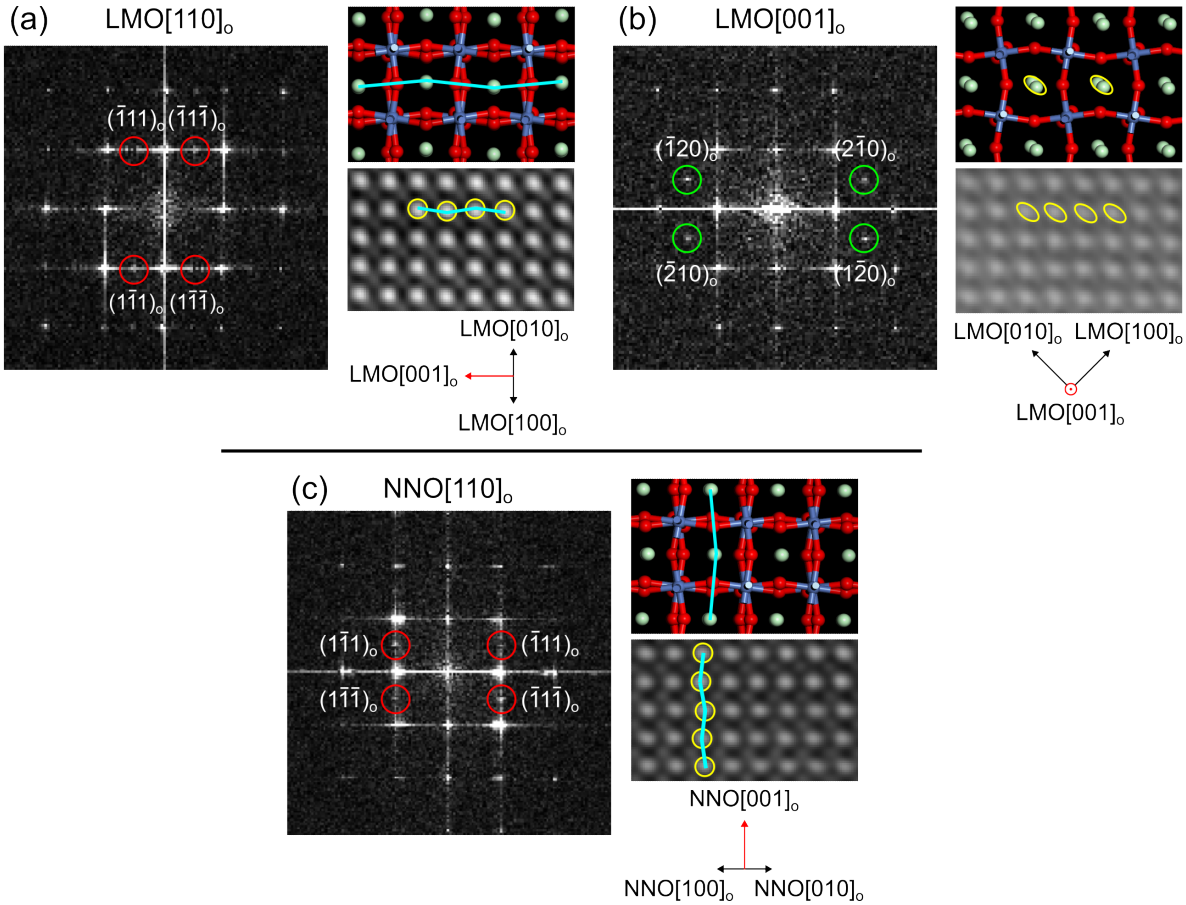


**Figure 5.9:** The possible crystal orientations of (**a,b**) LMO buffer layer and (**c**) NNO buffer layer, with the corresponding crystal structure models and magnified HAADF images. The LMO shows the (**a**) $[110]_o$ and (**b**) $[001]_o$ orientations which can be identified by the superstructure Bragg peaks encircled with the red and green circles, respectively; both orientations of LMO correspond to the in-plane orthorhombic *c*-axis. The yellow circles in HAADF images represent *A*-site atoms, and the cyan lines highlight their zigzag behaviors. (**c**) The NNO shows a unique orientation of $[110]_o$, while its orthorhombic *c*-axis lies in the out-of-plane direction.

In summary, the buffer layers are responsible for tuning the neighboring ferroelectric layers. The LMO favors a polarization pointing up, and the NNO favors a polarization pointing down. We will see in part II of this chapter that PZT of different thicknesses grown on NNO also favors downward polarization. This difference in PZT polarization is accompanied by a different mechanism for strain relaxation (through dislocation or ferroelectric $a/c$ domain). We then examined that the interface terminations of both buffer layers are similar (i.e., $[(Zr,Ti)O_2]^0/(AO)^{+1}$, with "*A*" being La or Nd), with comparable inter-diffusion, and might not be the prime origin of the difference. Additionally, the EELS measurements at the Mn-*L* and Ni-*L* edges at the interfaces do not evidence obvious chemical shift differences, which are not presented here. The most evident difference is in the buffer layer crystal orientations. Both buffer layers have octahedra rotation (formally, their space group of bulks are *Pbnm*), and the oxygen network will couple differently to the PZT, resulting in different polarizations.

## 5.4 Inhomogeneity of $NdNiO_3$ capping layer

The difference in the PZT ferroelectric polarization affected by the buffer layer gives the opportunity for an extended investigation into nickelate. One can grow a NNO layer on the PZT layer, having an as-grown stable interface with upward and downward polarizations, and the different ferroelectric polarizations could have an impact on the NNO capping layer. Our initial objective of the structural investigation by STEM of the NNO layers was to relate the different PZT polarization with the Ni-O-Ni angle in the nickelate, an essential structural parameter that controls the MIT and the magnetism.

Here, we explore the NNO capping layers of both samples through a combination of the atomic-resolved HAADF and ABF images, and of energy-filtered STEM-EELS maps. The NNO capping layer of the LMO-buffered PZT sample is presented in figure 5.10. First, a HAADF image (observed along $[110]_c$ direction) in figure 5.10(a) illustrates structural disorder in the NNO capping layer. For instance, it is possible to observe zigzag-type Nd atomic columns in the region enclosed by the green box on the left in figure 5.10(a), and the aligned Nd atomic columns enclosed by the other green box. At least two different crystal orientations are observed in this NNO capping layer, and then these two regions with different orientations are extracted to figure 5.10(b-e) and (f-i), respectively. The HAADF images (figure 5.10(b,f)) and ABF images (figure 5.10(c,g)) of these two regions are displayed. Since only the ABF image reveals the signals of oxygen atoms, HAADF and ABF images can be combined and reconstructed as a colored image to highlight the oxygen atoms, which are displayed in orange in figure 5.10(d,h). Additionally, the first 5-6 uc of the NNO capping layers exhibit well-developed crystal structures (defect-free NNO), and the crystal structure of this region will be discussed further below.

The magnified reconstructed colored images of the defect-free region of the NNO capping layers are shown in 5.10(e,i). The first crystal structure (figure 5.10(e)) reveals the Nd exhibiting zigzag off-aligned atomic columns and the oxygens are ellipse-shaped. Through this crystal structure and the superstructure Bragg peaks marked in the FFT image; as a result, this crystal structure corresponds to the NNO$[100]_o$ orientation. The observations are perfectly in agreement with the NNO$[100]_o$ crystal structure model. On the other hand, the second crystal structure (figure 5.10(i)) reveals that oxygen has zigzag off-aligned atomic columns and nearly aligned Nd atomic columns, indicating the NNO$[010]_o$ orientation. The orthorhombic diffraction patterns and corresponding crystal structure models are described in detail in appendix B. It is noted that the orthorhombic *c*-axis of these two orientations always lie in the out-of-plane direction, similar to NNO buffer layers (figure 5.9(c)).

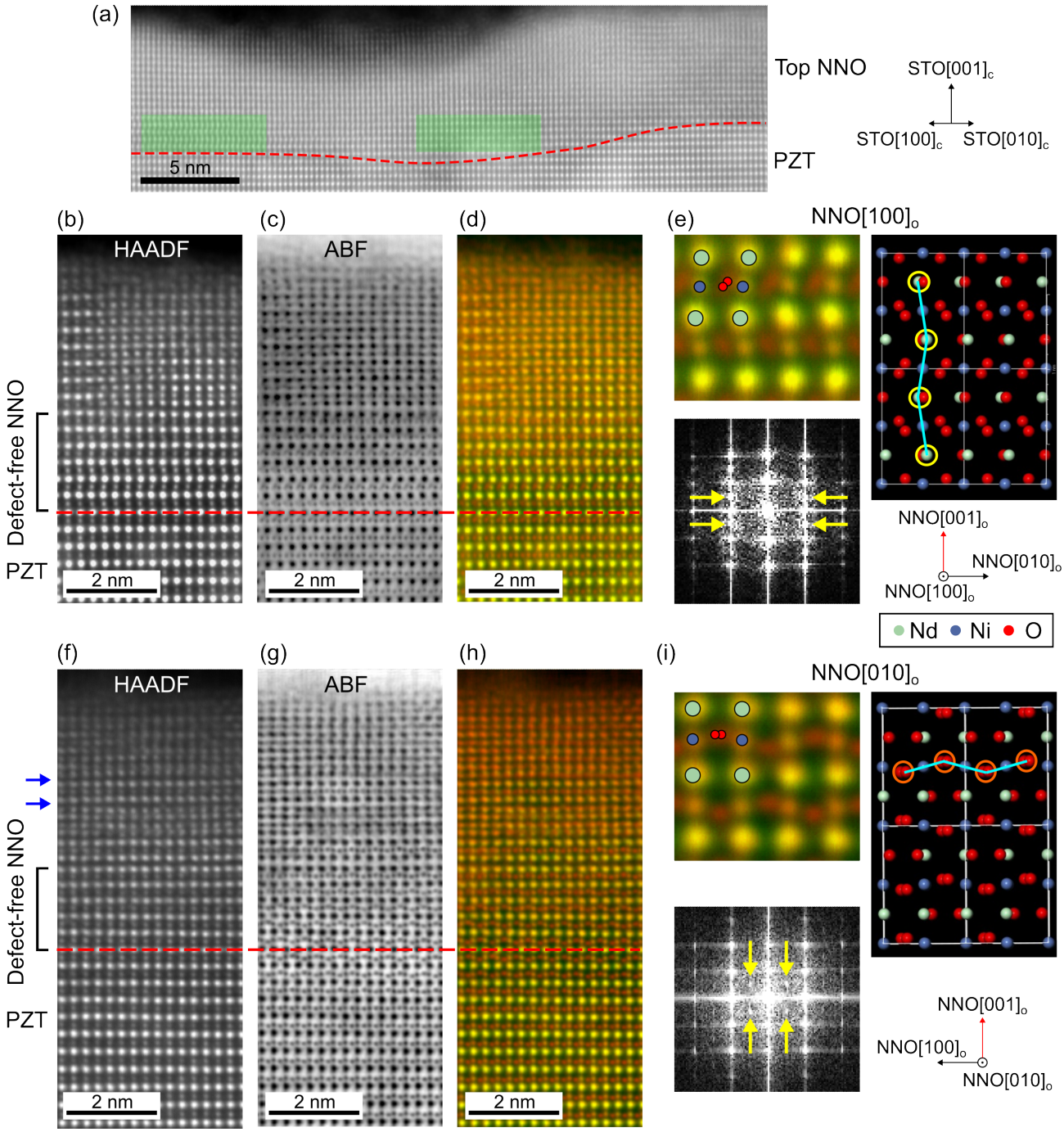


**Figure 5.10:** (**a**) The NNO capping layer of the LMO-buffered sample, observed along $STO[110]_c$ axis. The defect-free areas on the lower part of the NNO capping layers exhibit two distinct crystal orientations, which are marked by green boxes, and are extracted and shown in (**b-e**) and (**f-i**), respectively. (**b,f**) HAADF and (**c,g**) ABF images are combined to highlight the oxygen atoms in orange in (**d,h**). (**e,i**) The magnified reconstructed colored images of the defect-free region of the NNO capping layer, and the FFT images and corresponding crystal structure models. The structure in (e) reveals Nd with zigzag off-aligned atomic columns, and oxygen exhibits ellipse-shaped, indicating the $NNO[100]_o$ orientation. The yellow arrows indicate Bragg's superstructure peaks, and the cyan line highlights the zigzag behavior of Nd. Moreover, the other structure in (i) shows zigzag off-aligned oxygen columns coupled with nearly aligned Nd atomic columns, indicating the $NNO[010]_o$ orientation. The yellow arrows also indicate Bragg's superstructure peaks, and the cyan line highlights the zigzag behavior of O.

The NNO capping layers often exhibit well-developed perovskite structures at the first 5-6 uc for both LMO- and NNO-buffered samples, while disordered structures dominate beyond 5-6 uc of the NNO layers. It has been reported that the NNO layer often has numerous defects, such as RP fault in which the $AO$ monolayers are inserted in $ABO_3$ perovskite ($AO[ABO_3]_n$, where $n$ = 1, 2, or 3), and the defect can affect the crystal structure and physical properties [139]. Additionally, the first few unit cells exhibit defect-free NNO that might relate to the lattice strain [111, 140].

However, the NNO capping layers display more complex disorder structures, not only RP faults. For instance, the regions where two neodymium layers are present without a nickel layer in between (marked by blue arrows in figure 5.10(f)) seem to correspond to the crystal structure of $Nd_2NiO_4$. Consequently, the upper part of the NNO capping layer might mix various crystal structures of different components, such as $Nd_2NiO_4$ or NiO [113], rather than unique NNO. These disordered structures located above the defect-free layer are difficult to identify and cannot be explored further. In the subsequent step, STEM-EELS is used to examine defects in the NNO capping layers.

Using the energy-filter STEM-EELS map, we can reveal the chemical composition of the NNO capping layer. Figure 5.11(a) is an EELS spectrum extracted from the NNO capping layer and a portion of the PZT layer, showing Ti-$L_{2,3}$ (456-462 eV), O-$K$ ($\sim$ 532 eV), Ni-$L_{2,3}$ (855-872 eV), and Nd-$M_{4,5}$ (978-1000 eV) edges, which are used to extract the chemical composition maps below. The HAADF images and energy-filter STEM-EELS maps of the NNO capping layers of the LMO-buffered and NNO-buffered samples are shown in figures 5.11(b-f) and (g-k), respectively. The images from top to bottom represent the HAADF image, the chemical composition map of Nd (red), Ni (green), Ti (cyan), and the mixed map of these three chemical compositions. As a result, both NNO capping layers exhibit chemical inhomogeneity as a patchwork pattern, consisting of the nickel-rich regions (marked by the white arrows in figure 5.11(f,k)).

Despite the failure to achieve a defect-free NNO capping layer for both LMO- and NNO-buffered samples, we have investigated the NNO capping layer by atomic-resolved HAADF and ABF images, revealing that the first 5-6 uc of NNO have obvious either $[100]_o$ and $[010]_o$ orientation with the out-of-plane orthorhombic $c$-axis. As a result of the multi-orientation of the NNO layer, it is challenging to achieve quantitative measurements of oxygen octahedral and give a clear picture of the coupling between oxygen octahedral and the upward/downward ferroelectric polarization. In the similar multi-orientation LMO buffer layer, it was also not possible to quantify the Mn-O-Mn angle and draw a conclusion on the neighboring PZT having an upward polarization.

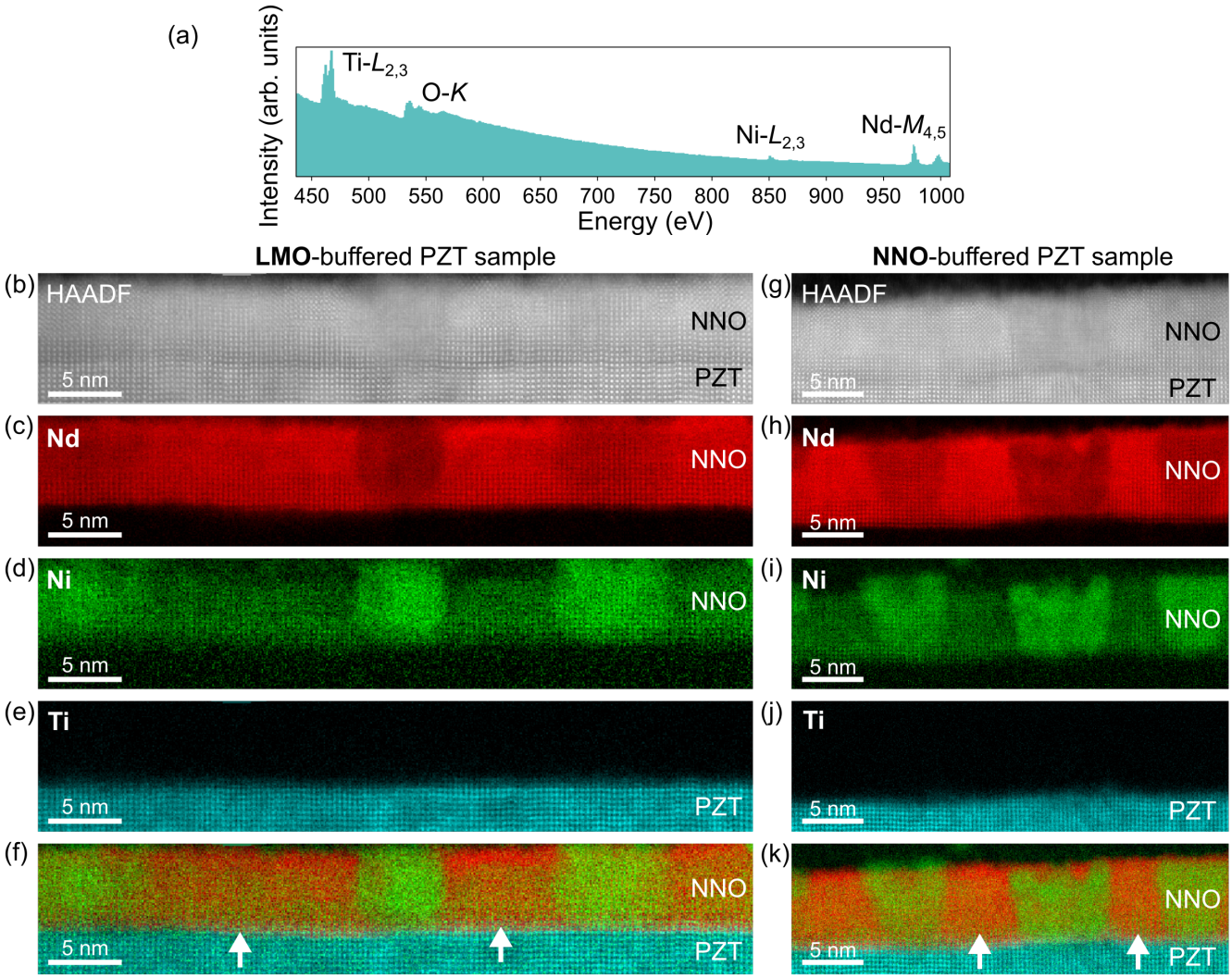


**Figure 5.11:** (**a**) The EELS spectrum of the NNO capping layer shows the Ti-$L_{2,3}$, O-$K$, Ni-$L_{2,3}$, and Nd-$M_{4,5}$ edges. The HAADF images and corresponding EELS chemical composition maps of the LMO-buffered and NNO-buffered samples are shown in (**b-f**) and (**g-k**), respectively. The images from top to bottom represent the HAADF images, the EELS maps of Nd (red), Ni (green), Ti (cyan), and the mixed maps of these three chemical compositions.

Due to the presence of numerous defects in the NNO capping layer, which is absent in the buffer NNO layer, the next part of this chapter will discuss the case of NNO thin film as buffer later on the STO substrate, modulated by varying the thickness of the PZT ferroelectric capping layer, and without additional NNO capping layer.

# PART II

## 5.5 Modulation of nickelate properties with varying ferroelectric film thickness

### 5.5.1 PFM and X-ray analyses of $Pb(Zr,Ti)O_3/NdNiO_3$ heterostructure

Following the understanding that properties of the ferroelectric layer can significantly be modulated through different buffer layers, and strain relaxation and crystal structure of the buffer layer play a crucial role, it would be interesting to investigate how the nickelate properties would respond when the ferroelectric layer is capped as a function of thickness. With increasing the ferroelectric thickness, the polarization can be modulated by strain-induced flexoelectric field, crystal structure, and oxygen octahedral distortion [9]. Here, we continue with a similar design of PZT heterostructures with the NNO buffer layer of 7 nm grown on the STO substrate, and the PZT thickness is from 30 nm, 13 nm, to 6 nm. However, these structures are not capped with the NNO layer due to the NNO capping layer is challenging to control its property.

Figure 5.12(a-c) shows the topography and PFM phase images of samples with PZT thicknesses of 30 nm, 13 nm, and 6 nm, respectively. Through the PFM phase images, the thickest PZT sample (30 nm) has mainly downward polarization, which is consistent with the sample discussed in PART I. On the other hand, the thinnest PZT sample (6 nm) might have a mixture of downward and upward polarizations. These samples exhibit evolution from monodomain to multidomain with decreasing thickness.

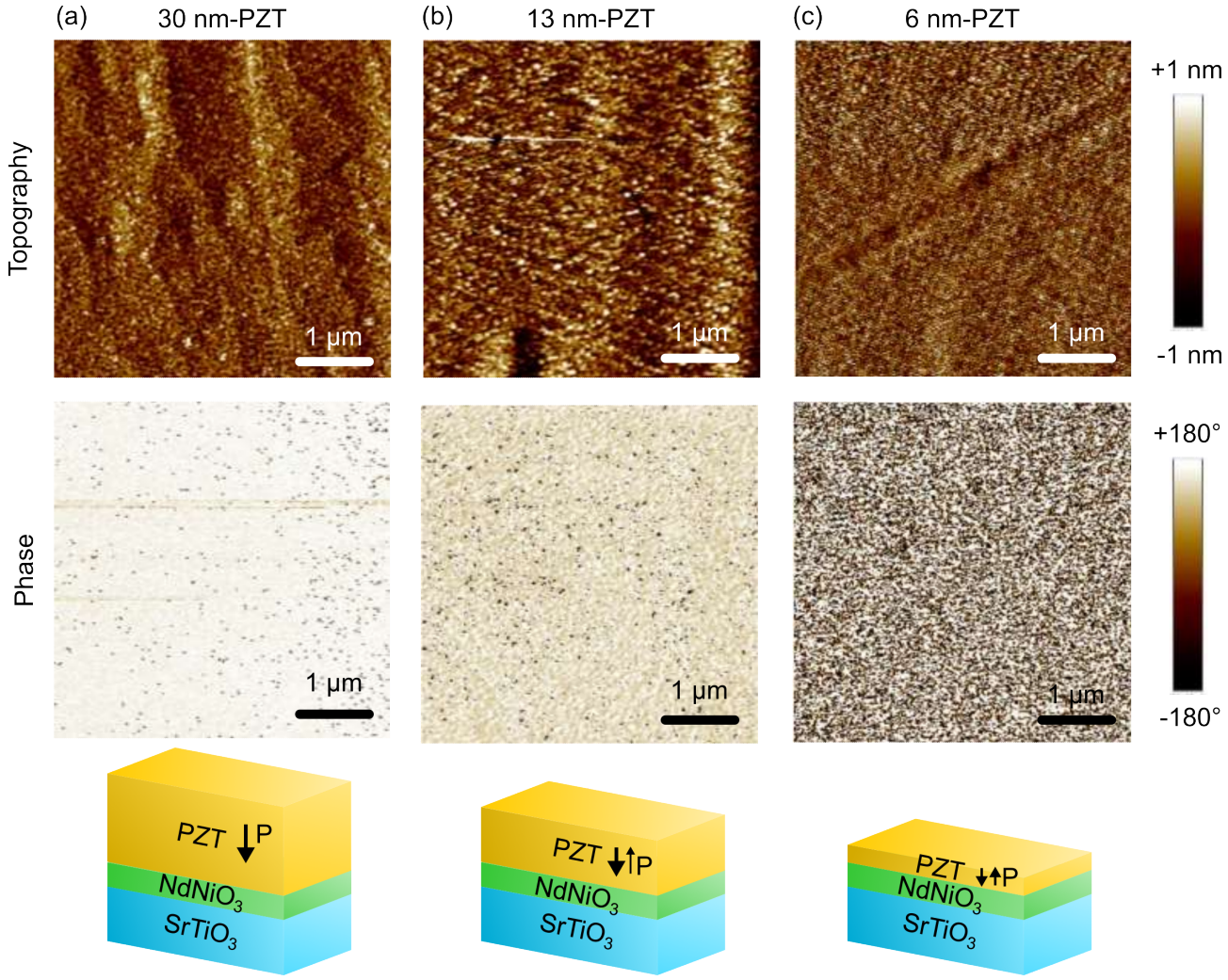


**Figure 5.12:** Topography and PFM phase images of the thin film heterostructures, which are composed of PZT layers with 8 nm NNO buffer layer grown on a STO substrate. After switching a negative (-2 V) and positive (+2 V) tip bias, the ferroelectric domain structure in the PZT layer with a thickness of (**a**) 30 nm, (**b**) 13 nm and (**c**) 6 nm is converted from monodomain to multidomain. This figure is reproduced courtesy of D. Preziosi at IPCMS, University of Strasbourg.

The XRD measurements in figure 5.13 are used to identify the differences in lattice parameters between these samples. Firstly, as the PZT thickness decreases from 30 nm to 6 nm (from figure 5.13(a) to figure 5.13(c)), the *c*-axis (out-of-plane) lattice parameter of the PZT increases, indicating that the PZT layer becomes more strained. Secondly, the PZT peaks condense along the *a*-axis (in-plane) direction, expecting the disappearance of the ferroelectric *a*-domain in the lower thickness sample.

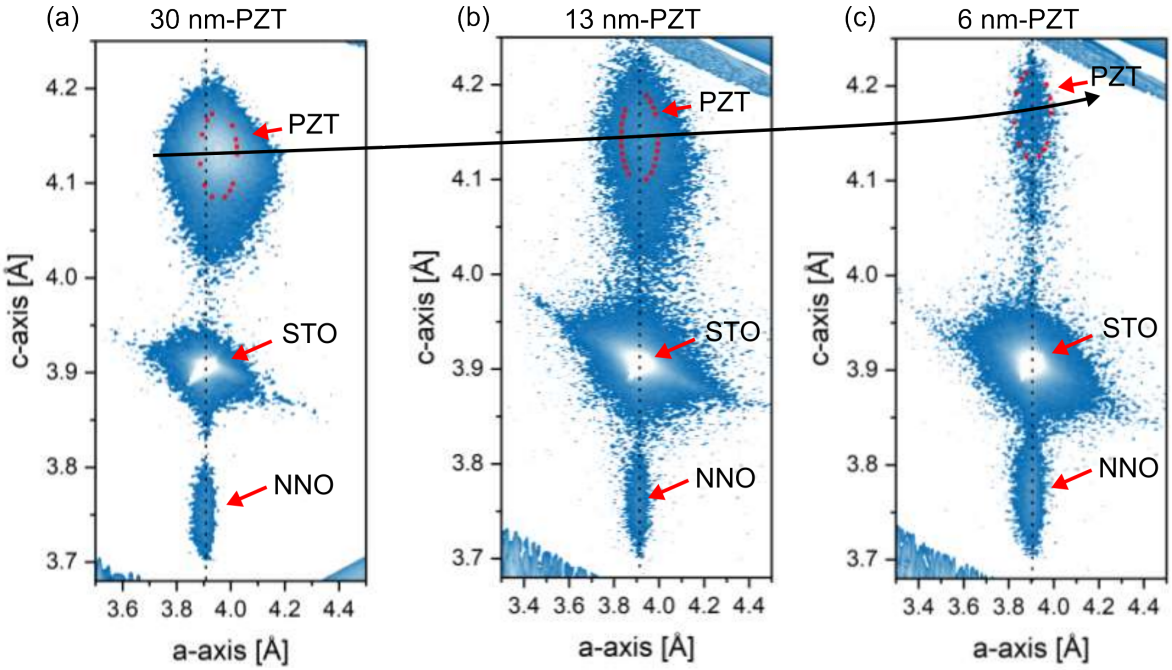


**Figure 5.13:** XRD reciprocal-space maps (RSM) of (**a**) 30 nm-PZT, (**b**) 13 nm-PZT, and (**c**) 6 nm-PZT samples. The peaks of PZT are marked by red-dashed circles. This figure is reproduced courtesy of D. Preziosi at IPCMS, University of Strasbourg.

In figure 5.14(a), the XAS measurements of the samples with PZT thickness of 6 nm (green), 13 nm (black), and 30 nm (red) reveal their electronic properties at low temperature (20 K). As the thickness increases, the expanded/compressed ($E/C$) octahedral intensity ratio decreases, indicating more compressed $NiO_6$ octahedra. The energy separation of the $E$ and $C$ peaks and their intensity ratio are compared in figure 5.14(b). There can be divided into two regions according to the PZT thickness; the thinner sample has stronger breathing distortion (larger $C$-$E$ energy separation and $E/C$ ratio) than the thicker sample, indicating an enhancement of bond disproportionation.

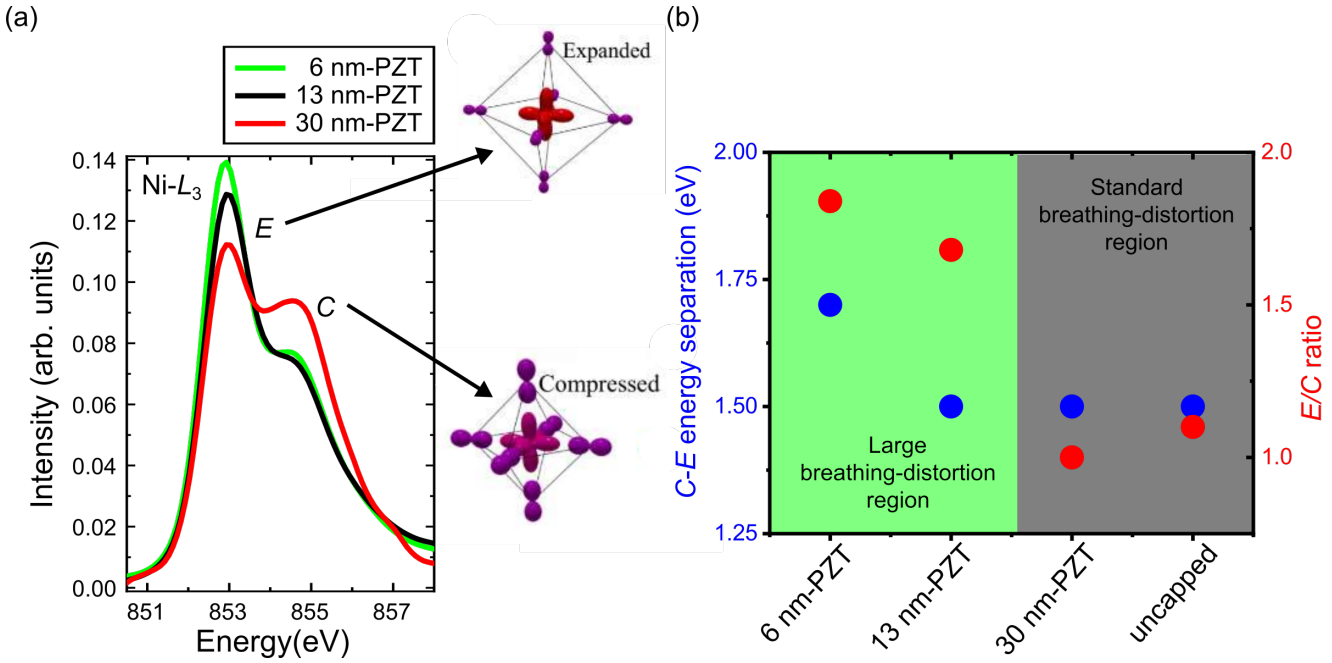


**Figure 5.14:** (**a**) Ni-$L_3$ edge of isoXAS spectra measured at low temperature (20 K) of the samples of 6 nm-PZT (green), 13 nm-PZT (black), and 30 nm-PZT (red) samples. The *E* and *C* peaks represent expanded and compressed octahedra in the distorted phase. (**b**) A comparison of these three samples and the uncapped NNO sample as a function of *C*-*E* energy separation and *E*/*C* ratio. This figure is reproduced courtesy of D. Preziosi at IPCMS, University of Strasbourg.

Following analyzing this series of samples using PFM, XRD, and XAS performed by our collaborators at the University of Strasbourg, these measurements indicated that the different thicknesses of PZT layers can affect the whole heterostructure in both structural and electronic properties.

### 5.5.2 Structural disorder

Using STEM-EELS, we examined two of these samples, the thickest (30 nm PZT) and the thinnest (6 nm PZT) in more detail. It is noted that we observed these two samples along different projection axes. The 30 nm-PZT sample is observed along STO$[100]_c$ axis, and it shows pseudo-cubic unit cells; the 6 nm-PZT sample is observed along STO$[110]_c$ axis, and it shows orthorhombic unit cells. The pseudo-cubic and orthorhombic unit cells can be referenced as figure B.1 top and bottom row, respectively.

Firstly, we observe these two samples through atomic-resolved HAADF images in figure 5.15. For the 30 nm-PZT sample (figure 5.15(a,b)), we observe RP faults in the NNO buffer layer as well as dislocations at the interface of PZT and NNO layer, as shown in figure 5.16, which magnifies the region with RP fault in figure 5.15(b). Misfit dislocations are mixed in the RP fault. As a result of the presence of both dislocations and the RP fault, it is believed that this sample is mostly relaxed. Additionally, the PZT layer exhibits downward polarization as expected.

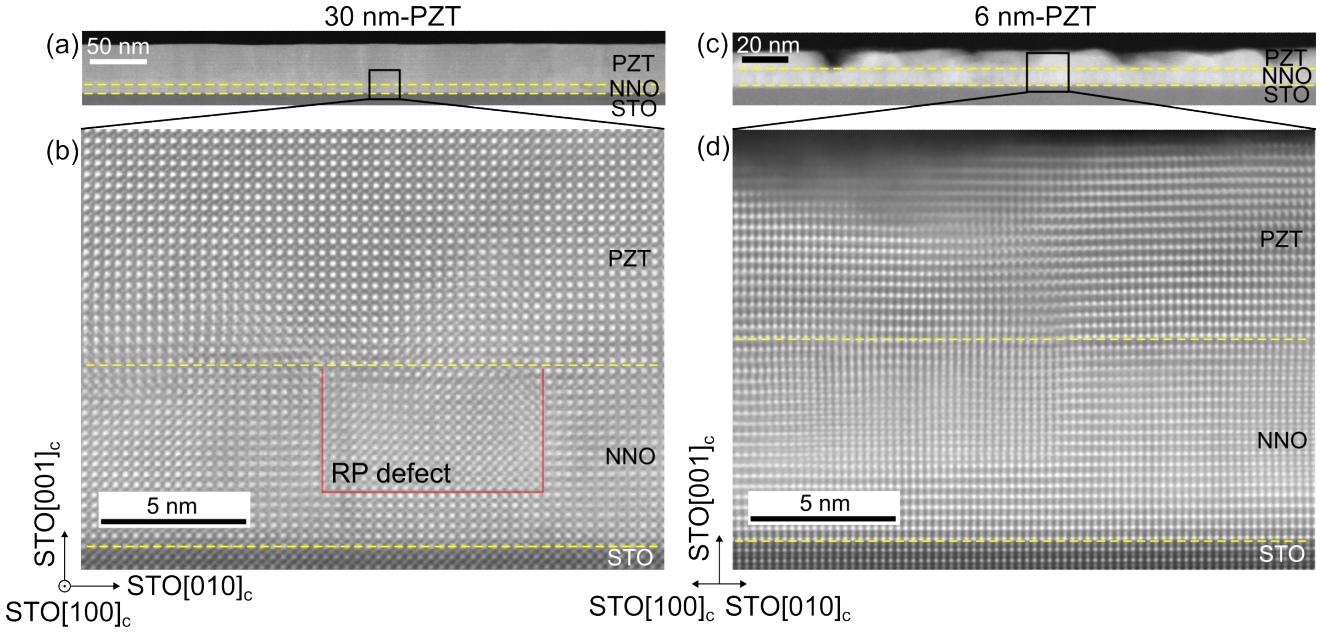


**Figure 5.15:** HAADF images of the (**a,b**) 30 nm-PZT and (**c,d**) 6 nm-PZT samples, observing along STO$[100]_c$ and STO$[110]_c$ axis, respectively.

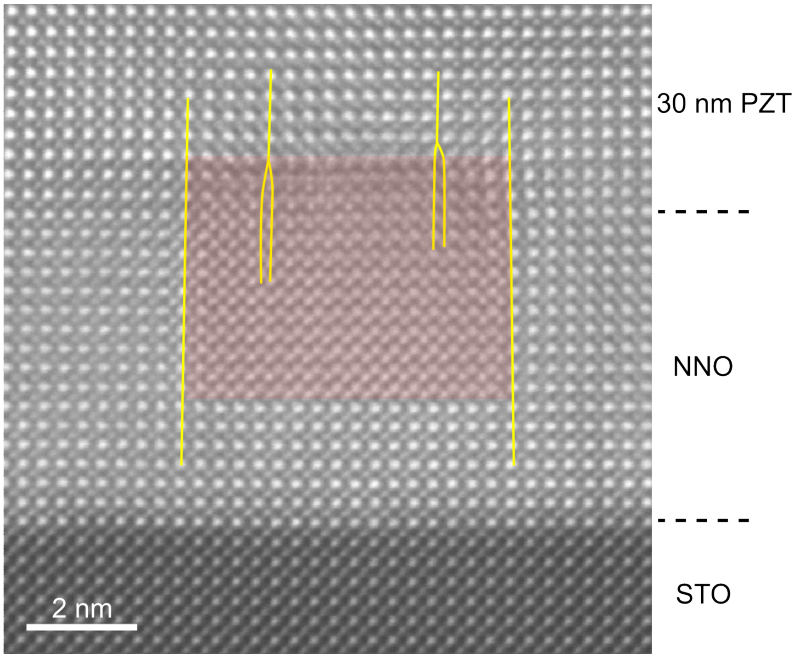


**Figure 5.16:** An RP fault (marked in red) in the buffer NNO layer of the 30 nm-PZT sample, magnifying the region marked by the red box in 5.15(b). This RP fault is accompanied by misfit dislocations at the interface between the NNO and PZT layers.

For the 6 nm-PZT sample (figure 5.15(c,d)), observing its low-magnification HAADF image (figure 5.15(c)), the PZT layer is incomplete and shows an island-like distribution with massive structural distortions. The PZT thin film has been reported to have island growth (Stranski-Krastanov growth) on the MgO substrate [141]. In the early stages of crystal growth, misfit strains could lead to changes in interface structural stability, and cause structural distortions in an ultrathin film. Additionally, the NNO layer seems to have RP faults as well, similar to the NNO buffer layer of the 30 nm-PZT sample.

By examining both NNO buffer layers in more detail in figure 5.15(b,d), the first $\sim$ 5 uc of the NNO layer usually shows a well-developed crystal structure, which has been presented in the NNO capping layer in figure 5.10 and defined its crystal orientations; above $\sim$ 5 uc NNO, some disordered structures appear, such as RP faults (highlighted with the red box in figure 5.10(b)).

Compared with the NNO buffer layer in PART I (the sample of the PZT layer sandwiched by the NNO layers), the NNO buffer layers of 30 nm-PZT and 6 nm-PZT samples (figure 5.15) exhibit more RP defects. There is the possibility that the RP fault can be helpful in relaxing the lattice misfit strain [111]. J. Bak reported that the $LaNiO_3$ thin film (lattice parameter of 3.838 Å) grown on different substrates, which has an intense compressive strain (on $LaAlO_3$ substrate with a 3.791 Å lattice parameter) or slight tensile strain (on STO substrate with a 3.905 Å lattice parameter), demonstrate different strain relaxations. The $LaNiO_3$ with a compressive strain needs both the dislocations and RP faults to relax it; in contrast, the $LaNiO_3$ with tensile strain is observed only with the RP faults. This

investigation indicates that strain can be relaxed by creating RP faults, without the association of dislocations. It is believed that numerous RP faults in our NNO layer contribute to strain relaxation.

### 5.5.3 Strain relaxation caused by different film thicknesses

Subsequently, the GPA analysis of the 30 nm-PZT (figure 5.17(a)) and 6 nm-PZT (figure 5.17(b)) samples indicates that both NNO layers of these samples display complex strain distributions accompanied by strong structural distortions, as we observed in the atomic-resolved HAADF images in figure 5.15(b,d).

For the 30 nm-PZT sample, the PZT layer exhibits homogenous out-of-plane ($\sim 5.5\%$) and in-plane ($\sim 1.2\%$) strains with respect to the STO substrate. The lattice parameters of the PZT layer can be estimated as the out-of-plane lattice parameter of $\sim 3.095 \times 1.055 = 4.120$ Å, and the in-plane lattice parameter of $\sim 3.905 \times 1.012 = 3.952$ Å, indicating the PZT is perfectly relaxed (out-of-plane lattice parameter of 4.150 Å and in-plane lattice parameter of 3.950 Å for bulk PZT).

For the 6 nm-PZT sample, the PZT layer might be relaxed by the island-like structure; however, as a result of the severe structural distortions in the PZT layer, its strain maps are difficult to interpret.

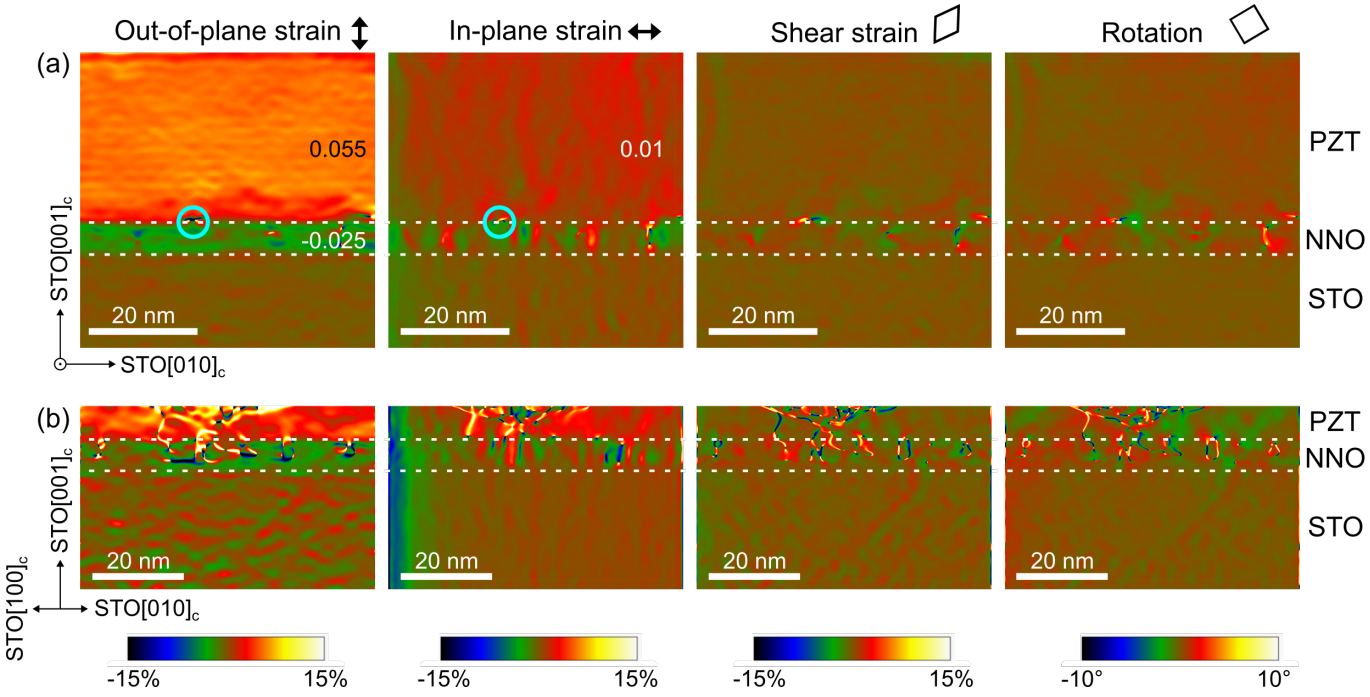


**Figure 5.17:** Strain maps for the (**a**) 30 nm-PZT and (**b**) 6 nm-PZT samples. The patterns from left to right correspond to the out-of-plane strain, in-plane strain, shear strain, and rotation, respectively. All strain maps are at the same color intensity scale from -15% to 15%, while the rotation map is from -10° to 10° (anticlockwise positive). For the 30 nm-PZT samples the dislocations are located at the interface between the NNO and PZT layers, where the regions are marked by cyan circles.

### 5.5.4 Crystal orientation of $NdNiO_3$ buffer layer

Finally, we use FFT analysis to identify the crystal orientations of these NNO layers. Figure 5.18(a) shows the HAADF image of the 30 nm-PZT sample observed along STO$[100]_c$, and its FFT image is shown in figure 5.18(b), whose superstructure Bragg peaks (marked by green arrows) indicate NNO$[110]_o$ orientation. By selecting these superstructure Bragg peaks in the FFT image, the FFT-filtered pattern in figure 5.18(c) reveals the spatial distribution of NNO$[110]_o$ orientation. The NNO layer is primarily composed of NNO$[110]_o$ orientation with the out-of-plane orthorhombic *c*-axis.

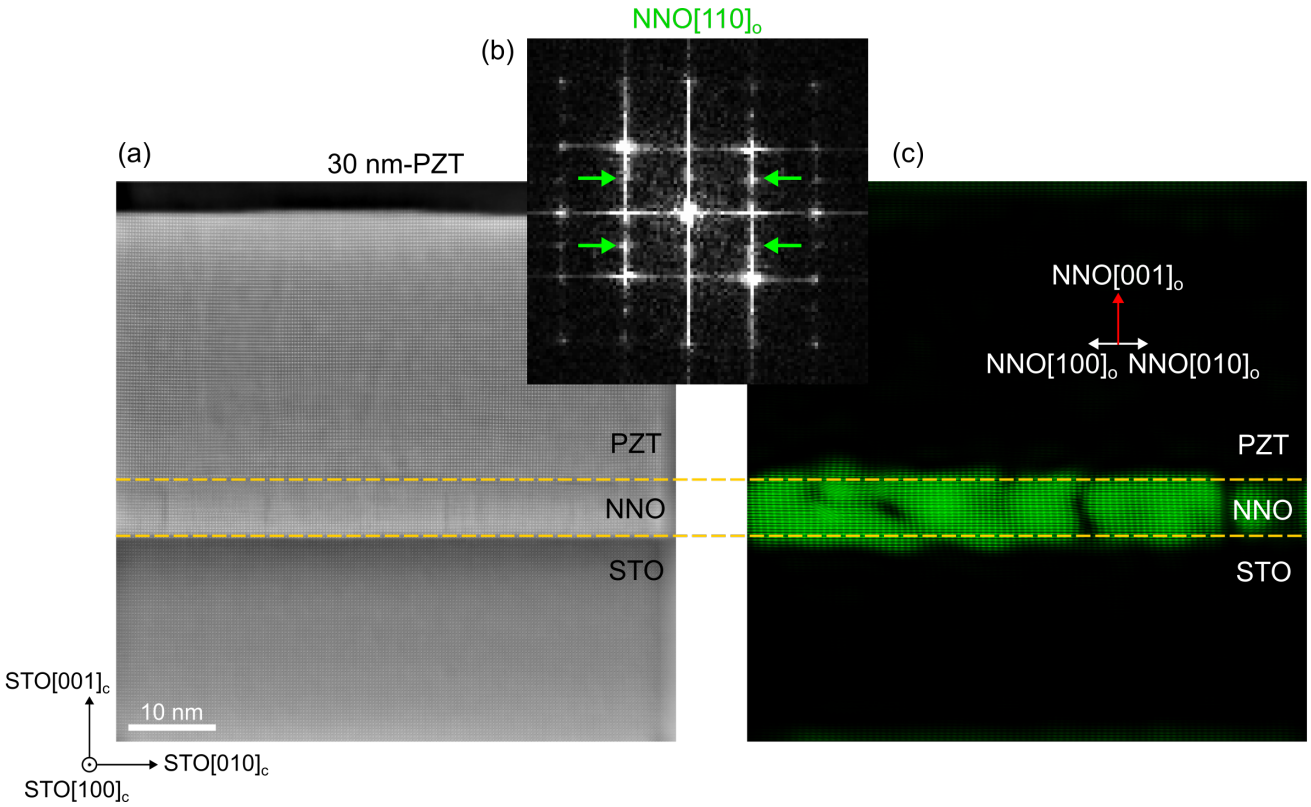


**Figure 5.18:** (**a**) HAADF image of the 30 nm-PZT sample, observed along STO$[100]_c$. (**b**) The FFT image of the NNO layer. The superstructure spots (marked by green arrows) indicate the orientation of NNO$[110]_o$. (**c**) A FFT-filtered pattern, which is filtered through the superstructure spots in (b), indicates the NNO layer is dominated by NNO$[110]_o$ orientation.

With regard to the 6 nm-PZT sample, figure 5.19(a) illustrates its HAADF image, which is observed along STO$[110]_c$, and the FFT image of the NNO layer is shown in figure 5.19(b). In the FFT image, there are multiple superstructure Bragg peaks; however, only two orientations are identifiable, the NNO$[100]_o$ marked by the red arrows and NNO$[010]_o$ marked by the green arrows. In figure 5.19(c), the FFT-filtered pattern highlights the regions with the NNO$[100]_o$ orientation in red, NNO$[010]_o$ orientation in green, and the unidentified orientation in blue. The corresponding magnified HAADF images and crystal structure models are displayed. The zigzag behavior of neodymium provides direct evidence to distinguish between the NNO$[100]_o$ (with zigzag Nd) and NNO$[010]_o$ (without zigzag Nd) orientations.

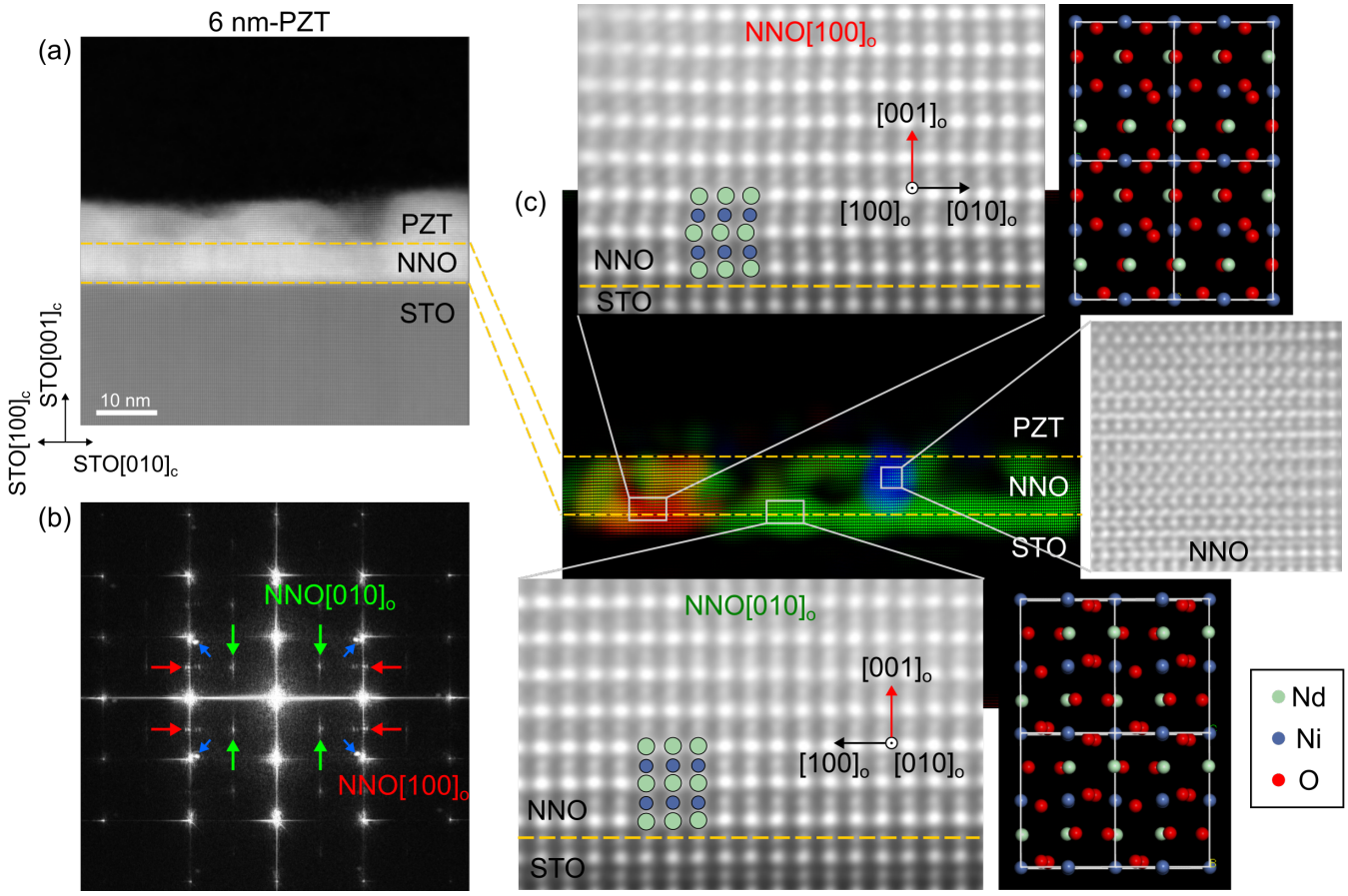


**Figure 5.19:** (**a**) HAADF image of the 6 nm-PZT sample, observed along STO$[110]_c$. (**b**) The FFT image of the NNO layer shows multiple superstructure spots, which are marked by green arrows for NNO$[010]_o$, red arrows for NNO$[010]_o$, and blue arrows for unidentified orientations. (**c**) A FFT-filtered pattern emphasizes the NNO$[100]_o$ in red, NNO$[010]_o$ in green, and the unidentified orientation in blue, alongside the respective zoomed-in HAADF images.

### 5.5.5 Behavioral characteristics of Ni-*L* edges

EELS spectrum can be used to estimate the Ni valence or reveal the fine structure of Ni-*d* orbitals (e.g., regarding $NiO_6$ octahedral distortion) in principle in comparison to the XAS results. The spectral resolution of EELS is more limited since we did not use the monochromated microscope on this series of samples. Furthermore, the NNO exhibits a metallic phase at room temperature where the EELS is done, while the XAS measurement in figure 5.14 was performed at low temperature (with a NNO transferred to an insulating phase). At room temperature, the Ni-$L_3$ peak separation is less evident, and the change of intensity ratio as well [142] and so a direct comparison between the XAS and the EELS will not hold at different temperatures.

Figure 5.20 shows the EELS spectra of Ni-$L_3$ and Ni-$L_2$ edges of the 30 nm-PZT (red) and 6 nm-PZT (green) samples. It is visible that the ratios of $L_3/L_2$ of these samples are slightly different and that the edges have different shapes. Notably, the 6 nm-PZT sample has a narrower Ni-$L_3$ edge and a smaller contribution at high energy ($\sim$ 859 eV) where a typical charge transfer configuration might sit. The peak broadness is semi-directly related to bandwidth and spectral density at $\sim$ 859 eV might be due to an increase in a charge transfer configuration, and the difference can arise from a different hybridization level (smaller hybridization for the 6 nm-PZT sample, or at least a smaller interaction between the charge transfer configuration $3d^8\underline{L}^1$ and the ionic configuration $3d^7$). While a direct comparison with XAS is not fully adequate, it is noteworthy that such a feature might be the correspondence of the XAS measurement but at room temperature before the breathing distortion happened.

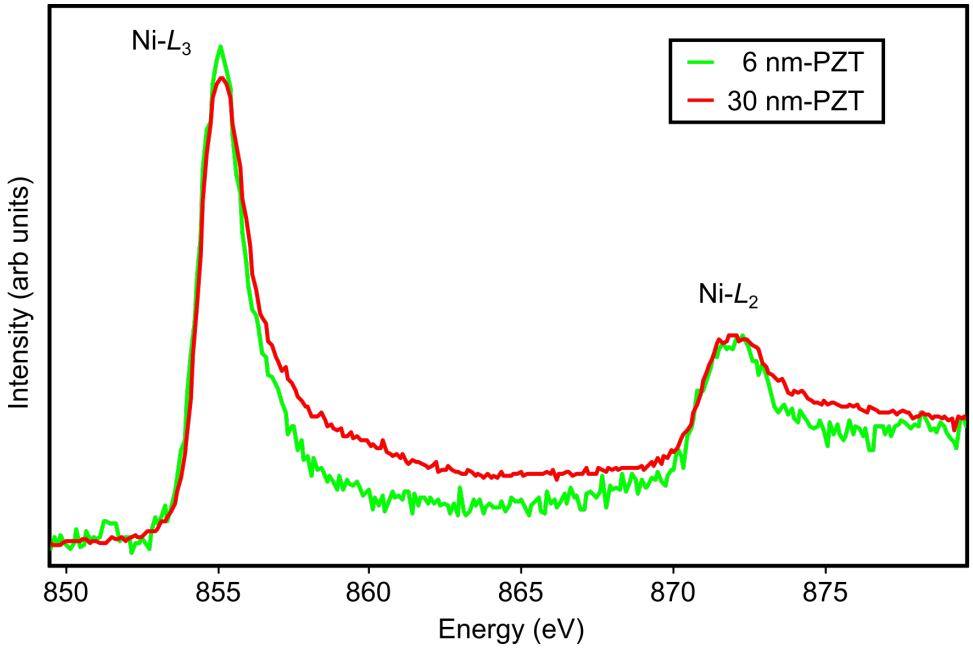


**Figure 5.20:** EELS Ni-$L_{2,3}$ edge spectra extracted from the NNO buffer layers of the 30 nm-PZT (red) and 6 nm-PZT (green) samples.

## 5.6 Summary

This chapter reports how the PZT ferroelectric polarization can interact with TMO (NNO and LMO) thin films for two series of samples. Firstly, it is reported that different buffer layers (NNO or LMO) can change the ferroelectric as-grown polarization of the PZT. The crystal orientation of the buffer layer, as well as the strain distribution within the heterostructure, are considered to be the main parameters for reversing ferroelectric polarization. Additionally, the NNO capping layers of both samples are accompanied by inhomogeneous chemical composition distributions, indicating that control of the NNO capping layer's properties has not yet been achieved using such a buffer layer method.

Second, PZT layers with varying thicknesses capped on the NNO buffer layer result in heterostructures with different structural and electronic properties. As the PZT thickness decreases, multiple crystal orientations in the NNO layer and island-grown PZT layer are observed, and the PZT layer displays more complicated strain relaxation.

The summary of the strain relaxations of these two series of samples can be found in table 5.2. The strain relaxation in the PZT layers is strongly associated with the RP faults in the nickelate and the misfit dislocations. Once the above two relaxation mechanisms do not entirely relax the strain, the ferroelectric *a*-domains probably are induced to relax the PZT layer.

| | Sample | Relaxation mechanism |
|---|---|---|
| PART I | NNO/PZT(60 nm)/LMO//STO | dislocation |
| | NNO/PZT(60 nm)/NNO//STO | dislocation + *a*-domain |
| PART II | PZT(30 nm)/NNO//STO | dislocation + RP fault |
| | PZT( 6 nm)/NNO//STO | island-grown PZT |

**Table 5.2:** An overview of the strain relaxation mechanisms results from two series of samples measured in this chapter.

To conclude, the thickness of the ferroelectric thin film and different buffer layers can be used to tune the ferroelectric layer itself and the neighboring nickelate layer regarding crystal structures, and consequently, their physical properties as a whole. The numerous defects and complex strain relaxations in the system of ferroelectric material and nickelate remain a challenge for the control of nickelate properties.

# Chapter 6

# Conclusions

Throughout this thesis, I have explored the coupling between ferroelectricity and the structural/electronic properties of TMO. The STEM-EELS technique has shown to be a powerful tool for microscopic investigation with high spatial and spectral resolution, allowing nanoscale exploration of nanostructures and thin film heterostructures.

In order to investigate the control of MIT by ferroelectricity, this thesis consists of three steps. To begin with, I investigated the plasmon properties of SVO bulk and nanostructures and indicated the possible MIT on the nanostructure. Second, I demonstrated the evolution of PTO ferroelectric domains as a function of thickness, as well as the effect of the ferroelectric domains on the SRO electrodes. Finally, I described how the buffer layers and film thickness modulate the ferroelectric polarization direction and strain relaxation, thereby affecting the NNO properties.

The spectroscopic signatures of SVO regarding plasmon excitations have been demonstrated, especially at the nanoscale. The monochromated EELS and numerical simulations confirmed the existence of intense bulk and surface plasmons. The SVO nanostructures exhibit LSP resonances, which strongly depend on geometry, and their high-quality factors indicate that SVO is promising as a TMO-based plasmonic material. Additionally, the EELS spectrum under non-dipole conditions provides efficient measurements of bulk-type plasmon excitations in the nanostructure. It predicts that MIT could occur between the shell and core areas of the nanorod, suggesting that MIT behavior can be observed at the nanoscale.

Systematic measurements have been conducted on the PTO ferroelectric thin film in contact with the SRO electrodes, demonstrating the evolution of ferroelectric domain configurations based on film thickness. Ferroelectric domains cause changes in the crystal structure on the neighboring SRO electrode, indicating that the ferroelectric field has the ability to affect the properties of nearby materials.

The polarization configurations of the PZT ferroelectric layers have shown strong correlations with the buffer layers and the film thickness, and the PZT layer exhibits a complex combination of ferroelectric and interfacial effects, which affect the strain relaxation mechanism and flexoelectricity. Additionally, NNO buffer and capping layers rarely display defect-free regions and then cause different strain relaxations and crystal orientations. As a result of the difficulty of growing the NNO layer and quantitative measurements of oxygen octahedra, there is still an open question regarding the role of ferroelectric proximity effects.

This thesis provides a few examples of the interfacial coupling between ferroelectric materials and TMO thin films by STEM-EELS techniques, revealing the controllable MIT properties of TMO thin film heterostructures by ferroelectric effects.

# Appendix A

# Searching for alternative plasmonic materials

Plasmonics has been dominated by noble metals for a long time, due to the fact that their real parts of permittivity have strong negative values, allowing them to exhibit excellent plasmons. Their imaginary permittivities, however, are high in visible and near-infrared wavelengths. As a result, they suffer from high losses in these ranges, which are caused by interband (an electron jumps from an occupied valence band to the next unoccupied conduction band) and intraband (electron transfers within the valence or conduction band) transitions. Noble metals are limited by their plasmon frequencies lying in the ultraviolet range and their loss issues. Illustrations of potential plasmonic materials are shown in figure A.1.

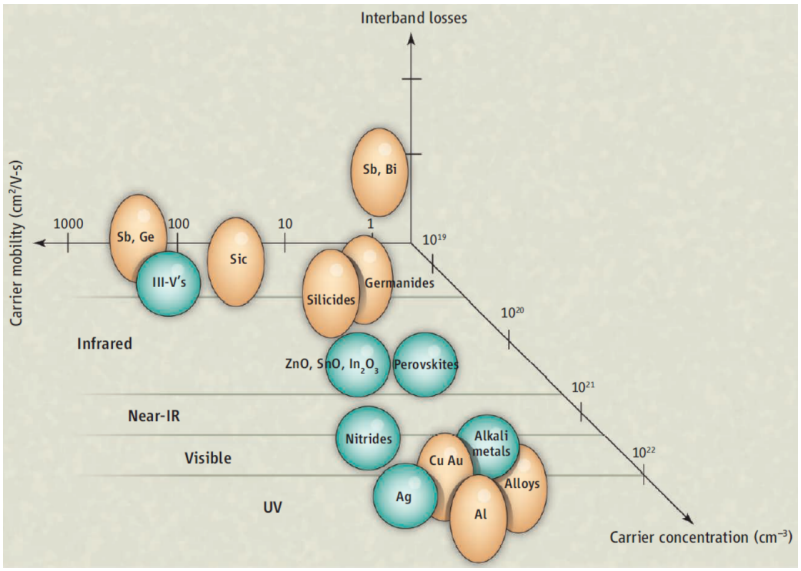


**Figure A.1:** Material space of potential plasmonic materials with carrier concentration, carrier mobility, and interband losses. The spherical (elliptical) bubbles represent material with lower (higher) interband loss. Reproduced from ref. [75].

First, we search for alternative plasmonic materials within metals. For example, alkali metals have lower loss issues than gold and silver, but extreme reactivity in ambient conditions restricts their fabrication. Copper, the second-best conductor among metals, has the potential to replace conventional materials, although it is challenging to fabricate electronic devices and overcome the problem of oxidation. The application of aluminum is more effective in the ultraviolet range than that of gold or silver; however, there are strong interband transitions in the visible range, and oxidation is another potential problem. The optical properties of a majority of the elements in the periodic table have been summarized by Blaber *et al.* [143].

Transparent conducting oxides (TCOs), such as Al-doped ZnO (AZO), Ga-doped ZnO (GZO), and Sn-doped $In_2O_3$ (ITO), can be candidates [144]. TCOs have a large bandgap, allowing them to be transparent in the visible range. Due to the high doping, they exhibit metal-like properties with high carrier concentration ($n > 10^{20}$ $cm^{-3}$), which results in the plasmon frequency lying in the near-infrared range. Their plasmon frequencies and properties are tunable by adjusting the doping level. A demonstration of plasmonic excitations has been made on thin films as well as nanostructures of TCOs [79].

The heavily-doped semiconductors (doping densities up to $10^{20}$ $cm^{-3}$) achieve a quasi-metallic behavior and a negative real permittivity in the infrared range [145, 146, 147]. A wide bandgap ($> 1.5$ eV) implies low interband losses. It is however a challenge to achieve such high doping within the solubility limit of the dopants.

Transition metal nitrides (TMNs) like TiN and ZrN show plasmonic properties in the visible range [144, 148]. Their optical properties are strongly related to deposition conditions because of their non-stoichiometric properties. These materials are chemically stable, hard, and refractory; moreover, they can be grown epitaxially in ultrathin films and ultrasmooth on varying substrates. With the advantages of fabrication, they could be helpful in plasmonic nanoelectronics [149].

# Appendix B

# Orthorhombic orientations and corresponding diffraction patterns

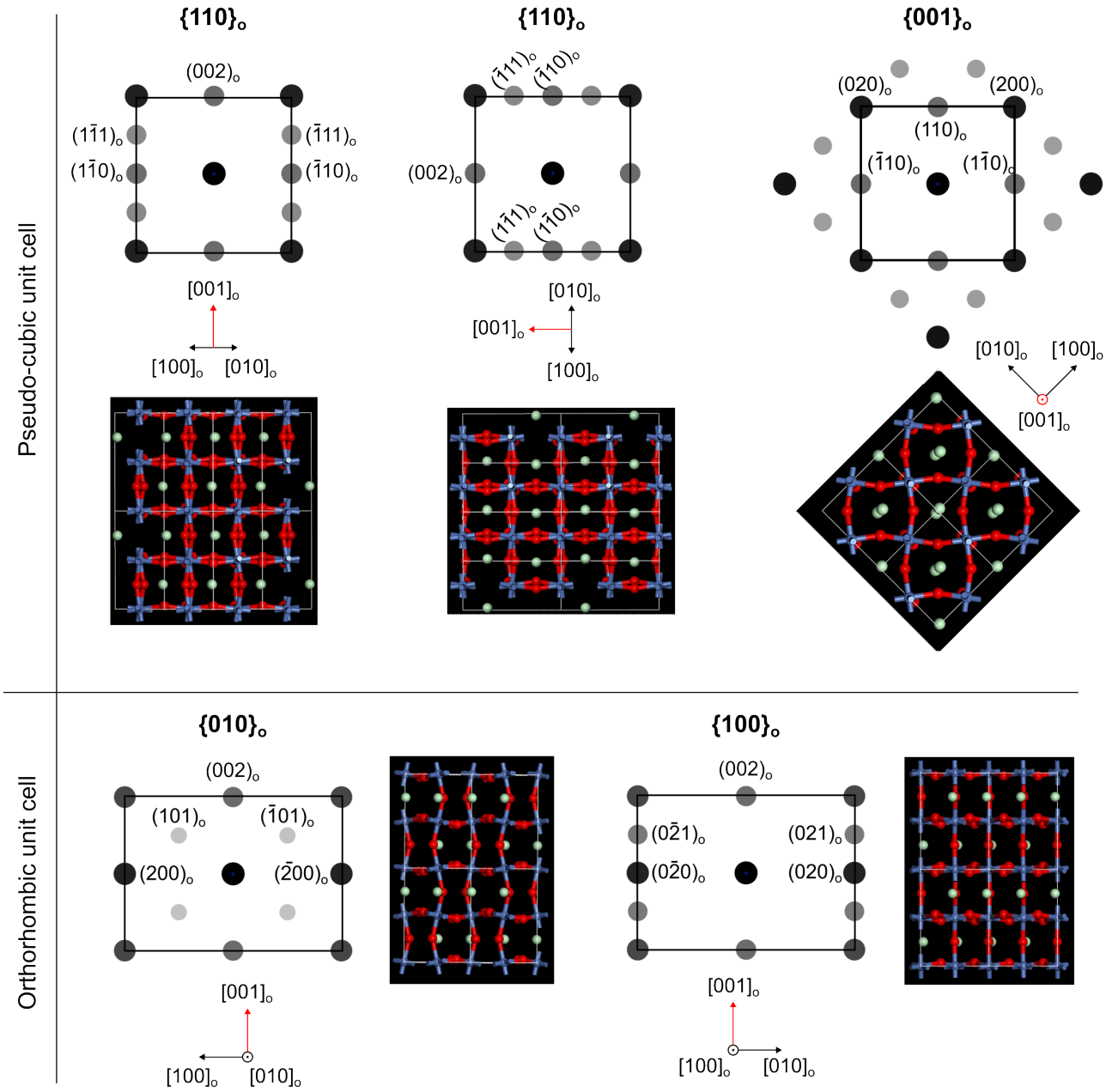


**Figure B.1:** The simulated diffraction patterns of an orthorhombic structure (*Pbnm*) by "JEMS" software, and the corresponding crystal structures in real space. $NdNiO_3$ is used as a reference in this simulation.

# List of abbreviations

| | |
|---|---|
| $[hkl]_c$ | Cubic orientation |
| $[hkl]_o$ | Orthorhombic orientation |
| $[hkl]_{pc}$ | Pesudo-cubic orientation |
| $a_o,\ b_o,\ c_o$ | Orthorhombic lattice parameters |
| $a_{pc}, b_{pc}, c_{pc}$ | Pesudo-cubic lattice parameters |
| ABF | Annular bright-field |
| AFM | Atomic force microscopy |
| ALDA | Adiabatic local-density approximation |
| AZO | Al-doped ZnO |
| BF | Bright-field |
| DSO | $DyScO_3$ |
| EELS | Electron energy loss spectroscopy |
| FDTD | Finite-difference time-domain |
| FE | Ferroelectric |
| FFT | Fast Fourier transform |
| FWHM | Full width at a half maximum |
| GPA | Geometric phase analysis |
| GZO | Ga-doped ZnO |
| HAADF | High-angle annular dark-field |
| ITO | Sn-doped $In_2O_3$ |
| LMO | $LaMnO_3$ |
| LSP | Localized surface plasmon |
| MAADF | Mid-angle annular dark-field |
| MIT | Metal-insulator transition |
| NNO | $NdNiO_3$ |
| PFM | Piezoresponse force microscopy |
| PTO | $PbTiO_3$ |
| PZT | $Pb(Zr,Ti)O_3$ |
| RP fault | Ruddlesden-Popper fault |
| RSM | Reciprocal space maps |
| SRO | $SrRuO_3$ |
| STEM | Scanning transmission electron microscopy |
| STO | $SrTiO_3$ |

| | |
|---|---|
| SVO | $SrVO_3$ |
| SXDM | Scanning X-ray nanodiffraction microscopy |
| TCOs | Transparent conducting oxides |
| TDDFT | Time-dependent density-functional theory |
| TMNs | Transition metal nitrides |
| TMO | Transition metal oxide |
| uc | Unit cell |
| XAS | X-ray absorption spectroscopy |
| XRD | X-ray diffraction |
| ZLP | Zero-loss peak |

# Bibliography


[1] C. N. R. Rao. Transition metal oxides. Annual Review of Physical Chemistry, 40: 291–326, 1989. DOI:10.1146/annurev.pc.40.100189.001451.

[2] M. Hepting. Introduction: Transition metal oxides and their heterostructures. In Ordering Phenomena in Rare-Earth Nickelate Heterostructures, pages 1–12. Springer International Publishing, Cham, 2017. DOI:10.1007/978-3-319-60531-9_1.

[3] P. Zubko, S. Gariglio, M. Gabay, P. Ghosez, and J.-M. Triscone. Interface physics in complex oxide heterostructures. Annual Review of Condensed Matter Physics, 2: 141–165, 2011. DOI:10.1146/annurev-conmatphys-062910-140445.

[4] H. Y. Hwang, Y. Iwasa, M. Kawasaki, B. Keimer, N. Nagaosa, and Y. Tokura. Emergent phenomena at oxide interfaces. Nature Materials, 11:103–113, 2012. DOI:10.1038/nmat3223.

[5] Y. Tokura and N. Nagaosa. Orbital physics in transition-metal oxides. Science, 288: 462–468, 2000. DOI:10.1126/science.288.5465.462.

[6] M. Imada, A. Fujimori, and Y. Tokura. Metal-insulator transitions. Reviews of Modern Physics, 70:1039, 1998. DOI:10.1103/RevModPhys.70.1039.

[7] Z.-X. Shen and D.S. Dessau. Electronic structure and photoemission studies of late transition-metal oxides — Mott insulators and high-temperature superconductors. Physics Reports, 253:1–162, 1995. DOI:10.1016/0370-1573(95)80001-A.

[8] M. Uehara, S. Mori, C. H. Chen, and S.-W. Cheong. Percolative phase separation underlies colossal magnetoresistance in mixed-valent manganites. Nature, 399:560–563, 1999. DOI:10.1038/21142.

[9] X. Yu, L. Wu, B. Zhang, H. Zhou, Y. Dong, X. Wu, R. Kou, P. Yang, J. Chen, C.-J. Sun, Y. Zhu, and G. M. Chow. Thickness-dependent polarization-induced intrinsic magnetoelectric effects in $La_{0.67}Sr_{0.33}MnO_3/PbZr_{0.52}Ti_{0.48}O_3$ heterostructures. Physical Review B, 100:104405, 2019. DOI:10.1103/PhysRevB.100.104405.

[10] H. Chen, Q. Qiao, M. S. J. Marshall, A. B. Georgescu, A. Gulec, P. J. Phillips, R. F. Klie, F. J. Walker, C. H. Ahn, and S. Ismail-Beigi. Reversible modulation of orbital occupations via an interface-induced polar state in metallic manganites. Nano Letters, 14:4965–4970, 2014. DOI:10.1021/nl501209p.

[11] D. Preziosi, M. Alexe, D. Hesse, and M. Salluzzo. Electric-field control of the orbital occupancy and magnetic moment of a transition-metal oxide. Physical Review Letters, 115:157401, 2015. DOI:10.1103/PhysRevLett.115.157401.

[12] C. Liu, Y. Liu, B. Zhang, C.-J. Sun, D. Lan, P. Chen, X. Wu, P. Yang, X. Yu, T. Charl-

ton, M. R. Fitzsimmons, J. Ding, J. Chen, and G. M. Chow. Ferroelectric self-polarization controlled magnetic stratification and magnetic coupling in ultrathin $La_{0.67}Sr_{0.33}MnO_3$ films. ACS Applied Materials & Interfaces, 13:30137–30145, 2021. DOI:10.1021/acsami.1c02300.

[13] J. J. P. Peters, N. C. Bristowe, D. Rusu, G. Apachitei, R. Beanland, M. Alexe, and A. M. Sanchez. Polarization screening mechanisms at $La_{0.7}Sr_{0.3}MnO_3$–$PbTiO_3$ interfaces. ACS Applied Materials & Interfaces, 12:10657–10663, 2020. DOI:10.1021/acsami.9b21619.

[14] L. Zhang, Y. Zhou, L. Guo, W. Zhao, A. Barnes, H.-T. Zhang, C. Eaton, Y. Zheng, M. Brahlek, H. F. Haneef, N. J. Podraza, M. H. W. Chan, V. Gopalan, K. M. Rabe, and R. Engel-Herbert. Correlated metals as transparent conductors. Nature Materials, 15:204–210, 2016. DOI:10.1038/nmat4493.

[15] Chia-Ping Su, Kari Ruotsalainen, Alessandro Nicolaou, Matteo Gatti, and Alexandre Gloter. Plasmonic properties of SrVO3 bulk and nanostructures. Advanced Optical Materials, page 2202415, 2023. DOI:10.1002/adom.202202415.

[16] Y. L. Tang, Y. L. Zhu, X. L. Ma, A. Y. Borisevich, A. N. Morozovska, E. A. Eliseev, W. Y. Wang, Y. J. Wang, Y. B. Xu, Z. D. Zhang, and S. J. Pennycook. Observation of a periodic array of flux-closure quadrants in strained ferroelectric $PbTiO_3$ films. Science, 348:547–551, 2015. DOI:10.1126/science.1259869.

[17] A. K. Yadav, C. T. Nelson, S. L. Hsu, Z. Hong, J. D. Clarkson, C. M. Schlepütz, A. R. Damodaran, P. Shafer, E. Arenholz, L. R. Dedon, D. Chen, A. Vishwanath, A. M. Minor, L. Q. Chen, J. F. Scott, L. W. Martin, and R. Ramesh. Observation of polar vortices in oxide superlattices. Nature, 530:198–201, 2016. DOI:10.1038/nature16463.

[18] K. Du, M. Zhang, C. Dai, Z. N. Zhou, Y. W. Xie, Z. H. Ren, H. Tian, L. Q. Chen, G. Van Tendeloo, and Z. Zhang. Manipulating topological transformations of polar structures through real-time observation of the dynamic polarization evolution. Nature Communications, 10:4864, 2019. DOI:10.1038/s41467-019-12864-5.

[19] M. Hadjimichael, Y. Li, E. Zatterin, G. A. Chahine, M. Conroy, K. Moore, E. N. O' Connell, P. Ondrejkovic, P. Marton, J. Hlinka, U. Bangert, S. Leake, and P. Zubko. Metal-ferroelectric supercrystals with periodically curved metallic layers. Nature Materials, 20:495–502, 2021. DOI:10.1038/s41563-020-00864-6.

[20] S. Li, Y. L. Zhu, Y. J. Wang, Y. L. Tang, Y. Liu, S. R. Zhang, J. Y. Ma, and X. L. Ma. Periodic arrays of flux-closure domains in ferroelectric thin films with oxide electrodes. Applied Physics Letters, 111:052901, 2017. DOI:10.1063/1.4996232.

[21] O. Scherzer. The theoretical resolution limit of the electron microscope. Journal of Applied Physics, 20:20, 1949. DOI:10.1063/1.1698233.

[22] S. J. Pennycook and P. D. Nellist, editors. Scanning Transmission Electron

Microscopy. Springer New York, New York, NY, 2011. DOI:10.1007/978-1-4419-7200-2.

[23] O. L. Krivanek, T. C. Lovejoy, N. Dellby, and R.W. Carpenter. Monochromated STEM with a 30 meV-wide, atom-sized electron probe. Microscopy, 62:3–21, 2013. DOI:10.1093/jmicro/dfs089.

[24] O. L. Krivanek, P. D. Nellist, N. Dellby, M. F. Murfitt, and Z. Szilagyi. Towards sub-0.5 Å electron beams. Ultramicroscopy, 96:229–237, 2003. DOI:10.1016/S0304-3991(03)00090-1.

[25] O. L. Krivanek, T. C. Lovejoy, N. Dellby, T. Aoki, R. W. Carpenter, P. Rez, E. Soignard, J. Zhu, P. E. Batson, M. J. Lagos, R. F. Egerton, and P. A. Crozier. Vibrational spectroscopy in the electron microscope. Nature, 514:209–212, 2014. DOI:10.1038/nature13870.

[26] M. J. Hÿtch, E. Snoeck, and R. Kilaas. Quantitative measurement of displacement and strain fields from HREM micrographs. Ultramicroscopy, 74:131–146, 1998. DOI:10.1016/S0304-3991(98)00035-7.

[27] C. Colliex. From early to present and future achievements of EELS in the TEM. The European Physical Journal Applied Physics, 97:38, 2022. DOI:10.1051/epjap/2022220012.

[28] Y. Y. Wang, S. C. Cheng, V. P. Dravid, and F. C. Zhang. Momentum-transfer resolved electron energy loss spectroscopy of solids: problems, solutions and applications. Ultramicroscopy, 59:109–119, 1995. DOI:10.1016/0304-3991(95)00022-S.

[29] B. C. Larson, W. Ku, J. Z. Tischler, C.-C. Lee, O. D. Restrepo, A. G. Eguiluz, P. Zschack, and K. D. Finkelstein. Nonresonant inelastic X-ray scattering and energy-resolved Wannier function investigation of $d$-$d$ excitations in NiO and CoO. Physical Review Letters, 99:026401, 2007. DOI:10.1103/PhysRevLett.99.026401.

[30] S. Huotari, T. Pylkkänen, G. Vankó, R. Verbeni, P. Glatzel, and G. Monaco. Crystal-field excitations in NiO studied with hard x-ray resonant inelastic x-ray scattering at the Ni $K$ edge. Physical Review B, 78:041102(R), 2008. DOI:10.1103/PhysRevB.78.041102.

[31] A. Gloter, M.-W. Chu, M. Kociak, C. H. Chen, and C. Colliex. Probing non-dipole allowed excitations in highly correlated materials with nanoscale resolution. Ultramicroscopy, 109:1333–1337, 2009. DOI:10.1016/j.ultramic.2009.06.005.

[32] Y. K. Sato, M. Terauchi, and K. Adachi. Anisotropic plasmons due to carrier electrons in Cs-doped hexagonal $WO_3$ studied by momentum transfer resolved electron energy-loss spectroscopy. Journal of Applied Physics, 126:185107, 2019. DOI:10.1063/1.5115068.

[33] R. Senga, K. Suenaga, P. Barone, S. Morishita, F. Mauri, and T. Pichler. Position

and momentum mapping of vibrations in graphene nanostructures. Nature, 573: 247–250, 2019. DOI:10.1038/s41586-019-1477-8.

[34] R. Qi, N. Li, J. Du, R. Shi, Y. Huang, X. Yang, L. Liu, Z. Xu, Q. Dai, D. Yu, and P. Gao. Four-dimensional vibrational spectroscopy for nanoscale mapping of phonon dispersion in BN nanotubes. Nature Communications, 12:1179, 2021. DOI:10.1038/s41467-021-21452-5.

[35] P. Shekhar, M. Malac, V. Gaind, N. Dalili, A. Meldrum, and Z. Jacob. Momentum-resolved electron energy loss spectroscopy for mapping the photonic density of states. ACS Photonics, 4:1009–1014, 2017. DOI:10.1021/acsphotonics.7b00103.

[36] E. Petri and A. Otto. Direct nonvertical interband and intraband transitions in Al. Physical Review Letters, 34:1283, 1975. DOI:10.1103/PhysRevLett.34.1283.

[37] A. Boileau, A. Cheikh, A. Fouchet, A. David, R. Escobar-Galindo, C. Labbé, P. Marie, F. Gourbilleau, and U. Lüders. Optical and electrical properties of the transparent conductor $SrVO_3$ without long-range crystalline order. Applied Physics Letters, 112:021905, 2018. DOI:10.1063/1.5016245.

[38] H. Makino, I. H. Inoue, M. J. Rozenberg, I. Hase, Y. Aiura, and S. Onari. Bandwidth control in a perovskite-type $3d^1$-correlated metal $Ca_{1-x}Sr_xVO_3$. II. Optical spectroscopy. Physical Review B, 58:4384, 1998. DOI:10.1103/PhysRevB.58.4384.

[39] H. He, Z. Yang, Y. Xu, A. T. Smith, G. Yang, and L. Sun. Perovskite oxides as transparent semiconductors: a review. Nano Convergence, 7:32, 2020. DOI:10.1186/s40580-020-00242-7.

[40] A. Boileau, A. Cheikh, A. Fouchet, A. David, C. Labbé, P. Marie, F. Gourbilleau, and U. Lüders. Tuning of the optical properties of the transparent conducting oxide $SrVO_3$ by electronic correlations. Advanced Optical Materials, 7:1801516, 2019. DOI:10.1002/adom.201801516.

[41] M. Mirjolet, H. B. Vasili, L. López-Conesa, S. Estradé, F. Peiró, J. Santiso, F. Sánchez, P. Machado, P. Gargiani, M. Valvidares, and J. Fontcuberta. Independent tuning of optical transparency window and electrical properties of epitaxial $SrVO_3$ thin films by substrate mismatch. Advanced Functional Materials, 29:1904238, 2019. DOI:10.1002/adfm.201904238.

[42] S. Choi, J. Kang, S. Ryu, H. Jeen, J. Son, and S. Lee. High infrared transparency up to 8-$\mu$m-wavelength in correlated vanadium Wadsley conductors. APL Materials, 8:041111, 2020. DOI:10.1063/1.5136059.

[43] Y. Park, J. Roth, D. Oka, Y. Hirose, T. Hasegawa, A. Paul, A. Pogrebnyakov, V. Gopalan, T. Birol, and R. Engel-Herbert. $SrNbO_3$ as a transparent conductor in the visible and ultraviolet spectra. Communications Physics, 3:102, 2020. DOI:10.1038/s42005-020-0372-9.

[44] V. Kapetanovic, I. C. Bicket, S. Lazar, M. J. Lagos, and G. A. Botton. Tunable infrared plasmon response of lithographic Sn-doped indium oxide nanostructures. Advanced Optical Materials, 8:2001024, 2020. DOI:10.1002/adom.202001024.

[45] H. Yang, A. Konečná, X. Xu, S.-W. Cheong, E. Garfunkel, F. J. García de Abajo, and P. E. Batson. Low-loss tunable infrared plasmons in the high-mobility perovskite (Ba,La)$SnO_3$. Small, 18:2106897, 2022. DOI:10.1002/smll.202106897.

[46] Y.-P. Zhu, J. K. El-Demellawi, J. Yin, S. Lopatin, Y. Lei, Z. Liu, X. Miao, O. F. Mohammed, and H. N. Alshareef. Unprecedented surface plasmon modes in monoclinic $MoO_2$ nanostructures. Advanced Materials, 32:1908392, 2020. DOI:10.1002/adma.201908392.

[47] M. Bosman, E. Ye, S. F. Tan, C. A. Nijhuis, J. K. W. Yang, R. Marty, A. Mlayah, A. Arbouet, C. Girard, and M.-Y. Han. Surface plasmon damping quantified with an electron nanoprobe. Scientific Reports, 3:1312, 2013. DOI:10.1038/srep01312.

[48] G. Wang, Z. Wang, M. Meng, M. Saghayezhian, L. Chen, C. Chen, H. Guo, Y. Zhu, E. W. Plummer, and J. Zhang. Role of disorder and correlations in the metal-insulator transition in ultrathin $SrVO_3$ films. Physical Review B, 100:155114, 2019. DOI:10.1103/PhysRevB.100.155114.

[49] D. Preziosi, L. Lopez-Mir, X. Li, T. Cornelissen, J. H. Lee, F. Trier, K. Bouzehouane, S. Valencia, A. Gloter, A. Barthélémy, and M. Bibes. Direct mapping of phase separation across the metal–insulator transition of $NdNiO_3$. Nano Letters, 18:2226–2232, 2018. DOI:10.1021/acs.nanolett.7b04728.

[50] S. Raza, S. Kadkhodazadeh, T. Christensen, M. Di Vece, M. Wubs, N. A. Mortensen, and N. Stenger. Multipole plasmons and their disappearance in few-nanometre silver nanoparticles. Nature Communications, 6:8788, 2015. DOI:10.1038/ncomms9788.

[51] H. Raether. Excitation of Plasmons and Interband Transitions by Electrons. Springer Tracts in Modern Physics. Springer, Berlin Heidelberg, 1980. DOI:10.1007/BFb0045951.

[52] J. Gong, R. Dai, Z. Wang, and Z. Zhang. Thickness dispersion of surface plasmon of Ag nano-thin films: Determination by ellipsometry iterated with transmittance method. Scientific Reports, 5:9279, 2015. DOI:10.1038/srep09279.

[53] S. Suto, K.-D. Tsuei, E. W. Plummer, and E. Burstein. Surface-plasmon energy and dispersion on Ag single crystals. Physical Review Letters, 63:2590, 1989. DOI:10.1103/PhysRevLett.63.2590.

[54] D. E. McNally, X. Lu, J. Pelliciari, S. Beck, M. Dantz, M. Naamneh, T. Shang, M. Medarde, C. W. Schneider, V. N. Strocov, E. V. Pomjakushina, C. Ederer, M. Radovic, and T. Schmitt. Electronic localization in $CaVO_3$ films via bandwidth

control. npj Quantum Materials, 4:6, 2019. DOI:10.1038/s41535-019-0146-3.

[55] M. Cazzaniga, H.-C. Weissker, S. Huotari, T. Pylkkänen, P. Salvestrini, G. Monaco, G. Onida, and L. Reining. Dynamical response function in sodium and aluminum from time-dependent density-functional theory. Physical Review B, 84:075109, 2011. DOI:10.1103/PhysRevB.84.075109.

[56] M. Kociak and O. Stéphan. Mapping plasmons at the nanometer scale in an electron microscope. Chemical Society Reviews, 43:3865–3883, 2014. DOI:10.1039/c3cs60478k.

[57] J. Nelayah, M. Kociak, O. Stéphan, F. J. García de Abajo, M. Tencé, L. Henrard, D. Taverna, I. Pastoriza-Santos, L. M. Liz-Marzán, and C. Colliex. Mapping surface plasmons on a single metallic nanoparticle. Nature Physics, 3:348–353, 2007. DOI:10.1038/nphys575.

[58] O. Nicoletti, F. de la Peña, R. K. Leary, D. J. Holland, C. Ducati, and P. A. Midgley. Three-dimensional imaging of localized surface plasmon resonances of metal nanoparticles. Nature, 502:80–84, 2013. DOI:10.1038/nature12469.

[59] V. Mkhitaryan, K. March, E. N. Tseng, X. Li, L. Scarabelli, L. M. Liz-Marzán, S.-Y. Chen, L. H. G. Tizei, O. Stéphan, J.-M. Song, M. Kociak, F. J. García de Abajo, and A. Gloter. Can copper nanostructures sustain high-quality plasmons? Nano Letters, 21:2444–2452, 2021. DOI:10.1021/acs.nanolett.0c04667.

[60] D. Rossouw, M. Couillard, J. Vickery, E. Kumacheva, and G. A. Botton. Multipolar plasmonic resonances in silver nanowire antennas imaged with a subnanometer electron probe. Nano Letters, 11:1499–1504, 2011. DOI:10.1021/nl200634w.

[61] M. J. Lagos, A. Trügler, U. Hohenester, and P. E. Batson. Mapping vibrational surface and bulk modes in a single nanocube. Nature, 543:529–532, 2017. DOI:10.1038/nature21699.

[62] I. C. Bicket, E. P. Bellido, D. M. McRae, F. Lagugné-Labarthet, and G. A. Botton. Carving plasmon modes in silver Sierpiński fractals. ACS Photonics, 6:2974–2984, 2019. DOI:10.1021/acsphotonics.9b01179.

[63] F. J. García de Abajo and M. Kociak. Probing the photonic local density of states with electron energy loss spectroscopy. Physical Review Letters, 100:106804, 2008. DOI:10.1103/PhysRevLett.100.106804.

[64] Y. Cao, A. Manjavacas, N. Large, and P. Nordlander. Electron energy-loss spectroscopy calculation in finite-difference time-domain package. ACS Photonics, 2: 369–375, 2015. DOI:10.1021/ph500408e.

[65] A. C. Lesina, A. Vaccari, P. Berini, and L. Ramunno. On the convergence and accuracy of the FDTD method for nanoplasmonics. Optics Express, 23:10481–10497, 2015. DOI:10.1364/OE.23.010481.

[66] N. Okada and J. B. Cole. Effective permittivity for FDTD calculation of plasmonic materials. Micromachines, 3:168–179, 2012. DOI:10.3390/mi3010168.

[67] A. Vial, T. Laroche, M. Dridi, and L. Le Cunff. A new model of dispersion for metals leading to a more accurate modeling of plasmonic structures using the FDTD method. Applied Physics A, 103:849–853, 2011. DOI:10.1007/s00339-010-6224-9.

[68] G.-Y. Yao, Q.-L. Liu, and Z.-Y. Zhao. Studied localized surface plasmon resonance effects of Au nanoparticles on $TiO_2$ by FDTD simulations. Catalysts, 8:236, 2018. DOI:10.3390/catal8060236.

[69] F. J. García de Abajo. Optical excitations in electron microscopy. Reviews of Modern Physics, 82:209, 2010. DOI:10.1103/RevModPhys.82.209.

[70] K. Yee. Numerical solution of initial boundary value problems involving maxwell's equations in isotropic media. IEEE Transactions on Antennas and Propagation, 14: 302–307, 1966. DOI:10.1109/TAP.1966.1138693.

[71] B. Ögüt, R. Vogelgesang, W. Sigle, N. Talebi, C. T. Koch, and P. A. van Aken. Hybridized metal slit eigenmodes as an illustration of Babinet's principle. ACS Nano, 5:6701–6706, 2011. DOI:10.1021/nn2022414.

[72] C. Huck, J. Vogt, M. Sendner, D. Hengstler, F. Neubrech, and A. Pucci. Plasmonic enhancement of infrared vibrational signals: nanoslits versus nanorods. ACS Photonics, 2:1489–1497, 2015. DOI:10.1021/acsphotonics.5b00390.

[73] M. Horák, V. Křápek, M. Hrtoň, A. Konečná, F. Ligmajer, M. Stöger-Pollach, T. Šamořil, A. Paták, Z. Édes, O. Metelka, J. Babocký, and T. Šikola. Limits of Babinet's principle for solid and hollow plasmonic antennas. Scientific Reports, 9:4004, 2019. DOI:10.1038/s41598-019-40500-1.

[74] E. L. Runnerstrom, A. Bergerud, A. Agrawal, R. W. Johns, C. J. Dahlman, A. Singh, S. M. Selbach, and D. J. Milliron. Defect engineering in plasmonic metal oxide nanocrystals. Nano Letters, 16:3390–3398, 2016. DOI:10.1021/acs.nanolett.6b01171.

[75] A. Boltasseva and H. A. Atwater. Low-loss plasmonic metamaterials. Science, 331: 290–291, 2011. DOI:10.1126/science.1198258.

[76] P. R. West, S. Ishii, G. V. Naik, N. K. Emani, V. M. Shalaev, and A. Boltasseva. Searching for better plasmonic materials. Laser & Photonics Reviews, 4:795–808, 2010. DOI:10.1002/lpor.200900055.

[77] J. B. Khurgin. Replacing noble metals with alternative materials in plasmonics and metamaterials: how good an idea? Philosophical Transactions of the Royal Society A: Mathematical, Physical and Engineering Sciences, 375:20160068, 2017. DOI:10.1098/rsta.2016.0068.

[78] J. B. Khurgin and A. Boltasseva. Reflecting upon the losses in plasmonics and meta-

materials. MRS Bulletin, 37:768–779, 2012. DOI:10.1557/mrs.2012.173.

[79] G. V. Naik, V. M. Shalaev, and A. Boltasseva. Alternative plasmonic materials: beyond gold and silver. Advanced Materials, 25:3264–3294, 2013. DOI:10.1002/adma.201205076.

[80] W. S. M. Werner, K. Glantschnig, and C. Ambrosch-Draxl. Optical constants and inelastic electron-scattering data for 17 elemental metals. Journal of Physical and Chemical Reference Data, 38:1013, 2009. DOI:10.1063/1.3243762.

[81] Y. Wang, A. Capretti, and L. Dal Negro. Wide tuning of the optical and structural properties of alternative plasmonic materials. Optical Materials Express, 5:2415–2430, 2015. DOI:10.1364/OME.5.002415.

[82] A. Fouchet, M. Allain, B. Bérini, E. Popova, P.-E. Janolin, N. Guiblin, E. Chikoidze, J. Scola, D. Hrabovsky, Y. Dumont, and N. Keller. Study of the electronic phase transition with low dimensionality in $SrVO_3$ thin films. Materials Science and Engineering: B, 212:7–13, 2016. DOI:10.1016/j.mseb.2016.07.009.

[83] N. A. Pertsev, A. G. Zembilgotov, and A. K. Tagantsev. Effect of mechanical boundary conditions on phase diagrams of epitaxial ferroelectric thin films. Physical Review Letters, 80:1988, 1998. DOI:10.1103/PhysRevLett.80.1988.

[84] D. G. Schlom, L.-Q. Chen, C.-B. Eom, K. M Rabe, S. K Streiffer, and J.-M. Triscone. Strain tuning of ferroelectric thin films. Annual Review of Materials Research, 37:589–626, 2007. DOI:10.1146/annurev.matsci.37.061206.113016.

[85] C.-L. Jia, K. W. Urban, M. Alexe, D. Hesse, and I. Vrejoiu. Direct observationo of continuous electric dipole rotation in flux-closure domains in ferroelectric $Pb(Zr,Ti)O_3$. Science, 331:1420–1423, 2011. DOI:10.1126/science.1200605.

[86] S. Das, Y. L. Tang, Z. Hong, M. A. P. Gonçalves, M. R. McCarter, C. Klewe, K. X. Nguyen, F. Gómez-Ortiz, P. Shafer, E. Arenholz, V. A. Stoica, S.-L. Hsu, B. Wang, C. Ophus, J. F. Liu, C. T. Nelson, S. Saremi, B. Prasad, A. B. Mei, D. G. Schlom, J. Íñiguez, P. García-Fernández, D. A. Muller, L. Q. Chen, J. Junquera, L. W. Martin, and R. Ramesh. Observation of room-temperature polar skyrmions. Nature, 568:368–372, 2019. DOI:10.1038/s41586-019-1092-8.

[87] X. Li, C. Tan, C. Liu, P. Gao, Y. Sun, P. Chen, M. Li, L. Liao, R. Zhu, J. Wang, Y. Zhao, L. Wang, Z. Xu, K. Liu, X. Zhong, J. Wang, and X. Bai. Atomic-scale observations of electrical and mechanical manipulation of topological polar flux closure. Proceedings of the National Academy of Sciences, 117:18954–18961, 2020. DOI:10.1073/pnas.2007248117.

[88] R. Egoavil, H. Tan, J. Verbeeck, S. Bals, B. Smith, B. Kuiper, G. Rijnders, G. Koster, and G. Van Tendeloo. Atomic scale investigation of a $PbTiO_3/SrRuO_3/DyScO_3$ heterostructure. Applied Physics Letters, 102:223106, 2013. DOI:10.1063/1.4809597.

[89] J. Junquera and P. Ghosez. Critical thickness for ferroelectricity in perovskite ultrathin films. Nature, 422:506–509, 2003. DOI:10.1038/nature01501.

[90] M. Stengel, D. Vanderbilt, and N. A. Spaldin. Enhancement of ferroelectricity at metal-oxide interfaces. Nature Materials, 8:392–397, 2009. DOI:10.1038/nmat2429.

[91] J. J. P. Peters, G. Apachitei, R. Beanland, M. Alexe, and A. M. Sanchez. Polarization curling and flux closures in multiferroic tunnel junctions. Nature Communications, 7:13484, 2016. DOI:10.1038/ncomms13484.

[92] B. Veličkov, V. Kahlenberg, R. Bertram, and M. Bernhagen. Crystal chemistry of $GdScO_3$, $DyScO_3$, $SmScO_3$ and $NdScO_3$. Zeitschrift für Kristallographie, 222:466–473, 2007. DOI:10.1524/zkri.2007.222.9.466.

[93] J. C. Jiang, W. Tian, X. Pan, Q. Gan, and C. B. Eom. Effects of miscut of the $SrTiO_3$ substrate on microstructures of the epitaxial $SrRuO_3$ thin films. Materials Science and Engineering: B, 56:152–157, 1998. DOI:10.1016/S0921-5107(98)00227-X.

[94] O. Nesterov, S. Matzen, C. Magen, A. H. G. Vlooswijk, G. Catalan, and B. Noheda. Thickness scaling of ferroelastic domains in $PbTiO_3$ films on $DyScO_3$. Applied Physics Letters, 103:142901, 2013. DOI:10.1063/1.4823536.

[95] K. Lee and S. Baik. Ferroelastic domain structure and switching in epitaxial ferroelectric thin films. Annual Review of Materials Research, 36:81–116, 2006. DOI:10.1146/annurev.matsci.36.090804.094613.

[96] S. J. Leake, G. A. Chahine, H. Djazouli, T. Zhou, C. Richter, J. Hilhorst, L. Petit, M.-I. Richard, C. Morawe, R. Barrett, L. Zhang, R. A. Homs-Regojo, V. Favre-Nicolin, P. Boesecke, and T. U. Schülli. The Nanodiffraction beamline ID01/ESRF: a microscope for imaging strain and structure. Journal of Synchrotron Radiation, 26:571–584, 2019. DOI:10.1107/S160057751900078X.

[97] S. Prosandeev and L. Bellaiche. Asymmetric screening of the depolarizing field in a ferroelectric thin film. Physical Review B, 75:172109, 2007. DOI:10.1103/PhysRevB.75.172109.

[98] L. Lu, Y. Nahas, M. Liu, H. Du, Z. Jiang, S. Ren, D. Wang, L. Jin, S. Prokhorenko, C.-L. Jia, and L. Bellaiche. Topological defects with distinct dipole configurations in $PbTiO_3/SrTiO_3$ multilayer films. Physical Review Letters, 120:177601, 2018. DOI:10.1103/PhysRevLett.120.177601.

[99] Y. Liu, Y.-J. Wang, Y.-L. Zhu, C.-H. Lei, Y.-L. Tang, S. Li, S.-R. Zhang, J. Li, and X.-L. Ma. Large scale two-dimensional flux-closure domain arrays in oxide multilayers and their controlled growth. Nano Letters, 17:7258–7266, 2017. DOI:10.1021/acs.nanolett.7b02615.

[100] G. Catalan, A. Lubk, A. H. G. Vlooswijk, E. Snoeck, C. Magen, A. Janssens, G. Rispens, G. Rijnders, D. H. A. Blank, and B. Noheda. Flexoelectric rotation

of polarization in ferroelectric thin films. Nature Materials, 10:963–967, 2011. DOI:10.1038/nmat3141.

[101] W. Wang, L. Li, J. Liu, B. Chen, Y. Ji, J. Wang, G. Cheng, Y. Lu, G. Rijnders, G. Koster, W. Wu, and Z. Liao. Magnetic domain engineering in $SrRuO_3$ thin films. npj Quantum Materials, 5:73, 2020. DOI:10.1038/s41535-020-00275-5.

[102] C. W. Huang, Z. H. Chen, and L. Chen. Thickness-dependent evolutions of domain configuration and size in ferroelectric and ferroelectric-ferroelastic films. Journal of Applied Physics, 113:094101, 2013. DOI:10.1063/1.4794005.

[103] N. A. Pertsev and A. G. Zembilgotov. Energetics and geometry of 90° domain structures in epitaxial ferroelectric and ferroelastic films. Journal of Applied Physics, 78: 6170, 1995. DOI:10.1063/1.360561.

[104] S. Catalano, M. Gibert, J. Fowlie, J. Íñiguez, J.-M. Triscone, and J. Kreisel. Rare-earth nickelates $R$$NiO_3$: thin films and heterostructures. Reports on Progress in Physics, 81:046501, 2018. DOI:10.1088/1361-6633/aaa37a.

[105] M. L. Medarde. Structural, magnetic and electronic properties of $RNiO_3$ perovskites (R = rare earth). Journal of Physics: Condensed Matter, 9:1679–1707, 1997. DOI:10.1088/0953-8984/9/8/003.

[106] J. B. Torrance, P. Lacorre, A. I. Nazzal, E. J. Ansaldo, and Ch. Niedermayer. Systematic study of insulator-metal transitions in perovskites $R$$NiO_3$ ($R$=Pr,Nd,Sm,Eu) due to closing of charge-transfer gap. Physical Review B, 45:8209(R), 1992. DOI:10.1103/PhysRevB.45.8209.

[107] J. Liu, M. Kargarian, M. Kareev, B. Gray, P. J. Ryan, A. Cruz, N. Tahir, Y.-D. Chuang, J. Guo, J. M. Rondinelli, J. W. Freeland, G. A. Fiete, and J. Chakhalian. Heterointerface engineered electronic and magnetic phases of $NdNiO_3$ thin films. Nature Communications, 4:2714, 2013. DOI:10.1038/ncomms3714.

[108] J. Mannhart and D. G. Schlom. Oxide interfaces—An opportunity for electronics. Science, 327:1607–1611, 2010. DOI:10.1126/science.1181862.

[109] J. Y. Zhang, H. Kim, E. Mikheev, A. J. Hauser, and S. Stemmer. Key role of lattice symmetry in the metal-insulator transition of $NdNiO_3$ films. Scientific Reports, 6: 23652, 2016. DOI:10.1038/srep23652.

[110] T. H. Kim, T. R. Paudel, R. J. Green, K. Song, H.-S. Lee, S.-Y. Choi, J. Irwin, B. Noesges, L. J. Brillson, M. S. Rzchowski, G. A. Sawatzky, E. Y. Tsymbal, and C. B. Eom. Strain-driven disproportionation at a correlated oxide metal-insulator transition. Physical Review B, 101:121105(R), 2020. DOI:10.1103/PhysRevB.101.121105.

[111] J. Bak, H. B. Bae, C. Oh, J. Son, and S.-Y. Chung. Effect of lattice strain on the formation of Ruddlesden–Popper faults in heteroepitaxial $LaNiO_3$ for oxygen evolution electrocatalysis. Journal of Physical Chemistry Letters, 11:7253–7260, 2020.

DOI:10.1021/acs.jpclett.0c01426.

[112] C. Coll, L. López-Conesa, J. M. Rebled, C. Magén, F. Sánchez, J. Fontcuberta, S. Estradé, and F. Peiró. Simulation of STEM-HAADF image contrast of Ruddlesden–Popper faulted $LaNiO_3$ thin films. Journal of Physical Chemistry C, 121:9300–9304, 2017. DOI:10.1021/acs.jpcc.6b12484.

[113] B. Mundet, J. Jareño, J. Gazquez, M. Varela, X. Obradors, and T. Puig. Defect landscape and electrical properties in solution-derived $LaNiO_3$ and $NdNiO_3$ epitaxial thin films. Physical Review Materials, 2:063607, 2018. DOI:10.1103/PhysRevMaterials.2.063607.

[114] S. J. May, J.-W. Kim, J. M. Rondinelli, E. Karapetrova, N. A. Spaldin, A. Bhattacharya, and P. J. Ryan. Quantifying octahedral rotations in strained perovskite oxide films. Physical Review B, 82:014110, 2010. DOI:10.1103/PhysRevB.82.014110.

[115] Q. He, R. Ishikawa, A. R. Lupini, L. Qiao, E. J. Moon, O. Ovchinnikov, S. J. May, M. D. Biegalski, and A. Y. Borisevich. Towards 3D mapping of $BO_6$ octahedron rotations at perovskite heterointerfaces, unit cell by unit cell. ACS Nano, 9:8412–8419, 2015. DOI:10.1021/acsnano.5b03232.

[116] A. Vailionis, H. Boschker, W. Siemons, E. P. Houwman, D. H. A. Blank, G. Rijnders, and G. Koster. Misfit strain accommodation in epitaxial $ABO_3$ perovskites: Lattice rotations and lattice modulations. Physical Review B, 83:064101, 2011. DOI:10.1103/PhysRevB.83.064101.

[117] J. A. Alonso, J. L. García-Muñoz, M. T. Fernández-Díaz, M. A. G. Aranda, M. J. Martínez-Lope, and M. T. Casais. Charge disproportionation in $RNiO_3$ perovskites: Simultaneous metal-insulator and structural transition in $YNiO_3$. Physical Review Letters, 82:3871, 1999. DOI:10.1103/PhysRevLett.82.3871.

[118] M. Zaghrioui, A. Bulou, P. Lacorre, and P. Laffez. Electron diffraction and Raman scattering evidence of a symmetry breaking at the metal-insulator transition of $NdNiO_3$. Physical Review B, 64:081102(R), 2001. DOI:10.1103/PhysRevB.64.081102.

[119] S. Johnston, A. Mukherjee, I. Elfimov, M. Berciu, and G. A. Sawatzky. Charge disproportionation without charge transfer in the rare-earth-element nickelates as a possible mechanism for the metal-insulator transition. Physical Review Letters, 112:106404, 2014. DOI:10.1103/PhysRevLett.112.106404.

[120] R. J. Green, M. W. Haverkort, and G. A. Sawatzky. Bond disproportionation and dynamical charge fluctuations in the perovskite rare-earth nickelates. Physical Review B, 94:195127, 2016. DOI:10.1103/PhysRevB.94.195127.

[121] L. C. Moreno, J. S. Valencia, D. A. Landínez Téllez, J. Arbey Rodríguez M., M. L. Martínez, J. Roa-Rojas, and F. Fajardo. Preparation and structural study of $LaMnO_3$

magnetic material. Journal of Magnetism and Magnetic Materials, 320:e19–e21, 2008. DOI:10.1016/j.jmmm.2008.02.052.

[122] P. Norby, I. G. Krogh Andersen, E. Krogh Andersen, and N. H. Andersen. The crystal structure of lanthanum manganate(iii), $LaMnO_3$, at room temperature and at 1273 K under $N_2$. Journal of Solid State Chemistry, 119:191–196, 1995. DOI:10.1016/0022-4596(95)80028-N.

[123] J. L. García-Muñoz, M. A. G. Aranda, J. A. Alonso, and M. J. Martínez-Lope. Structure and charge order in the antiferromagnetic band-insulating phase of $NdNiO_3$. Physical Review B, 79:134432, 2009. DOI:10.1103/PhysRevB.79.134432.

[124] P.-E. Janolin, B. Fraisse, B. Dkhil, F. Le Marrec, and E. Ringgaard. Domain structure sequence in ferroelectric $Pb(Zr_{0.2}Ti_{0.8})O_3$ thin film on MgO. Applied Physics Letters, 90:162906, 2007. DOI:10.1063/1.2727563.

[125] D. Lee, A. Yoon, S. Y. Jang, J.-G. Yoon, J.-S. Chung, M. Kim, J. F. Scott, and T. W. Noh. Giant flexoelectric effect in ferroelectric epitaxial thin films. Physical Review Letters, 107:057602, 2011. DOI:10.1103/PhysRevLett.107.057602.

[126] B. C. Jeon, D. Lee, M. H. Lee, S. M. Yang, S. C. Chae, T. K. Song, S. D. Bu, J. S. Chung, J. G. Yoon, and T. W. Noh. Flexoelectric effect in the reversal of self-polarization and associated changes in the electronic functional properties of $BiFeO_3$ thin films. Advanced Materials, 25:5643–5649, 2013. DOI:10.1002/adma.201301601.

[127] D. Lee, B. C. Jeon, A. Yoon, Y. J. Shin, M. H. Lee, T. K. Song, S. D. Bu, M. Kim, J.-S. Chung, J.-G. Yoon, and T. W. Noh. Flexoelectric control of defect formation in ferroelectric epitaxial thin films. Advanced Materials, 26:5005–5011, 2014. DOI:10.1002/adma.201400654.

[128] W. Ma and L. E. Cross. Flexoelectric effect in ceramic lead zirconate titanate. Applied Physics Letters, 86:072905, 2005. DOI:10.1063/1.1868078.

[129] S. C. Abrahams, S. K. Kurtz, and P. B. Jamieson. Atomic displacement relationship to Curie temperature and spontaneous polarization in displacive ferroelectrics. Physical Review, 172:551, 1968. DOI:10.1103/PhysRev.172.551.

[130] Y. Z. Dai, L. Lu, F. Zhang, L. Jin, Y. Jiang, D. W. Wang, Z. P. Li, and C.-L. Jia. Atomic-scale understanding of enhanced polarization of highly strained nanoscale columnar $PbTiO_3$. Physical Review B, 104:184111, 2021. DOI:10.1103/PhysRevB.104.184111.

[131] P. Yu, W. Luo, D. Yi, J. X. Zhang, M. D. Rossell, C.-H. Yang, L. You, G. Singh-Bhalla, S. Y. Yang, Q. He, Q. M. Ramasse, R. Erni, L. W. Martin, Y. H. Chu, S. T. Pantelides, S. J. Pennycook, and R. Ramesh. Interface control of bulk ferroelectric polarization. Proceedings of the National Academy of Sciences, 109:9710–9715, 2012. DOI:10.1073/pnas.1117990109.

[132] D. Li, D. Zheng, J. Gong, W. Zheng, C. Jin, and H. Bai. Self-poling-induced magnetoelectric effect in highly strained epitaxial $BiFeO_3/La_{0.67}Sr_{0.33}MnO_{3-\delta}$ multiferroic heterostructures. ACS Applied Materials & Interfaces, 9:24331–24338, 2017. DOI:10.1021/acsami.7b05803.

[133] P. Gao, H.-J. Liu, Y.-L. Huang, Y.-H. Chu, R. Ishikawa, B. Feng, Y. Jiang, N. Shibata, E.-G. Wang, and Y. Ikuhara. Atomic mechanism of polarization-controlled surface reconstruction in ferroelectric thin films. Nature Communications, 7:11318, 2016. DOI:10.1038/ncomms11318.

[134] R. Jacobs, J. Booske, and D. Morgan. Understanding and controlling the work function of perovskite oxides using density functional theory. Advanced Functional Materials, 26:5471–5482, 2016. DOI:10.1002/adfm.201600243.

[135] J. Roqueta, A. Pomar, L. Balcells, C. Frontera, S. Valencia, R. Abrudan, B. Bozzo, Z. Konstantinović, J. Santiso, and B. Martínez. Strain-engineered ferromagnetism in $LaMnO_3$ thin films. Crystal Growth & Design, 15:5332–5337, 2015. DOI:10.1021/acs.cgd.5b00884.

[136] X. Guan, X. Shen, J. Zhang, W. Wang, J. Zhang, H. Wang, W. Wang, Y. Yao, J. Li, C. Gu, J. Sun, and R. Yu. Tuning magnetism and crystal orientations by octahedral coupling in $LaCoO_3/LaMnO_3$ thin films. Physical Review B, 100:014427, 2019. DOI:10.1103/PhysRevB.100.014427.

[137] B. Pang, L. Sun, X. Shen, Y.-Y. Lv, X. Li, F.-X. Wu, S.-H. Yao, J. Zhou, S.-T. Zhang, and Y.B. Chen. The microstructural characterization of multiferroic $LaFeO_3$-$YMnO_3$ multilayers grown on (001)- and (111)-$SrTiO_3$ substrates by transmission electron microscopy. Materials, 10:839, 2017. DOI:10.3390/ma10070839.

[138] A. K. Choquette, C. R. Smith, R. J. Sichel-Tissot, E. J. Moon, M. D. Scafetta, E. Di Gennaro, F. Miletto Granozio, E. Karapetrova, and S. J. May. Octahedral rotation patterns in strained $EuFeO_3$ and other *Pbnm* perovskite films: Implications for hybrid improper ferroelectricity. Physical Review B, 94:024105, 2016. DOI:10.1103/PhysRevB.94.024105.

[139] C. Yang, Y. Wang, D. Putzky, W. Sigle, H. Wang, R. A. Ortiz, G. Logvenov, E. Benckiser, B. Keimer, and P. A. van Aken. Ruddlesden–Popper faults in $NdNiO_3$ thin films. Symmetry, 14:464, 2022. DOI:10.3390/sym14030464.

[140] J. Bak and S.-Y. Chung. Observation of fault-free coherent layer during Ruddlesden–Popper faults generation in $LaNiO_3$ thin films. Journal of the Korean Ceramic Society, 58:169–177, 2021. DOI:10.1007/s43207-020-00080-7.

[141] T. Kiguchi, Y. Kodama, T. Shimizu, T. Shiraishi, N. Wakiya, and T. J. Konno. Interface structure of $Pb(Zr,Ti)O_3/MgO(001)$ epitaxial thin film in early stage of Stranski–Krastanov growth mode. Japanese Journal of Applied Physics, 58:SLLA08,

2019. DOI:10.7567/1347-4065/ab3b13.

[142] V. Bisogni, S. Catalano, R. J. Green, M. Gibert, R. Scherwitzl, Y. Huang, V. N. Strocov, P. Zubko, S. Balandeh, J.-M. Triscone, G. Sawatzky, and T. Schmitt. Ground-state oxygen holes and the metal–insulator transition in the negative charge-transfer rare-earth nickelates. Nature Communications, 7:13017, 2016. DOI:10.1038/ncomms13017.

[143] M. G. Blaber, M. D. Arnold, and M. J. Ford. A review of the optical properties of alloys and intermetallics for plasmonics. Journal of Physics: Condensed Matter, 22: 143201, 2010. DOI:10.1088/0953-8984/22/14/143201.

[144] G. V. Naik, J. Kim, and A. Boltasseva. Oxides and nitrides as alternative plasmonic materials in the optical range [Invited]. Optical Materials Express, 1:1090–1099, 2011. DOI:10.1364/OME.1.001090.

[145] D. Li and C. Z. Ning. All-semiconductor active plasmonic system in mid-infrared wavelengths. Optics Express, 19:14594–14603, 2011. DOI:10.1364/OE.19.014594.

[146] A. J. Hoffman, L. Alekseyev, S. S. Howard, K. J. Franz, D. Wasserman, V. A. Podolskiy, E. E. Narimanov, D. L. Sivco, and C. Gmachl. Negative refraction in semiconductor metamaterials. Nature Materials, 6:946–950, 2007. DOI:10.1038/nmat2033.

[147] X. Liu and M. T. Swihart. Heavily-doped colloidal semiconductor and metal oxide nanocrystals: an emerging new class of plasmonic nanomaterials. Chemical Society Reviews, 43:3908–3920, 2014. DOI:10.1039/C3CS60417A.

[148] U. Guler, G. V. Naik, A. Boltasseva, V. M. Shalaev, and A. V. Kildishev. Performance analysis of nitride alternative plasmonic materials for localized surface plasmon applications. Applied Physics B, 107:285–291, 2012. DOI:10.1007/s00340-012-4955-3.

[149] M. B. Cortie, J. Giddings, and A. Dowd. Optical properties and plasmon resonances of titanium nitride nanostructures. Nanotechnology, 21:115201, 2010. DOI:10.1088/0957-4484/21/11/115201.